UNIVERSITÀ
DEGLI STUDI
DI PADOVA

Head Office: Università degli Studi di Padova

Department of Biology

Ph.D COURSE IN: BIOSCIENCE

CURRICULUM: BIOCHEMESTRY AND BIOTECHNOLOGY

SERIES: XXXI°

Nanocomposite scaffolds and biomimetic peptides in neural regenerative medicine

Coordinator: Ch.mo Prof. Ildikò Szabò

Supervisor: Ch.mo Prof. Francesco Filippini

Ph.D student: Yuriko Suemi Hernandez Gomez

INDEX

ABSTRACT

The incapacity of injured adult central nervous system to restore damaged neuronal circuitry and the large peripheral nervous system nerve defect inability to be naturally regenerated are a critical medical and social issue.

An emerging approach in neuronal regenerative medicine is the use of native extracellular stimuli at nano-scale level influencing cell growth, differentiation and regeneration. Our biomimetic nanosystems mimic as much as possible the nanotopographic, conductive features and guidance cues of the neuronal extracellular environment. They are made of a freestanding and biocompatible nanocomposite scaffold, combining conductive, mechanical and topographical feature of carbon-based nanomaterials with the biocompatible properties of the poly-L-lactic acid (PLLA) matrix. Moreover, biomimetic peptides have been developed deriving them from neuronal proteins involved in the control of neurite outgrowth and axon pathfinding. In recent work from our team, the combination of the nanocomposite scaffold and the peptides proved to enhance neuronal differentiation of a human neuroblastoma cell line and to promote *per se* neural differentiation of human multipotent stem cells, even in the absence of exogenously added neurotrophins.

In my PhD project I further developed such biomimetic nanosystems.

About the scaffold, we checked the biocompatibility and effect on neuronal differentiation of varying types and concentration of nanofiller. We increased from 0.25 to 5% CNTs dispersed in the PLLA-matrix to improve electrical conductivity and nanoroughness of our nanocomposite scaffold. The enhanced CNTs concentration doesn't affect cell proliferation, viability and adhesion while promoting neurite elongation. Moreover, we tested the same range of carbon nanohorns (CNHs) and reduced graphene oxide (RGO) dispersed in the PLLA matrix and proved they are as biocompatible as CNTs. Interestingly, 5%RGO has an inductive effect on neuronal differentiation. In last months, 3D printing has been used for patterned scaffold that allow to control the cell growth direction.

About biomimetic peptides, we focused on the characterization of novel peptides sharing a conserved motif to better reproduce neuronal biochemical cues. These peptides are derived from the Ig-like domain of a number of proteins playing important roles in neuronal differentiation and axon elongation: CHL1, Neurofascin, NrCAM, DCC, ROBO2 and 3, Contactin 1, 2 and 5. All such peptides were able to promote neuritogenesis and neuronal differentiation of SH-SY5Y cells, with efficacy similar to previously tested peptides.

In order to shed light on the mechanism by which our peptides act, we studied L1-A peptide in comparison to L1CAM extracellular domain it is derived from. As negative controls we used a scrambled and mutant version of the L1-A peptide. In silico simulations and in vitro evidence suggest an agonist-antagonist mechanism for our peptides: L1-A peptide binds L1CAM and exerts the same neuritogenic effect of the protein acting as L1CAM's agonist; scrambled and mutant peptides bind the protein and inhibit the L1CAM homophilic binding, but they are not able to activate the signalling intracellular pathway leading to neuronal differentiation, acting as antagonists of L1CAM.

In conclusion, our new nanocomposite scaffold and biomimetic peptides are potential tools for neuronal regenerative medicine, even if further investigations are needed to check their effect in combination.

ABBREVIATIONS

AA: aminoacid
AFSCs: Amniotic fluid-derived stem cells
AMD: age-related macular degeneration
ANS: autonomic nervous system
BDNF: Brain-derived neurotrophic factor
Calcein-AM: Calcein acetoxymethyl ester
CAMs: Cell adhesion molecules
CD: Circular dichroism
CMCs: Circulating multipotent cells
CNHs: carbon nanohorns
CNS: Central nervous system
CNTs: Carbon nanotubes
Da: Dalton
DMEM/F-12: Dulbecco's Modified Eagle Medium/Nutrient Mixture F-12
DMSO: Dimethyl sulfoxide
DRG: Dorsal root ganglion
ECM: Extracellular matrix
EGF: Epidermal growth factor
ER: endoplasmic reticulum
ESCs: Embryonic stem cells
FBS: Foetal bovine serum
FDA: Food and Drug Administration
FnIII: Fibronectin type III
GFP: Green fluorescent protein
GO: graphene oxide
GPI: glycosyl phosphatidyl inositol
HBSS: Hank's Balanced Salt Solution
hCMCs: Human circulating multipotent cells
Ig: Immunoglobulin
iNCs: induced neuronal cells
iNSCs: induced neuronal stem cells
iPSCs: induced pluripotent stem cells
LDH: Lactate dehydrogenase
LRR: Leucine rich repeat
MAG: myelin-associated glycoprotein
MAP2: Microtubule associated protein 2
MS: Mass Spectroscopy

MSCs: mesenchymal stem cells
MTs: Microtubules
MWCNTs: Multi-walled carbon nanotubes
MW: Molecular Weight
NGC: nerve guide conduit
NCAM: Neural cell adhesion molecule
NeuN: Neuronal nuclear antigen
NSCs: Neural stem cells
PBS: Phosphate buffered saline
PCL: Poly-caprolactone
PCR: Polymerase Chain Reaction
PhOMe: Methoxyphenyl group
PLGA: Poly-lactic-co-glycolic acid
PLLA: Poly-L-lactic acid
PM: plasma membrane
PNS: peripheral nervous system
Ppy: Polypyrrole
PSCs: pluripotent stem cells
PVA: Poly-vinyl alcohol
RA: all-trans-retinoic acid RARE:
RARE: Retinoic acid response element
RARs: Retinoic acid receptors
RGO: reduced graphene oxide
REST: Repressor Element-1 Silencing Transcription factor
RP-HPLC: Reversed-phase high-performance liquid chromatography
RTKs: Receptor tyrosine kinases
SCI: Spinal cord injury
SWCNTs: Single-walled carbon nanotubes
SWCNHs: Single-walled carbon nanohorns
SYP: Synaptophysin
TBI: traumatic brain injury
TRKB: Tyrosine receptor kinase B
TUBβ3: Tubulin β III
VAMP7: Vesicle associated membrane protein 7

AMINOACID ABBREVIATIONS

Aminoacid	Three-letter code	One-letter code
Alanine	Ala	A
Arginine	Arg	R
Asparagine	Asn	N
Aspartic Acid	Asp	D
Cysteine	Cys	C
Phenilalanine	Phe	F
Glycine	Gly	G
Glutamic Acid	Glu	E
Glutamine	Gln	Q
Isoleucine	Ile	I
Histidine	His	H
Leucine	Leu	L
Lysine	Lys	K
Methionine	Met	M
Proline	Pro	P
Serine	Ser	S
Tyrosine	Tyr	Y
Threonine	Thr	T
Triptophan	Trp	W
Valine	Val	V

1. INTRODUCTION

1.1 REGENERATIVE MEDICINE AND NANOTECHNOLOGY

Regenerative medicine is an interdisciplinary approach addressed to create living, functional tissues to repair or replace tissue or organ function lost due to age, disease, damage, or congenital defects according the definition of the US National Institutes of Health. It wants to replace the current therapy of transplantation of intact organs and tissues to treat organ and tissue failures and loss that often is limited by donor supply and characterized by severe immune complications. Basically, there are two approaches: the first one is addressed to stimulate or reactivate the natural regeneration ability of the human body at the target site; the second one wants to inject cells/ tissue/ synthetic organ to replace the damaged part. Recent advancements in both approaches are based on the synergy between regenerative medicine and nanotechnology, due to the evidence that cell identity and function is strongly influenced by nanoscale changes in the dynamic extracellular environment, where the size of most biomolecules and structural components ranges from 0.2 nm to 200 [1]. About the first aim, researches are focusing in defining the environment stimuli promoting or inhibiting natural cell regeneration to mimic or to antagonize them. About the second aim, nanotechnology is often combined to stem cell biology to characterize the environmental stimuli able to promote stem cell differentiation toward specific cell lineage [2].

1.1.1 Micro and nano-extracellular cues regulating cell behaviour

The extracellular stimuli acting at micro and nanoscale level can be divided in biochemical, physical and mechanical cues.

Biochemical cues are provided by the multiple interactions that cell faces during its development, that are: i) cell-cell interactions by specific cell receptors such as cadherins, cell adhesion molecules (CAMs), and ephrins; ii) cell interactions with ECM components such as fibronectin, laminin, heparin sulfate; iii) cell interactions with soluble factors i.e. growth factors, cytokines and ions. Such biochemical cues interact with cell receptors activating signalling cascade and determining cell behaviour. Notably, current researches indicate that temporally and spatially regulated presentation of these stimuli is fundamental to control cell function in the proper way.

Physical cues and mechanical cues are tissue properties such as stiffness, elasticity, μpatterned structure, matrix degradability, permeability and conductivity. The microscale reflects the tissue architecture while the nanoscale indicates surface modification (e.g. biomolecule attachment for cell adhesion, proliferation, and differentiation). Recent researches report that interaction between cells and their microenvironment can reorganize cytoskeleton and induce specific cell signalling that regulates cell behaviour, including polarity, migration, proliferation, and differentiation. The conversion of mechanical and physical force into biochemical information is known as mechanotransduction, an essential process for the development and physiology of the organism. Moreover, spatio-temporal regulation of the mechanotransduction pathways involved in cell-matrix interaction is essential to modulate cellular behaviour correctly [3].

1.2 STRATEGIES IN REGENERATIVE MEDICINE

Strategies in regenerative medicine can be distinguished in three different approaches:

- Biomaterial-based therapy, that is usually addressed to mimic extracellular environment features of a target tissue or organ that lead repair processes and/or cell recruitment and growth at the lesion site. The physical and mechanical stimuli of the ECM are usually reproduced by scaffolds, while bioactive molecules, proteins or peptides can be used to mimic the native biochemical features.
- Cell-based therapy, which consists of injecting novel and healthy cells in pathologic or damaged tissues.
- Combinatorial therapy, a combination of the previous two strategies. It is based on the construction of a biocompatible scaffold that, in combination with living cells and bioactive molecules, replaces, regenerates or repairs damaged cells or tissue.

1.2.1 Biomaterial-based therapy: the scaffold/matrix

In regenerative medicine, the development of scaffolds has intensively been investigated using either natural or synthetic material.

Natural material usually derives from human or animal (xenogeneic) sources and it includes extracellular components, collagen, alginate, chitosan, gelatine, hyaluronic acid, silk protein or agarose. The major advantage of natural polymers is that they usually can be integrated perfectly into the target tissue. However, their usage requires to solve issues especially about their potential immunogenicity and cross-contamination: they are furnished by other living organisms, thus residual cellular components may induce an immune

response [4]. An innovative approached is represented by the so-called **decellularized tissue matrices**, that are ECM derived from the target tissue, in which all cellular and nuclear contents are removed while retaining the structural components and bioactive molecules. Efficient decellularization methods include chemical, enzymatic, and physical approaches and they have been applied to several types of tissues. Decellularized matrices that have been applied clinically include decellularized dermis to treat burn injuries and decellularized small intestine ureter, or xenogeneic vessels to restore vascular function. Despite these successes, several problems remain: the decellularization process can affect mechanical properties of tissues or it could remove various types and amounts of ECM-associated signalling molecules [5]. Moreover, both naturally derived materials and acellular tissue matrices are very expensive because they cannot be produced easily in large quantities according to good manufacturing practice.

Synthetic scaffolds are made of synthetic materials or a combination between natural and synthetic materials. Poly-L-lactic acid (PLLA), poly-lactic-co-glycolic acid (PLGA), poly-caprolactone (PCL), or poly-vinyl alcohol (PVA) polymers, poly-hydroxic acids, poly-tetrafluoroethylene, steel titanium, ceramics or silk, are the most common synthetic materials employed for the fabrication of scaffolds. In contrast to natural polymer, synthetic materials allow a better control of their chemical, physical and mechanical properties, as well as degradation rate. They can be identically reproduced on a large scale with desired porosity, morphologies, and anisotropies to improve cell attachment and migration. The disadvantages of synthetic scaffolds are possible toxicity, undesired inflammatory responses and they often lack biologic recognition. However, recent researches show an improvement of synthetic scaffold recognition from the tissue target by coupling biological molecule to the scaffold [6].

Good scaffolds are expected to respond to specific requirements such as biocompatibility, stiffness, controlled porosity and permeability, suitable mechanical and degradation kinetics properties comparable to the targeted tissue. **Hydrogels** are a very promising solution because they are composed largely of water with a structure and composition like that of the ECM. For example, soft fibrin-collagen hydrogels have been used to mimic lymph node, alginate hydrogels improved regeneration of critical defects in bone. Notably, the polymer's mechanical properties alone seem to produce therapeutic effect since alginate hydrogel injections to the left ventricle reduce the progression of heart failure in models of dilated cardiomyopathy [7]. Another strategy is based on **electrospun nanofibers** with controlled architectures and diameter, that are obtained by electrospinning techniques. They provide topographical cues to cells by presenting geometries mimetic of the scale and 3D

arrangement of the collagen and laminin fibrils of the ECM. Such polymer fibres present a high surface-to-volume ratio and porosity that promote cell adhesion, growth and differentiation and enable growth factor/drug loading. In addition, in case of neurons, they seem to guide the direction of neurite elongation [8].

However, the advent of nanotechnology has allowed further developments in the field of biomaterials and current researches are addressing to design scaffolds with the same ECM features of the target tissue at nanoscale level. First, they should mimic physical and mechanical cues providing structural and functional cell support. For example, chondrocyte adhesion and proliferation and ECM production have been accelerated by nano-structured PLGA surfaces. Furthermore, nanometer surface roughness in vascular graft made of PLGA and stent of titanium improve endothelial cell functions as compared to nano-smooth polymer and titanium surfaces. **3D printing** has been employed to obtain the correct nanotopography (especially the dimensions and porosity) by producing layer by layer structures with a good and regular interconnectivity between pores and good mechanical properties. Bio-degradable materials are already in use as filaments and their price is low. Among them there is PLLA, a biodegradable material that is normally used in tissue engineering [9].

1.2.2 Biomaterial-based therapy: the biochemical cues

As well as physical and mechanical cues, biochemical cues characterize extracellular environment and influence cell behaviour. They can be reproduced by bioactive factors able to interact specifically with cell receptors or proteins to control processes such as cell survival, cell recruitment, cell proliferation, and cell differentiation. Two general strategies are used:

i) Incorporation and release of bioactive molecules in a specific matrix. For example, Regranex uses platelet derived growth factor conjugated to scaffolds to promote wound healing; and Infuse is aimed to improve bone formation via delivery of bone morphogenic proteins 2 and 7. Although these types of product are already available, they have several potential collateral effects due to the poor control over factor release kinetics [10].

ii) Surface modification of biomaterials with bio-adhesive ECM macromolecules or specific binding motifs. For example, incorporation of cysteine-tagged functional domains of fibronectin into thiol-modified HA gels was found to stimulate spreading and proliferation of human fibroblasts in vitro, and to promote recruitment of dermal fibroblasts in an in vivo cutaneous wound model [4].

However, the use of entire proteins challenges several problems. First, recombinant proteins or native matrix macromolecules extracted from animal tissues elicit immunoresponses, when using proteins from different species. Furthermore, production and purification processes of recombinant proteins are expensive and often show batch to batch variability. In addition, protein conformation can be affected by these processes or by the immobilization of proteins onto the scaffold surface. For these reasons, regenerative medicine approaches prefer to use **peptides** mimicking functional motifs able to mediate protein regulatory signals. In fact peptides have different advantages compared to the entire protein: i) chemical production of peptides is simple and it can be performed at large scale in a very reproducible way; ii) the chemical synthesis avoids contaminants of the recombinant protein production thus the peptide immunogenic activity is lower than proteins iii) peptide production costs are lower iv) the better control over the conjugation chemistry leads to better efficiency of the immobilization step on biomaterial surfaces, v) the smaller dimensions of peptide allow to reach higher densities at the scaffold surface [11]. However, macromolecules usually contain numerous receptor-binding motifs, which renders it difficult to determine the protein region regulating a specific cell function. Moreover, proteins can present multiple conformations under different conditions with time-dependent ligand specificity and dynamics. Thus, designing functional peptides for specific protein is a complex process and peptides could mimic only some functions of the entire protein. Such problem can be solved using a combination of several short peptides, each directed at only one function, in order to integrate multiple functions within synthetic matrices [12].

Currently, peptides used within biomaterials possess a diversity of functions. The biomimetic peptides most used for scaffold functionalization are the ECM protein mimetics promoting cell adhesion and subsequent activation of signalling pathways. Among them, the tripeptide RGD is the most known. It is the minimal recognition sequence for integrin binding and it triggers different cell lines to adhere and proliferate on the scaffold surface. Beyond cell binding, peptide functions include specific proteolytic susceptibility, surface binding, self-assembly and growth factor binding. Peptide proteolytic susceptibility can be exploited to design matrices with controllable degradation kinetics. For example, enzyme substrate sequences of different proteases (including matrix metalloproteinases or plasmin) have been coupled to hydrogels in order to enable the tailored degradation of the material or the release of a matrix-tethered payload via proteolysis [12]. Peptides can also be used to design self-assemble peptide scaffold to mimic the ECM native ability of self-polymerization through precise protein-protein interactions. Several classes of peptides have been designed and exploited in biomaterials contexts for their self-assembling behaviours such

as b-sheet fibrillating peptides, peptide amphiphiles, coiled coil peptides and short aromatic peptide derivatives. These peptides are characterized by their periodic repetition of alternating ionic hydrophilic and hydrophobic amino acids that spontaneously form various nanostructures like nanotubes, vesicles, helical ribbons, and fibrous scaffolds. One example is the artificial peptides that self-assemble to form hydrogels with high water content, responsive to changes in pH and other environmental factors, to be used for advanced wound closure and tissue repair in regenerative medicine [13]

1.2.3 Cell-based therapy

Cell therapy consists of injecting differentiated cells or on undifferentiated stem cells, which can differentiate upon specific stimuli, into the target tissue.

The differentiated endogenous primary cells can be either autologous or allogeneic and they are already available as therapeutic products. For example, the first FDA-approved biologic product in the orthopaedic field for the treatment of focal articular cartilage defects is Carticel, that uses autologous chondrocytes harvested from articular cartilage, expanded ex vivo, and implanted at the site of injury [10]. Although differentiated endogenous primary cells don't show rejection and important inflammatory responses, they will be always less used because it is difficult to get a considerable number of them in vitro, where they usually loss their replication potential.

In contrast, stem cells are able to self-renew indefinitely and differentiate into other cell types. Their ability to differentiate into other cell types is defined as "cell potency" and present several levels. Stem cells represent the body's natural reservoir of undifferentiated cell, used to development or to replace specialized cells that have been used up or damaged in the adult life. They can be distinguished in autologous if derived from patient, allogeneic if derived from a human donor and xenogeneic if derived from another animal. Furthermore, they can be divided based on their sources in:

- **Embryonic stem cells (ESCs)** derive from the inner cell mass of a blastocyst (5 days post fertilization). They are also known as pluripotent stem cells (PSCs) because they can differentiate into cells of any of the three germ layer lineages ectoderm, mesoderm, and endoderm. ESCs can be obtained also by the so-called therapeutic cloning or somatic cell nuclear transfer (SCNT), an approach based on the transfer of a somatic cell nucleus into an oocyte. In this way, early stage embryos are cultured to produce ESCs with the potential to become almost any adult cell types or to cloning animals. Through this technology, pathologic cell lines can be obtained to study the effects of some molecules in cells with specific diseases;

- **Adult stem cells** that can be found in most tissues where they are fundamental during the tissue development and to heal and replace worn out cells. They are multipotent stem cells because they have a more restricted differentiation ability compared to PSCs. Among these cells, the bone marrow-derived mesenchymal stem cells (MSCs) had been studied deeply because they are able to differentiate into many kinds of cells, useful to treat bone, cartilage, nervous, muscle, cardiovascular, blood and gastrointestinal diseases;
- **Induced pluripotent stem cells (iPSCs)** that are adult somatic cells artificially reprogrammed to become pluripotent and self-renewing [14]. A human clinical trial with iPSCs is being conducted at Japanese RIKEN Center for Developmental Biology: skin cells of a 70-year-old woman affected by exudative age-related macular degeneration were taken and induced to differentiate into retinal pigment epithelium (RPE) cells, which were used to create a small monolayered RPE sheet to implant into the patient's eye, without any biomaterials.
- **Amniotic fluid-derived stem cells (AFSCs)**, so called because they derive from amniotic fluid and placenta by amniocentesis or chorionic villous sampling in the developing fetus or from the placenta at birth. These cells are multipotent and can be used as autologous cell source in several clinical applications, but no human clinical trials have been performed yet.

Each of these stem cell categories show specific advantages and lacks: PSCs can differentiated in all human tissue but there are a lot of ethical concerns about their use; MSCs can only differentiate toward specific target tissue according where they derive from and generally they can be obtained at low yields; iPSCs have the same cell potency as ESCs, but the efficiency of reprogramming is still quite low (about at 1%) and stochastic and recent researches also shed light on their long-term tumorigenic potential; AFSCs do not develop neoplasms but they have to be stored in specific cell bank in order to supply as autologous cell source [2] .

Unfortunately, direct transplantation of cells at the injury site showed limited clinical efficacy leading poor cell survival, uncontrolled differentiation, and ineffective integration into the host tissue, primarily due to an inhospitable environment around the injury site.

1.2.4 Combinatorial approach

It is a combination of the previous two strategies: cells are seeded on scaffolds mimicking both biochemical and physical properties of the cellular microenvironment to enhance cell adhesion, proliferation and/or differentiation. This approach has been extensively exploited

with stem cells because it allows to reproduce environmental factors modulating stem cell differentiation towards specific cell lineage. The traditional approach for stem cell growth and differentiation is based on biochemical modulation using small molecules and growth factors, but it presents several problems such as the high cost, the long time consuming and the low yield of fully differentiated cells. However recent evidences indicate that biophysical cues can direct stem cell behaviour by either maintaining their phenotype or improving lineage commitment, and they are of great interest because they are cost effective, longer lasting, easily characterized, and can be manufactured with high reproducibility [15].

Therefore, researchers have focused on the production of nanomaterials able to generate active biophysical and biochemical signals for directing stem cell fate obtaining material directed differentiation of mesenchymal stem cells, neural stem/progenitor cells, adipose derived stem cells, hematopoietic stem/progenitor cells, embryonic stem cells and other cell towards specific cell lineages (**Fig.1**).

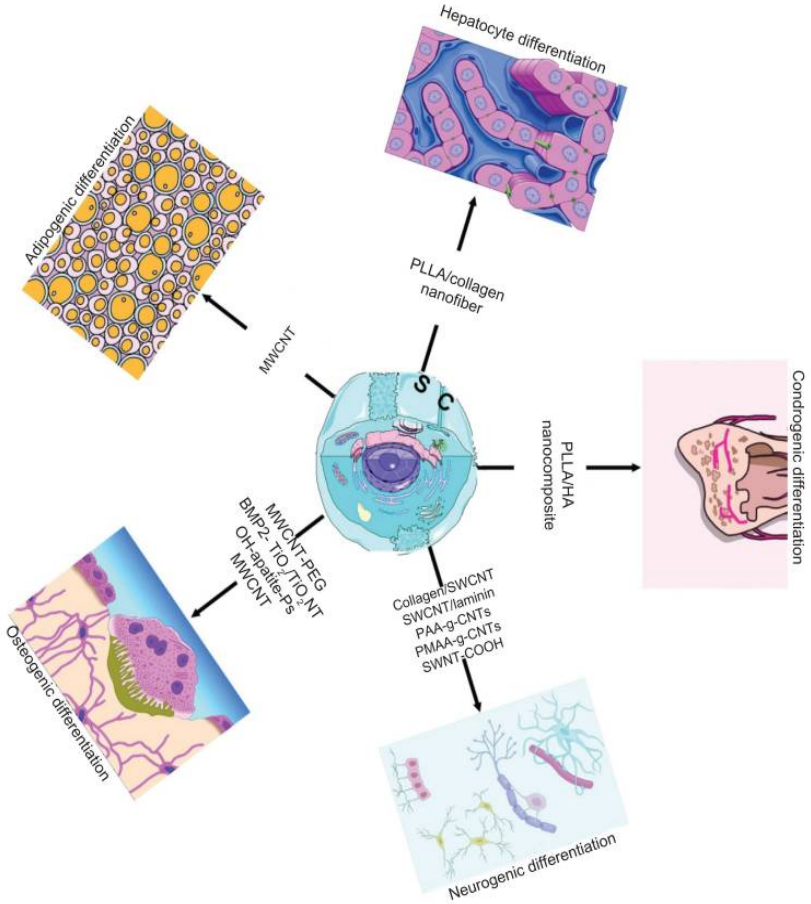

Figure 1. Examples of combinatorial approaches for different target tissues [154].

Different types of biophysical signals have been observed to modulate stem cell behaviour including material elasticity/rigidity, micropatterned structure, ECM coated materials, material transmitted external stress and strain, electrical stimulation, hydrostatic pressure, electromagnetic fields, ultrasound and photostimulation [16].

The biochemical stimuli for stem cell differentiation include the conventional growth factors and small molecules which target specific intracellular pathway. They are usually used in a soluble form in culture media, but now researches are addressed to their immobilization on cell culture substrates or on the surface of implantable scaffolds. In this way, more defined culture systems are obtained, and they could be used in future clinical applications. Notably, the most of studies in stem cell regenerative medicine uses combinational protocols which contain both biophysical and biochemical cues [16].

A promising tool in this field is the **3D bioprinting** using, in most of cases, biodegradable polymers and stem cells as printing inks. They are printed layer by layer to form 3D tissue/organ-like constructs, in which biodegradable polymers are used as support scaffolds, while stem cells can be engaged to differentiate into different cell/tissue types. This technique is characterized by high precision, easy reproduction, fast manipulation and high-resolution control over material and cell placement within engineered constructs and it is used to fabricate a wide range of tissues. There are two bioprinting strategies, inkjet and microextrusion. Inkjet bioprinting uses pressure pulses, created by brief electrical heating or acoustic waves, to create droplets of ink that contains cells at the nozzle. This approach has been used to produce cartilage by alternating layer-by-layer depositions of electrospun polycaprolactone fibers and chondrocytes suspended in a fibrin–collagen matrix. Cells deposited this way were found to produce collagen II and glycosaminoglycans after implantation. In contrast, microextrusion bioprinting dispenses a continuous stream of ink onto a stage and it has been used to print complex 3D tubular networks, which were then seeded with endothelial cells to mimic vasculature [17].

1.3 THE NERVOUS SYSTEM

1.3.1 Nervous System Organization

The vertebrate's nervous system can be divided into two major parts: **the central nervous system** (CNS) and the **peripheral nervous system** (PNS). The CNS consists mainly of the brain and the spinal cord, but there also are the optic, olfactory and auditory systems; it acts as carrier and interpreter of signals from outside and it generates stimuli to the PNS.

The PNS is responsible for innervating muscle tissue and it works as the connection between the CNS and peripheral structures, because it conveys sensory and excitatory signals in both directions, from CNS to peripheral structures and vice versa. The PNS consists mainly of a collection of nerves, which are enclosed bundles of the long fibers that connect the CNS to every other part of the body. Based on how they are connected to the CNS, such nerves are classified in cranial nerves originating from or terminating in the brain/cranium, and spinal nerves originating from or terminating at the spinal cord. We can also distinguish nerves based on the direction of nerve propagation between sensory or afferent neurons transmitting signals from the body to the CNS and motor or efferent nerves transmitting signals from the CNS to effectors (muscle or glands). Motor neurons can be further classified according to the effectors they target: the somatic nervous system (SNS) mediate voluntary movement by the regulation on the contraction of skeletal muscles, the autonomic nervous system (ANS) controls the activities of organs, glands, and various involuntary muscles, such as cardiac and smooth muscles. The ANS consists of the sympathetic nervous system, activated in cases of emergencies to mobilize energy, and the parasympathetic nervous system, activated when organisms are in a relaxed state [18].

1.3.2 Cells of the Nervous System

There are two main classes of cells in the nervous system: nerve cells or neuron and glial cells or glia. Neurons are characterized by their ability to process information and communicate with other cells via synapses, that allows rapid transmission of signals (either electrical or chemical), while glia provides the neurons with mechanical and metabolic support [19].

Neurons can be divided in three categories based on their role: sensory neurons, motor neurons, and interneurons. Sensory neurons transmute physical stimuli taking place inside and outside of the body into neural signals that are conveyed into the CNS, so they can be processed. Motor neurons get information from other neurons and send signals to the muscles and glands of the body. Interneurons receive signals from and send signals to other nerve cells. Interneurons serve to process information and constitute the bulk of the human nervous system.

A typical neuron has four morphologically and functional defined regions: the cell body, dendrites, the axon, and presynaptic terminals. The cell body, known as **soma**, is the metabolic centre of the cell and it usually gives rise to two types of neurites, different in both function and morphology, known as dendrites and axon. The **dendrites** appear as many short and thick branching processes, and in most excitatory neurons, they possess dendritic

spines. Functionally, dendrites are input elements of the neuron: they receive, process and propagate incoming information from other neural cells through neurotransmitter receptors to soma. The **axon** is the long and thin protoplasmic protrusion, and it is the output element of the neurons and they typically conducts signals to other neurons. CNS axons are very thin, between 0.2 and 20 μm in diameter, compared with the diameter of the cell body of about 50 μm; instead, axon length varies greatly, and it can extend more than 3 m within the body. Many axons are insulated by a fatty sheath of myelin that is interrupted at regular intervals by the nodes of Ranvier. The cell's conducting signal, known as action potential, is initiated either at the axon hillock, the initial segment of the axon, or in some cases slightly farther down the axon at the first node of Ranvier.

In general, axon terminals containing synaptic vesicle of the presynaptic neuron transmits signals to the postsynaptic neuron through several synaptic contacts. **Synapses** are membrane-to-membrane junctions containing molecular machinery that allows rapid transmission of signals, either electrical or chemical. Incoming signals can be either excitatory, able to make the neuron generate an electrical impulse, or inhibitory, able to keep the neuron from firing. Whether or not a neuron is excited into firing an impulse depends on the sum of all the excitatory and inhibitory signals it receives.

Glial cells surround the cell bodies, axon and dendrites of neuronal cells. They play several roles in the nervous system: they support neurons and hold them in place; they supply nutrients to neurons; some of them act as scavengers, destroying pathogens and removing dead neurons; and certain classes of glial cells, known as radial cells, provide guidance cues directing the outgrowth of axons towards their targets. Two types of glial cell (oligodendrocytes in the CNS, and Schwann cells in the PNS) generate layers of a fatty substance called myelin that wraps around axons and provides electrical insulation which allows them to transmit action potentials much more rapidly and efficiently.

Glial cells in the vertebrate nervous system are divided into two major classes: microglia and macroglia. **Microglia** are phagocytes of the CNS that are mobilized and activated after injury, infection, or disease. The activated cell expresses a range of antigens, which suggests that may serve as the major antigen presenting cell of the CNS, and recent evidence indicates that activated microglia may have a role in several neurological diseases. **Macroglia** cells can be divided in three types: astrocytes, oligodendrocytes and the Schwann cells. Oligodendrocytes and the Schwann cells are small cells with few processes, producing myelin sheath by tightly winding their membranous processes around the axon in a spiral. Oligodendrocytes envelope an average of 15 axonal internodes each, while Schwann cells envelop just one internode from one axon. Astrocytes are the most

numerous of glial cells and their name is due to their irregular, star-shaped cell bodies. They regulate blood flow in the brain and maintain the composition of the fluid that surrounds neurons and they mediate communication between neurons at the synapse. During development, astrocytes help neurons find their way to their destinations and contribute to the formation of the blood-brain barrier, which helps isolate the brain from potentially toxic substances in the blood [18].

1.3.3 Neurite outgrowth and neural circuit development

Neurons are polarized cells that require a complex interplay of both extracellular and intracellular signals for their development. Neuron polarization is essential for the establishment of neural functional circuits during nervous system development. The process of neuronal morphogenesis and polarization under culture conditions have been extensively described and it have been divided in five developmental stages according to morphology of in vitro cultured hippocampal neurons (**Fig.2**). In stage 1, several thin filopodia appears shortly after the dissociated neurons are seeded. In stage 2, these neurons extend multiple immature neurites that undergo repeated random growth and retraction, without morphological differences among them. Stage 3 shows initial neuron polarized morphology: several minor neurites and one neurite that is much longer than the others that eventually becomes the axon. In stage 4 (within 7 days), the remaining neurites develop into dendrites. Stage 5 is reached when neurons form premature dendritic spines and axonal branches. Interestingly, neurons determine their polarity in a stochastic manner in the absence of additional extracellular signals [20,21].

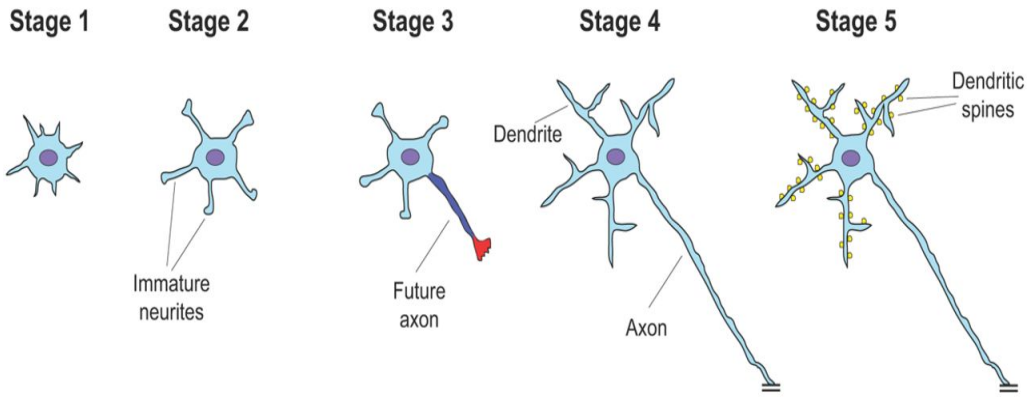

Figure 2. Establishment of polarity and stages of neuronal development in hippocampal neurons [21].

Neural circuits are the basis of neural function and they are represented by the structure of axons and dendrites, in which individual axons stimulating multiple targets and single dendrites assimilating inputs from various sources. During the development of neural

circuits, axons present a highly dynamic structure on their elongating tip, known as the 'growth cone', that expresses surface receptors by which it senses and integrates multiple stimuli provided by extracellular environment with an impressive level of accuracy. The growth cone sums all these inputs providing the initiation and guidance of neurites and the navigation of axon elongation direction toward its target cell.

These inputs can be subdivided into positive (permissive or attractive), negative (inhibitory or repulsive), or guiding (affecting the advance of the growth cone). They can act either over long distances or locally, in a contact dependent manner and recent studies have revealed that cooperation between long- and short-range guidance cues and between attractive and repulsive cues is required for the correct navigation of growing axons to their target cells. Furthermore, they have showed axons also use intermediate targets on the way to their final target, especially when they have to cover long distances and these intermediate targets provide important guidance information and prepare axons for the following steps [22].

They can arise from: i) adhesive molecules presented on neighbouring cells (such as CAMs) to which growth cone receptors can adhere ii) the ECM that regulates cellular processes either by ECM-associated molecules (including Laminin and Fibronectin) or by growth factors and cytokines retained by it iii) anti adhesive surface-bound molecules (such as Slits and Ephrins) that prohibit growth cone advance iv) diffusible chemotropic cues that work as the 'road signs' that present further steering instructions to the travelling growth cone [23].

1.3.4 Mechanism of neural growth and polarization

Cell morphology and motility are based on growth cone dynamics, which is essentially modulated by neuron cytoskeletal organization of microtubules (MTs) and actin filaments. MTs are heterodimers of alpha-tubulin and beta-tubulin and possess two distinct ends: the plus end, a crucial site for tubulin polymerization and the minus end that is often anchored to a microtubule-organizing centre, such as the centrosome and the Golgi complex. They usually regulate polarity in many types of cells, including neurons, where dendritic microtubules show mixed orientation, and axonal microtubules show plus-end-distal orientation (**Fig.3**).

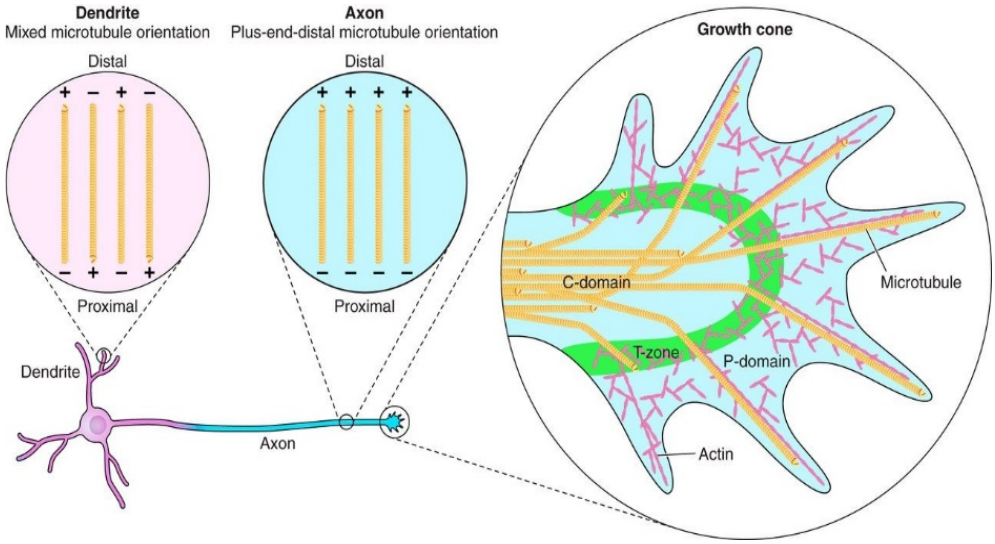

Figure 3. The cytoskeletal structures in neurons. The dendrites and axons have different microtubule orientations; dendritic microtubules show mixed orientation, and axonal microtubules show plus-end-distal orientation. Growth cones are divided into three regions based on their cytoskeletal components. The central (C) domain mainly contains microtubules, and the peripheral (P) domain is enriched in actin filaments and contains filopodia and lamellipodia-like structures. The transition (T) zone contains an acto-myosin contractile structure [24].

Actin filaments are composed of actin and have barbed ends and pointed ends. Actin-severing proteins enhance actin disassembly and the dynamic organization of the actin directs the morphology of growth cone. The growth cone can be divided into three regions based on their cytoskeletal components. The central (C) domain mainly contains stable and bundled MTs, numerous organelles, vesicles and central actin bundles. The peripheral (P) domain that is rich in long F-actin filaments and contains filopodia and lamellipodia-like structures. Additionally, individual dynamic "pioneer" MTs explore this region, usually along F-actin bundles. Between these domains, there is the transition (T) zone in which an acto-myosin contractile structures, known as actin arcs, lie perpendicular to F-actin bundles and form a hemicircumferential ring [23].

In the axon outgrowth process the growth cone dynamics follow three steps of advance that are influenced by environmental factors: membrane protrusion, engorgement, and consolidation.

Membrane protrusion is primarily driven by permissive and adhesive substrate and growth cone receptors interaction, that actives intracellular signalling cascades and induces the formation of a molecular `clutch' binding the substrate with the receptors and F-actin filaments. The clutch provides attenuation of F-actin retrograde flow and it drives actin-based forward growth cone protrusion on the adhesive substrate, as F-actin polymerization goes on in front of the clutch site and the filopodia and lamellipodia-like veils of the peripheral (P)-domain move forward to extend the leading edge. At this level, filopodia and lamellipodia-like veils act as guidance sensors of the growth cone and they might have a major role in establishing growth cone-substrate adhesive contacts during environmental exploration. Engorgement stage starts when F-actin arcs reorient from the C-domain towards the site of new growth, then T-zone actin arcs and C-domain actin bundles guide C-domain MTs towards the site of new growth. In addition, MTs mediate transport of membranous organelles and vesicles.

Lastly, the recently advanced C-domain undergoes consolidation process: the proximal part of growth cone compacts at the growth cone neck to form a new segment of axon shaft. MTs are compressed into the newly localized C-domain by myosin II-containing actin arcs while filopodias leave the area of new growth [24].

In summary, the combination of F-actin tread milling and F-actin retrograde flow (the continuous movement of F-actin from the leading edge towards the centre of the growth cone) provide the ‘motor’ that keeps the growth cone engine idling and available to drive movement in response to directional cues during formation of nascent axons, and also when new growth cones form from an axon shaft during axon branching [23].

1.3.5 PNS regenerative capacity

Injury in peripheral nerves could lead to loss of communication along nerves between the CNS and the peripheral organs causing reduction in motor and sensory functions and they are generally caused by accidental trauma, surgery, drug therapy and metabolic dysfunction.

In contrast to the CNS, adult PNS axons spontaneously regrow to a significant extent; in fact, they are often used as a model to identify the players in axon regeneration. Besides to intrinsic ability of PNS neurons to regrow, the PNS regenerative capacity is based also on extrinsic factors that comprise targets able to accept new axons and a growth-permissive

and supportive distal environment, where specific cell signalling pathways are activated turning on pro-growth genes, leading to reformation of a functional growth cone and successful axonal regeneration. Notably regeneration doesn't imply the formation of functional connections and the extent of functional outcome after repair depend on several factors including the patient's age, delay before intervention, and type of injury.

After axotomy, we usually can distinguish the end attached to the cell body, known as the proximal segment, and the other end, known as the distal segment. These ends can undergo toward spontaneous regeneration process that can be divided in the following phases (**Fig.4**)[25]:

I. The proximal end swells and starts to degenerate, but once the debris is cleared, it begins to sprout axons and the presence of growth cones can be detected. During this process, the proximal segment shows a *retrograde signalling* from the injury to the soma by importin proteins, which form a complex with dynein in rodent models of nerve regeneration. This complex bind to transcription factors and transports them to the nucleus, enabling retrograde signalling that leads to transcriptional changes and functional recovery of injured neurons. However, whether these processes also occur in long nerves in humans remains to be seen. The length of human axons presents a special challenge, as injury signals might have to travel a metre to get to the nucleus [26]. Notably, regeneration happens in the proximal segment only if the cell body is intact and not so far from axon lesion and if there are Schwann cells in the proximity of the injury axon.

II. The distal segment undergoes molecular and morphological changes leading to the *Wallerian degeneration,* during which axonal and myelin-derived material are removed to prepare the environment where regenerating axons grow. Both the axon and the myelin degenerate and macrophages migrate to the site of injury and contribute to clear away debris such as damaged tissue which is inhibitory to regeneration.

III. Within the distal nerve stump, Schwann cells proliferate and align along the basal lamina tube that surrounded the original nerve fiber and they form ordered columns, known as bands of Büngner. During this phase, Schwann cells switch from a myelinating to a regenerative phenotype, required to support axon outgrowth. In particular, the regenerative Schwann cells down-regulate myelin basic protein and myelin-associated glycoprotein, while they upregulate CAM and they secrete neurotrophic factors to enhance neuron regrowth and chemotactic factors necessary to guide the axon growth. The switch of Schwann cells might be actively triggered by an injury signal or might occur because of loss of axonal signals.

IV. Lastly, the regenerating axon enters the distal nerve, where they are guided by tubes of Schwann cell basal lamina, and successfully reinnervate the target organ. If the distance to be travelled is short, the axons soon reach distal nerve, and target organ can accept reinnervation. If the distance is long, reinnervation is delayed and problems can arise: misdirection towards the wrong target, degeneration of the Schwann cell tubes that are no more able to promote axon growth, the target muscle atrophy or satellite cells undergo apoptosis leading the loss of receptivity to neuromuscular synapse formation [25].

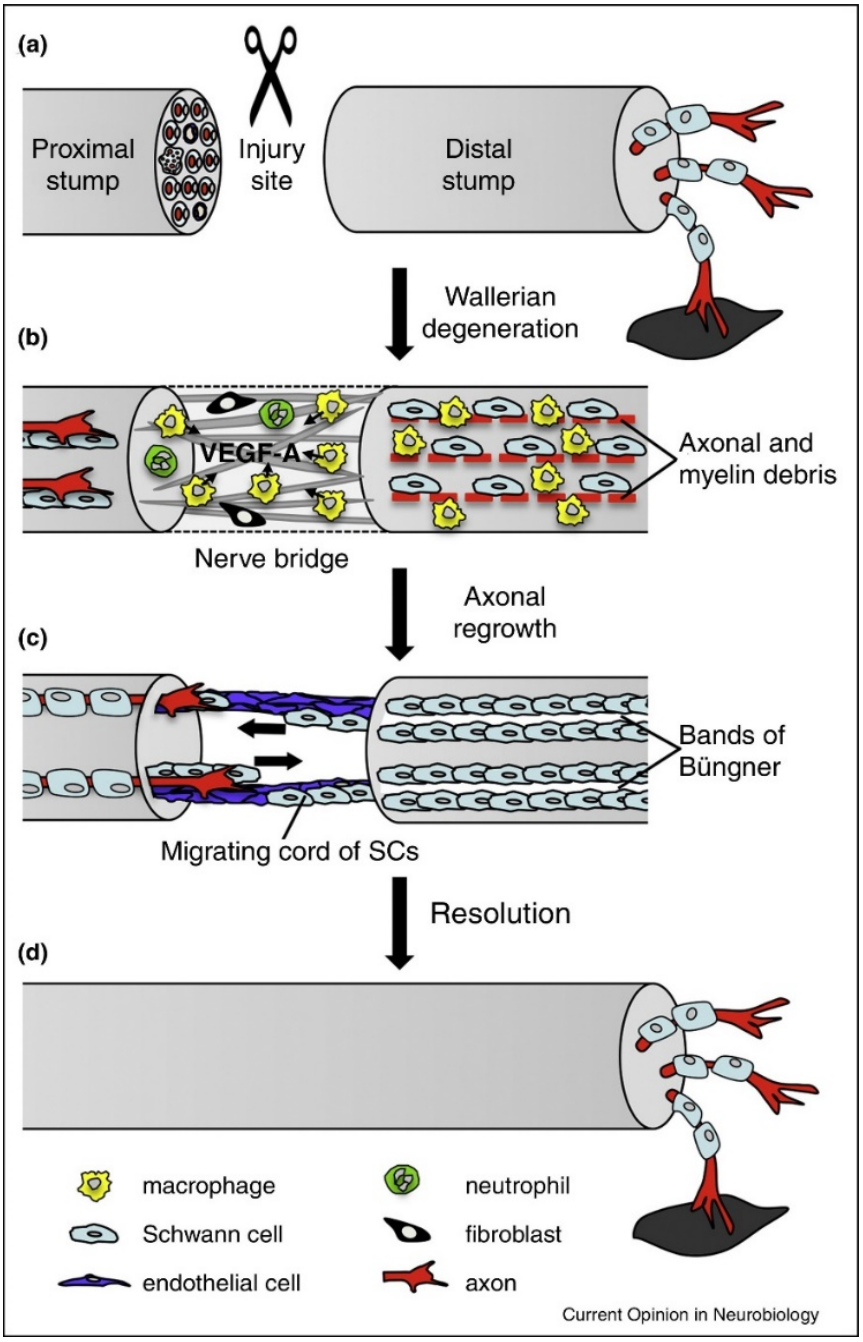

Figure 4. Different stages of peripheral nerve regeneration following a transection [25].

1.3.6 CNS regenerative capacity

Regeneration of PNS and CNS neurons differs in the functional mechanism, especially in the extent and speed of their regenerative capacity because nerve regeneration is much more effective in the PNS than in the CNS.

In contrast to peripheral nerves, adult central neurons have been considered intrinsically unable to regenerate for a long time. This paradigm has been rejected by studies of Ramón y Cajal of 1928, in which adult CNS neurons have been induced to grow long axons by attractive and trophic factors originating from peripheral nerve graft. These results were confirmed also by Aguayo and colleagues, who definitively demonstrated the lack of regeneration in adult CNS is due to extrinsic factors [27]. Currently, the inability of CNS regeneration is attributed to the CNS non-permissive environment, where oligodendrocytes don't have the ability of the PNS Schwann cells to support axonal regeneration. In addition, inhibitory molecules are enriched in CNS oligodendrocyte myelin compared to Schwann cell one, and the physiological response to injury creates obstacles to regeneration. First, the blood- spine barrier limits macrophage entry into the nerve tissue making macrophages infiltration very slow and delaying removal of inhibitory myelin at the site of CNS injury. Then, CNS injury is characterized by the glial scar, composed of proliferative and reactive astrocytes and microglia that blocks axon growth. By contrast, no glial scar forms in the PNS, and Schwann cells aid axon guidance and regeneration [27].

Understanding differences in CNS and PNS regeneration is essential to adopt the best regenerative strategies in case of NS injury [6].

1.4 THE REGENERATIVE MEDICINE IN THE NERVOUS SYSTEM

1.4.1 Regenerative strategies in PNS

Peripheral nerve injuries are commonly caused by working or motor vehicle accidents, tumour damage, side effects of neurosurgery and even viral infections.

As previously stated, in case of injury, PNS neurons have intrinsic ability to regenerate while Schwann cells and resident and infiltrating macrophages clean up inhibitory debris, enabling new axon sprouts to grow into the degenerating nerve. Nevertheless, the PNS spontaneous regeneration capacity is not as efficient as desirable, especially in axon regeneration over long distances, that often remains incomplete leading to poor recovery and lifelong disabilities. Direct end-to- end surgical reconnection can repair small defects or gaps in the nerve, but it can't be used for longer nerve gaps, where any tension introduced into the

nerve cable would inhibit nerve regeneration. Thus, new regenerative strategies for PNS have been developed.

Nerve autografts and allograft approach has been the only therapeutic approach to treat the transacted nerves. The autografts consist in harvesting a nerve segment from another site of the body to gather the stumps of the injured nerve. However, this method has several disadvantages including tissue availability, differences in tissue size and structure, and high donor site morbidity.

In the allograft there is an abundant supply of donor nerves and nerve segments are usually harvested from human cadavers. Unfortunately, this technique presents problems such as the need for systemic immunosuppressive therapy, making the patient prone to infections, disease transmission risk and in the most severe cases, even tumour formation. A partial solution has been found using decellularized allografts such as the FDA approved Avance, that is made of cadaveric material. It has all the advantages associated with the nerve allografts even if, over time, immunosuppression may be required [6].

Due to these problems, suitable replacements for nerve autografts and allograft have been investigated leading to **the nerve guide conduit (NGC) approach**. NGCs are tubular nerve conduits of various compositions that are sutured or fixed to the two stumps of the injured nerve, providing adequate micro-environment to guide axons and to support the different phases of the nerve regeneration. These conducts should be capable of create a channel that allows the diffusion of neurotropic and neurotrophic factors secreted by the nerve stumps, guide the regenerated axons from the proximal to distal nerve stump, provide mechanical support for the new fibers and prevent the wound healing space from being invaded by scar tissue and cells that could inhibit nerve recovery. After the first stages of regeneration, depending on the size and type of injury, NGC should start to degrade slowly with no swelling, constriction or foreign body response; thus, the NGC should be semi-permeable. NGC can be made of different material including natural materials (e.g. blood vessels, muscle, tendon), biopolymers (e.g. collagen, chitosan, alginate) and synthetic polymers (e.g. silicone, PGA, PCL). On one hand natural material and biopolymers show high biocompatibility, biodegradability, and biomimetic features, on the other one synthetic polymers can be easily tailored and they allow the nerve conduit to be easily processed into a variety of shapes and forms. Furthermore, polymers with conductive properties have very recently been subject to intensive study in this field, since electrical conductivity is one of the intrinsic nerve features and it has a positive influence in the regeneration of the new axons. Unfortunately, conductive polymers (e.g. Ppy) are usually non-biodegradable thus they may constrict the new nerve fibers making a second surgical intervention to be needed

for its removal [28]. Another strategy to improve the design of NGCs is their functionalization with diverse bioactive cues, intended to interplay in vivo. They can be growth factors or also accessory cells such as Schwann cells, bone-marrow stromal cells, mesenchymal stem cells and fibroblasts. This approach achieved improvements in the efficiency of reconstruction in case of large gaps where the therapeutic strategies are still suboptimal [29].

1.4.2 Regenerative strategies in CNS

Effects of CNS damage are very critical, resulting usually in loss of sensory, motor, and cognitive functions; they can be caused by spinal cord injury (SCI) and traumatic brain injury (TBI), and chronic disease like neurodegeneration disease like Parkinson's disease, Alzheimer's disease, multiple sclerosis and age-related macular degeneration (AMD). Several mechanisms contribute to CNS injury, including apoptotic and necrotic death of neurons, astrocytes and oligodendrocytes, axonal injury, demyelination, excitotoxicity, ischemia, oxidative damage, and inflammation [30]. In addition, CNS regeneration is more challenging due to the inhibitory environment, characterized by an overall absence of axon growth promoting factors and presence of axonal growth inhibitory/repulsive molecules (e.g. myelin-associated proteins, the glial scar) at the lesion site [31]. Different therapeutic strategies have been developed and tested targeting the different aspects of the CNS regeneration process.

Cellular replacement has been the first approach adopted in the context of injury to the brain and spinal cord, where functional capacity is lost mainly because of the death of neurons (e.g., Parkinson's and Alzheimer's Diseases, SCI) and glia (e.g. multiple sclerosis, demyelination in SCI) and CNS system cannot supplant the function of these lost cells. At first, fetal tissue grafts have been used to replace cells after a variety of CNS insults and some of them are currently in clinical trials for humans. However, the inherent mechanical, physical and ethical issues of using fetal tissue limit its large-scale use [32]. In last years, different types of cells have been tested for the transplantation in CNS including MSCs, ESCs, iPSCs and their differentiated progeny into the injured CNS tissue. One of most promising result is the study showing the replacement of oligodendrocytes by transplanted ESCs in a spinal cord-injured rat leading to an improved locomotion [33]. Furthermore, ESCs and bone marrow stromal cells have been transplanted to the adult brain, where they are reported to differentiate into neural cells [34]. The discovery of the neural stem cells resident within the CNS and the ability to regulate their behaviour provide an alternative to transplantation using an endogenous replacement strategy. In fact, recent studies showed that that CNS stem cells can participate in cell replacement, extending new axons several

millimetres through the intact CNS, after specific lesion conditions. For example, intraventricular sequential delivery of epidermal growth factor (EGF) and erythropoietin into the stroke- injured rat brain showed enhanced migration of endogenous NSPCs to the injury site, resulting in neurogenesis and improved functional recovery [35]. However, endogenous stem cells can't produce complete recovery in cases of severe trauma. Moreover, more improvements are needed in transplantation or endogenous replacement strategies such as making these new cells resistant to the environment of the injured CNS and able to be functionally integrated into the remaining circuitry. Molecular mechanism of these processes is still unclear, and some recent reports suggest that the regeneration of damaged host tissue is not due to the structural integration of these cells into the tissue while it is manly caused by factors secreted by grafted or endogenous cells, which promote neuroprotection or neurogenesis. In fact, cell replacements strategies showed that grafted stem cells produce neurotrophic factors such as nerve growth factor, brain-derived neurotrophic factor, neurotrophin-3, ciliary neurotrophic factor and glial cell-derived neurotrophic factor [36,37].

As previously stated, neurotrophic and growth factors and the ECM proteins are implicated in neuroregeneration mechanisms such as neurogenesis, plasticity, axonal guidance and neuronal regeneration. Therefore, **bioactive molecules delivery approaches** have been developed in replace of stem cell injection and they are based on the direct delivery of pro-active molecules (axon guidance molecules, neurotrophins and growth factors) in the CNS to promote CNS regeneration processes. For example, injection of interferon-γ and GDNF has a neuroprotective effect and promote axonal outgrowth, following SCI [31]. Nevertheless, problems arose about the correct administration route for this kind of approach. In fact, the blood-brain barrier and blood–spinal cord barrier don't allow to use conventional delivery strategies, while systemic administration leads to off-target distribution of therapeutic molecules and can result in undesired side effects. The direct injection into the injury site or intrathecal space or intraventricular injection are associated with possible risks such as cerebral edema and convulsions [27]. Currently, the most promising drug/biomolecules delivery strategy is via liposomes or nanoparticles or using different kinds of scaffolds/matrices providing the appropriate growth-permissive substrate. However, the bioactive molecules delivery has showed a limited clinical efficacy in vivo due to the non-growth-permissive environment of the CNS and considerable effort has been placed on identifying and reversing the effects of growth inhibitory molecules. Many studies confirmed that natural regeneration potential of injured nerves can be enhanced by delivery of molecules able to eliminate endogenous white matter inhibitors, as showed by vaccination

with myelin self-antigens, suppression of myelin-associated inhibitor molecules (*e.g.*, NOGO-A, myelin-associated glycoprotein (MAG), OMgp) and its pathways [30,38]. However, strategies addressed only to these molecular inhibitors are not sufficient to solve the lack of CNS regeneration. Thus, the complexity of the CNS makes necessary the advancement of those strategies or the combination of them by manipulation of both axon guidance molecules, inhibitory and permissive cues.

Currently, approaches in CNS regenerative medicine prefer to use **combination strategies** that include the controlled and sustained delivery of both bio active molecules and cells capable of regenerating damaged tissue using scaffolds as delivery carrier. Currently, hydrogel, self-assembling peptide and nanofibers are the most promising forms of scaffolds for the CNS treatment, especially in case of SCI [31].

1.4.3 Tools used in neuronal regenerative medicine

New promising tools used in strategies for neuronal regenerative medicine have been developed in last year, such as:

- **Nanofibers** used as scaffold mimicking both physical and biochemical cues of native ECM to differentiate stem cells towards neuronal target tissue. For such approach, nanofibers provide the best nanoarchitecture resembling the neuronal environment because they arrange in a three-dimensional network, in which the fibers morphology and diameter are like the components of neural ECM. In addition, their extraordinary mechanical strength and high surface area/volume ratio made nanofibers suitable for neural tissue engineering, as reported in many studies [6]. For example, the results of in vitro NSC culture study indicate that the nanofibers scaffold not only supports cell adhesion and neurites outgrowth, but also promotes NSC differentiation [39]. In most of studies, nanofibers are produced by elettrospinning, a very good approach in terms of cost and efficiency, and they have been tested using different polymer composition and diverse forms such as random fibers, aligned fibers, 3D fibers, fibrous conduits and core-shell fibers. Notably, aligned nanofibers were able to guide the neurite grow direction and facilitate nerve cell alignment. In addition, to mimic the electrical property of neuronal native nerve structure, research on conductive polymers and electrical stimulation emerge as a relatively novel approach to increase neurite extension and axonal regeneration.
- **Peptides** are used to reproduce biological property of the native neuronal ECM, especially the biomolecules known to influence neuronal cell behaviour. Since a large variety of biomolecules characterize nervous system, peptides reproducing specific

regulating motifs are preferred for the scaffold functionalization. First, the short synthetic peptide, arginine–glycine–aspartate (RGD) from fibronectin has proved to bind integrin and to promote axonal regeneration of adult neurons [40]. Then, numerous other ECM-derived synthetic peptides have been identified. Laminin-derived peptides are tyrosine–isoleucine–glycine–serine–arginine (YIGSR) and isoleucine–lysine–valine– alanine–valine (IKVAV), that respectively promote neural cell adhesion and neurite outgrowth. Adhesive peptides are derived from collagen (DGEA) and fibronectin (REDV, RGDS) and they are able to promote neurogenesis. Moreover, the neural cell adhesion molecule (NCAM)- derived amino-acid sequence, EVYVVAENQQGKSKA, induces neurite outgrowth and increases neuronal survival [31].

- **Stem cells** used in CNS regenerative medicine mainly include induced neuronal stem cells iPSC, neural stem cells (NSCs) and MSCs.

  In last years **induced neuronal stem cells (iNSCs) and induced neuronal cells (iNCs)** have been produced using novel direct reprogramming methods. In 2014 Han and collaborators evaluated the therapeutic effect of cell transplantation using iNSCs in the SCI rat model, reporting that engrafted iNSCs could differentiate into neuronal lineages forming synapses and enhancing the recovery of locomotor function [41]. iNCs and iNSCs can thus be regarded as a promising cell resource for cell transplantation/replacement therapy but the derivation of iPS lines and their subsequent differentiation is a long and complicate process, with low yield and tumorigenic risk.

  NSCs are cells with the potential for self-renewal and differentiation into neurons, astrocytes, and oligodendrocytes. They mainly derived from ESCs and fetal tissue. Surprisingly NSCs have been found to exist not only in the developing brain but also in the mature mammalian brain where they persist in two main areas: the ventricular-subventricular zone, where NSCs give rise to olfactory neurons, and the hippocampus, where new neurons involved in cognitive processes are generated. NSCs are thought to be an optimal cell source for the treatment of neurological disorders but they are difficult to isolate from autologous brain biopsies and there are problems about the use of fetal tissues associated with abortion. Since they are able to migrate at the injury site, current strategies about their use are based on the activation of the endogenous neural stem cells [42].

  MSCs are adult stem cells that are found mainly in the bone marrow, but they are also in other tissues like adipose tissue, dental pulp, placenta, umbilical cord blood and brain. MSCs populations can be sub-passaged and differentiated in vitro into different cell lineages such as osteoblasts, chondrocytes, adipocytes, and myoblasts. Despite their

mesenchymal origin, they also been to trans-differentiate into neuronal and glial populations under proper conditions and they have been proposed as a possible therapeutic tool for CNS disorders. In fact, the widespread availability of MSCs throughout the human body make them a promising cell source for the autologous transplant in regenerative medicine. However, most of them are isolated from the iliac crest of the patient and therefore through a quite invasive method [43].

1.5 THE CELL SYSTEM

1.5.1 hCMCs

Human circulating multipotent cells (hCMCs) are a new population of adult stem cells that has been isolated by Ficoll density gradient separation from human donor peripheral blood. They are mononucleated cells with a fibroblast-like morphology during long term culture and a doubling time of 48 hours over 31 passages. By flow cytometry, they show immunophenotypical phenotype of stem cell population (CD44, CD73, CD105, Nestin) with similarities to mesenchymal stem cells (CD105, CD166, CD73, CD29) and meso-angioblasts (CD34).

Their intrinsic ability to secrete a large amount of several cytokines and growth factors allow hCMCs to control their own proliferation and differentiation. Notably, these cells are extremely responsive to changes in culture conditions that lead to their sudden gene expression and cell differentiation.

When cultured under proper inductive conditions, they can differentiate into progenitors for several mesodermal lineages as adipocytes, osteoblasts, chondroblasts or muscle cells. Neuronal differentiation can also be induced in these cells using a proper mix of growth factor, as confirmed by immuno-analysis of the expression of TUBβ3 (Tubulin β III), MAP2 (Microtubule associated protein 2), NeuN (Neuronal nuclear antigen), SYP (Synaptophysin), NCAM, dopamine transporter and neurofilaments (NF) [44].

Moreover, a recent study has reported that hCMCs are very responsive to nanotopographical stimuli: they have been cultured onto CNT-based scaffolds where neuronal differentiation could be promoted without addition of classic neurotrophins or other inducers, using only scaffold capacity to mimic relevant nanotopographical features of the tissue [45]. In addition, the presence of electrospun fibers guide protrusion extensions along the scaffold fiber orientation during neuronal differentiation [46].

In summary, hCMCs are a very promising source for stem cells in regenerative medicine applications because they are: i) characterized by a high degree of stemness and multidifferentiative potential ii) not subjected to ethical restrictions like ESCs iii) not genetically transformed so they are free from tumorigenic risk associated to iPSCs (iv) obtained in larger amounts in a less invasive and easier way in comparison to both NSCs and MSCs (v) a valid source for the autologous transplant in order to avoid rejection problems.

1.5.2 SH-SY5Y CELL LINE

SH-SY5Y cell line is a human catecholaminergic neuroblastoma cell line that was derived from a subclone of the parental neuroblastoma cell line SK-N-SH cells, originally established from a bone marrow biopsy of a neuroblastoma patient in the early 1970's.

SH-SY5Y cells resembles immature chatecolaminergic neurons in culture: they are highly proliferative and prone to grow in clusters showing neuroblast-like, non- polarized cell bodies with few truncated processes. They are locked in an early neuronal differentiation stage, biochemically characterized by typical immature neuronal marker; in particular, they express nestin, proliferating cell nuclear antigen and inhibiting factors for differentiation such as ID1, ID2 and ID3 [47].

However, SH-SY5Y cells can be differentiated from such neuroblast-like stat [48] into mature human neurons through a variety of different treatments including the use of retinoic acid (RA), phorbol ester, 12-O-tetradecanoylphorbol-13-acetate (TPA), BDNF, dibutyryl cyclic AMP, purine or staurosporine. SH-SY5Y cells can be driven toward a variety of adult neuronal phenotypes including cholinergic, adrenergic, or dopaminergic, depending on media conditions [48].

One of the best-optimized differentiation methods is treatment with RA that is directly added to the cell culture medium. RA is a vitamin A derivative and it is known to have strong growth-inhibiting and cellular differentiation-promoting properties. RA acts by binding to two families of nuclear receptors: the RA receptors (RARs) family and the retinoid X receptors (RXRs) family. Activated RAR heterodimerizes with RXR, then binding of RAR/RXR heterodimers to RA response element (RARE) influencing the transcription of the genes presenting the RARE element in the promoter. RA treatment induces the expression of TRKB, which is the high affinity catalytic receptor for several neurotrophins, including BDNF, and BDNF binding to TRKB activates pathways controlling cell differentiation. RA also plays a role in regulating transition from the proliferating precursor cell to post-mitotic differentiated cell; indeed, after in vitro treatment with RA, SH-SY5Y cells arrest in the G1-

phase of the cell cycle, DNA synthesis is inhibited, and growth inhibition is detected 48 h after treatment. After treatment with RA or other inducing agents, SH-SY5Y cells do not cluster because of the decrease in proliferation and their morphology resembles more closely primary neurons with pyramidal-shaped cell body and extend long branched processes. Differentiated SH-SY5Y cells have been reported to express a variety of different markers of mature neurons including growth- associated protein (GAP-43), βIII-tubulin, neuronal nuclei (NeuN), synaptophysin (SYN), synaptic vesicle protein II (SV2), neuron specific enolase (NSE) and microtubule associated protein (MAP). However, expression pattern of markers for receptor and transporters changes according to the phenotype obtained [49].

Therefore, SH-SY5Y share many biochemical and functional properties with neurons, representing a useful model system for in vitro studies of molecular mechanisms underlying neuronal behaviour.

Moreover, they have different advantages compared to primary mammalian neurons. First, SH-SY5Y cell line is human-derived, so it expresses protein isoforms that are absent in rodent cells. Second, immortalized cell lines can be propagated also when they undergo differentiation. Thirdly, SH- SY5Y cells can be further differentiated with inducing medium containing differentiating agents selecting for specific neuron subtypes. These aspects make SH-SY5Y cells useful for a multitude of neurobiology experiments.

1.6 CONTACTIN FAMILY

The Contactin family includes six proteins: Contactin-1/F3/F11, Contactin-2/TAG-1/Axonin-1, Contactin-3/Big-1, Contactin-4/Big-2, Contactin-5/FAR-2/ NB-2 and Contactin- 6/NB-3. Contactin proteins are all over 1000 AA in size and they show 40–60% identity as far as primary structure is concerned. They share a similar structure made of an extracellular domain consisting of six Ig-like and four fibronectin type III (FnIII) domains, followed by a glycosyl phosphatidyl inositol (GPI)-anchoring domain by which it binds to the extracellular part of the cell membrane. The main structural differences between Contactin proteins are especially located in the 4th and 5th FnIII domains [50].

The first four Ig-Domains of chick Contactin-2 and rat Contactin-4 have been structurally identified by X-ray crystallography showing a similar U-shaped arrangement in which domain 1 is connected to 4 and domain 2 to 3 and a flexible linker binds domains 2 and 3 [51,52]. These structural analyses indicate that U-shaped conformation characterizes whole Contactin family. Moreover, such conformation pattern resembles the horseshoe structure

of L1 family proteins, suggesting it could mediate interactions between ectodomains of Ig-CAM proteins. The essential role of such conformation has further proved by the evidence that mutation of any domains causes the loss of axonin-1 binding ability towards its ligand NgCAM.

Contactin proteins are mainly expressed in the nervous system as membrane proteins but they can also be secreted into the ECM after activation of extracellular phosphoinositide-specific phospholipase C (PI-PLC), an enzyme that regulates protein expression on cell surface and functional properties of GPI-anchored proteins. In the nervous system Contactin proteins mediate neural cell adhesion and migration, neurite outgrowth and fasciculation, axon guidance and myelination although the precise molecular mechanisms involved in their effects on neurite outgrowth have not been identified yet. Since they lack any cytoplasmic domain (they are GPI-anchored proteins), they can exert their function only through homo- and heterophilic extracellular domain interactions that occur in cis and/or in trans with several transmembrane proteins (including those from L1CAM family) and ECM components [53]. Therefore, their ability to modulate neurite outgrowth depends on their adhesive properties and it may also involve other molecules and receptors that can transduce signals to cytoplasm.

Notably, Contactins have been shown to interact with other Ig-CAMs. Contactin-1 binds to L1 in trans and NrCAM both in cis and trans. TAG-1/contactin-2 can participate in trans or cis-binding with L1 while it interacts with NCAM only in trans. 15 FAR-2, a chick orthologue of NB-2/contactin-5, has been observed to weakly bind L1. NB- 3/contactin-6 has been found in association with CHL1 and their cis-binding enhances cell surface expression of NB-3 [50,54]. Other important binding partners of the Contactin family are the receptor protein tyrosine phosphatises (RPTPs): CNTN 3, 4, 5, and 6 interact with the receptor protein tyrosine phosphatases gamma (PTPRG), found almost exclusively on neurons, while the CNTN1 binds receptor protein tyrosine phosphatases zeta (PTPRZ) localized on glial cells. The crystal structure of a complex of PTPRG and Ig domain 1-4 of CNTN 4 shows this binding is mediated by Ig2 and Ig3 domains of contactin-4 and all CNTN4 residues that interact with PTPRG are conserved in CNTN3, 5, and 6. The same Ig domains (Ig 2-3) mediate PTPRZ-CNTN1 interactions [52,54]. Furthermore, the protein tyrosine phosphatase α (RPTPα) has been shown involved in cis–interactions with contactin1, recruiting intracellular src family tyrosine kinases while the association RPTPα and NB3/contactin-6 has been reported to regulate apical dendrite orientation in the visual cortex. Interestingly, Contactin proteins have been observed to interact with amyloid precursor protein (APP) and Notch protein [50].

As far, Contactin1 and contactin2 have been investigated extensively, while fewer details are known about the remaining Contactin proteins.

1.6.1 Contactin-1

Contactin-1 (CNTN1), also called Glycoprotein gp135, was identified in the late 1980's as F11 in chicken and F3 in mouse.

It is mainly expressed in brain, but it can be found at low levels in lung, pancreas, kidney and skeletal muscle. The expression of CNTN1 is time and site-specific in neuronal system, in fact it seems to be a key regulator for axonal growth of cerebellar neurons during neural development. Moreover, CNTN1 is essential in axogenesis and myelination and it is part of specialized domains of myelinated fibers, the nodes of Ranvier and the paranodes. In the nodes of Ranvier, CNTN1 interact with the β1-subunit of the voltage-gated sodium channels responsible for action potential conduction, up-regulating their cell surface expression and stabilization in the membrane. At paranode level, CNTN1 is located on axolemma where mediates axonal contact to glia cell by binding to Contactin-associated protein Caspr, also known as paranodin, and neurofascin155 (NF-155), a glial isoform of Neurofascin. These interactions control the formation of the paranodal junction during myelination: the cis-binding between CNTN1 and Caspr in the endoplasmic reticulum (ER) induces ER to plasma membrane (PM) sorting of both proteins; then cell surface expression of CNTN1 and Caspr allows them to be clustered at paranodes through the binding to NF-155 expressed by oligodendrocytes. The absence of Contactin-1, Caspr or NF-155 causes the loss of this paranodal junction [55].

In addition, CNTN1 has a key role the neuromuscular junction since its absence at this level causes loss of communication or adhesion between nerve and muscle resulting in the severe myopathic phenotype [56]. In fact, Contactin-1 is also correlated to a familial form of lethal congenital myopathy and cntn1-null mouse presents ataxia, progressive muscle weakness, and postnatal lethality like the affected members by this disease.

Moreover, CNTN1 is involved in cancer: its overexpression increases tumour invasivity and development of metastases [57].

1.6.2 Contactin-2

Contactin-2/TAX1 (CNTN2), was first identified as TAG-1 in rat and as axonin-1 in chick. CNTN2 is the first Contactin expressed during development of the nervous system and its expression appears finely regulated in several subpopulations of neurons. In early stage development, it plays different roles including the regulation of migration, neurite outgrowth

and axon guidance. In the late phase of neuronal development CNTN2 regulates axon guidance and migration and its high expression on growth cone of extending axons, suggesting a function in initiating axon extension and fasciculation [58]. CNTN2 is also expressed in non-neuronal cell types such as Schwann cells and oligodendrocytes, confirming its importance in myelination [59]. It is located at the juxtaparanodal axolemma in myelinated fibers, where it is co-expressed with Shaker-type K+ channels and Caspr2 protein. The cis binding complex Caspr2/CNTN2 forms an axonal heterodimer that can associate in trans with CNTN2 expressed in the glial membrane. This complex is involved in the clustering of K+ channels at the juxtaparanodes. Recently, it was shown that CNTN2 can also interact directly with K+ channels [50].

Therefore, the contactin-2 is essential for the nervous system, as proved by its loss or mutation that causes cause epilepsy familial adult myoclonic 5 (FAME5), a syndrome characterized by cortical myoclonus and variable occurrence of epileptic convulsion. Furthermore, mutations in Caspr2 (CNTN2 binder) have been associated with different neuropsychiatric disorders, including seizures, mental retardation, schizophrenia and autistic spectrum disorder [60]

1.6.3 Contactin-3/4/5/6

Contactin 3 (BIG-1 in rat) is highly expressed in the adult brain especially in frontal and occipital lobe, cerebellum and amygdale. The specific roles of CNTN3 have not been clarified yet, although it could be implied in neurite outgrowth [50]. Contactin-4/CNTN4 (BIG-2 in rat) is mostly expressed in the adult brain where it is highly expressed in cerebellum and weakly expressed in corpus callosum, caudate nucleus, amygdala and spinal cord. In mouse, it is strongly expressed in mouse olfactory system where it seems to act as axon guidance molecule. Like other Contactins, it participates in formation, maintenance, and plasticity of neuronal networks and it could be involved in synaptogenesis or axon guidance due to his expression mostly restricted to the axons [54]. Notably, CNTN4 is associated with 3p deletion syndrome, a rare contiguous gene disorder involving the loss of the telomeric portion of the short arm of chromosome 3 and characterized by developmental delay, growth retardation, and dysmorphic features [61]. CNTN4 mutations have also been found in patients with autistic spectrum disorder [62].

Contactin-5/CNTN5 is known as FAR-2 and NB-2. It is found in restricted brain regions such as in subpopulations of Purkinje cells and neurons of the deep cerebellar nuclei. CNTN5 has also been shown to increase neurite outgrowth in cerebral cortical neurons, but not in hippocampal neurons and a clear functional characterization of CNTN5 is not available [63].

However, it is essential for the development of glutamatergic neurons in the rat auditory brainstem therefore it is probably involved in neuronal activity in the auditory System [64]. Contactin-6/CNTN6, also called NB-3, is a neuronal protein highly expressed in cerebellum, at intermediate level in thalamus, subthalamic nucleus and weakly expressed in corpus callosum, caudate nucleus and spinal cord. Like CNTN1 and CNTN2, it is expressed during development of mouse cerebellum where it is found in radially migrating granule cells located underneath the inner CNTN2-positive zone. Therefore, CNTN6 has been suggested to participate in granule cell maturation and/or synaptic formation in the developing cerebellum. In addition, movement impairment in NB-3-deficient mice suggests a function in cerebellar control of motor coordination in adulthood. CNTN6 also act as activator of Notch signalling pathways that is involved in oligodendrocyte differentiation, suggesting its role in regulation of neural precursor cell differentiation [54].

1.7 ROBO FAMILY

Insects and vertebrates have bilateral CNS, divided into right and left halves by a special midline structure. Communication between the two halves is essential for superior function and it is controlled by axon tracts connecting the left and the right half of the CNS during development. These connections, called commissures, cross the midline to connect and coordinate the two cerebral hemispheres. This midline crossing is finely regulated by roundabout receptors (Robo) and their Slit ligands that prevent aberrant axonal overpassing. In humans, three Slit proteins (Slit1-3) and four Robos (Robo1-4) have been identified [65].

Slits are large glycoproteins secreted by the midline cells and their expression pattern remains constant during brain development. They are constituted by several LRR, EGF like domains and a Laminin G domain. A cleavage site has been identified for Slits generating a still active N-Terminal and an inactive C-terminal fragment [66].

Robo1-3 are Type I transmembrane proteins expressed in many tissues, particularly at the surface of the growing axons in the nervous system [67].

Robo transcriptional pattern is finely regulated during development. Especially, Robo1 and Robo2 are expressed in overlapping pattern after midline crossing, while Robo3 is produced before the axon reaches commissure[68]. Instead, Robo4 is specifically expressed in endothelial cells, and its activity has been linked to tumour angiogenesis [67].

Robos belong to the Ig-CAM family and they have Ig-like and three FnIII domains, a transmembrane spanning region and four C-terminal domains (CC0–3) (**Fig. 5**). Still, in the

mammalian Robo family, the structure of Robo3 and Robo4 shows some differences: Robo3 lacks the CC1 domain and Robo4 lacks three Ig-like domains, one FnIII domain and both the CC1 and the CC3 domains. There also are alternative isoforms for Robo1-3: isoforms with variations at the N-terminal are referred to as Robo1-3 A or B whereas isoforms differing at the C-terminus are referred to as Robo3.2. In addition, Robo1 can be proteolytically cleaved to yield a soluble receptor [65].

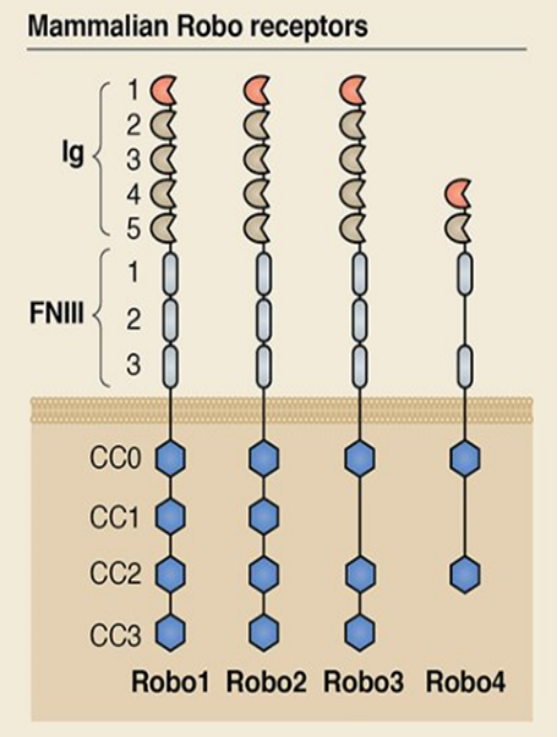

Figure 5. Structure of the Robo family: they contain immunoglobulin (Ig) motifs, three or two fibronectin (Fn III) motifs, a transmembrane domain and a conserved cytoplasmic domain (CC0–CC3) [65].

The cytoplasmic domain (CC0-CC3) in Robos lacks any enzymatic activity, so that its intracellular signalling can be modulated by coreceptors. In fact, according to the proteins bound to the cytoplasmic tail, Robo can exert several effects [69]. Intriguingly, the Robo cytosolic domains are predicted to contain little regular secondary structure and may thus belong to the class of intrinsically unstructured protein regions: in this case the ~500 cytosolic residues of Robos would occupy a very large volume of space explaining its ability to interact simultaneously with many adaptor molecules. Robo ectodomain is involved in interaction with CAM proteins: Robo1, Robo3 and Robo2 bind homophilically in trans and Robo1 heterophilically with other Robos or with DCC. Instead, interaction between Robos and L1 has not been observed [70].

Furthermore, recent researches hypnotize that the specific responses encoded by different Robos could be mediated by differences in the extracellular Ig domain structures of the receptors [71]. In fact, specific Ig domains in Robo receptor subtypes were found to encode

different functions such as the Ig1 and Ig3 of Robo2 which were important in specifying lateral positioning of longitudinal axons whereas the Ig2 domain functions mostly in promoting midline crossing. Notably, Slit/Robo interaction occurs between the second LRR repeat of Slit and the first two Ig domains of the latter, forming a 1:1 complex [72].

Slits constitute Robos' primary ligands. Slit–Robo Signalling regulates the guidance of axons of several commissural tracts including the corpus callosum, the optic chiasm, the anterior commissure and the hippocampal commissure [65]. It controls the migration of several neuronal subtypes including cortical interneurons, cerebellar granule neurons and inferior olivary neurons [73–75]. Studies suggest that Slit/Robo can control two properties in migrating cells, namely their directionality as well as their motility [68]. Moreover, Slit and Robo play a role in regulating the dendritic growth and branching, in different cell types and species [76].

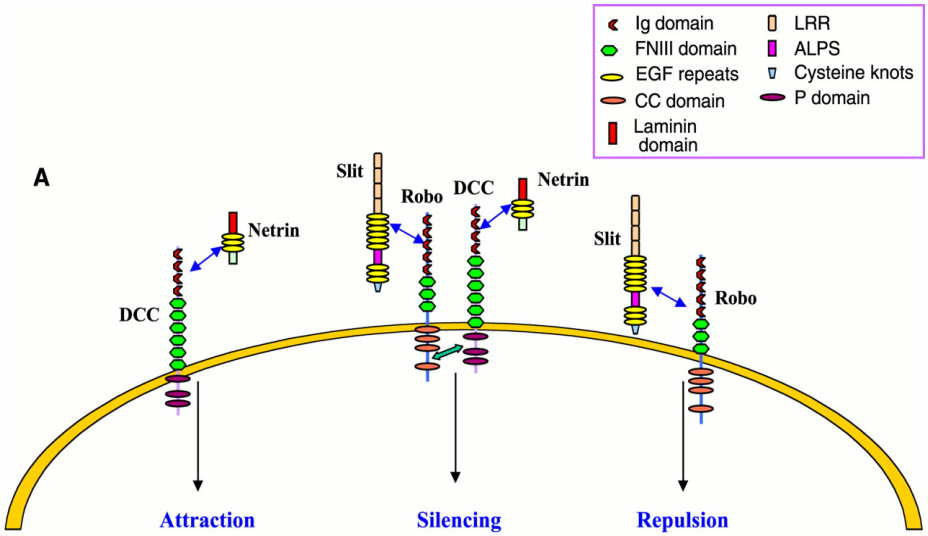

Figure 6. The interplay between Slit/Robo and netrin/DCC signalling. Netrin induce an attraction effect through its receptor, DCC. Slit induces axonal repulsion by binding to Robo. When the Robo receptor interacts with DCC, Slit functions as a silencer of the attractant netrin [78].

As far as cell adhesion is concerned, Robo/Slit system can mediate either inhibition or enhancement depending on the type of cells and coreceptor involved. Generally, Slit/Robo interaction mediate a repulsive signal expelling axons from the midline and preventing their inappropriate midline recrossing: the secreted protein Slit acts as a chemorepulsive midline cue that binds to the transmembrane receptor Robo, which is expressed on axonal growth cones, to control midline crossing [77]. However, Robo–Slit signalling is highly context dependent as both Robos and Slits have other binding partners which can modulate it. One of the main modulators of the Robo-Slit signalling is another major axon guidance signalling pathway: the Netrin–DCC pathway (**Fig. 6**). The interplay between these guidance-signalling pathways has been shown to have an important role in defining the topographical

maps that help axonal pathfinding. In spinal cord motorneurons, DCC interaction with Robo1 leads to the inhibition of Netrin1-mediated attraction. After metalloprotease cleavage of DCC, DCC stubs are no longer able to interact with Robo1 but retain the ability to mediate Netrin1 attraction. Thus, motorneurons gain responsiveness to Netrin1 [78].

There is an association between deregulated Robo/Slit signalling and several neuropathological and psychiatric disorders, such as dyslexia, autism and schizophrenia [79–81]. Especially, Robo3 mutations in the hinge between Ig2 and Ig3 prevent correct midline crossing, and they are the only identified genetic cause for HGPPS disease (horizontal gaze palsy with progressive scoliosis), characterized by defective eye movement and abnormal curvature of the spine [82].

Robo3 is considered a “black sheep” into Robo family. It undergoes extensive alternative splicing, and it is selectively expressed in the nervous system while the other Robos are expressed also in several tissues. Initially, Robo3 was thought to inhibit Slit interactions with Robo1 and Robo2 by binding to Robo1/2 in cis and thereby preventing their interaction with Slit. A new model suggests that Robo3.1 and Robo3.2 isoforms have opposite functions for commissural axons in the spinal cord: whereas Robo3.1 on pre-crossing axons promotes midline crossing preventing repulsive interactions between Robo1 and Slit, after midline crossing Robo3.2 is expressed instead of Robo3.1 in post-crossing axons, and Robo1, Robo2, and Robo3.2 detect the Slit proteins, which repel the spinal commissural axons away from the floorplate[83]. Moreover, studies have proved that ROBO3 interacts with DCC and function as a Netrin1 coreceptor to potentiate commissural axonal outgrowth and attraction [84]. Thus, ROBO3 is critically important for commissural axon guidance.

Notably, Robos have been implicated in a variety of other neuronal and non-neuronal processes such as cell migration, angiogenesis, even organogenesis of tissues such as kidneys, lungs, heart and breasts, as well as involvement in cancer invasion and metastasis [85].

1.8 DCC PROTEIN

Deleted in Colorectal Cancer (DCC) is a Type I transmembrane glycoprotein, with an extracellular domain consisting of four Ig-like and six FnIII domains. A single transmembrane segment is followed by a large cytosolic portion that contains three highly conserved sequence motifs termed P1, P2 and P3, of which P3 is involved in homophilic binding. Like other proteins in the L1CAM family, Ig domains organize themselves into a horseshoe conformation, where Ig1 bends to Ig4. Such N-terminal horseshoe is a structural

feature in many neuronal receptors and it might be evolutionally selected as a structural platform for specific functional purposes.

DCC protein was originally identified as a tumour suppressor gene located on chromosome 18q: its deletion in several tumour forms is implicated in differentiation and proliferation [86]. DCC is constitutively expressed in all adult tissues, but the highest levels are found in neural tissue, where it is involved in complex regulatory mechanism of axon wiring. In fact, it may act as both attractive and repulsive cue for the growth cone according to the context: for this reason, DCC is considered as a molecular switcher [87].

The best-characterized ligand of DCC is Netrin-1, a secreted protein that acts as a neuronal axon guidance cue involved in determining the direction and extent of cell migration and axonal outgrowth in the developing nervous system. Structural studies reveal that Netrin binds DCC close to the transmembrane domain, at level of the 5th and 6th FnIII repeats, domains, and that attractive axon guidance requires binding to two of these sites [88]. The binding of a single molecule of netrin-1 to two receptors induces DCC homodimerization via its very C-terminal cytoplasmic P3 motifs. These binding-site-rich intracellular domains form a scaffold for the recruitment of downstream effectors and regulatory proteins that leads to Src family kinase activation and eventually the rearrangement of the cytoskeleton, giving rise to the attraction effect. However, when UNC5 co-expresses with DCC, their heterodimerization converts the attraction into repulsion. The intracellular domain of UNC5 contains a binding site for the P1 domain of DCC, and the association between UNC5 and DCC mediates long-range netrin-dependent axon repulsion (**Fig. 7**) [89,90].

Additional complexity is due to other modulators of netrin-1 such as the draxin protein, secreted from the floor plate, acting as its antagonist in the developing spinal cord. Structural studies demonstrate that a draxin/netrin-1 complex binds in trans two DCC molecules from neighbouring axons simultaneously, promoting fasciculation. This could additionally lead to higher-order multimers of DCC, which would induce attractive signalling cascades along with linking axons [91].

Therefore, the growth cones reach an intermediate target and needs to move to the next target during navigation, and the switch from attraction to repulsion can be mediated by DCC, in addition to involving other guidance systems such as the Robo receptor responding to the Slit guidance cue, especially at midline [92]. In such site, commissural axons are finely regulated and DCC interacts with Robo1 via conserved cytoplasmic motif, located on segment P3 of DCC. Formation of the DCC–Robo1 complex is crucial for the neutralizing effects of slit-2, suggesting that integration of contradictory axon guidance signals

(represented by the attractive molecule DCC and the repulsive one Robo) may take place directly at the growth cone membrane [88].

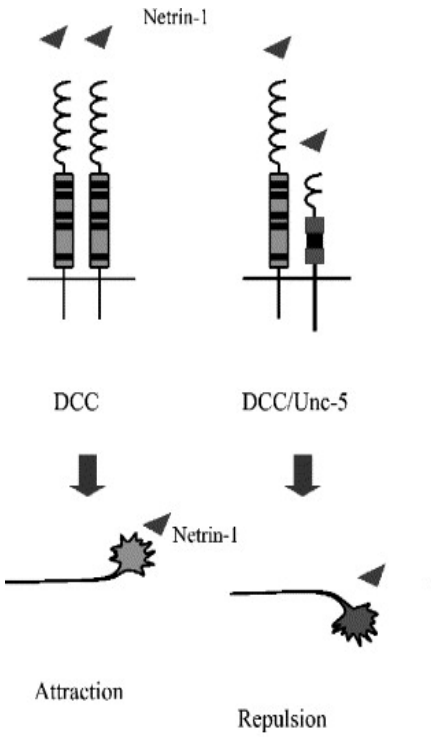

Figure 7. Summary of the distinct receptor complexes formed by DCC and the responses that they may transduce. Activation of DCC by netrin leads to attraction, while expression of UNC5 proteins in neurons expressing DCC converts netrin-mediated attraction to repulsion [90].

1.9 L1CAM FAMILY

The L1CAM family is composed by four members L1CAM, CHL1, NrCAM, Neurofascin, predominantly expressed by neuronal and glial cells especially during the development of the nervous system, where they have been implicated in several different cellular processes such as neuronal cell migration, myelination, axonal growth, pathfinding, neurite fasciculation and inter neuronal adhesion. Moreover, they all enhance neurite outgrowth in vitro and in vivo [93].

Interestingly, a small fraction of L1CAM proteins is also found in cells outside of the nervous system and it has been observed that non-neuronal cells usually express different isoforms of L1-CAM proteins from those expressed in neurons: except for CHL1, all the other members of L1 family contain a well-conserved 12-nucleotide miniexon, which encodes an RSLE amino acid motif in the cytoplasmic L1 protein domain of the neuronal splice isoforms. The RSLE motif generates a tyrosine-based signal that results in the sorting of L1-CAM protein to the growth cone and induces the AP-2-mediated endocytosis of L1-CAM and

presumably other L1-type paralogous proteins via Clathrin-coated pits [94]. Instead, the functional role of L1 molecules in non-neuronal tissues remains largely unknown although they have been heavily implicated in diseases, including cancers of the lung, pancreas, kidney and colon [95].

The L1CAM family members are highly glycosylated type transmembrane CAMs and belong to the immunoglobulin superfamily (IgSF), and they shared a large ectodomain of six Ig-like domains with up to five FnIII domains, a single transmembrane hydrophobic region and a short highly conserved cytoplasmic tail that presents two characteristic tyrosine-containing sequence motifs (LVDY and FIGQY) of the ankyrin-binding domain [96].

The ectodomain of L1CAM members is responsible of their adhesive function that comprises Ca-independent homophilic or heterophilic binding involving different extracellular binding partners including other CAMs, RGD-specific integrins, proteoglycans and RTKs. The ectodomain sequences and their related ability to interact with extracellular are very different between the L1CAM

proteins while their cytoplasmic domains are most highly conserved [94].

Cytoplasmic binding partners of L1-type proteins include cytoskeletal elements, protein kinases, and cellular protein complexes involved in endocytosis and intracellular protein trafficking, but it has been observed that L1CAM proteins can have different cytoplasmic binding partners, and even those with similar binding partners may be involved in different signalling complexes and mechanisms. However, all of them show the ability to interact with the actin cytoskeletal protein Ankyrin (**Fig. 8**).

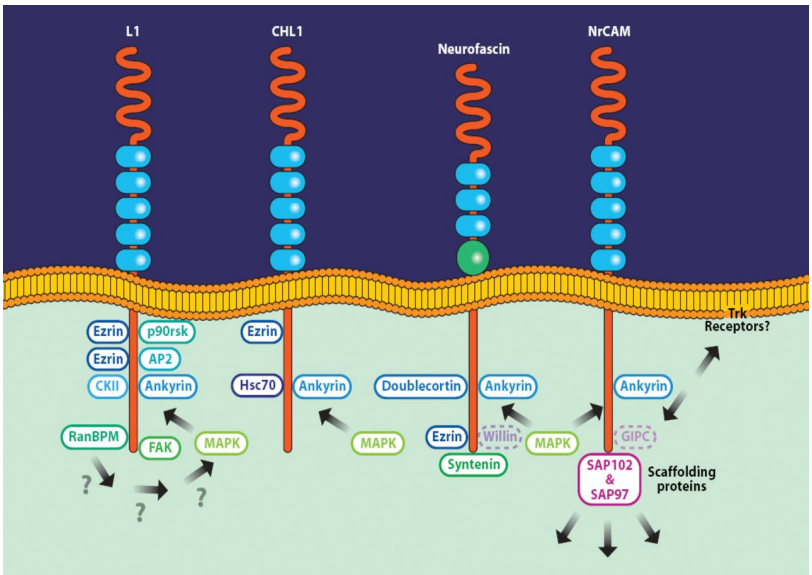

Figure 8. Members of L1CAM family. Summary of the reported interactions between intracellular proteins and the cytoplasmic domains of the L1-CAM family members [96].

Ankyrins are a family of adaptor proteins that mediate the attachment of integral membrane proteins, such as ion channels, ion exchangers and ion transporters, to the spectrin-actin based membrane cytoskeleton. The two major isoforms of the ankyrin-family expressed in the developing nervous are ankyrin B (ANK2) and ankyrin G (ANK3), and they bind the cytoplasmic domain of L1CAM proteins, coupling them to the spectrin cytoskeleton. Ankyrin binds the highly conserved 25-amino acid sequence in the L1-CAM family cytoplasmic terminus containing, the motif SFIGQY in which Y1229 phosphorylation regulates L1CAM-ankyrin mediated signalling. In fact, this interaction is disrupted by the phosphorylation of Y1229, thereby, enhances the neurite-growth-promoting activity of L1-type proteins [96].

1.9.1 L1CAM PROTEIN

L1CAM, discovered in the mid-1980s as a CAM in the nervous system, is the founding member of the L1CAM family. It is composed of six Ig-like domains and five FnIII repeats in the extracellular region, a single pass transmembrane region and a short cytoplasmic tail. It is highly conserved in mammals: human, rat and mouse share about 80% of the sequence encoding the extracellular domain, while the cytoplasmic tract is 100% identical [97].

L1CAM is expressed in three alternatively spliced isoforms depending on RE-1- Silencing Transcription factor (REST), the master factor governing neural cell differentiation. The main isoform is typical of low-REST neural cells, where it has been observed on the cell bodies, on growing axons and on growth cone of both differentiating and differentiated neurons as well as on glial cell. It is the only isoform presenting the peptide sequence YEGHHV encoded by exon 2, that is implied in binding to neuronal ligands and is important for growth-promotion of neural cells [98]. In fact, L1CAM plays an important role in brain development: it is involved in neurite outgrowth and fasciculation, neuron adhesion and survival, migration and myelination. It also modulates important functions in adulthood, such as synaptic plasticity and axonal regrowth and remyelination after nervous system injury [99,100]. The importance of this protein in human nervous system is underlined by more than 200 human L1CAM gene mutations that cause a variety of neurological disorders referred to as L1 syndrome or summarized by the abbreviation MASA (mental retardation, aphasia, shuffling gait, adducted thumbs) or CRASH (corpus callosum hypoplasia, retardation, adducted thumbs, spasticity, hydrocephalus). The interesting fact is that mutations in the L1CAM cytoplasmic domain are less likely to cause life-threatening disease, while mutations in the ectodomain produce severe pathologic conditions: the most critical phenotype is caused by a R184Q missense mutation at the Ig2 domain [101,102].

Recently, two isoforms of L1CAM ware discovered in glia cells but also in other non-neural tissues: they are overexpressed in many human cancers where their expression induces a motile and invasive phenotype, supporting an aggressive tumor growth, metastasis and chemo-resistance [103].

In addition, L1 can also undergo shedding: metalloproteinases ADAM10 and ADAM17 exert a photolytic cleavage within the third FnIII repeat or between the fifth one and the transmembrane region, which generate functionally active soluble fragments of the L1 extracellular domain [104].

In any cases, most of the functions of L1CAM are related to his ability to establish homophilic both in cis and in and heterophilic interactions with other CAMs, ECM proteins and proteoglycans. L1CAM homophilic binding is thought to be crucial for neurite outgrowth so mechanisms of binding have been investigated for a comprehensive interpretation of the process. Zhao et al. identified the homophilic binding site of L1CAM to the 14-amino acid sequence 178-HIKQDERVTMGQNG-191 of its second Ig-like domain using recombinant L1 from E. coli. They have produced this region as a synthetic peptide called L1-A and they have observed it inhibited binding of GST-Ig2-conjugated covaspheres to substrate-coated GST-Ig2, possibly because of peptide competition for the homophilic binding between the two Ig2 domains. As a negative control, they used a mutant version of L1-A peptide in which Arg was replaced by Ala, hence underling the importance of the conserved Arg184 residue in L1 homophilic binding [105,106]. Similarly, L1–Fcs bearing mutations in Ig domain 2 affect L1CAM homophilic binding [107].

Later, domain-mapping experiments were done with recombinant glycosylated L1 constructs from eukaryotic hosts, showed that homophilic binding involves more domains. SPR analyses show the first four Ig domains of L1 are the minimum unit required for its homophilic binding and adhesive activities. L1/ECD and L1/Ig1–4 were shown to be active in homophilic binding in trans, with domains Ig1–4 exhibiting a dissociation constant (130 nM) comparable with that of the entire ectodomain (116 nM) [108,109]. This data supports the model, based on crystal structure of L1 homologue Hemolin, proposing the horseshoe conformation of domains Ig1–Ig4 as the active form able to mediate the interaction in trans of opposing L1 molecules [110]. This hypothesis has been also suggested by electron microscopic (EM) studies on L1CAM proteins that suggest an equilibrium between folded (horseshoe) and extended conformations of L1CAM extradomain [111].

The correlation between homophilic binding and neuritogenic potential was also investigated showing that L1/ECD and L1/Ig1–4 were able to promote neurite outgrowth from human postmitotic NT2N neurons [109].

1.9.2 NEUROFASCIN PROTEIN

Neurofascin (NFASC) is the L1CAM family member with the highest number of splicing variants with different expression patterns during CNS development, suggesting it is a major player in the establishment and maintenance of the axonal pathways. In fact, the name “neuro-fascin” is due to the fact that antibodies against this molecule inhibit the formation of neurite fasciculations/bundles [112]. NFASC knockout studies in mice indicate that it also plays critical roles in axo-glial signalling and organization of proteins at the node of Ranvier and paranodal adhesion junctions of oligodendrocytes in the CNS and Schwann cells in the peripheral nervous system [113]. Moreover, different NFASC splice variants are directly involved in synaptic plasticity: in fact, they exhibit significant differences in interactions with various extracellular ligands due to their differences in the ectodomain that vary in the number of their FnIII extracellular domains and in the presence of an unusual PAT domain. The PAT domain, usually between the fourth and fifth FnIII domains in NFASC and it rich in the amino acids proline, alanine, and threonine and appears to be the target of O-linked glycosylation (**Fig. 9**). NFASC isoforms also have different subcellular localization in neuronal cells [114]. Currently, there are two major variants known: the 186-kDa axonal isoform (NF186) and the 155-kDa glial isoform (NF155).

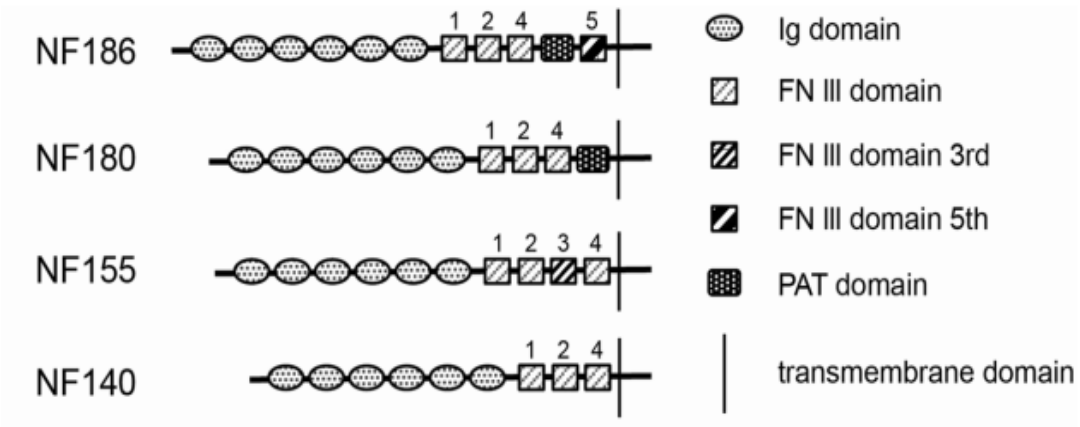

Figure 9. Structure of Neurofascin protein isoforms. NF isoforms consist of six Ig-like domains with different combinations of FnIII-like domains in the ectodomain [114].

The neuronal isoform NF186 is expressed at the axon initial segment (AIS) and at developing nodes of Ranvier. Here, they are required for clustering voltage-gated Na + channels thereby controlling rapid impulse conduction in these axons. NF155 is expressed on glia and its expression is transiently upregulated at the onset of myelinogenesis in the CNS. It is required for the node formation and the correct assembly of paranodal junctions,

where it interacts with axonal CNTN1 and Caspr1 to form a septal barrier excluding the nodal complex from internodes (**Fig. 10**) [115].

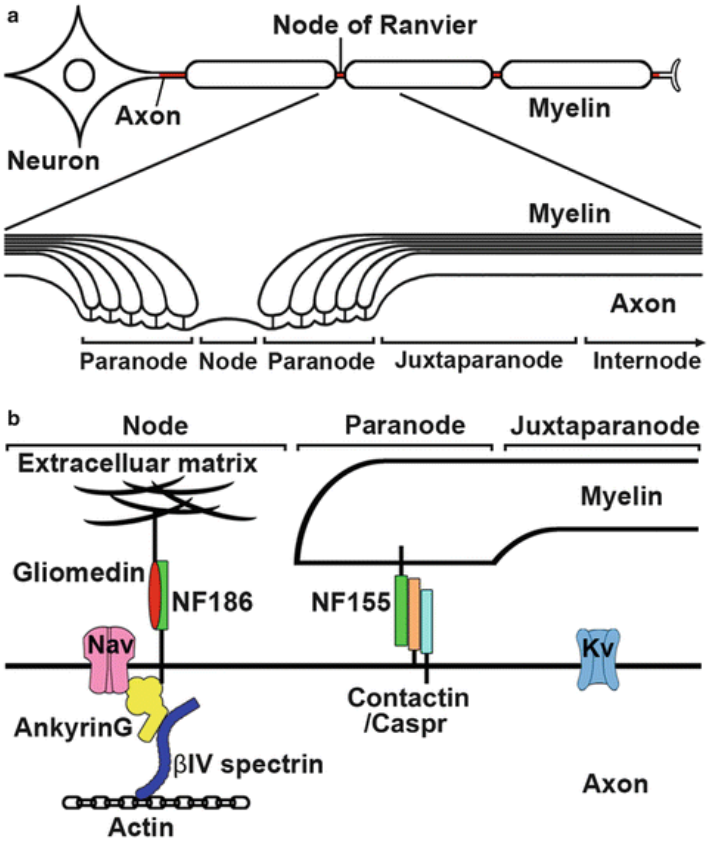

Figure 10. a) Schematic presentation of structures of the myelinated nerve fiber and axonal subdomains: nodes of Ranvier, paranode, juxtaparanodes, and internode. **b)** Schematic presentation showing molecular organization at nodes, paranodes, and juxtaparanodes: NF186 binds Gliomedin at PNS nodes, and NF155 forms a complex Contactin-1/Caspr-1/NF155 at paranodes [115].

Analysis of Fc fusion proteins representing different extracellular regions of NFASC indicate that different splicing variants of NFASC expressed on neurons and glia play distinct roles during neural development: NF186 inhibits cell adhesion and neurite outgrowth, and the inhibition is associated with the region containing the mucin-like domain. NF155 promotes neural cell adhesion and neurite outgrowth, and the RGD motif in its third FnIII repeat is critical for cell spreading and neurite outgrowth [116].

NF155 structure has been solved, unveiling the structures of a dimeric adhesion complex of the neurofascin N-terminal Ig domains in two independent crystal forms. The structures indicate that horseshoe conformation for its four N-terminal Ig-like domains, based on the interaction of a wide hydrophobic surface between Ig1 and Ig4 and between Ig2 and Ig3, is an integral structural module primed for recognition. In addition, dimerization in solution is mediated mostly by the side chains in the Ig2 domain, rising to a supramolecular ß–sheet with two-fold-symmetry; and horseshoes are paired in orthogonal side-to-side stacking

mode. Mutagenesis combined with gel filtration assays suggested that the side chain hydrogen bonds at the intermolecular ß sheet are essential for the homophilic interaction and that the residues at the hydrophobic cluster play supplementary roles. Such interaction mode is likely a conserved adhesion mode for the entire L1 family [110].

1.9.3 NRCAM

NrCAM (neuron–glia-related cell adhesion molecule) was the third vertebrate L1CAM member to be identified and it was being found mainly in the nervous system.

NrCAM is expressed in both neurons and glial cells in the developing and adult nervous system, where it plays a wide variety of roles in neural development, including cell proliferation and differentiation, axon growth and guidance, synapse formation, and the formation of the myelinated nerve structure [117]. However, it is also expressed in other organs such as placenta, kidney and pancreas. The importance of NrCAM is also supported by its involvement in the pathogenesis of a wide variety of human disorders, including psychiatric disorders and cancers [118,119]. In addition, NrCAM knockout studies have indicated that loss of expression can lead to changes in cerebellum morphology, eye development and development of the node of Ranvier; it has also been linked to an increased vulnerability to addiction and autism [120–123].

Like Neurofascin, NrCAM also undergoes alternative splicing, generating isoforms: the most prominent splicing is a 93 amino acid deletion in the fifth FnIII domain, resulting in the prevalent form of NrCAM in the brain that has only four, instead of five FnIII repeats. Recently, a soluble form of NrCAM has been observed at the node of Ranvier and it is produced by myelinating Schwann cells but it is not clear if this is a cleaved form of NrCAM or one of its splicing isoforms [124].

Although no biochemical/biological differences among isoforms have been demonstrated, it is possible that they could show different affinities towards ligands and thereby different biological functions. In fact, NrCAM functions are mediated by binding ability of its ectodomain both in cis and in trans with several receptors and ligands extracellularly and intracellularly. Homophilic binding enhances cell adhesion, while interaction with Neurofascin, Contactin 1 and 2 raises selective cell adhesion and neurite outgrowth [125,126]. NrCAM can act as a coreceptor for Semaphorins, whether it binds with Neuroplin, modulating axon guidance in the developing nervous system. Notably, interactions with Semaphorins seem to be an evolutionary conserved property of the L1 family of CAMs. NrCAM was also found in a complex with Integrins, Laminin, and neuronal proteoglycans. NrCAM interacts with several cytoplasmic and cytoskeletal proteins such that the

consequence of its interactions through its extracellular region could be directly linked to modulation of intracellular components [118].

To summarize NrCAM activity and function in vivo; NrCAM can support selective adhesion through multiple molecular interactions, and it direct axon growth, either through axon–axon interactions or axon–other cell interactions. These interactions can be modulated by the presence of other interacting molecules that can change the binding ability of the molecular complex to other molecules. Furthermore, NrCAM also modulates signalling mediated by other families of molecules that are involved in brain development and function. These features result in modulation of the responsiveness of neurons to guidance molecules and to cell proliferation signals.

1.9.4 CHL1

The close homologue of L1, CHL1, is first expressed at times of neurite outgrowth during brain development, and is detectable in subpopulations of neurons, astrocytes, oligodendrocyte precursors and Schwann cells both in CNS and PNS. The observation that CHL1 and L1 show overlapping and distinct patterns of synthesis in neurons and glia, suggests differential effects of L1-like molecules on neurite outgrowth. Furthermore, CHL1 is expressed even outside the nervous system, and it has been found in heart, intestine and gonads [127]. CHL1 has two main isoforms: a membrane-bound one (185 kDa) and a soluble one (165 kDa), which can also be obtained by interaction with protease ADAM8 [128].

In the developing brain, CHL1 regulates neuronal differentiation and survival, neurite outgrowth, and axon guidance, as supported by mice deficient in CHL1 showing reduced migration of pyramidal cells and wrong orientation of dendrites in the neocortex [129]. In the mature nervous system, both soluble and transmembrane isoforms of CHL1 are involved in regulation of synaptic activity and plasticity, including learning and memory. According to this fact, mutations in the CHL1 gene and protein have been implicated in several human neuronal diseases such as mutations in CALL gene leads to a down-expression of CHL1 are associated with the 3p syndrome, which is characterized by low IQ and mental retardation [130]. Moreover, mutations in the signal peptide are involved in schizophrenia [131].

As L1, CHL1 extracellular domain mediates homophilic adhesion as well as heterophilic interaction with other CAMs or membrane-bound proteins, such as Vitronectin, Integrins, and the Plasminogen Activator Inhibitor-2, NB-3, semaphorin 3A and neuropilin 1 [132]. Interestingly, CHL1 homophilic interactions inhibit neurite outgrowth of neurons from the developing CNS [133,134]. In contrast, CHL1 heterophilic interactions promote neurite

outgrowth, except when CHL1 or its proteolytic fragment generated by BACE1 interacts to Sema3A inducing growth cone collapse in thalamic and hippocampal neurons [135].
CHL1 triggers several intracellular signalling pathways that are comparable with the ones triggered by its homolog L1 [93]. Notably, CHL1 expression is upregulated in neurons that are capable of axonal regrowth after injury, preventing L1 from enhancing neurite repair. After SCI, CHL1 is overexpressed by glial scar forming astrocytes, where its homophilic interactions on severed axons inhibit axonal regrowth and impair locomotor recovery [136]. CHL1 also induces overexpression of NB-3 that inhibit axonal regeneration after SCI via receptor protein tyrosine phosphatase σ (RPTPσ)-dependent downregulation of mammalian target of rapamycin (mTOR) activity in neurons [137].

1.10 CARBON NANOSTRUCTURES FOR POLYMER-BASED NANOCOMPOSITES

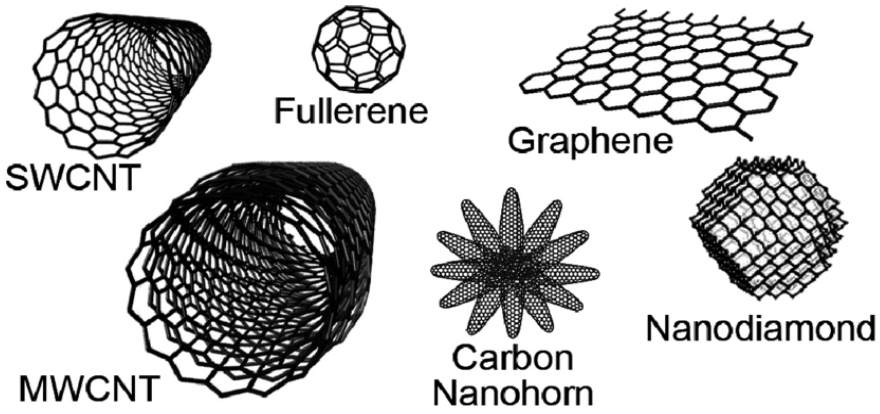

Figure 11. 3D sketches of carbon nanostructures [140].

The use of composite materials is steadily growing in biomedical applications. They are obtained by combining two or more materials with different physical and chemical properties, most of which are still retained in the composite, giving to it a unique character. Composites are made by one or more phases (the fillers) dispersed among a continuous phase (the matrix) and they are called nanocomposite when the size of at least one of the filler components is on a nanometer scale (<100 nm). Polymers are widely used for the matrix phase because of their ease of production and lightweight and ductile features and the nanoscale dispersion of the filler within the polymer matrix leads to extremely large interfacial contacts between the components, thus resulting in superior properties with respect to bulk polymer phases [138]. Among biocompatible, FDA approved, polymeric materials, poly(L-lactic-acid) (PLLA) has attracted great attention due to its renewable

origin, excellent mechanical properties and transparency. Instead carbon nanostructures are considered ideal nanofillers to improve the electrical, thermal, and mechanical properties of polymers because of their unique structures composed of sp2-hybridized carbon networks, characterized by high aspect ratios, electrical and thermal conductivities, high Young's modulus, and tensile strength [46].

In regenerative medicine several CNSs have been studied as promising nanofillers including single, double and multi-walled carbon nanotubes (SWCNTs, DWCNTs, MWCNTs), carbon nanohorns (CNHs), and graphene-based materials (GBMs) such as single-layer graphene, graphite nanoplatelets (GNPs), and particularly graphene oxide (GO) and reduced graphene oxide (RGO) (**Fig. 11**) [139,140].

1.11 CARBON NANOTUBES (CNTS)

CNTs are nanostructures made of a thick layer of six-membered carbon atom rings (i.e., graphene) rolled up into cylinders. CNTs with only one layer have diameters typically range between 0.8 and 2 nm with a tube length that can be many millions of times longer and they are known as SWCNTs. CNTs with two or more layers are known MWCNTs and depending on the number of layers, they have a larger diameter that can reach 100 nm (**Fig. 12**) [141].

Since their discovery in 1991 by Iijima, CNTs have attracted wide interest in most fields of science and engineering due to their unique physical and chemical characteristics [142]. The major areas of CNTs research are the polymer composites and biomedical devices including scaffold for regenerative medicine, biosensors, cell tracking and drug delivery carriers [143,144].

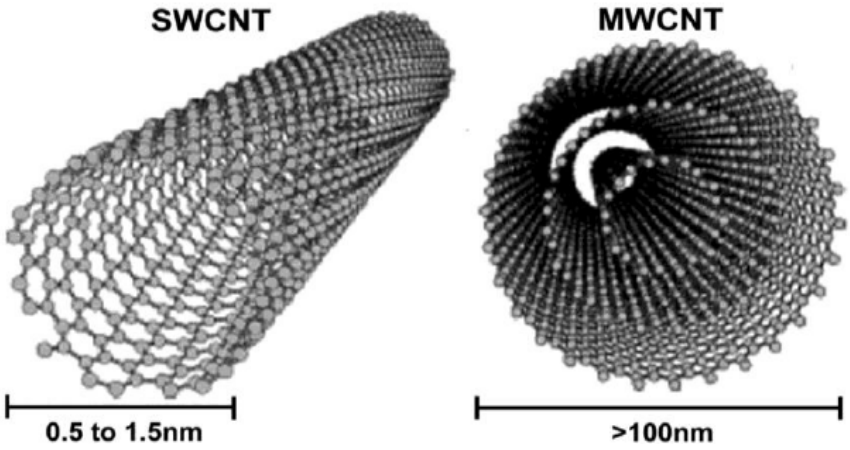

Figure 12. Schematic structure of SWCNT and MWCNT [144].

1.11.1 CNTs and neural regenerative medicine

Several features make CNTs a promising nanomaterial for developing scaffolds to be used in neural regenerative medicine including nanotopography, electrical conductivity, chemically modifiable surface and mechanical properties [144].

CNTs morphology and dimensions are similar to neuronal processes and to components of neuronal extracellular environment as proteins of the ECM and cytoskeletal elements [145]. Such CNT nanoroughness favours neuronal adhesion and differentiation. In fact, neuronal processes onto CNT film were shown to entangle around CNT nanostructures improving the binding of their membranes to surface [146]. Furthermore, their enhanced surface area and their chemical properties allow CNTs to adsorb adhesion proteins from the serum, and growth factors produced by the cells during their differentiation. The absorbed proteins can form a bioactive layer promoting cell adhesion and proliferation, and CNTs act as storage site that progressively release such proteins during cell maturation, in a "signal-buffered" environment suitable for long term neuronal growth and differentiation [39].

Furthermore, **CNT specific patterns** can be induced to act as guidance cues for axonal growth. Park and colleagues developed patterns of CNTs onto the biocompatible polymer polyimide, showing that hNSCs preferentially adhere in correspondence of the CNT patterned surfaces, and that CNT geometries can be modulated to tune both cell nuclei localization and neurite extension along the CNT patterns. Interestingly, the authors showed that such control on cell polarization can be obtained at single cell level [147]. The neuronal elongation can also be regulated by using electrospun CNT nanofibers: CNT coating of aligned electrospun PLCL nanofibers improves the neurites outgrowth of cultured DRG neurons and PC-12 cells along the scaffold fibres [148]; CNT–PLLA electuspun fibers, resembling the nanotopography of ECM proteins (i.g. fibrillar collagenous and laminin) boosted hCMC differentiation toward neuronal lineage with protrusions following the scaffold fiber orientation [45]. Thus, the use of CNTs to guide neurite elongation is a promising tool to develop an effective neural network.

Moreover, **CNTs electrical conductivity** is suitable to mimic the features of the electrically conductive nervous tissue promoting neuronal maturation and excitability. Hippocampal neurons grown onto SWCNTs or MWCNT substrate show an enhanced network activity and very tight contacts between CNTs and neuronal membrane, supporting the hypothesis that improved neuronal electrical signals depends on CNT properties [149]. Also, transmission electron microscopy analysis shows a direct electrical coupling between CNTs and neuronal membranes: CNTs can pinch neuronal membranes, and when such neurons are forced to fire, CNT substrates strongly impact on single-cell regenerative electrical properties

possibly due to electrical shortcut between adjacent dendritic compartments mediated by the conductive substrate [150].

Notably, the conductivity of CNT scaffolds can be finely tuned to enhance scaffold performance on neuronal electrical signalling and differentiation. In fact, SWCNT scaffolds with different conductivities and the same nanoroughness have different effects on the hippocampal neurite outgrowth depending on narrow ranges of conductivity [151].

In addition, CNT substrates can be used to electrically stimulate cultured neurons inducing neuronal differentiation and neurite extension. Improved neurite extension has been observed by electrical stimulation of PC-12 cell through a CNT/collagen composite [152]. A SWCNT substrate has been used to cultivate and electrically stimulate NSCs observing a boosted neuronal differentiation in the early culture stage [153]. Similarly, NCS in presence of SWCNTs-polymer electrospun scaffolds show an enhanced NSC differentiation ability after electrical stimulation [154].

Therefore, electrical stimulation through CNT-based matrixes can be used for enhancing and controlling neuronal differentiation and neurite extension in an electrically driven way. This approach is being explored for developing novel neural electrodes based on CNTs as coating material for metal electrodes [155].

CNTs have **chemically modifiable surfaces** and their functionalization is mainly based on two general approaches: on attachment of organic moieties to the carboxylic groups that are formed by oxidation of CNTs with strong acids or on direct bonding to the surface double bonds.

Chemical functionalization is used to improve scaffold properties. First, CNTS are highly hydrophobic so organic functional groups have been attached to CNT materials to enhance their solubilization in organic solvents for obtaining more homogeneous material. Also, the CNT surface charge can be modified by functionalization. For example, Hu et co-workers have set up the functionalization of MWCNT substrate with carboxyl groups, poly-m-aminobenzene sulfonic acid or ethylenediamine to create negatively, zwitterionic or positively charged CNTs, respectively. Improved neurite elongation and branching were found when cells were seeded onto positively charged CNT scaffolds, according to the known preference of neuronal cells for positive substrates such as poly-lysine [156]. Therefore, manipulation of CNT surface charge by chemical functionalization can be successfully used to tune neurite outgrowth.

Finally, biologically active molecules able to promote neuronal cell adhesion and differentiation can be attached to CNTs. Such bioactive molecules can be linked to CNT surfaces through covalent or non-covalent functionalization, this last based on weak forces

unable to retain for long periods the interacting molecules. For example, non-covalent functionalization of pristine MWCNT substrates with 4-hydroxynonenal, a molecule promoting neurite elongation, has showed an enhanced number of neurite per cell and total neurite length of cultured embryonic rat hippocampal neurons [157]. Also, covalent functionalization of MWCNTs with NGF and BDNF has been explored to culture embryonic chick dorsal root ganglion (DRG) neurons, observing that attached factors can maintain their bioactivity [158].

Moreover, CNTs are characterized by interesting **mechanical properties** mainly due to the sp2 bonds. The tensile strength of single-walled nanotubes is about one hundred times higher than that of steel, while their specific weight is about six times lower. Thus, they are among the toughest and strongest nanomaterials, but they can also have good flexibility.

For all the properties listed above, CNTs have been investigating as nanofillers in composite scaffolds. The incorporation of CNTs into polymeric scaffolds provide additional advantages: i) CNT can be used to modulate polymeric scaffold mechanical properties to mimic the ECM mechanical properties of the tissue of interest; indeed, it has been shown that, increasing the percentage of incorporated CNTs, the scaffold toughness and tensile strength also increase [159]; ii) CNTs reduce the polymer electrical resistance and they achieve their percolation threshold in polymer matrix composites at low concentrations ranging from 0.0025 to 4 wt%. This allows for the modulation of the polymer electrical properties, without changing other important aspects as processability [160].

As far, different type of scaffolds able to support neuronal cell adhesion and growth have been developed by combining CNT with polymers: MWCNT-PLCL scaffolds showed improved adhesion, proliferation and neurite outgrowth of PC-12 cells [148]; MWCNT-enhanced electrospun collagen/PCL conduit promote regeneration of sciatic nerve defects in rats and prevent muscle atrophy without invoking body rejection or serious chronic inflammation [161]; CNT–PGF (aligned phosphate glass microfibers) nerve conduit have been implanted into the 10 mm gap of a transacted rat sciatic nerve, resulting in a higher number of regenerating axons crossing the scaffold, demonstrating an effective role for CNTs in nerve regeneration [162].

However, the use of CNTs has been strongly debated for many years because it has been associated to toxicity and inflammation. Such effects are attributed to: i) CNTs sample often have contaminants and residual impurities (typically amorphous carbon, graphite nanoparticles, and transition-metal catalyst particles), that produce reactive oxygen species and induce cell oxidative stress; ii) low CNTs solubility leading to bundles or aggregates in aqueous solutions. It has been observed that CNTs can penetrate the cells membranes,

and depending on their length, CNTs can accumulate in the cytoplasm leading to cell death [163]. Also, a study showed that SWCNT form bundles above 10 μm in length after intraperitoneal administration in mice and such aggregates induce granuloma formation [164]. The problem with impurity and insolubility has now been alleviated using several purification techniques and a wide variety of noncovalent and covalent methods for CNT functionalization. This strongly improved CNT level of biocompatibility [165]. In addition, CNTs can be eliminated through renal excretion, so they can be used for their high loading capacity as drug delivery agents [166]. Therefore, it is very important to optimize type, doses, length and functionalization of CNTs being employed for each specific application.

1.12 GRAPHENE

Graphene is a two-dimensional monolayer of sp2-hybridized carbon atoms packed in a hexagonal honeycomb lattice. Since the discovery of graphene, many techniques to produce graphene and graphene-derived have been reported, including mechanical exfoliation, chemical exfoliation, and chemical vapor deposition. Chemical exfoliation from bulk graphite yields /produces graphene oxide (GO) that is a type of graphene nanosheet rich in hydrophilic oxygenated functional groups such as -OH and -COOH). GO can be reduced thermally or chemically to prepare reduced graphene oxide (RGO), which could restore the physical and chemical properties of graphene (**Fig. 13**)[167].

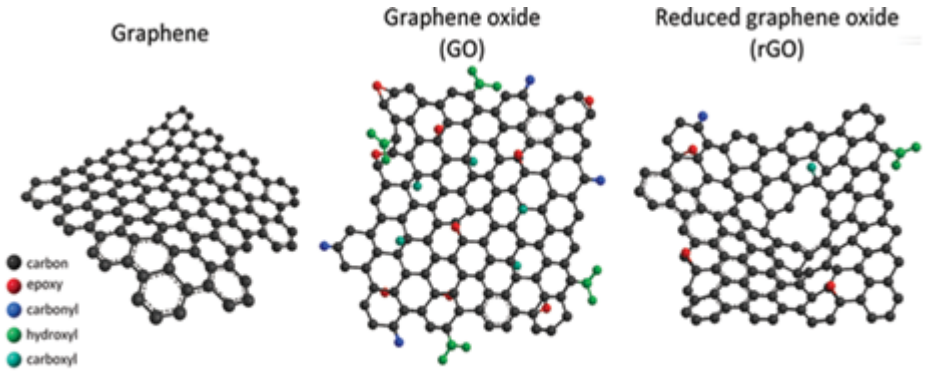

Figure 13. Schematic chemical structures of graphene, graphene oxide, and reduced graphene oxide [167]

The extended *p*-conjugation of graphene honeycomb arrangement yields unique physical-chemical properties such as excellent electrical and thermal conductivity, fast mobility of charge carriers, a high fracture strength, a high surface area–to-volume ratio. Furthermore, its chemical modifiability allows functionalization by attachment of reactive functional groups (such as amino, carboxyl, hydroxyl, alkyl halogen, or azide groups) to improve scaffold properties and the conjugation of different biomolecules. In fact, graphene represents a

suitable nanoscaffold to immobilise many substances, including small-molecule drugs, genes, antibodies, metals, biomolecules, fluorescent probes, and cells [168,169]. These properties confer significant potential of graphene for numerous applications in biotechnology, such as biosensing, disease diagnostics, antibacterial functionality, cancer targeting, photothermal therapy and electrical stimulation electrodes [170,171].

Due to the increasing interest in the use of graphene in biomedical applications, its potential toxicity has been investigated with different cells and animal models. These studies proved that graphene cytotoxicity is correlated to its hydrophobicity. In fact, suspended hydrophobic graphene particles have poor dispersion in aqueous media and they tend to agglomerate rapidly in cell culture medium with increasing concentration; such aggregates limit nutrient supply and subsequently induce oxidative stress, which triggers apoptotic pathways or programmed cell death. In contrast, hydrophilic GO or chemically functionalized graphene result in stable dispersions. They also tend to adsorb proteins on their surface, limiting direct interaction with cells, thereby minimizing cytotoxicity. Moreover, cells on graphene-based substrates appear to be responsive to the stiffness, roughness and nontopographical features of graphene. Surface-functionalized graphene film or substrate may provide sites for adsorption of biomolecules and formation of focal adhesions for enhanced cell attachment and proliferation. In addition, the conductive nature of a graphene film influences cellular behaviour [167,170]. For all these reasons graphene is a promising nanomaterial in regenerative medicine field, where several studies clearly indicate it can promote the adhesion, proliferation, and differentiation of various cells such as embryonic stem cells (ESCs), neural stem cells (NSCs), mesenchymal stem cells (MSCs), and induced pluripotent stem cells (iPSCs) [172–175].

1.12.1 Graphene and neural regenerative medicine

Different studies have assessed the biocompatibility of graphene with neural cells and its ability to functionally interface with neuronal tissue. For instance, cultures of neural cells on 2D graphene substrates have been found to exhibit enhanced adhesion, good viability as well as improved neurite sprouting and outgrowth [176]. A comparison between the effects of carbon nanotubes, GO, and graphene nanoparticles on the dopamine neural differentiation of mouse ESCs reports that only GO nanoparticles could promote the differentiation of ESCs into dopamine neurons, whereas carbon nanotubes and graphene nanoparticles did not show any important promotion of dopamine neural differentiation [173]. Nanostructured RGO microfibers also have been tested as scaffolds for NSCs culturing in vitro proving to be a substrate for NSCs adhesion and proliferation more powerful then 2D graphene film.

Notably, they regulate the NSCs differentiation into neurons and form a dense neural network surrounding the microfiber [177]. In another study, GO-coated electrospun-nanofibers or GO nanosheets functionalized with specific biomolecules have been used to selectively differentiate rat NSCs into oligodendrocytes, even in the absence of inductive factors in the culture medium. This ability of selective differentiation of stem cells into either neurons or oligodendrocytes is very promising for CNS regeneration[168,178,179].

Graphene proved to be able to form a functional neural network. Neurospheres derived from NSCs were seeded on graphene substrates and after 14 days of culture the process of network formation was visualised by beta-tubulin immunostaining. Embryonic neural progenitor cells seed on 3D GO-based scaffolds can differentiate into neurons and glial cells, establishing interconnected neural networks rich in dendrites, axons, and synaptic connections [168].

Furthermore, graphene modulates neuronal communication by tuning the distribution of extracellular ions at the interface with neurons, a key regulator of neuronal excitability [180]. In fact, graphene has been used for the development of electroactive scaffolds that may be able to transmit the externally applied electrical signal to promote neuroregeneration: NSCs differentiated on the surface of graphene electrodes exhibited not only an improved amount of differentiation to the neuronal lineage, but also improved functional maturation into electrically active neurons [181]. Electrical stimulation has also been used on retinal ganglion cells seeded on PPy functionalized graphene based aligned nanofibers, obtaining an enhancement of cell viability, neurite elongation, and antiaging properties [182].

1.13 CARBON NANOHORNS (CNHs)

Carbon nanohorns were discovered in 1999 by Iijima et al. They are composed of single-graphene_layer organized in horn-shaped single-walled tubules with a conical tip. Single-walled carbon nanohorns (SWCNHs) usually have the diameter of 2–5 nm and tubule length of 40–50 nm, and normally self-assembles in spherical dahlia-like aggregates with diameters of about 50–100 nm (**Fig. 14**) [183].

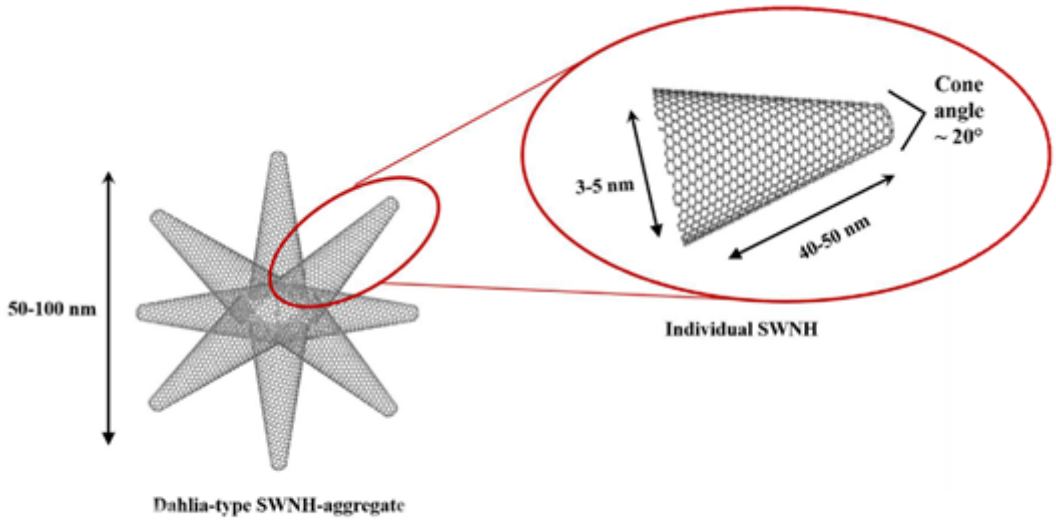

Figure 14. Illustrative structure and dimension of CNHs [183].

They are generally synthesized by laser ablation of pure graphite without using potentially toxic metal catalysts. In contrast, the metal catalysts are introduced during the production CNTs production, and treatments with strong acids are needed to remove any residual metal compounds and impurities; such treatment may damage the carbon structure, and simultaneously cause significant loss of the carbon material. Instead, CNHs are obtained with high production rate and high yield, their mass production occurs at room temperature and the final product is usually metal free and highly pure, making CNHs user-friendly and environmentally benign [184]. In fact, all the studies both in vivo and in vitro on SWCNHs toxicity approve the safety of this nanomaterial. Oral administration of 2000 mg/kg body weight of SWCNHs in several animal models have not induced any sign of toxicity even after the 2-week test period [185]. Additionally, histological studies have shown that SWCNHs can be accumulated in liver and spleen with no symptoms of haematological or immunological toxicity [186], although there is a study reporting their toxicity toward macrophages [187].

On other advantage of CNHs is represented by its easily multi-modifiable surface due to the higher chemically reactivity of CNHs than CNTs or graphene. Like CNTs, they are extremely hydrophobic, but they can be functionalized with oxygenated groups, such as carboxylic

acid groups, by oxidative treatment, to obtain hydrophilic oxidized SWCNH. This treatment promotes the opening of the horn tip while preserving the conductivity and electrochemical properties. The presence of the cylindrical inner nanospace and interstitial channels make CNTs well suited for both incorporation and slow release of materials and drugs [188]. Additionally, the opening of holes at both the tips and sidewalls of CNHs can be controlled with hole sizes that can exceed 2 nm. From such large holes, the incorporation and release of drugs or other biologically active molecules is easier as compared to SWCNTs. Furthermore, the secondary spherical superstructure of CNHs, forming dahlia-like aggregates, is intentionally appropriate and useful for immobilizing metal catalysts or other species[184]. Other positive CNHs features are their semi-conducting properties, field-emission characteristics, and thermal stability, while also displaying high resistance to oxidation [189].

Nevertheless, development of CNHs must face some problems such as CNHs aggregation tendency during synthesis, rendering their dispersion and separation difficult, and thus blocking functionalization and treatment of individual nanohorns. However new approach to separating these “dahlia- like” clusters into individual nanohorns are being developing [184].

Thus, there is great interest in applying CNHs to various applications in biotechnology and medicine, such as drug delivery, magnetic resonance analysis, biosensing and photodynamic therapy. Especially, SWCNHs have been used as a drug carrier to tumour tissue because SWNHs aggregate size matches the condition for achieving the enhanced accumulation in inflamed tissues also due to enhanced permeability and retention effect [189,190].

However, relatively little is still known about the use of carbon nanohorns for regenerative medicine purposes. A study reported that composites of PSU and SWCNHs supported the adhesion, spreading, viability and development of human osteoblast-like MG 63 cells in cultures on these materials. Interestingly, scaffold based on natural collagen with CNHs enhance the differentiation and maturation of neonatal rat ventricular myocytes and promote the expressions of electrical and mechanical proteins (Cx-43 and NC) [191]. Effect of nanohorns based scaffolds on neuronal regeneration must be investigated yet.

2. AIM OF THE PROJECT

Neural regeneration is a complex mechanism that can be promoted by both physical and biochemical cues of the extracellular environment. Thus, I have been working on the two main tracks of our developing biomimetic nanosystems:

1) The scaffold, used to reproduce mechanical, physical and electrical of ECM. We varied the type and concentration of nanofillers dispersed in the PLA matrix using from 0.25% to 5% of MWCNTs, RGO and CNHs. We wanted to check if their different electrical-physical-chemical properties could influence neuronal commitment and differentiation. Furthermore, we designed patterned scaffolds to regulate the direction of cell growth.

2) The biomimetic peptides, used to reproduce native biochemical cues regulating cell growth and differentiation. We worked on the development of novel biomimetic peptides and on the characterization of their mechanism of action.

3. RESULTS

My results are divided in two sections corresponding the main tracks of my PhD project: the scaffold and the biomimetic peptides.
In agreement with the international standards about PhD theses, I attached papers - either published or in preparation - including my results. These papers report on-going collaborative projects between our lab and other research groups. Therefore, they also include results from co-authors, giving a more completed overview about the subject of our research. However, individual contribution of each author can be clearly inferred as it is reported in the specific section of each paper.
For the scaffold section, I attached a published paper, a manuscript in preparation and a chapter including some preliminary results of our work.
For the biomimetic peptides; I attached one paper in preparation.

3.1 THE SCAFFOLD

In the first prototype of our biomimetic nanocomposite scaffold, purified and PhOMe-functionalized MWCNTs have been dispersed at 0.25%, in the PLLA matrix, combining the conductive, mechanical and topographical features of MWCNTs with the FDA-certified biocompatibility, processability, low cost, implantability of the PLLA matrix. The low concentrations of purified CNTs in the PLLA matrix strongly reduced CNT component cost and cytotoxicity while preserving its positive features. This nanocomposite scaffold proved to grant (i) full biocompatibility, (ii) good support to cell growth/differentiation, (iii) conductivity and (iv) mechanical flexibility required for implant purposes.
In last years, we have been working at further developing the nanocomposite scaffold by checking the biocompatibility and effect on the neuronal differentiation of varying types and concentration of nanostructures.
In the meantime, we have worked on the design of patterned scaffolds, by which control the cell growth direction.

3.1.1 Effect of different functionalized CNSs as fillers on the physical properties of biocompatible PLLA composites

In the following published paper, the three types of PhOMe-functionalized CNSs, namely MWCNTs, RGO and CNHs, have been used as nanofillers for the preparation of homogeneous and well-dispersed composites of PLLA.

We have tested RGO films and CNHs because they share mechanical properties, electrical conductivity and nanoscale dimensions of CNTs with additional specific advantages, as reported in the introduction section. We also have tested increased CNTs concentration, from 0.25 to 5%, dispersed in the PLLA-matrix to improve improve electrical conductivity and nanoroughness, two fundamental physical cues for neuronal differentiation. We have used the same range of NHs or rGO concentration dispersed in the PLLA matrix and we have compared them with already developed CNT-based scaffolds.

PhOMe-functionalized-CNS@PLLA composites have been characterized in their thin film forms by assessing the variation in thermal, mechanical and electrical properties**.** The analysis is carried out with the awareness that physical stimuli (including electrical, mechanical and topographic cues) influence growth and differentiation of cells and thus could be act as a guidance for future studies of neurogenesis. Thus, this paper aim is addressed to increase the understanding about physical properties driving cellular processes in vitro at first instance. Significant differences are observed among the different types of CNS nanofillers, underlying the key role played by the nanoscale shape and distribution of the components in driving the macroscopic behaviour of the composite material.

Also, we have observed that the new types and concentrations of our nanostructures don’t affect cell proliferation, viability and adhesion of human neuronal precursor cell line SH-SY5Y, proving to be biocompatible and opening the route to a future comparative analysis on their ability to boost neuronal differentiation.

Materials Chemistry and Physics 214 (2018) 265–276

Contents lists available at ScienceDirect

Materials Chemistry and Physics

journal homepage: www.elsevier.com/locate/matchemphys

Effect of different functionalized carbon nanostructures as fillers on the physical properties of biocompatible poly(L-lactic acid) composites

Nicola Vicentini [a], Teresa Gatti [a, **], Marco Salerno [b], Yuriko Suemi Hernandez Gomez [c], Mattia Bellon [c], Sasha Gallio [a], Carla Marega [a], Francesco Filippini [c], Enzo Menna [a, d, *]

[a] Department of Chemical Sciences, University of Padova and INSTM UdR Padova, Via Marzolo 1, 35131 Padova, Italy
[b] Materials Characterization Facility, Istituto Italiano di Tecnologia, Via Morego 30, 16163 Genova, Italy
[c] Department of Biology, University of Padova, Via Bassi 58/B, 35131 Padova, Italy
[d] Centre for Mechanics of Biological Materials, University of Padova, Via Marzolo 9, 35131 Padua, Italy

HIGHLIGHTS

- Nanocomposites were obtained based on carbon nanostructures and poly-L-lactic acid.
- Functionalized graphene, carbon nanotubes and nanohorns are compared as fillers.
- Composite electrospun nanofibers have also been prepared.
- Scanning probe techniques highlight electrical properties of nanofibers.
- Proven biocompatibility fosters future neuronal tissue engineering investigations.

GRAPHICAL ABSTRACT

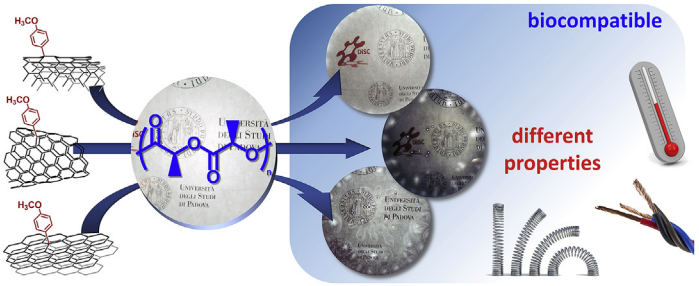

ARTICLE INFO

Article history:
Received 23 January 2018
Received in revised form
9 March 2018
Accepted 9 April 2018
Available online 23 April 2018

Keywords:
Nano composites
Carbon nanostructures
Biocompatibility
Electrical properties
Mechanical properties
Thermal properties
Electro-spinning

ABSTRACT

Composites of carbon nanostructures (CNSs) and biocompatible polymers are promising materials for a series of advanced technological applications, ranging from biomedicine and bioelectronics to smart packaging and soft robotics. In this work, we present three types of organic-functionalized CNSs, namely *p*-methoxyphenyl functionalized multi-walled carbon nanotubes, carbon nanohorns and reduced graphene oxide, used as nanofillers for the preparation of homogeneous and well-dispersed composites of poly(L-lactic acid), a biocompatible and biodegradable FDA-approved polymer. A thorough characterization of the composites is given in terms of calorimetric response, electrical and mechanical properties. Significant differences are observed among the different types of CNS nanofillers, underlying the key role played by the nanoscale shape and distribution of the components in driving the macroscopic behavior of the composite material. Surface properties are probed through advanced atomic force microscopy techniques, on both flat substrates (films) and confined systems (nanofibers). All these composites proved to be biocompatible and to support as scaffolds the proliferation of human neuronal precursor cell line SH-SY5Y, opening the route to a future comparative analysis on their ability to boost neuronal differentiation.

** Corresponding author.
* Corresponding author. Department of Chemical Sciences, University of Padova and INSTM UdR Padova, Via Marzolo 1, 35131 Padova, Italy.
E-mail addresses: teresa.gatti@unipd.it (T. Gatti), enzo.menna@unipd.it (E. Menna).

https://doi.org/10.1016/j.matchemphys.2018.04.042
0254-0584/

1. Introduction

Carbon nanostructures (CNSs), including carbon nanotubes (CNTs) and graphene-based materials (GBMs), are largely employed fillers for polymer phases, being able to confer novel properties to these last ones, such as improved electrical/thermal conductivities and mechanical reinforcement [1–5].

Among polymeric materials, biocompatible and biodegradable polymers [6] are of great interest for the scientific and industrial community due to their intrinsic sustainability, being derived from renewable sources and being suitable for recycling and/or biodegradation.

Composites of CNSs and biocompatible polymers can combine the properties of the two constituents and act as functional materials for a number of technological applications [7,8], which include medical devices and implants [9–12], tissue engineering [13–24], drug delivery [25,26], bio-, green and wearable electronics [27–29], biosensing [29–34], soft robotics [35,36] and smart packaging [37–39].

When attempting to combine biocompatible polymers with CNSs with the aim of fabricating a good quality composite, one has to face major obstacles related to the often profound physical incompatibility between the two materials. In fact, while the polymer is more hydrophilic, pristine CNSs are hydrophobic and in addition have a pronounced tendency to aggregate, because of the strong van der Waals interactions between π-electron clouds. High-power ultrasonication and/or shear mixing can sometimes help in blending the two components [40], however these processes are not always effective, and harsher conditions can induce deterioration of the CNSs [41–43]. As alternative approaches, current chemical strategies aim to increase the affinity between the two phases by either adding surfactants [44] or chemically functionalizing the external surface of CNSs with suitable organic groups [8,45–47]. This latter option, particularly suitable for high added-value applications, has the advantage of being tunable with respect to the type and amount of organic moieties inserted onto the CNSs, making it possible to direct the properties of the final material [48]. In this case, the primary goal is an improved compatibility and homogeneous dispersion in an environment having a given polarity, either a solvent or a polymer matrix. We have recently demonstrated the effectiveness of this strategy, by functionalizing multi-walled CNTs (MWCNTs) with *p*-methoxyphenyl groups through a diazotization process, involving the *in situ* generation of aryl radical reactive species starting from the corresponding aniline derivative [49]. By tuning reactant amounts and reaction times, solubility of the functionalized species can be directed towards different solvent polarities.

In addition, we have shown that *p*-methoxyphenyl functionalized MWCNTs (MWCNT-PhOMe) can be efficiently dispersed in poly(l-lactic acid) (PLLA), - a FDA-approved biocompatible and biodegradable polymer - and the resulting composites (MWCNT-PhOMe@PLLA) can be processed in the form of free-standing homogeneous films [13] and electrospun nanofibers [14] able to promote neuronal growth and differentiation starting from either SH-SY5Y human neuroblastoma cells [13,14] or human circulating multipotent stem cells from peripheral blood [15].

Different dimensionalities of CNSs such as CNTs, reduced graphene oxide (RGO) and carbon nanohorns (CNHs) give rise to different properties and may induce different behaviors on composite materials when used as fillers [50–52]. A comparison of the physical properties of the resulting composites could help tailoring novel materials for specific applications and, when considering cell growth scaffolds, hints could be gained about physical properties' influence on cellular processes. We report in the present work novel types of functionalized-CNS@PLLA composites based on different CNSs, namely *p*-methoxyphenyl decorated RGO [53] (RGO-PhOMe) and *p*-methoxyphenyl decorated CNHs (CNH-PhOMe), synthesized analogously to MWCNT-PhOMe. We also consider more MWCNT-PhOMe@PLLA composites, by testing the effect of increasing CNT contents in PLLA. A detailed overview of the macroscopic properties of these composite materials is provided, involving electrical, mechanical and thermal characterizations as a function of the type and concentration of nanofillers. Surface properties are probed through advanced atomic force microscopy (AFM) techniques on both flat and nanoscale confined systems (single composite nanofibers). Finally, proofs of their biocompatibility with neuronal precursors are given, opening the route to future experiments testing their ability to favor neuronal differentiation.

2. Experimental

2.1. Materials

All reagents and solvents were purchased from Sigma-Aldrich and used as received if not otherwise specified. MWCNTs were produced by SouthWest NanoTechnologies with the CVD method and have the following dimensions: outer diameter 10 nm ± 1 nm, internal diameter 4.5 nm ± 0.5 nm, lengths 3–6 μm. CNHs were purchased from Carbonium s.r.l. (Padua, Italy) and present a dahlia-type shape with a diameter of 60–120 nm. RGO powder was purchased from ACS Material, LLC (product No.: GnP1L-0.5 g). The RGO production method, as reported by the supplier, consists in completely reducing graphene oxide obtained via the Hummer's method through thermal exfoliation reduction and further hydrogen reduction. Reduced graphene oxide flakes have lateral dimensions between 1 and 2 μm, are constituted of few layers overlapping irregularly and have many corrugations (see Refs. [53–56]).

2.2. Synthesis of p-methoxyphenyl functionalized CNSs

Functionalization of MWCNTs, CNHs and RGO was carried out following the previously reported diazotization procedure (Scheme S1), with slight modifications [14,53]. For each CNS, the stoichiometry of the reaction has been optimized in order to obtain the maximum gain in chloroform solubility. For the sake of clarity, details are given here.

A dispersion of as purchased CNSs (75 mg, 6.25 mmol of C) in 1-cyclohexyl-2-pyrrolidone (CHP) (35 mL), pre-sonicated for 10 min (power level: 2.0, pulse on: 3 s, pulse off: 3 s) was transferred to a two-necked round-bottomed flask. A solution of 4-methoxyaniline (385 mg, 3.13 mmol for the functionalization of MWCNTs and RGO; 770 mg, 6.25 mmol for the functionalization of CNHs) in 15 mL of CHP was added and the mixture was heated to 80 °C under a nitrogen atmosphere. Then, isopentylnitrite (0.42 mL, 3.12 mmol for the functionalization of MWCNTs and RGO; 0.84 mL 6.25 mmol for the functionalization of CNHs) was added carefully. After 15 min of continuous stirring, the reaction mixture was diluted with cold methanol (500 mL) and filtered on a PTFE membrane (Fluoropore 0.2 μm). The filtrate was washed with methanol (4 × 200 mL) and dried under an IR lamp for 30 min. For each CNS the functionalization procedure was repeated 3 times in order to obtain the amount of *p*-methoxyphenyl functionalized CNSs required for the preparation of the composite materials.

2.3. Preparation of functionalized-CNS@PLLA films

p-methoxyphenyl-CNS@PLLA blend solutions in $CHCl_3$ were prepared by adding a dispersion of MWCNT-PhOMe or CNH-

PhOMe or RGO-PhOMe in chloroform obtained through sonication (power level: 2.0, pulse on: 3 s, pulse off: 3 s, 5 min) to a chloroform solution of PLLA (6 wt%) under continuous stirring. The amount of *p*-methoxyphenyl-CNS within the various blends was varied among 0.1, 0.25, 0.5, 1 and 5 wt% with respect to the polymer content. Films of the various composite materials were obtained through solvent evaporation into a petri dish at 50 °C and each of them had a diameter of 6 cm (see Fig. S4 in the Supplementary Information – S.I. - for pictures). For mechanical characterization, samples were cut into 5 identical specimens each with sizes of 40 mm × 10 mm x 0.3 mm. These are not standardized specimens, intended for internal comparison only, and the tensile data are not therefore comparable with literature data.

2.4. Characterization of functionalized-CNS@PLLA films

Absorbance values at 1000 nm were measured with a Varian Cary 5000 spectrophotometer. DSC measurements were carried out with a DSC Q20 (TA Instruments) under nitrogen by heating the samples at 1 °C min^{-1} over a temperature range from 40 to 200 °C. A complete heating-cooling-reheating cycle was carried out to eliminate thermal history of the samples, and thermograms from the second heating stage (reheating) are reported. The thickness of each sample was measured in different points using a Mitutoyo Digimatic micrometer with a precision of 10^{-4} cm. Tensile mechanical properties of rectangular-shaped specimens were measured using an Instron model 3300 mechanical tester at room temperature. The strain rate was 10 mm min^{-1}. At least five measurements were performed for each sample. The surface resistance of the films was measured with two different instruments depending on resistance. For films with resistance lower than 10^6 Ω a digital multimeter, Keithley 2000 provided with 4 probes positioned at a distance of 1 cm with respect to each other was used. Each film sample was measured at different points and average values are given. For films with resistance higher than 10^6 Ω a Keithley electrometers for Ultra-High Resistance *6517B*, implemented with a resistivity test fixture (Model 8009) for measuring surface resistivity was used. Measurements were performed alternating the polarity between 100 V and −100 V and acquiring each point for 60 s. Average values over 10 repetitions are reported.

2.5. Preparation of functionalized-CNS@PLLA electrospun nanofibers

Solutions of *p*-methoxyphenyl-CNSs/PLLA blends (5 wt%) to be used for electrospinning were prepared following the same procedure described for the preparation of the films but using a $CHCl_3$:DMF 9:1 (v/v) mixture as solvent. The small DMF portion in the solvent was introduced in order to increase the boiling point, i.e. to optimize conditions for electrospinning. Electrospinning was performed on a home-made apparatus with an applied voltage of 18 kV, tip to collector distance of 20 cm and by maintaining a solution flow rate of 0.03 mL min^{-1} on the syringe pump injector. Transmission electron microscopy (TEM) images were recorded, on samples spun directly onto TEM copper grids for 60 s, with a Tecnai G2 microscope (FEI) operating at 100 kV. AFM images were recorded on samples spun onto Graphene Supermarket silicon prime wafers (oxide thickness: 285 nm) for 60 s (see AFM details later in the text).

2.6. Sample preparation for AFM

For the film samples, small specimens (~5 × 5 mm) were cut and mounted each on a different optical microscope glass slide (1" × 3") by means of double-sided sticky tape. In case of topographic-only measurements a standard tape was used, while for the CAFM measurements a conductive carbon tape (normally used for scanning electron microscopy as a drain layer for the injected electron beam current) was employed. The goal was to obtain a measurement of local transversal (i.e. out of plane) conductivity, perpendicularly to the film and through that, like the case of macroscopic measurements of film conductance. For the fiber samples, few fibers were directly deposited by electrospinning on an insulating substrate of oxidized silicon wafer. The fibers were sparse enough to allow us to address and image them independently. The fibers crossed the whole silicon substrate diameter and touched the substrate edges on both opposite sides. There, a contact was provided all around the substrate edges by means of silver paste. The goal was to obtain a measurement of local longitudinal (i.e. in plane) conductivity, axial to the fibers, and provide a value of single fiber conductivity. Because the fibers were contacted on both opposite side ends, and in order to minimize the possible voltage drop along the fiber, the measurements were always carried out on fiber regions close to one edge of the silicon substrate, in the range of 100–300 μm distance from that. In both cases of CAFM samples (films on carbon pad or fibers with silver paint) the contact was taken away to the AFM head by means of adhesive copper tape stuck to the glass slide, and, later on, at a magnetic contact pad, to the head through a thin compliant wire.

2.7. AFM measurements

All the AFM images were 256 × 256 pixels and were acquired on an MFP-3D instrument (Asylum Research, US) in ambient air. For the conductive AFM (CAFM) measurements, a probe of type AC240TM-R3 (Olympus, Japan) was employed, with cantilever resonance frequency of 66.62 kHz and spring constant of 1.81 N/m. The tip had a Ti/Pt coating of ~20 nm thickness, and thus an effective apex diameter of ~60 nm. Further technical details about the CAFM measurements are reported in the S.I., for the sake of space. For SKPM a probe of type PPP-EFM (Nanosensors, Switzerland) was used, with resonance frequency of 95.90 kHz. The tip has a Ti/PtIr5 coating of ~25 nm thickness, and thus an effective apex diameter of ~70 nm. The AFM was operated in lift (Nap) mode, with tapping tracking of the topography during the first pass, and at an elevation of 100 nm during the second pass. During the latter pass, a feedback was applied on the tip voltage, a sum of AC and DC components, such that the electrical force between tip and sample (set at virtual ground) was canceled out. In some cases, to provide better understanding of the electrical surface properties, the analysis was switched from SKPM to qualitative EFM mode. While this is also based on two-pass technique, during the second pass the cantilever is dithered mechanically and the open-loop changes in oscillation phase are observed. On average, lower local phase lags of the oscillating cantilever should correspond to net repulsive forces, while higher local phase lags should correspond to attractive forces. For the roughness measurements, tapping mode AFM was carried out with a probe of type SSS-NCHR (Nanosensors, Switzerland), with cantilever resonance frequency of ~312.53 kHz. The most important amplitude parameter of surface roughness, namely 2-D root mean square S_q has been extracted from the height distributions in the images, and averaged over all the images ($N \geq 5$).

2.8. Biological methods for the assessment of biocompatibility of the functionalized-CNS@PLLA scaffolds

Exponential growing human neuroblastoma SH-SY5Y cells [57] were cultured with Dulbecco's Modified Eagle Medium/Nutrient Mixture F-12 (DMEM/F-12) GlutaMAX™ supplement (Invitrogen) supplemented with 10% heat-inactivated fetal bovine serum (FBS,

Euroclone) and 25 μg/ml of gentamicin (growth medium), in a humidified atmosphere of 5% of CO_2 in air at 37 °C. Cells were subcultured - 900000 into 25 cm^2 flasks (Sarstedt) - every 2 days (i.e. at 90% confluence approximately). In control, scaffold-free samples, cells were seeded in a 24-well plate (15000 cells/well) coated with a gelatin (porcine skin 0.005% in H_2O milliQ)/poly-L-lysine (Invitrogen, 1 mg/ml) solution. Poly-L-lysine is widely used as a good substrate for neural cell adhesion and growth. PLLA and CNS@PLLA films were cut into round slices with 13 mm diameter for well positioning into 24-well plates. After sterilization by UV irradiation, the films were incubated for 24 h in growth medium and then cells (15000/well) were seeded onto their surfaces. Cell death and proliferation were assessed at day 0 (24 h after cell seeding) and day 2 (72 h after cell seeding) as reported in the S.I.

3. Results and discussion

3.1. Preparation of functionalized-CNS@PLLA composites

The three types of CNSs considered in this work, namely MWCNTs, RGO and CNHs, were first subjected to the functionalization process to obtain the corresponding *p*-methoxyphenyl derivatives. The functionalization reaction was carried out in cyclohexyl pyrrolidone (CHP) in the presence of *p*-methoxyaniline and isoamyl nitrite (see Scheme S1 and experimental details in section 2), as reported for both MWCNTs [14,49], RGO [53] and CNHs (for the first time here). This direct arylation reaction (Tour-type reaction [58]) is a convenient procedure to obtain functionalized-CNSs with improved solubility profiles and diminished tendency to self-aggregation. In relatively short times (15 min in the present case) and in a single step, it is possible to obtain covalently decorated CNSs for the desired purpose. The choice to employ the same reaction and the same type of functional groups for all three selected CNSs is based on the need for comparing properties of the nanomaterials *per se* and of the final PLLA composites containing them. Reactants amounts were screened in order to determine the best condition for achieving the highest dispersion of the functionalized CNSs in chloroform (the solvent of choice for PLLA). Particularly, the maximum dispersion of MWCNTs and RGO in chloroform was obtained when the reaction was carried out with 0.5 equivalents of *p*-methoxyaniline and isoamyl nitrite as compared to the moles of carbon contained in the CNSs, whereas for CNHs this happened when using 1 equivalent of reactants. The need for different amounts of reactants to gain the best solubility appears reasonable when considering the huge differences in nanomorphology existing among the three CNSs, which leads to different reactivity and tendency to aggregate. The resulting functionalized CNSs, namely MWCNT-PhOMe, RGO-PhOMe and CNH-PhOMe were characterized in terms of functionalization degree (FD), already used in previous works [49,53,54], which was determined with a good precision through thermogravimetric analysis (TGA; the corresponding thermograms are reported in Fig. S1, S2 and S3 in the S.I., together with an explanation of how FDs were calculated). Particularly FD values of 1/118, 1/47 and 1/44 were found for MWCNT-PhOMe, RGO-PhOMe and CNH-PhOMe, respectively, indicating that one *p*-methoxyphenyl substituent is present every 118, 47 and 44 carbon atoms of the CNS (the highest number obtained for MWCNT-PhOMe is consistent when considering that only carbons of the outer walls are reactive). The obtained CNS derivatives were effectively dispersed in chloroform and then mixed with PLLA in different weight percentages (wt%) with respect to the polymer, following the procedure described in the Experimental Section. In this way films of MWCNT-PhOMe@PLLA, RGO-PhOMe@PLLA and CNH-PhOMe@PLLA were prepared containing 0, 0.1, 0.25, 0.5, 1 and 5 wt% of functionalized CNSs in PLLA. The resulting films were all free-standing and characterized by a glossy texture (see Fig. S4 in the S.I.). Resulting thicknesses were uniform among the films and all included in the range between 300 and 350 μm (see Table S1 for the exact values). The good dispersion of the functionalized CNSs within the polymer matrix was evident after backlight inspection of the films with the lower concentrations of CNSs (0.1 wt%, see Fig. 1a), in which the presence of macroscopic aggregates was not evident, while at higher concentrations transparency was lost and backlight inspection was not feasible. Furthermore, it is worthy to state here that attempts to prepare composite films with pristine-CNSs and PLLA at 0.25 wt% (a relatively low nanofiller concentration) following the same procedures, resulted in the formation of highly un-homogeneous materials, presenting internal fractures and CNS aggregates visible to the naked eye. For the case of MWCNT-PhOMe@PLLA films an almost linear trend in the optical absorption at 1000 nm (a wavelength where only CNSs absorb) can be observed for the first three wt% examined, as reported in Fig. 1b, while at higher wt% saturation of the signal was achieved, not allowing to extend the extrapolation. For the other two functionalized-CNS@PLLA films only two points were measured due to saturated absorption at lower wt% as compared to MWCNT-PhOMe@PLLA films (see Fig. 1b). For the RGO-PhOMe@PLLA films the trend in absorbance was likely not linear, as inferred by guessing an absorbance of the 0.5 wt% film higher than 4 and therefore already out of a linear trend and a residual absorbance at 0 wt% CNS content (this last one resulting, at a lower extent, also for the other two types of functionalized-CNS@PLLA composites). Attempts to characterize the composites through FT-IR analysis failed due to the absence of any significant IR absorption feature in the functionalized-CNSs and to their low percentage in PLLA (only IR signals of the polymer were detected, with no shifts or intensity changes when going from the pure material to its composites).

The 5 wt% functionalized-CNS@PLLA composites were also produced in the form of nanofibers through the electrospinning technique (see the Experimental Section for details about the preparation), in order to investigate how such morphology would affect the electrical properties of our composite materials.

3.2. Thermal, mechanical and electrical characterization of the functionalized-CNS@PLLA composites

A further proof for the homogeneity of the dispersion of functionalized CNSs within the PLLA phase was obtained by considering the crystallization temperature (T_c) extrapolated from calorimetric data resulting after differential scanning calorimetry (DSC) analysis (see Figs S5, S6 and S7 for the DSC traces of the three types of functionalized-CNS@PLLA composites at all the studied concentrations, and Tables S2, S3 and S4 for a complete resume of calorimetric data).

Actually, T_c values are significantly influenced by the presence of well-dispersed nanofillers, which can act as nucleating agents, allowing crystallization to happen at lower temperatures (PLLA crystallizes on heating; cold crystallization) [14]. This was particularly evident in MWCNT-PhOMe@PLLA composites [59] for which an almost linear decrease of T_c was observed when increasing the quantity of nanofillers up to the 1 wt% limit (see Fig. 2b; Fig. 2a reports the detail of DSC traces in the region where polymer crystallization takes place).

A decrease in T_c was also recorded for the RGO-PhOMe@PLLA composites as a function of CNS concentration (Fig. S7), but it did not follow an almost linear regime as for MWCNTs. For CNH-PhOMe@PLLA composites an apparent opposite behavior was observed, since at lower CNH-PhOMe concentrations (up to 1 wt%) an increase in T_c was detected, followed by a decrease at the highest

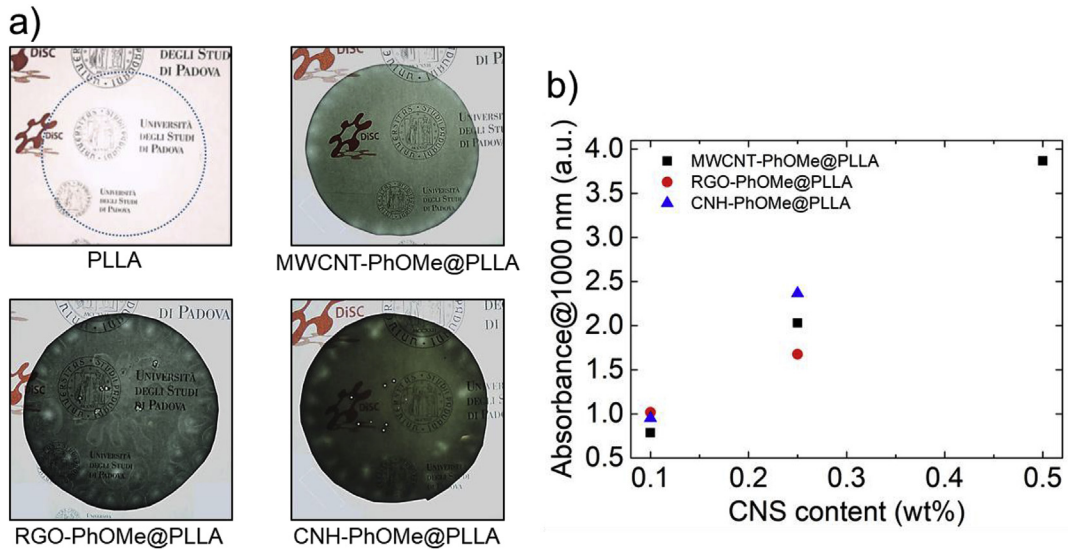

Fig. 1. a) Backlight photos of sample films (~6 cm diameter) of 0.1 wt% functionalized-CNS@PLLA films and of a pure PLLA (lighter color spots in the films are due to thinner areas and air bubbles which were discarded for all the following physical tests. They were present only in the 0.1 wt% samples, as shown by pictures of the other composites reported in the S.I.). b) Absorbance at 1000 nm of nanocomposite films as a function of filler wt% (high filler concentrations giving signal saturation are omitted). (For interpretation of the references to color in this figure legend, the reader is referred to the Web version of this article.)

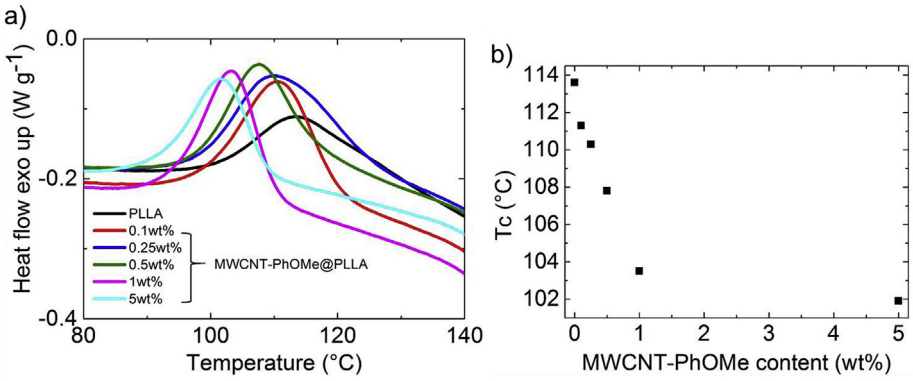

Fig. 2. a) Zoom of DSC traces (second heating scans after a previous heating-cooling cycle) of MWCNT-PhOMe@PLLA composites with five different filler concentrations and of pure PLLA in the zone where polymer crystallization takes place. b) Variation of T_c (taken at maximum of the curves in a) as a function of MWCNT-PhOMe in the composite.

concentration examined (5 wt%, Fig. S6. For this sample, as well as for the 5 wt% MWCNT-PhOMe@PLLA sample, DSC were performed on more than one portion, to rule out inhomogeneity issues, but no differences among replicates were evidenced). The percent crystallinity of PLLA [60] decreases slightly after inclusion of all the types of nanofillers, but does not show a precise trend with increasing concentrations (see Table S2, S3 and S4). This might be somehow related to the analogous decrease in melting enthalpies in the composites compared to the pure polymer (see Table S2, S3 and S4). On the other hand, melting temperatures remain almost unvaried from case to case (see again Table S2, S3 and S4).

The mechanical behavior of the functionalized-CNS@PLLA composites was investigated to determine the effect of the three nanofiller types at their different relative concentrations. The tensile strength was measured for all the examined materials on samples of the same size and thickness, except for the 5 wt% RGO-PhOMe@PLLA composite, which was too brittle to undergo mechanical testing (too brittle even for handling, as it can be somehow inferred from its picture in Fig. S4). Representative entire tensile stress-strain curves for each type of composite at the different filler content in PLLA are reported in the S.I. (Figs S8, S9 and S10); here we present the variation in Young's modulus (Fig. 3a) and the variation in the percentage of film deformation at the fracture point (Fig. 3b) as a function of the nanofiller concentration.

The elastic modulus changes significantly when functionalized-CNSs are dispersed in PLLA (Fig. 3a): the pure polymer has a modulus of 871 MPa, whereas the inclusion of small amounts of fillers (0.1 wt%) surprisingly drops it down to 745, 538 and 458 MPa for MWCNT-PhOMe, RGO-PhOMe and CNH-PhOMe, respectively. In general instead, loading polymers with stiffer fillers (normally in the pristine form and thus lacking functionalization) is expected to increase Young's modulus [61]. In the present case, functionalized-CNSs in PLLA behave more as plasticizers rather than as reinforcing agents. This has been observed before for poly(lactic-acid) phases plasticized with palm oil and filled with small amounts (up to 1 wt %) of graphene nanoplatelets [62]. Since in our case no plasticizers have been added to PLLA, the effect must be likely driven by the presence of the *p*-methoxyphenyl substituents covalently bound to the CNSs, that allow their homogeneous dispersion within the polymeric phase. On the other hand, the formation of voids (defects) in the PLLA phase following nanofillers insertion, might be also the cause of lower stiffness in the composites compared to the

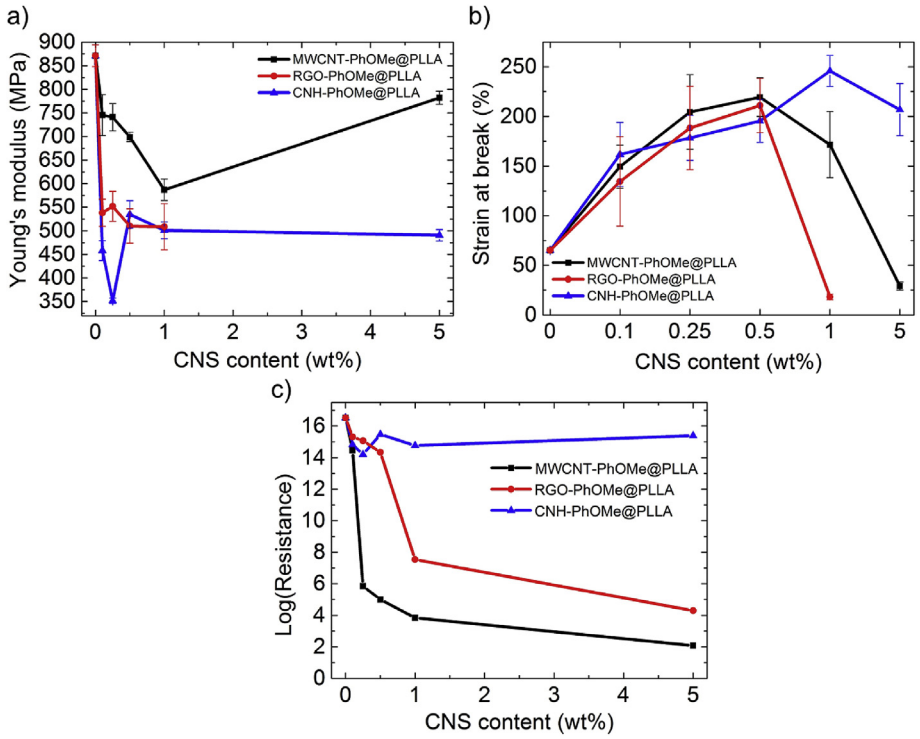

Fig. 3. a) Young's modulus, b) strain at break and c) electrical resistance in a logarithmic scale for functionalized-CNS@PLLA composites as a function of nanofiller concentration.

pristine polymer. This aspect might be also connected with the diminished crystallinity found in composites (see the previous discussion on DSC results). After the initial decrease at low CNS concentrations, Young's modulus undergoes a slight increase only at higher concentrations of the fillers for the case of MWCNT-PhOMe (at 5 wt%) and CNH-PhOMe (at 0.5 wt%), but remains still lower than that of bare PLLA. However, the trend in elongations at the fracture point for the three types of composites (Fig. 3b) is noteworthy: the increase in ductility with increasing filler content, up to 0.5 wt% for both MWCNT-PhOMe and RGO-PhOMe, and up to 1 wt% for CNH-PhOMe, brings to final lengths at break which are 3–4 times longer than for PLLA. Unfortunately, in the RGO and MWCNT based composites, this effect drops down for higher concentrations, eventually leading to materials which are more fragile than bare PLLA at 1 wt% for RGO-PhOMe and 5 wt% for MWCNT-PhOMe. For the RGO-based composite at 5 wt% concentration it is not even possible to measure any tensile strength, because of the brittleness of the material, as already mentioned. Such a drop in ductility is instead not observed with CNH-PhOMe as a filler up to 5 wt%. While at lower concentrations CNS fillers are more homogeneously dispersed, it is reasonable to assume that at higher loadings they start to form larger aggregates, which affect the macroscopic ductility of the resulting composite. The overall mechanical response of the three types of composites must be significantly influenced by the type of contained nanofiller, as it was observed for the calorimetric behavior. Different behaviors among CNSs can be due, in particular, to their different size and shape, and can be driven by their different tendency to aggregate, though strongly mitigated by the covalent functionalization.

The bulk electrical properties of the functionalized-CNS@PLLA films were measured, showing again a behavior deeply influenced by the type of CNS used as nanofiller. In Fig. 3c the electrical resistance is shown as a function of the concentration of CNSs in PLLA. A percolation threshold at very low filler content is observed for the composites based on MWCNTs, with a significant change in resistance when moving from 0.1 to 0.25 wt%, corresponding to the formation of conductive networks. Indeed, it is known that CNTs are more effective than other standard fillers, such as carbon black, in conferring conductive properties to insulating polymers [63]. The fact that this happens at a low concentration of MWCNT-PhOMe deserves special attention [64], confirming that the CNS dispersion is optimized and the occurrence of aggregates is negligible, which is possible thanks to the organic functionalization that drives the homogeneous distribution of nanotubes among PLLA chains. The recorded conductivity also evidences that our functionalization approach avoided excessive modification of the CNT structure, which could result in the partial loss of the electronic properties of pristine nanotubes [65]. For the RGO-PhOMe@PLLA composites a percolation threshold was found between 0.5 and 1 wt% nanofiller concentration. These fillers appeared to be less effective in inducing electrical conductivity in PLLA, with electrical resistance being 2 order of magnitudes higher than that reached with CNTs at the maximum concentration (5 wt%). On the other hand, with the CNH-PhOMe fillers no percolation threshold was observed at the considered CNS concentrations, demonstrating again that the differences in nanomorphology among the components largely determine the macroscopic behavior. Indeed CNH species, existing in their aggregated “dahlia-like” globular shape [47], have sizes of 100 nm (see TEM images of fibers containing them in Fig. S11b in the S.I.) and are therefore not likely to form conductive pathways within the polymer phase at such low concentrations.

3.3. Atomic force microscopy characterization of the functionalized-CNS@PLLA composites

In order to electrically characterize the composites at the single filler size resolution, the materials were also investigated by means of AFM techniques. Only composites with the highest filler concentration (5 wt%) were considered.

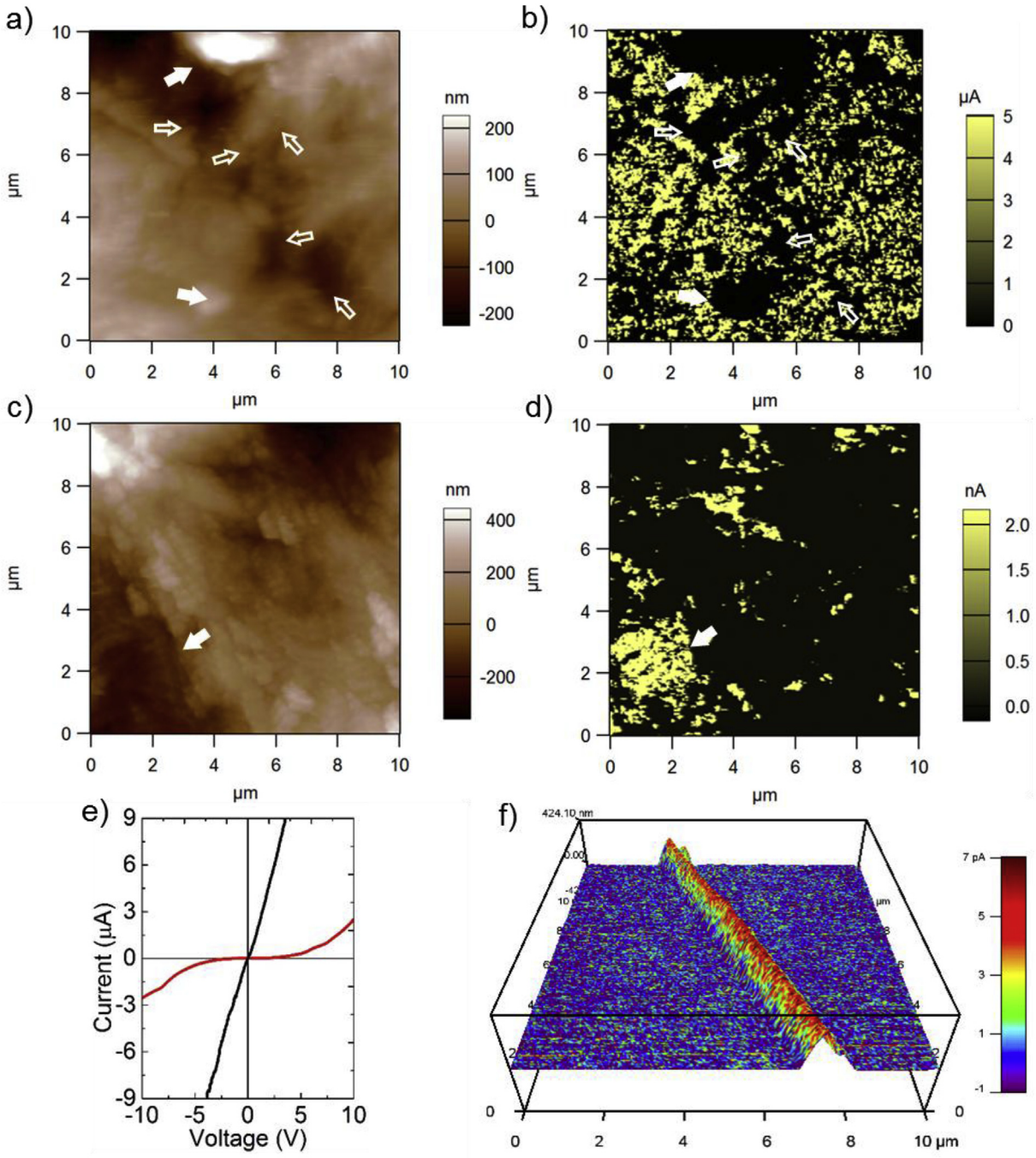

Fig. 4. a-d) Representative CAFM images of films of a,b) MWCNT-PhOMe@PLLA and c,d) RGO-PhOMe@PLLA; a,c) topography, b,d) current images (at +1 V). d) I-V characteristic curves obtained at conductive points on the two samples of composite films. Black curve: MWCNT-PhOMe@PLLA film; red curve: RGO-PhOMe@PLLA film. f) 3D rendering of a current image taken on a MWCNT-PhOMe@PLLA electrospun nanofiber, with the current overlaid as a color onto the topographic 3D profile. (For interpretation of the references to color in this figure legend, the reader is referred to the Web version of this article.)

The conductance was addressed by means of conductive AFM (CAFM) measurements. The film of bare PLLA did not show any measurable current, as expected, and the same occurred also for the CNH-PhOMe@PLLA composite film, even when probed at several different positions on its surface and with different contact forces (see details in the S.I.). This confirmed the data obtained through the macroscopic electrical characterization. The samples of MWCNT-PhOMe@PLLA and RGO-PhOMe@PLLA exhibited instead measurable currents. Representative current images for the MWCNT-PhOMe@PLLA and for the RGO-PhOMe@PLLA samples are presented in Fig. 4b and d, respectively (Fig. 4a and c report the corresponding topography).

When considering for example the MWCNT-PhOMe@PLLA composite film (Fig. 4b), one can see that the current image is partly correlated with the surface topography, as few high regions show no current (see filled arrows). However, these are real effects associated with the feature contents and not topographical artifacts. The different compositional contents in the aforementioned tall features is also apparent in other surrounding regions with similar low current level (black areas) yet without outstanding

heights (see void arrows). Obviously, independently on their height, areas of the films exist which are locally devoid of the CNS fillers imparting conductance to the composite. Conversely, the conducting regions emerging in Fig. 4b show a finer structure (down to the single pixel size i.e. ~40 nm) than in Fig. 4d. Indeed, in the former case they are likely associated with smaller sizes of the carbon-based fillers (single MWCNTs or bundles of few of them), whereas in Fig. 4d the bright regions include several adjacent pixels up to ~2 μm linear size (see the arrowed zone) which are likely associated with sparse RGO flakes.

Fig. 4 further shows that, under the same conditions of vertical force (~18 nN) and bias (+1 V), the current levels observed on the MWCNT-PhOMe@PLLA film surface are higher than those for the RGO-PhOMe@PLLA one (see the vertical scale bar of the color palettes). Additionally, the total conductive area is higher for the MWCNT-PhOMe@PLLA composite, (17 ± 5% versus 7 ± 4% of the RGO containing composite film). When considering the means of the current levels on the different images of the samples, and averaging them, from the applied sample voltage (+1 V) resistance values of 2.6 ± 1.2 MΩ and 530 ± 230 MΩ are obtained for the MWCNT-PhOMe@PLLA and the RGO-PhOMe@PLLA sample, respectively, which can be considered representative of the whole films. These values are in a similar ratio (about 200 ×) to that of film resistances measured macroscopically (see Fig. 3c), yet are both shifted to approximately 4 orders of magnitude higher values. This likely depends on the very small contact area of the AFM tip, for the considered technique, at the limited vertical force used (see details in the S.I.). The agreement between electrical measurements made at the macro and nanoscale is a proof of the good homogeneity achieved in dispersing the functionalized-CNS within the polymer matrix.

In Fig. 4e also single I-V curves typical of points in which conduction occurred (i.e. within bright regions in Fig. 4a and b) have been plotted. One can see that the composite film with CNT fillers exhibit an almost 'metallic' behavior (straight Ohmic I-V profile), while the RGO film shows a passive region close to zero bias (sigmoidal profile), more similar to a semiconductor. An analogous difference in current values (about two orders of magnitude) between the two different samples is observed as described above, in favor of the MWCNT-PhOMe@PLLA film. When only the same range of the I-V curves as used in the current images (±1 V) is considered, the following values of resistance are obtained, from a linear fit: 0.48 MΩ for the MWCNT-PhOMe@PLLA sample and 26.7 MΩ for the RGO-PhOMe@PLLA sample. These values are higher than the means on the image areas (affected by the 'dark' regions of no current, so weighted with the coverage coefficients), yet are roughly in the same ratio of approximately 200 × in favor of the CNT containing composite.

Finally, we investigated with CAFM the conductive properties of the functionalized-CNS@PLLA composites in the form of nanofibers, obtained with the electrospinning technique, as reported [14] (for transmission electron microscopy images of the fibers see Fig. S11 in the S.I.). This morphology was selected in order to study the electrical properties of the composites in nanoscale-confined model systems, along a single direction. It is worthy to mention that the electrical conductivity measurements carried out on films (see previous section) would hardly apply to fibrous phases, because of the very low density of the material preventing a proper contact with the electrodes. In Fig. 4f a CAFM image of a single MWCNT-PhOMe@PLLA nanofiber is shown. The current level has been rendered as the color, overlaid on the 3D profile of the height. For composite nanofibers, the CNT based sample was the only one which allowed current imaging, while in this form also the RGO-based composite did not show any conductivity. This can be justified by considering that, for the same filler concentration, percolation along a narrow conductor such as a nanofiber (200–600 nm diameter) is more difficult and is detected in the present case only for monodimensional conductive fillers as CNTs. Also the geometry of the CAFM contact was significantly different in this case, in-plane along the fiber axis and not through the fiber towards the substrate. Actually, in the case of fibers, the substrate used was insulating, which allows to obtain a typical value of fiber conductance. When the resistance is calculated, a value of ~7.1 GΩ is obtained, another factor 300 × higher than what measured for the film of the same composite, and close to the lower detection limit level of the setup (mean current along fiber axis in Fig. 4f is 4.8 pA). In order to support the electrical characterization of the different composites, we carried out AFM electrostatic measurements (scanning Kelvin probe microscopy –SKPM- and/or electrostatic force microscopy –EFM-) on the functionalized-CNS@PLLA composite nano-confined systems with fibrous morphology. These AFM techniques are based on potential contrast due to accumulation of electrical charges, instead of their flow within a current, as for CAFM. Therefore, insulating fiber portions, not allowing the charge to be drained away, are expected to exhibit stronger contrast. This was actually observed with fibers of bare PLLA (see Fig. S12a and b). The typical nature of the electrostatic contrast is apparent when noticing that the bright regions spread around the physical lateral extension of the fibers, which was not the case for the current in Fig. 4f. Similar results have been obtained also for the other samples of insulating (i.e. non-conductive) fibers (namely those containing RGO and CNH fillers). For the fibrous sample containing MWCNTs instead, in few cases, we observed fibers that looked from less bright (i.e. with only some degree of conduction, Fig. S12c and d) on to completely dark (i.e. completely conductive, Fig. S12e and f). Unfortunately, it was not possible to acquire CAFM and SKPM/EFM images simultaneously on the same fiber portion, because the two classes of techniques require different probe-holders. An interesting representative SKPM image of the MWCNT-PhOMe@PLLA fibers is shown in Fig. 5. In Fig. 5a a region is evident where several fibers cross each other. In the corresponding surface potential (SKPM) image of Fig. 5b three different levels appear, namely an intermediate level background (associated with the substrate); a higher level (bright regions) spreading around the fibers (the typical bleeding effect of electrostatic charging); and a negative contrast (black) region localized only on some positions along the fibers, which can be associated with the functionalized MWCNT fillers (see TEM images in Fig. S11a for comparison). Such three regions are more clearly represented in Fig. 5c, where the same maps of topography (height) and surface potential and as in a) and b) have been rendered again in 3D fashion, using a multicolor palette to segment the above-mentioned regions in different levels associated with red, green and blue colors, respectively.

As a final step of surface characterization of the functionalized-CNS@PLLA composites, the roughness of the film samples has been assessed by standard AFM (in non-contact mode). In Fig. S14 in the S.I. the 2D roughness amplitude parameter S_q, is presented. The two composite materials based on CNH and RGO fillers result in films with higher surface roughness (S_q~155 nm), whereas the composite based on MWCNTs is smoother, on the same level as the film of bare PLLA (S_q~70 nm). The differences between the two groups are statistically significant ($p < 0.05$). Therefore, the well-dispersed MWCNT-PhOMe fillers provide a good uniformity in the overall electrical properties, resulting in a percolation network that endows the films with a good electrical conductivity and, in addition, turns out to determine the least amount of surface roughening, as compared to the bare polymer film.

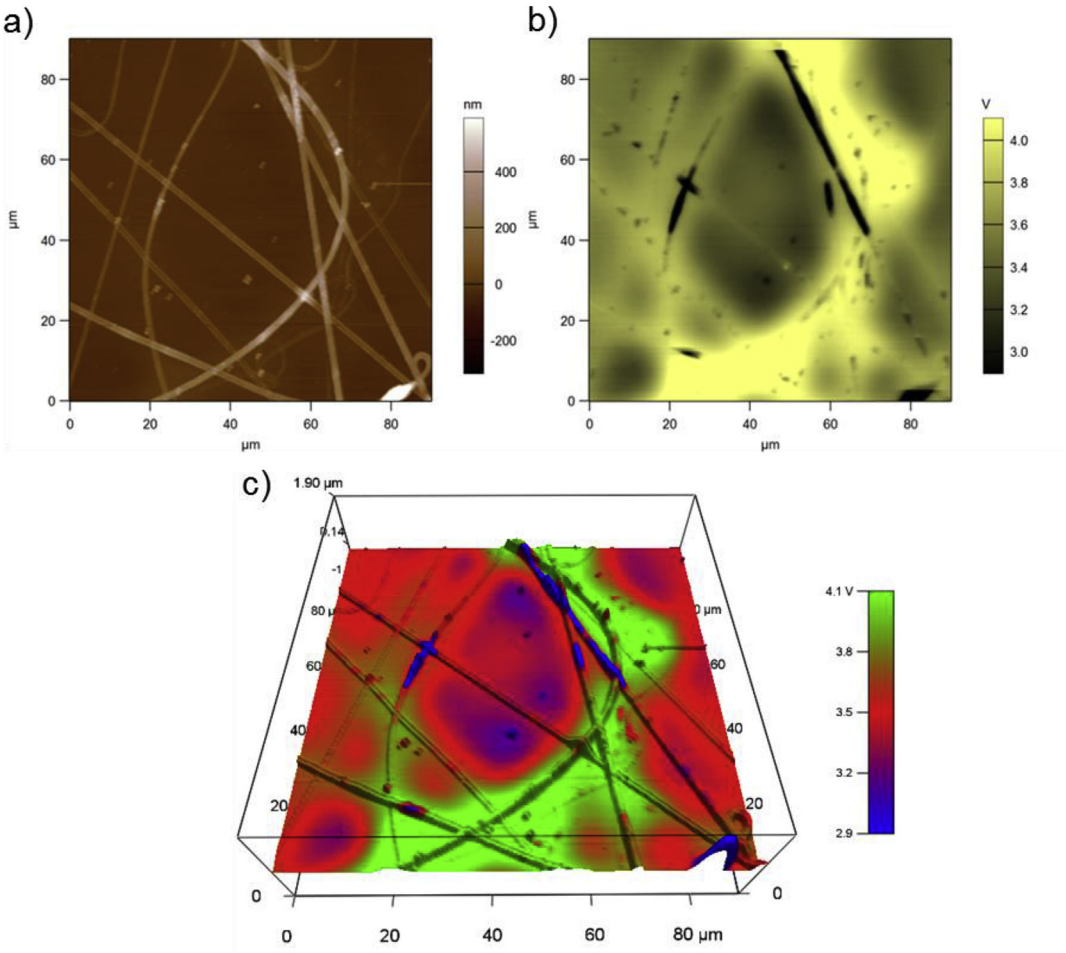

Fig. 5. Large-area SKPM images of a sample of MWCNT-PhOMe@PLLA composite fibers, a) topography; b) surface potential; c) 3D topography of a) 'colored' with the surface potential in b).

3.4. Biocompatibility of the functionalized-CNS@PLLA composites

The functionalized-CNS@PLLA films were tested for biocompatibility by employing them as scaffolds for the growth of SH-SY5Y cells. For both cell death and cell proliferation assays, only two percentages per each type of CNS filler were selected, namely a lower one (0.25 wt%) and a higher one (5 wt%). Together with control cells grown onto poly-L-lysine or onto FDA-certified PLLA polymer, which has an already established usage in regenerative medicine, CNTs at 0.25 wt% also represent a 'positive control' for biocompatibility, as this concentration was well characterized and proved fully biocompatible (when dispersed in either PLLA films of electrospun PLLA) [13–15]. In this work, CNTs concentrations up to 5% and novel nanocomposites including RGO or CNHs are tested for the first time with SH-SY5Y cells, to check whether viability values are kept. According to previous studies, cell viability was evaluated at 24 and 72 h combining evaluation of cell death to proliferation data, in order to properly consider factors underlying cell viability. Cells grown onto 0.25 or 5% functionalized-CNS@PLLA films showed viability values in the same range as control and PLLA samples (Fig. 6a) and no meaningful effect on cell proliferation (Fig. 6b), thus demonstrating biocompatibility is kept and the potential cytotoxicity of the three types of CNSs is prevented when employing them well functionalized and dispersed within a biocompatible polymer matrix.

4. Discussion

The functionalized-CNS@PLLA composites were thoroughly characterized in their thin film forms by assessing the variation in thermal, mechanical and electrical properties as a function of CNS loading over a range between 0.1 wt% and 5 wt%. The homogeneity of the CNS nanofillers dispersion within the polymer phase was stated, particularly for the MWCNT-based samples for which an almost linear trend was found in the decrease of the crystallization temperature of the polymer as a function of the increased filler concentration.

The mechanical properties were found to be highly influenced by the presence of the *p*-methoxyphenyl functional groups covalently bound to the CNS surfaces, which confer to the fillers an unusual character of plasticizing agents rather than of reinforcing ones. The ductility of the composites is extremely improved with respect to bare PLLA for concentrations of CNSs around 0.5–1 wt%, even though for RGO-based samples the limits to obtain an improved plasticity are lower than for MWCNT and CNH-based samples, with the 5 wt% concentration already too high to furnish a durable material.

Electrical percolation in the composites was found to take place only with MWCNT and RGO fillers, within the range of concentrations considered. Thresholds were differently located for the two cases, with the MWCNT-PhOMe@PLLA composites showing a sharp

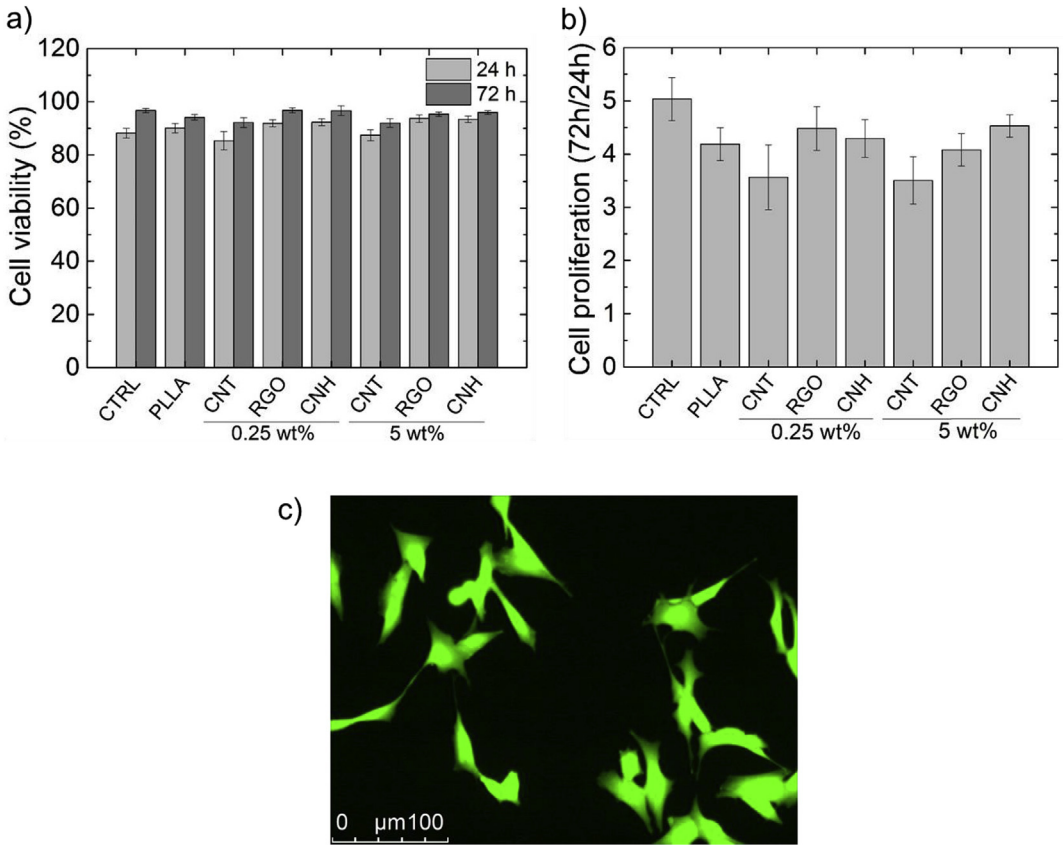

Fig. 6. Percentage of viability a) or proliferation b) for SH-SY5Y cells grown onto control (poly-L-lysine coated) wells, pure PLLA film or functionalized-CNS@PLLA films. Data represents the mean ± SEM of four independent experiments performed in duplicate. An example c) of SH-SY5Y cells grown on MWCNT-PhOMe@PLLA film at 72 h. Cells are stained with Calcein-AM. Image magnification is 20×. No meaningful difference is observed in images with RGO-PhOMe@PLLA and CNH-PhOMe@PLLA.

increase in conductivity at a lower CNS concentration with respect to RGO-PhOMe@PLLA. The extent of conductivity after the percolation threshold was also significantly higher for the former as compared to the latter. A strong influence of the filler dimensionality on the electrical behavior of the composite is evident: monodimensional CNSs like MWCNTs are able to arrange in conductive domains within polymer chains much more effectively than bidimensional CNSs like RGO. Finally, zero-dimensional species such as CNHs likely require high concentrations to give rise to conductive pathways within an insulating matrix. The superior ability of CNTs to form conductive networks over a long distance is further confirmed by the CAFM data obtained on both film surfaces and along single nanofibers. Particularly for these last ones, a measurable current could be detected only for CNT-based samples. Also considering the increasing interest on nanofibrous biomedical materials [66,67], the ability to originate long range and directional percolation pathways might be promising to provide next scaffold design with a selective guidance to neurites elongation.

5. Conclusions

In this work a thorough assessment of the physical properties of functionalized-CNS@PLLA composites is essayed, both at the macroscopic level and at the nanoscale, directly on surfaces, which are the part of the samples directly responsible for the interaction with living cells. The analysis is carried out with the awareness that a combination of stimuli coming from the substrate is responsible for the growth and differentiation of cells, including electrical, mechanical and topographic cues and thus will act as a guidance for future studies of neuritogenesis. These characterization efforts are addressed at increasing the understanding about physical properties driving cellular processes *in vitro* at first instance. These results also provide a basic set of information for the design and selection of optimized scaffolds to be tested *in vivo*, aiming at the future development of biomedical devices and implants for tissue engineering applications.

Acknowledgements

The authors acknowledge the financial support from University of Padova (Project PRAT2015 CPDA151948 to FF and contract P-DiSC #05BIRD2016-UNIPD to EM). They also thank Dr. Giorgia Scapin for helpful information and suggestions.

Appendix A. Supplementary data

Supplementary data related to this article can be found at https://doi.org/10.1016/j.matchemphys.2018.04.042.

References

[1] S. Bhattacharya, S.K. Samanta, Soft-nanocomposites of nanoparticles and nanocarbons with supramolecular and polymer gels and their applications, Chem. Rev. 116 (19) (2016) 11967–12028.
[2] Z. Spitalsky, D. Tasis, K. Papagelis, C. Galiotis, Carbon nanotube–polymer composites: chemistry, processing, mechanical and electrical properties, Prog. Polym. Sci. 35 (3) (2010) 357–401.
[3] A. Sherif, M. Qingshi, Z. Liqun, Z. Izzuddin, M. Peter, M. Jun, Elastomeric composites based on carbon nanomaterials, Nanotechnology 26 (11) (2015) 112001.
[4] M. Wang, X. Duan, Y. Xu, X. Duan, Functional three-dimensional graphene/

polymer composites, ACS Nano 10 (8) (2016) 7231–7247.
[5] J. Du, H.-M. Cheng, The fabrication, properties, and uses of graphene/polymer composites, Macromol. Chem. Phys. 213 (10–11) (2012) 1060–1077.
[6] Y. Zhu, C. Romain, C.K. Williams, Sustainable polymers from renewable resources, Nature 540 (7633) (2016) 354–362.
[7] C. Goncalves, I.C. Goncalves, F.D. Magalhaes, A.M. Pinto, Poly(lactic acid) composites containing carbon-based nanomaterials: a review, Polymers 9 (7) (2017).
[8] T. Gatti, N. Vicentini, M. Mba, E. Menna, Organic functionalized carbon nanostructures for functional polymer-based nanocomposites, Eur. J. Org Chem. 2016 (6) (2016) 1071–1090.
[9] F.M. Michael, M. Khalid, R. Walvekar, C.T. Ratnam, S. Ramarad, H. Siddiqui, M.E. Hoque, Effect of nanofillers on the physico-mechanical properties of load bearing bone implants, Mater. Sci. Eng. C-Mater. Biol. Appl. 67 (2016) 792–806.
[10] M.S. Mozumder, A. Mairpady, A.H.I. Mourad, Polymeric nanobiocomposites for biomedical applications, J. Biomed. Mater. Res. Part B 105 (5) (2017) 1241–1259.
[11] A.J.T. Teo, A. Mishra, I. Park, Y.-J. Kim, W.-T. Park, Y.-J. Yoon, Polymeric biomaterials for medical implants and devices, ACS Biomater. Sci. Eng. 2 (4) (2016) 454–472.
[12] B.Q.Y. Chan, Z.W.K. Low, S.J.W. Heng, S.Y. Chan, C. Owh, X.J. Loh, Recent advances in shape memory soft materials for biomedical applications, ACS Appl. Mater. Interfaces 8 (16) (2016) 10070–10087.
[13] G. Scapin, P. Salice, S. Tescari, E. Menna, V. De Filippis, F. Filippini, Enhanced neuronal cell differentiation combining biomimetic peptides and a carbon nanotube-polymer scaffold, Nanomed. Nanotechnol. Biol. Med. 11 (3) (2015) 621–632.
[14] N. Vicentini, T. Gatti, P. Salice, G. Scapin, C. Marega, F. Filippini, E. Menna, Covalent functionalization enables good dispersion and anisotropic orientation of multi-walled carbon nanotubes in a poly(l-lactic acid) electrospun nanofibrous matrix boosting neuronal differentiation, Carbon 95 (2015) 725–730.
[15] G. Scapin, T. Bertalot, N. Vicentini, T. Gatti, S. Tescari, V. De Filippis, C. Marega, E. Menna, M. Gasparella, P.P. Parnigotto, R. Di Liddo, F. Filippini, Neuronal commitment of human circulating multipotent cells by carbon nanotube-polymer scaffolds and biomimetic peptides, Nanomedicine 11 (15) (2016) 1929–1946.
[16] M. Kharaziha, S.R. Shin, M. Nikkhah, Tough and flexible CNT-polymeric hybrid scaffolds for engineering cardiac constructs, Biomaterials 35 (2014).
[17] S. Soltani, M. Ebrahimian-Hosseinabadi, A. Zargar Kharazi, Chitosan/graphene and poly(D, L-lactic-co-glycolic acid)/graphene nano-composites for nerve tissue engineering, Tissue Eng. Regen. Med 13 (6) (2016) 684–690.
[18] A. Gupta, T.A. Liberati, S.J. Verhulst, B.J. Main, M.H. Roberts, A.G.R. Potty, T.K. Pylawka, S.F. El-Amin III, Biocompatibility of single-walled carbon nanotube composites for bone regeneration, Bone and Joint Res. 4 (5) (2015) 70–77.
[19] E. Murray, S. Sayyar, B.C. Thompson, R. Gorkin Iii, D.L. Officer, G.G. Wallace, A bio-friendly, green route to processable, biocompatible graphene/polymer composites, RSC Adv. 5 (56) (2015) 45284–45290.
[20] S. Sayyar, E. Murray, B.C. Thompson, J. Chung, D.L. Officer, S. Gambhir, G.M. Spinks, G.G. Wallace, Processable conducting graphene/chitosan hydrogels for tissue engineering, J. Mater. Chem. B 3 (3) (2015) 481–490.
[21] M. Silva, S.G. Caridade, A.C. Vale, E. Cunha, M.P. Sousa, J.F. Mano, M.C. Paiva, N.M. Alves, Biomedical films of graphene nanoribbons and nanoflakes with natural polymers, RSC Adv. 7 (44) (2017) 27578–27594.
[22] A. Motealleh, N.S. Kehr, Nanocomposite hydrogels and their applications in tissue engineering, Adv. Healthc. Mater 6 (1) (2017).
[23] D.P. Li, T.J. Liu, X.Q. Yu, D. Wu, Z.Q. Su, Fabrication of graphene-biomacromolecule hybrid materials for tissue engineering application, Polym. Chem. 8 (30) (2017) 4309–4321.
[24] T.H. Kim, T. Lee, W.A. El-Said, J.W. Choi, Graphene-based materials for stem cell applications, Materials 8 (12) (2015) 8674–8690.
[25] K.Y. Yasoda, K.N. Bobba, D. Nedungadi, D. Dutta, M.S. Kumar, N. Kothurkar, N. Mishra, S. Bhuniya, GSH-responsive biotinylated poly(vinyl alcohol)-grafted GO as a nanocarrier for targeted delivery of camptothecin, RSC Adv. 6 (67) (2016) 62385–62389.
[26] A. Antonucci, J. Kupis-Rozmyslowicz, A.A. Boghossian, Noncovalent Protein, Peptide Functionalization, Of single-walled carbon nanotubes for biodelivery and optical sensing applications, ACS Appl. Mater. Interfaces 9 (13) (2017) 11321–11331.
[27] M. Irimia-Vladu, E.D. Głowacki, G. Voss, S. Bauer, N.S. Sariciftci, Green and biodegradable electronics, Mater. Today 15 (7–8) (2012) 340–346.
[28] Q. Zhang, W. Wei, J. Li, J. Wei, J. Guo, Insertion of a biocompatible polymer between graphene and silver nanowires for novel flexible transparent electrode, Synth. Met. 221 (2016) 192–200.
[29] T. Zhang, J. Liu, C. Wang, X. Leng, Y. Xiao, L. Fu, Synthesis of graphene and related two-dimensional materials for bioelectronics devices, Biosens. Bioelectron. 89 (Part 1) (2017) 28–42.
[30] M. Hasanzadeh, F. Mokhtari, N. Shadjou, A. Eftekhari, A. Mokhtarzadeh, V. Jouyban-Gharamaleki, S. Mahboob, Poly arginine-graphene quantum dots as a biocompatible and non-toxic nanocomposite: layer-by-layer electrochemical preparation, characterization and non-invasive malondialdehyde sensory application in exhaled breath condensate, Mater. Sci. Eng. C 75 (2017) 247–258.
[31] F. Lamberti, S. Giulitti, M. Giomo, N. Elvassore, Biosensing with electroconductive biomimetic soft materials, J. Mater. Chem. B 1 (38) (2013) 5083–5091.
[32] Y. Zhou, X.X. Jing, Y. Chen, Material chemistry of graphene oxide-based nanocomposites for theranostic nanomedicine, J. Mater. Chem. B 5 (32) (2017) 6451–6470.
[33] J. Pan, F.R. Li, J.H. Choi, Single-walled carbon nanotubes as optical probes for bio-sensing and imaging, J. Mater. Chem. B 5 (32) (2017) 6511–6522.
[34] J. Bartelmess, S.J. Quinn, S. Giordani, Carbon nanomaterials: multi-functional agents for biomedical fluorescence and Raman imaging, Chem. Soc. Rev. 44 (14) (2015) 4672–4698.
[35] C. Hu, Z. Li, Y. Wang, J. Gao, K. Dai, G. Zheng, C. Liu, C. Shen, H. Song, Z. Guo, Comparative assessment of the strain-sensing behaviors of polylactic acid nanocomposites: reduced graphene oxide or carbon nanotubes, J. Mater. Chem. C 5 (9) (2017) 2318–2328.
[36] L. Hines, K. Petersen, G.Z. Lum, M. Sitti, Soft actuators for small-scale robotics, Adv. Mater. 29 (13) (2017). 1603483-n/a.
[37] J. Ahmed, M. Mulla, Y.A. Arfat, L.A. Thai T, Mechanical, thermal, structural and barrier properties of crab shell chitosan/graphene oxide composite films, Food Hydrocolloids 71 (2017) 141–148.
[38] N. Pal, P. Dubey, P. Gopinath, K. Pal, Combined effect of cellulose nanocrystal and reduced graphene oxide into poly-lactic acid matrix nanocomposite as a scaffold and its anti-bacterial activity, Int. J. Biol. Macromol. 95 (2017) 94–105.
[39] N. Yan, F. Capezzuto, M. Lavorgna, G.G. Buonocore, F. Tescione, H. Xia, L. Ambrosio, Borate cross-linked graphene oxide-chitosan as robust and high gas barrier films, Nanoscale 8 (20) (2016) 10783–10791.
[40] K. Zhang, J.Y. Lim, H.J. Choi, J.H. Lee, W.J. Choi, Ultrasonically prepared polystyrene/multi-walled carbon nanotube nanocomposites, J. Mater. Sci. 48 (8) (2013) 3088–3096.
[41] G. Pagani, M.J. Green, P. Poulin, M. Pasquali, Competing mechanisms and scaling laws for carbon nanotube scission by ultrasonication, Proc. Natl. Acad. Sci. U. S. A 109 (29) (2012) 11599–11604.
[42] M.D. Rossell, C. Kuebel, G. Ilari, F. Rechberger, F.J. Heiligtag, M. Niederberger, D. Koziej, R. Erni, Impact of sonication pretreatment on carbon nanotubes: a transmission electron microscopy study, Carbon 61 (2013) 404–411.
[43] J. Stegen, Mechanics of carbon nanotube scission under sonication, J. Chem. Phys. 140 (24) (2014).
[44] S. Barrau, P. Demont, E. Perez, A. Peigney, C. Laurent, C. Lacabanne, Effect of palmitic acid on the electrical conductivity of carbon Nanotubes–Epoxy resin composites, Macromolecules 36 (26) (2003) 9678–9680.
[45] D. Tasis, N. Tagmatarchis, A. Bianco, M. Prato, Chemistry of carbon nanotubes, Chem. Rev. 106 (3) (2006) 1105–1136.
[46] V. Georgakilas, M. Otyepka, A.B. Bourlinos, V. Chandra, N. Kim, K.C. Kemp, P. Hobza, R. Zboril, K.S. Kim, Functionalization of graphene: covalent and non-covalent approaches, derivatives and applications, Chem. Rev. 112 (11) (2012) 6156–6214.
[47] N. Karousis, I. Suarez-Martinez, C.P. Ewels, N. Tagmatarchis, Structure, properties, functionalization, and applications of carbon nanohorns, Chem. Rev. 116 (8) (2016) 4850–4883.
[48] T. Gatti, G. Girardi, N. Vicentini, R. Brandiele, M. Wirix, C. Durante, E. Menna, Physico-chemical, electrochemical and structural insights into poly(3,4-ethylenedioxythiophene) grafted from molecularly engineered multi-walled carbon nanotube surfaces, J. Nanosci. Nanotechnol. 18 (2) (2018) 1006–1018.
[49] P. Salice, E. Fabris, C. Sartorio, D. Fenaroli, V. Figà, M.P. Casaletto, S. Cataldo, B. Pignataro, E. Menna, An insight into the functionalisation of carbon nanotubes by diazonium chemistry: towards a controlled decoration, Carbon 74 (0) (2014) 73–82.
[50] B. Debalina, N. Vaishakh, M. Jagannatham, K. Vasanthakumar, N.S. Karthiselva, R. Vinu, P. Haridoss, S.R. Bakshi, Effect of different nano-carbon reinforcements on microstructure and properties of TiO2 composites prepared by spark plasma sintering, Ceram. Int. 42 (12) (2016) 14266–14277.
[51] D. Iglesias, S. Bosi, M. Melchionna, T. Da Ros, S. Marchesan, The glitter of carbon nanostructures in hybrid/composite hydrogels for medicinal use, Curr. Top. Med. Chem. 16 (18) (2016) 1976–1989.
[52] M. Radtke, A. Ignaszak, Grafting of the carbon allotropes and polypyrrole via a Kevlar-type organic linker: the correlation of carbon structure/morphology with electrochemistry of the composite electrode, Mater. Renew. Sustain. Energy 6 (1) (2017).
[53] T. Gatti, S. Casaluci, M. Prato, M. Salerno, F. Di Stasio, A. Ansaldo, E. Menna, A. Di Carlo, F. Bonaccorso, Boosting perovskite solar cells performance and stability through doping a poly-3(hexylthiophene) hole transporting material with organic functionalized carbon nanostructures, Adv. Funct. Mater. 26 (41) (2016) 7443–7453.
[54] T. Gatti, N. Manfredi, C. Boldrini, F. Lamberti, A. Abbotto, E. Menna, A D-π-A organic dye – reduced graphene oxide covalent dyad as a new concept photosensitizer for light harvesting applications, Carbon 115 (2017) 746–753.
[55] P. Guarracino, T. Gatti, N. Canever, M. Abdu-Aguye, M.A. Loi, E. Menna, L. Franco, Probing photoinduced electron-transfer in graphene-dye hybrid materials for DSSC, Phys. Chem. Chem. Phys. 19 (40) (2017) 27716–27724.
[56] L. Gabrielli, G. Altoè, M. Glaeske, S. Juergensen, S. Reich, A. Setaro, E. Menna, F. Mancin, T. Gatti, Controlling the decoration of the reduced graphene oxide surface with pyrene-functionalized gold nanoparticles, Phys. Status Solidi 254 (11) (2017) 1700281.
[57] R.A. Ross, B.A. Spengler, J.L. Biedler, Coordinate morphological and

biochemical interconversion of human neuroblastoma Cells2, JNCI-j natl, Cancer I 71 (4) (1983) 741–747.
[58] J.L. Bahr, J.M. Tour, Covalent chemistry of single-wall carbon nanotubes, J. Mater. Chem. 12 (7) (2002) 1952–1958.
[59] Z.-J. Zhang, W. Cui, H. Xu, L. Xie, H. Liu, L.-M. Zhu, H. Li, R. Ran, A free radical assisted strategy for preparing functionalized carbon nanotubes as a highly efficient nucleating agent for poly(l-lactide), RSC Adv. 5 (21) (2015) 16604–16610.
[60] V.S.G. Silverajah, N.A. Ibrahim, W.M.Z.W. Yunus, H.A. Hassan, C.B. Woei, A comparative study on the mechanical, thermal and morphological characterization of poly(lactic acid)/epoxidized palm oil blend, Int. J. Mol. Sci. 13 (5) (2012) 5878.
[61] M. Kaseem, K. Hamad, F. Deri, Y.G. Ko, A review on recent researches on polylactic acid/carbon nanotube composites, Polym. Bull. (2016) 1–17.
[62] B.W. Chieng, N.A. Ibrahim, W.M.Z. Wan Yunus, M.Z. Hussein, Y.Y. Loo, Effect of graphene nanoplatelets as nanofiller in plasticized poly(lactic acid) nanocomposites, J. Therm. Anal. Calorim. 118 (3) (2014) 1551–1559.
[63] M. Moniruzzaman, K.I. Winey, Polymer nanocomposites containing carbon nanotubes, Macromolecules 39 (16) (2006) 5194–5205.
[64] N.K. Shrivastava, B.B. Khatua, Development of electrical conductivity with minimum possible percolation threshold in multi-wall carbon nanotube/polystyrene composites, Carbon 49 (13) (2011) 4571–4579.
[65] P. Salice, C. Sartorio, A. Burlini, R. Improta, B. Pignataro, E. Menna, On the trade-off between processability and opto-electronic properties of single wall carbon nanotube derivatives in thin film heterojunctions, J. Mater. Chem. C 3 (2) (2015) 303–312.
[66] J.J. Xue, J.W. Xie, W.Y. Liu, Y.N. Xia, Electrospun nanofibers: new Concepts, materials, and applications, Acc. Chem. Res. 50 (8) (2017) 1976–1987.
[67] A.P. Kishan, E.M. Cosgriff-Hernandez, Recent advancements in electrospinning design for tissue engineering applications: a review, J. Biomed. Mater. Res. 105 (10) (2017) 2892–2905.

Supporting Information

Effect of different functionalized carbon nanostructures as fillers on the physical properties of biocompatible poly(L-lactic acid) composites

Nicola Vicentini,[a] Teresa Gatti,[a,*] Marco Salerno,[b] Yuriko Suemi Hernandez Gomez,[c] Mattia Bellon,[c] Sasha Gallio,[a] Carla Marega,[a] Francesco Filippini,[c] Enzo Menna[a,d,*]

[a] Department of Chemical Sciences, University of Padova and INSTM UdR Padova, Via Marzolo 1, 35131 Padova, Italy

[b] Materials Characterization Facility, Istituto Italiano di Tecnologia, Via Morego 30, 16163 Genova, Italy

[c] Department of Biology, University of Padova, Via Bassi 58/B, 35131 Padova, Italy

[d] Centre for Mechanics of Biological Materials, University of Padova, Via Marzolo 9, 35131 Padua, Italy

[*] Corresponding authors: teresa.gatti@unipd.it; enzo.menna@unipd.it

Table of contents

Thermogravimetric analysis

Thermogravimetric analysis (TGA) of MWCNT-PhOMe, CNH-PhOMe and RGO-PhOMe was carried out with a Q5000IR TGA (TA Instruments) under nitrogen by an isotherm at 100 °C for 10 min followed by heating at 10 °C/min rate until 1000 °C (Figure S1, S2 and S3, respectively). Determination of the functionalization degree (FD) from thermogravimetric data was performed as described in our previous work [1], also briefly reported here for the sake of clarity.

FD has been calculated according to the general formula:

$$FD = \frac{mmol\ FG}{mmol\ C}$$

where FG stands for "functional group". The number of mmol FG has been derived by dividing the percentage of mass loss, determined by thermogravimetric analysis, due to thermal degradation of the functional group (Δm_{FG}), by the molecular weight of this last one (in the present case for the *p*-methoxyphenyl moiety equal to 122.15). On the other hand, mmol C has been calculated by dividing the percentage of mass loss due to C (Δm_C) by the atomic weight of C (12.01).

Δm values used for the above described calculations are indicated in Figure S1, S2 and S3.

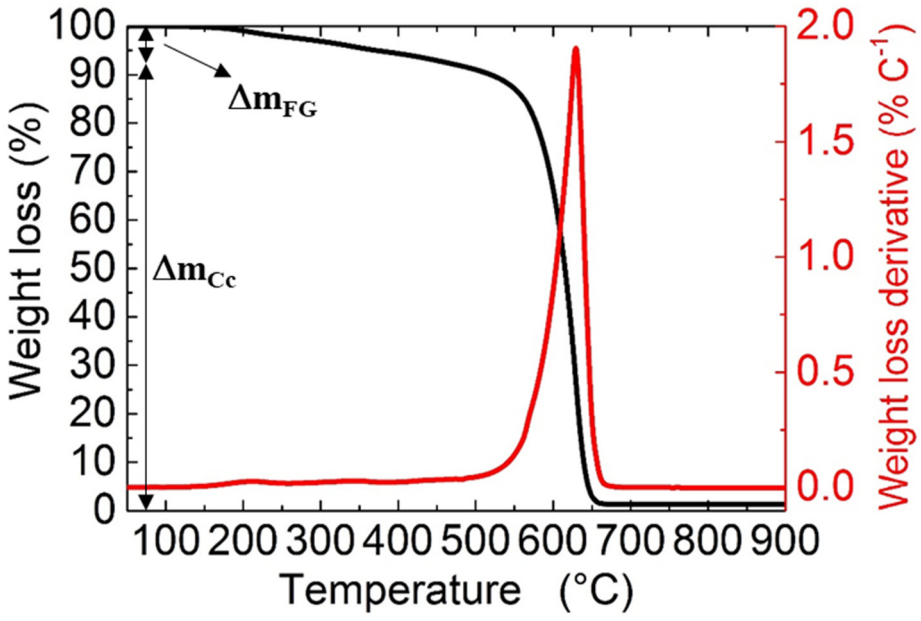

Fig. S1. Thermogram of MWCNT-PhOMe acquired under a nitrogen atmosphere. Black line represents the weight percentage loss, while the red line is the corresponding derivative curve.

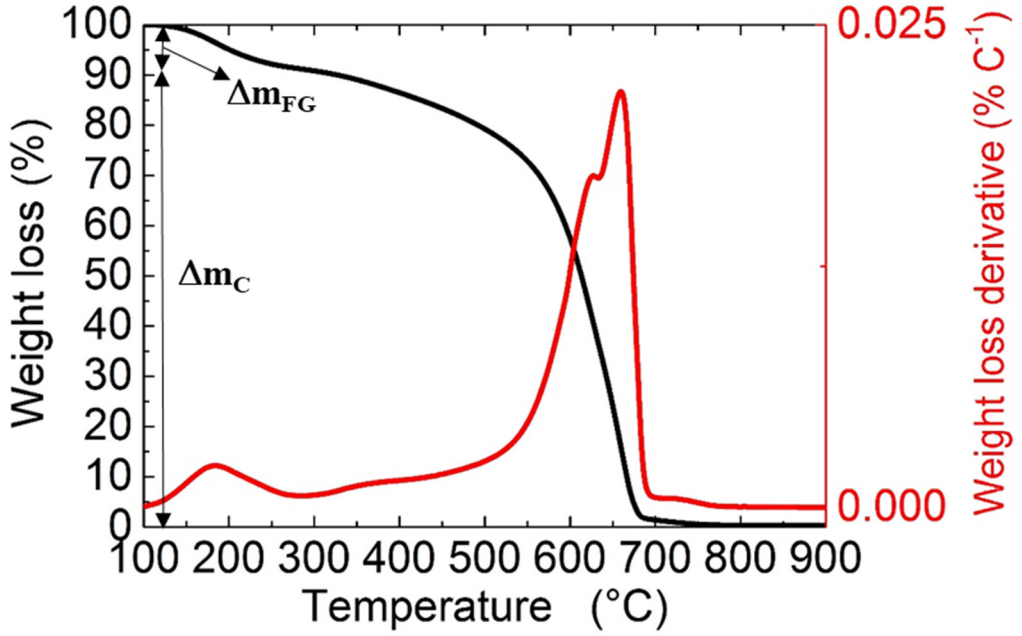

Fig. S2. Thermogram of CNH-PhOMe acquired under a nitrogen atmosphere. Black line represents the weight percentage loss, while the red line is the corresponding derivative curve.

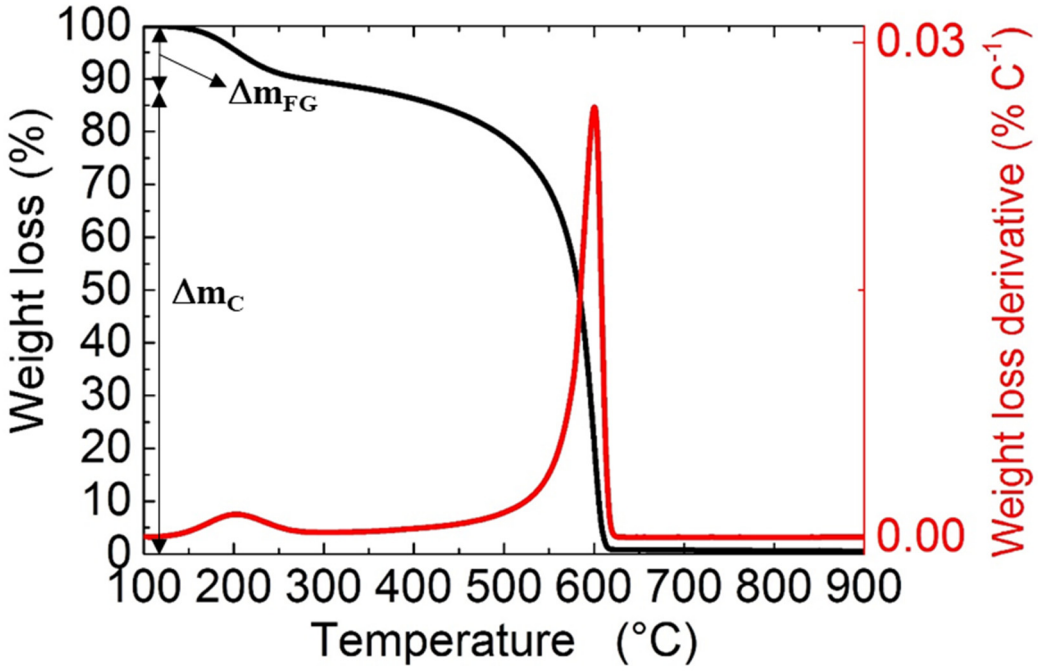

Fig. S3. Thermogram of RGO-PhOMe acquired under a nitrogen atmosphere. Black line represents the weight percentage loss, while the red line is the corresponding derivative curve.

Functionalized-CNS@PLLA films

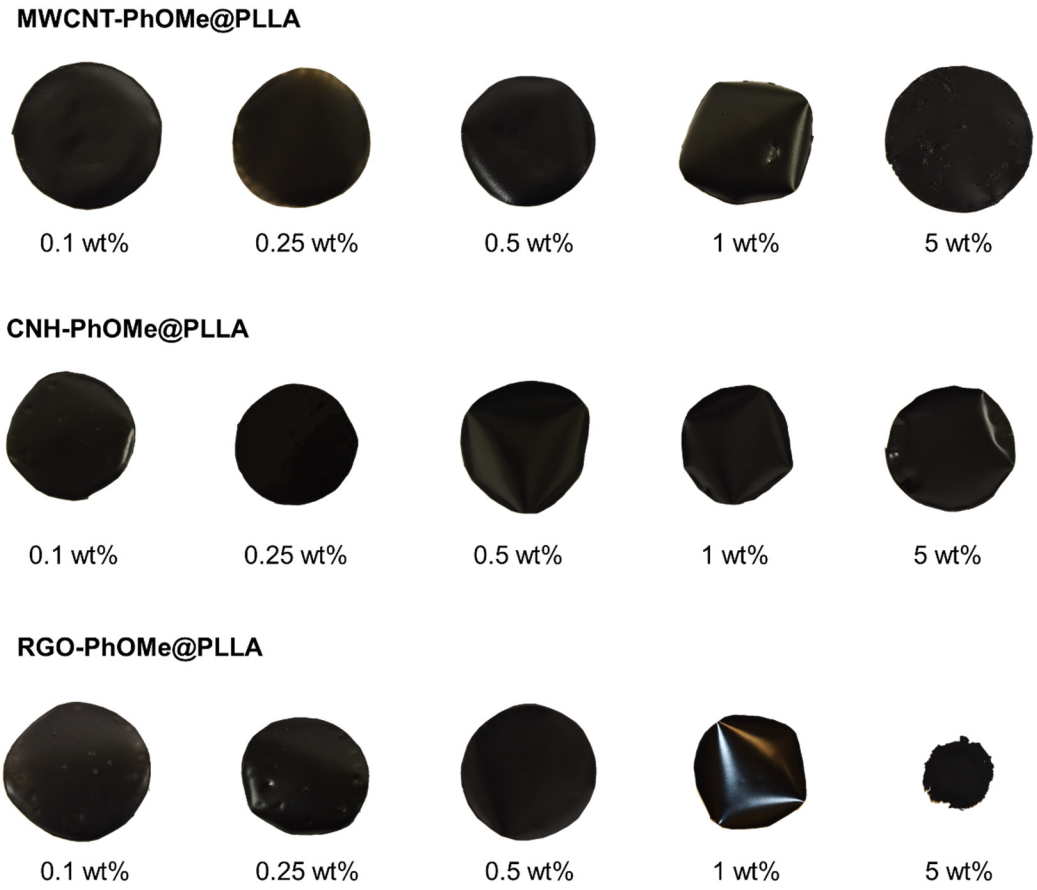

Fig. S4. Photographic images of the functionalized-CNS@PLLA films considered in this work.

Table 1. Measured film thicknesses for the functionalized-CNS@PLLA films considered in this work.[a]

wt%	MWCNT-PhOMe@PLLA (µm)	CNH-PhOMe@PLLA (µm)	RGO-PhOMe@PLLA (µm)
0.1	325	330	331
0.25	320	338	325
0.5	305	331	340
1	323	340	345
5	322	345	-[b]

[a] For the pure PLLA film a thickness of 335 µm was measured. [b] Not measurable due to extreme fragility of the specimen.

Calorimetric analysis of the functionalized-CNS@PLLA films

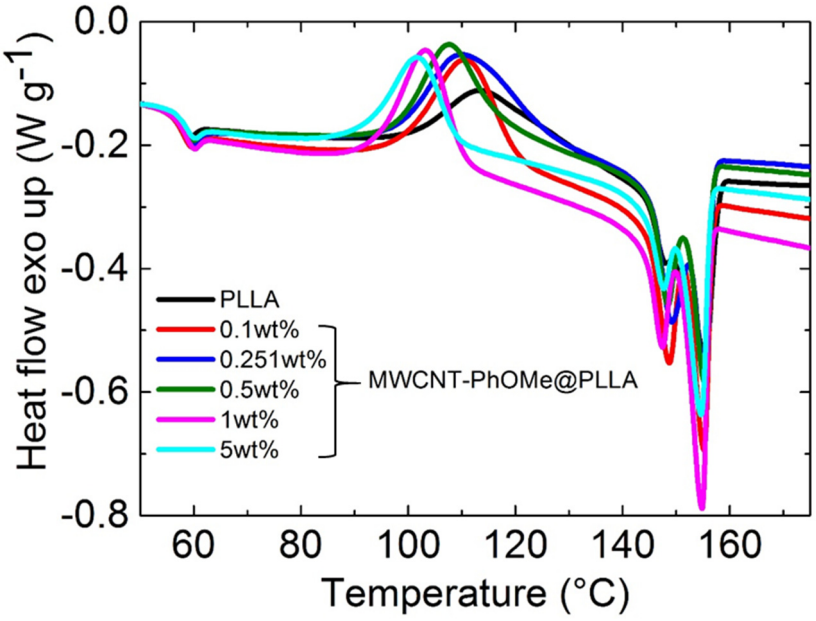

Fig. S5. DSC traces (second heating scans after a previous heating-cooling cycle) for the five types of MWCNT-PhOMe@PLLA composites having different concentrations of nanofillers in the polymer phase and for pure PLLA.

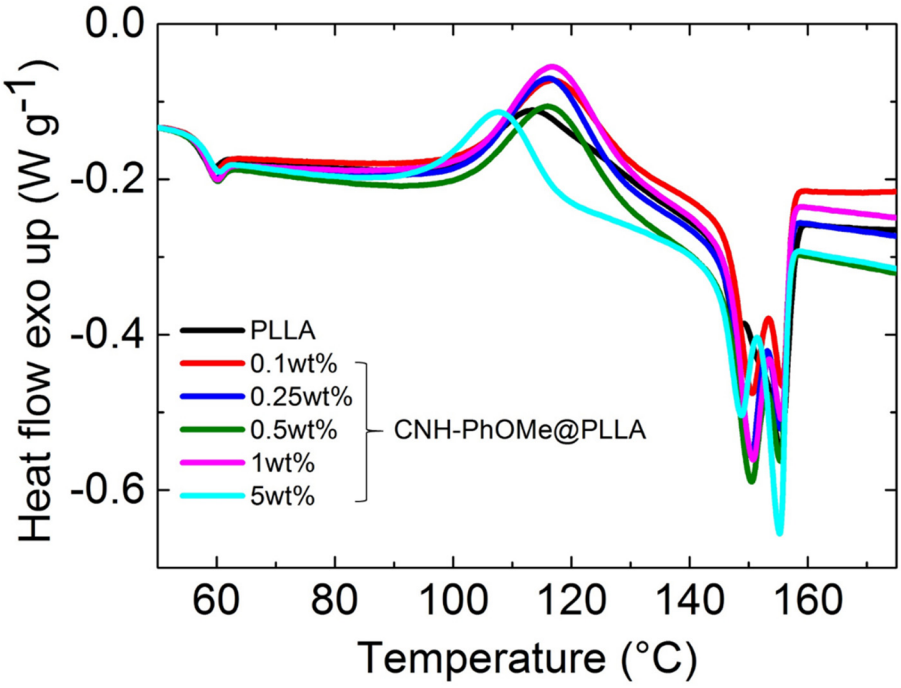

Fig. S6. DSC traces (second heating scans after a previous heating-cooling cycle) for the five types of CNH-PhOMe@PLLA composites having different concentrations of nanofillers in the polymer phase and for pure PLLA.

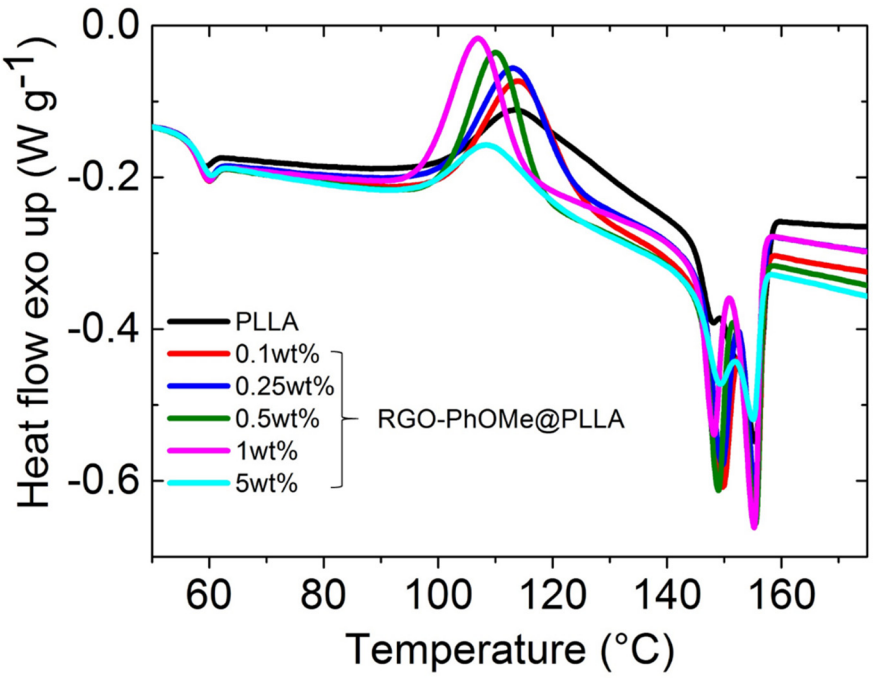

Fig. S7. DSC traces (second heating scans after a previous heating-cooling cycle) for the five types of RGO-PhOMe@PLLA composites having different concentrations of nanofillers in the polymer phase and for pure PLLA.

Table S2. Calorimetric data for the MWCNT-PhOMe@PLLA composites having different concentrations of nanofillers in the polymer phase and for pure PLLA.

MWCNT-PhOMe@PLLA						
	Cristallization		Melting			
Conc (wt%)	Tmax (°C)	ΔH (J g^{-1})[a]	Tonset (°C)	ΔH (J g^{-1})[a]	Tg (°C)	Cristallinity (%)[b]
0	114	15.84	149	27.97	55	30.08
0.1	111	23.43	152	23.50	56	25.27
0.25	110	22.55	151	22.67	57	24.38
0.5	108	20.74	151	22.91	56	24.63
1	103	18.28	151	20.76	56	22.32
5	102	16.90	150	21.63	56	23.26

[a] Calculated from peak area. [b] Degree of crystallinity calculated by comparison with theoretical data for 100% crystalline PLLA.[2]

Table S3. Calorimetric data for the CNH-PhOMe@PLLA composites having different concentrations of nanofillers in the polymer phase and for pure PLLA.

CNH-PhOMe@PLLA						
	Cristallization		Melting			
Conc (wt%)	Tmax (°C)	ΔH (J g^{-1})[a]	Tonset (°C)	ΔH (J g^{-1})	Tg (°C)	Cristallinity (%)[b]
0	114	15.84	149	27.97	55	30.08
0.1	117	23.04	151	23.41	57	25.17
0.25	116	22.41	151	22.95	56	24.68
0.5	117	20.33	150	23.11	56	24.85
1	117	22.09	151	23.77	56	25.56
5	117	23.83	151	23.83	56	25.62

[a] Calculated from peak area. [b] Degree of crystallinity calculated by comparison with theoretical data for 100% crystalline PLLA.[2]

Table S4. Calorimetric data for the RGO-PhOMe@PLLA composites having different concentrations of nanofillers in the polymer phase and for pure PLLA.

RGO-PhOMe@PLLA						
	Cristallization		Melting			
Conc (wt%)	Tmax (°C)	ΔH (J g^{-1})	Tonset (°C)	ΔH (J g^{-1})	Tg (°C)	Cristallinity (%)
0	114	15.84	149	27.97	55	30.08
0.1	114	20.54	152	23.63	56	25.41
0.25	114	23.19	152	24.41	56	26.25
0.5	110	22.13	152	21.88	56	23.53
1	107	22.08	152	22.87	56	24.59
5	109	10.73	149	16.68	57	17.94

[a] Calculated from peak area. [b] Degree of crystallinity calculated by comparison with theoretical data for 100% crystalline PLLA.[2]

Mechanical characterization of the functionalized-CNS@PLLA films

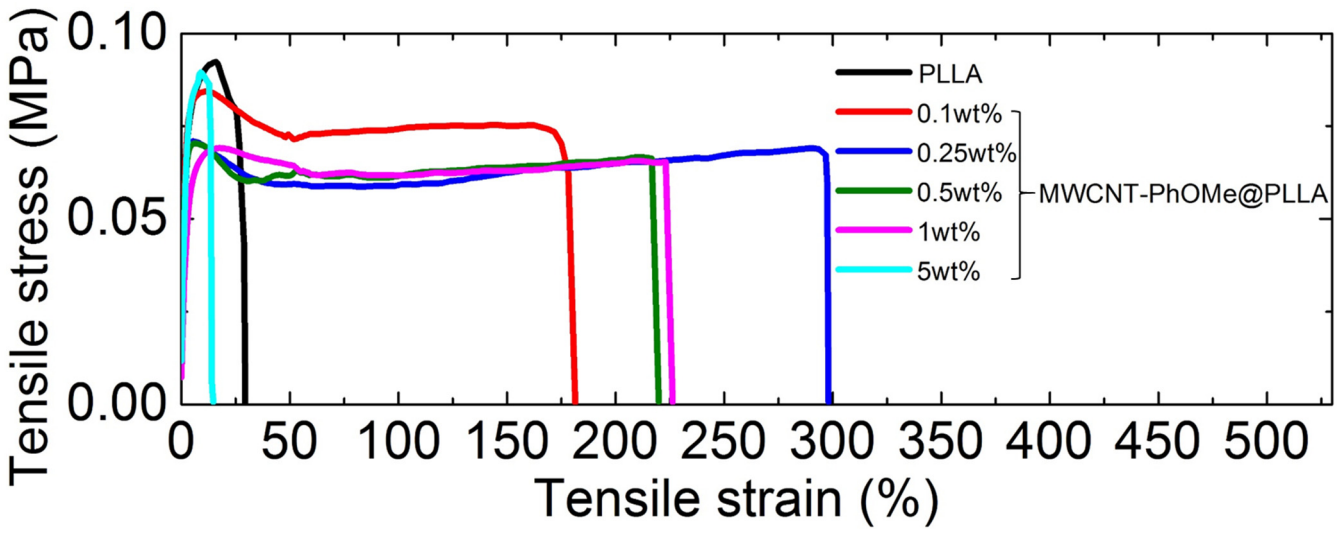

Fig. S8. Representative tensile stress-strain curves for the MWCNT-PhOMe@PLLA composites having different concentrations of nanofillers in the polymer phase and for pure PLLA.

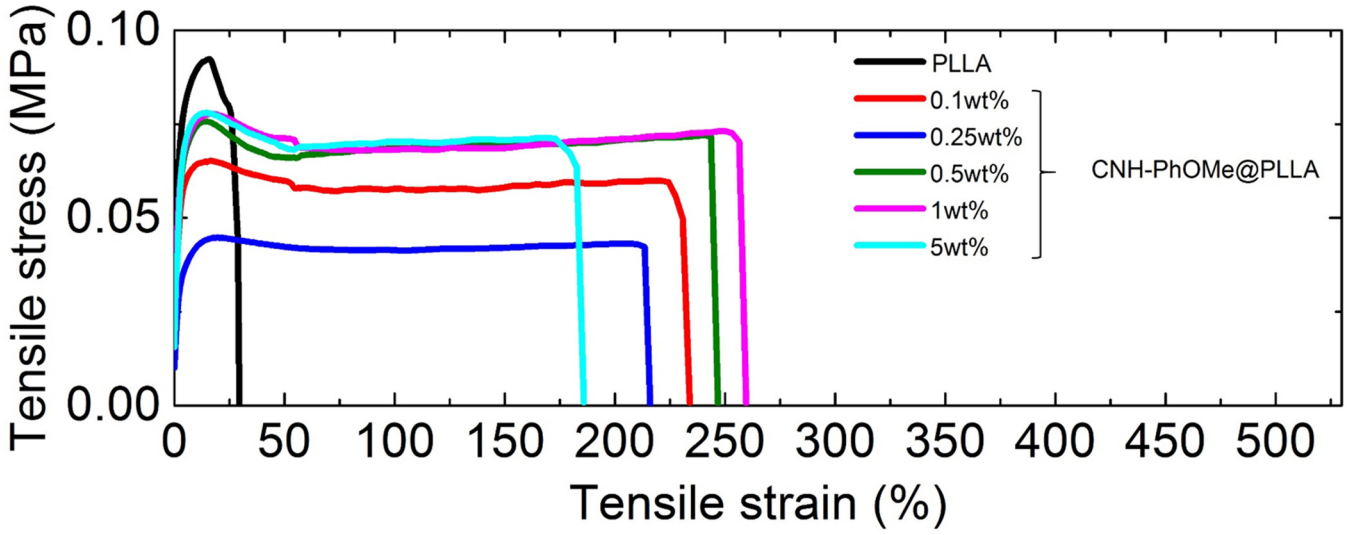

Fig. S9. Representative tensile stress-strain curves for the CNH-PhOMe@PLLA composites having different concentrations of nanofillers in the polymer phase and for pure PLLA.

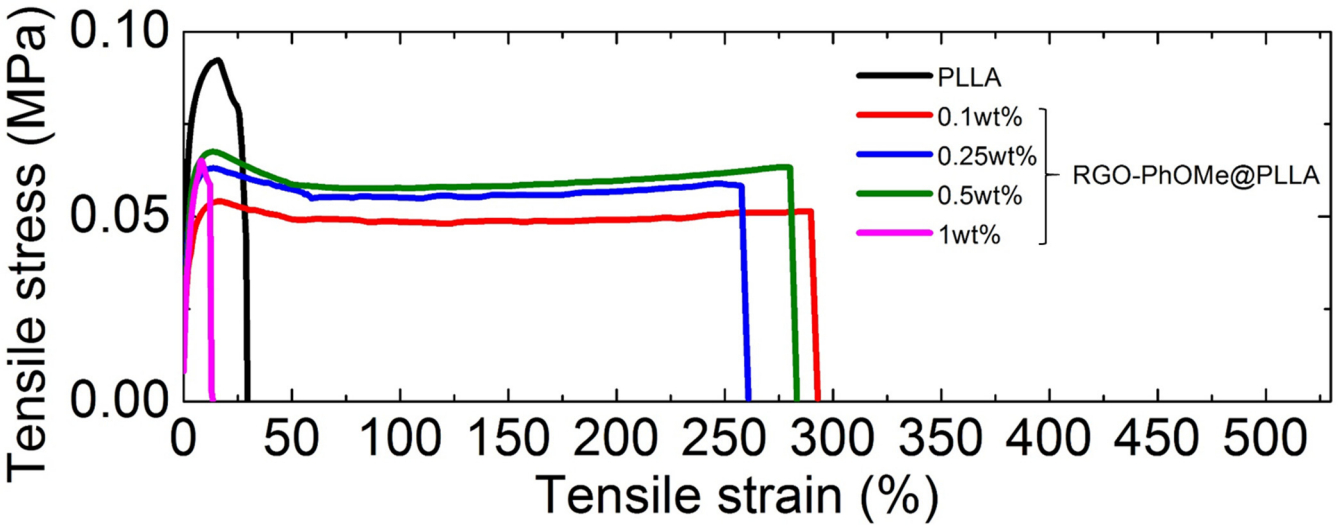

Fig. S10. Representative tensile stress-strain curves for the RGO-PhOMe@PLLA composites having different concentrations of nanofillers in the polymer phase and for pure PLLA.

Functionalized-CNS@PLLA nanofibers characterization

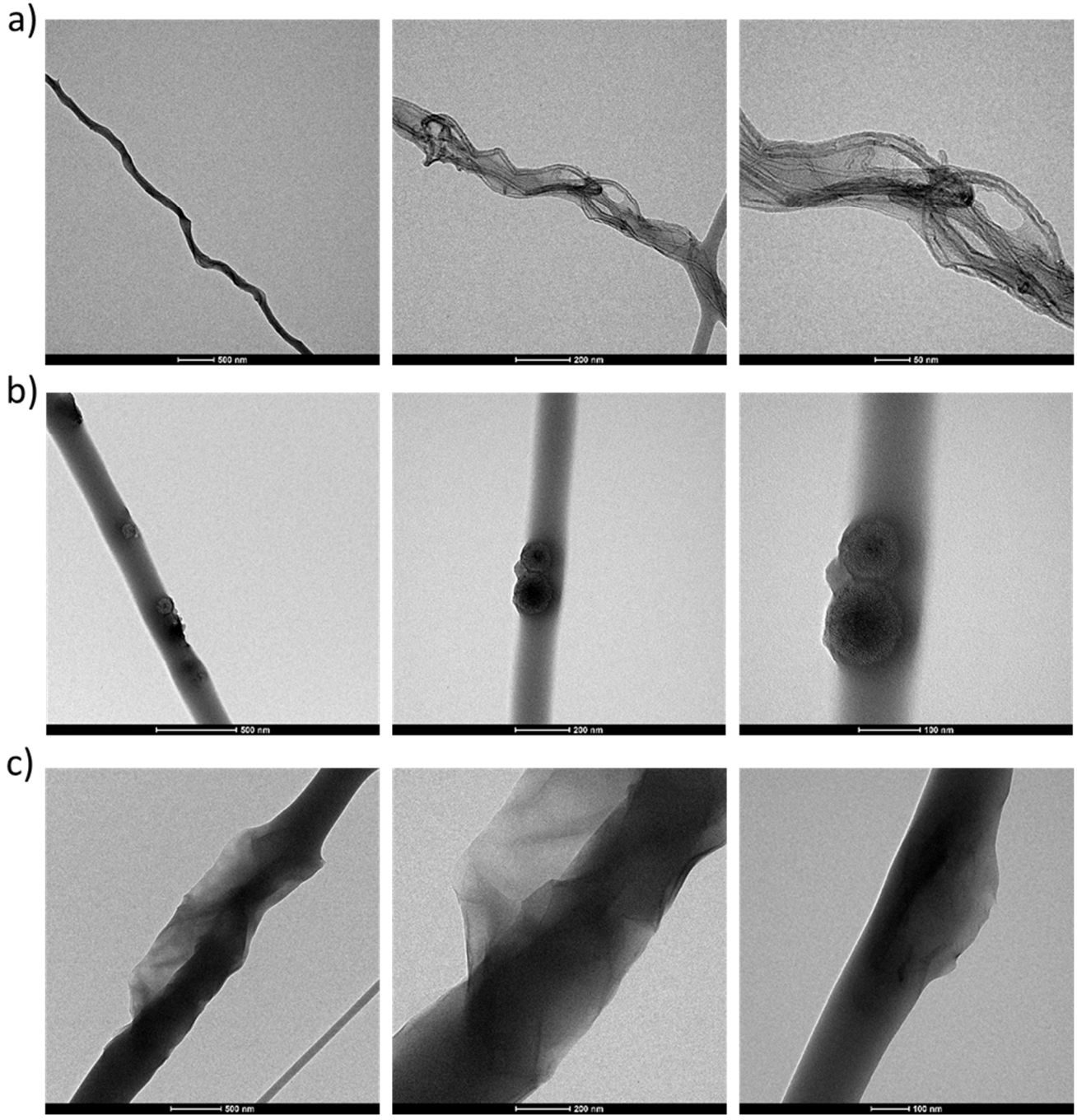

Fig. S11. TEM images of a) 5wt% MWCNT-PhOMe@PLLA, b) 5wt% CNH-PhOMe@PLLA and c) 5wt% RGO-PhOMe@PLLA nanofibers.

Details of AFM measurements

The nanoscale electrical conductivity was assessed within the range of process parameters accessible for this DC based technique (±10 V maximum sample bias with tip set to virtual ground, and current detection limit down to ~ 1 pA level). The current mapping measurements were carried out at the lowest possible, yet stable, vertical contact force (~0.1 V in arbitrary deflection value, corresponding to ~18 nN) that allowed to measure some current level, in order not to damage either the sample or the tip. The CAFM was equipped with a dual-gain Orca probe-holder (Asylum Research, US), with two current converters and amplifiers of sensitivities 1 V/μA and 1 V/nA for the C2 and Cu channels, respectively, to be used in the current ranges (absolute values) of 10 nA-10 μA and 0-10 nA, respectively. Only when no current was detected at even the highest possible bias (±10 V to the sample, with tip at virtual ground) on the more sensitive Cu channel, was the contact force increased up to a factor of 4, to check for possible conductance. Both current images and local I-V curves at given points of conductive film, as previously identified in a current image, were acquired. By using the contact mode, at the base of CAFM, with fast scan at 90° with respect to the cantilever axis, the lateral deflection (so-called lateral force) images were also collect and the qualitative tip-surface friction was mapped (by making the calculation of lateral deflection trace minus lateral deflection retrace, divided by 2). This channel was used to check for possible chemical inhomogeneity of the surface, correlated to either the sample composition or possible ambient contaminants.

Figs. S12b (EFM) and S12c (SKPM) of the bare PLLA fibers sample show very good correlation, exhibiting contrast at both the (insulating) fibers and at a contamination on the substrate (probably due to a dried drop of some liquid, e.g. solvents). Fig. S12c in particular is quantitative, and described better the excess accumulation of charge at the large polymer beads formed during electrospinning at the fiber on the left hand side. On fibers of CNH and RGO containing composites similar results were obtained, with only bright contrast at the fibers (no voltage drop i.e. electrical conduction detected). For the images of CNT containing composite fibers, instead, regions with either local lower contrast at some fibers (e.g. that on the right in Figure S12e or even no contrast (top-left in Fig. S12g) appeared. There, some loss of potential probably due to either conductive fillers or conduction along the fiber obviously occurred. In Fig. S12h the potential of panel S12g has been overlaid as color on the 3D topography of panel S12f, showing more clearly the effect of spread of EFM/SKPM contrast around the structure, due to the long range of the electrostatic forces in-plane (and partly also to the effect of the elevation height).

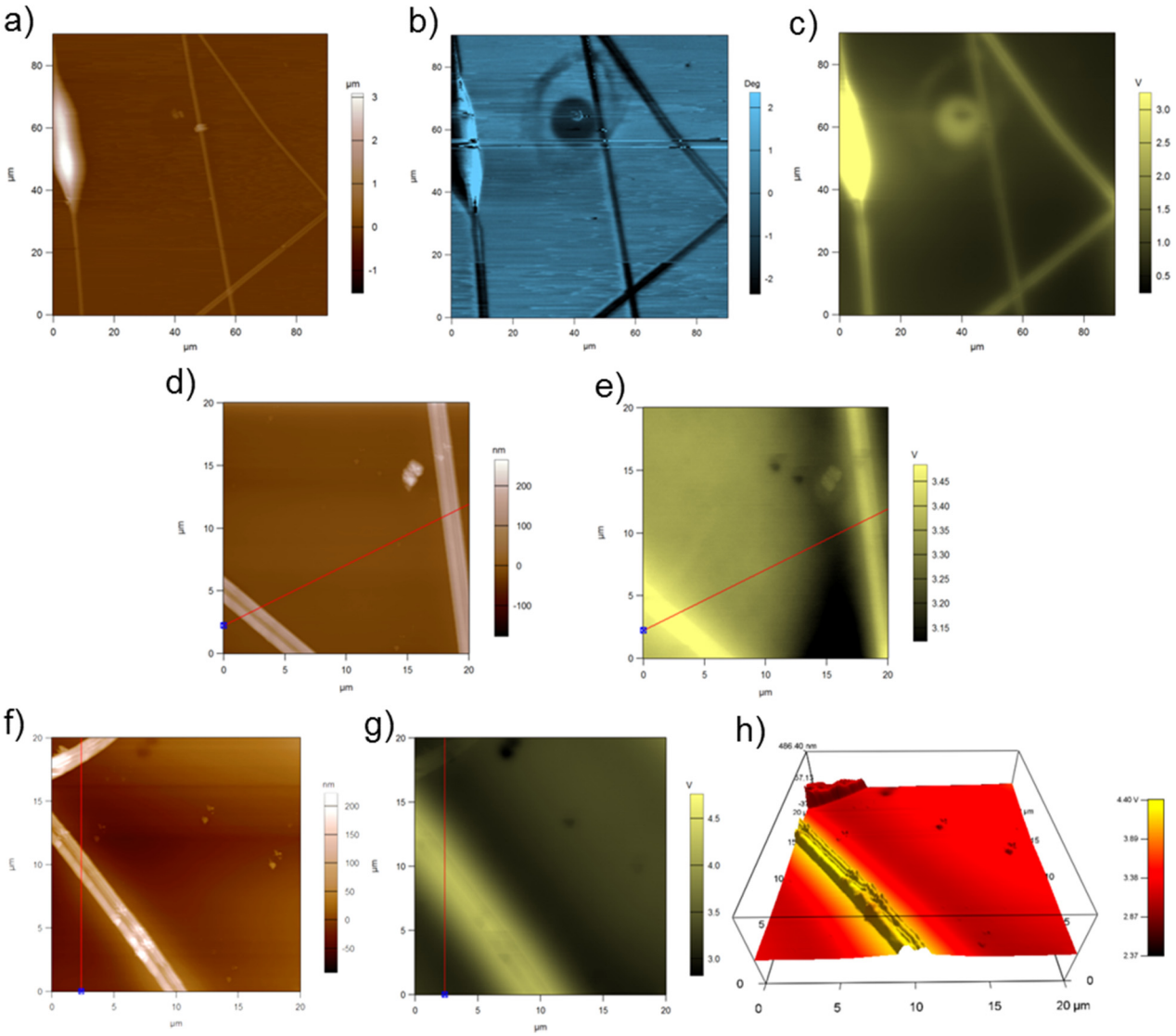

Fig. S12. Examples of EFM/SKPM images of fiber composite samples. a-c) bare PLLA fibers: a) is the topography, b) is the phase of the Nap pass i.e. the EFM image; c) is the SKPM image of surface potential on the same region. d,e) and f-h): two regions of a samples of MWCNT composite fibers, (with combined topographic-potential rendering of the second region in h).

Finally, in Fig. S13 the same region of the SKPM images in Fig. 5 of the main text is shown again, when subsequently imaged in EFM mode. A substantial qualitative agreement in assignment of the filler regions appear in the phase of oscillation, Fig. S13b, with SKPM surface potential image of Fig. 5b, with only a reversal of contrast for the present signal, where the fillers appear as 'bright' phase regions, as compared to the 'dark' potential regions in Fig. 5b. This is probably a mechanical effect due to the higher stiffness of the CNTs as compared to the PLLA fiber matrix. Also, the occasionally invasive effect of repeated scanning appears in Fig. S13, as a suspended fiber having been picked by

the scanning tip at some point during the scan and deflected (according to the arrow direction) up to forming a sharp right corner.

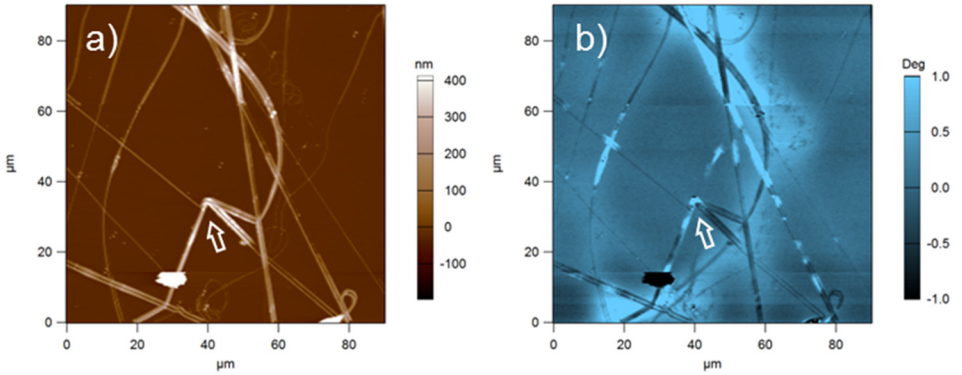

Fig. S13. EFM images of the same region as shown in Figure 5 in the main text; a) topography, b) phase of cantilever oscillation. Filler identification consistent with SKPM technique of Figure 5 emerges, along with demonstration of possible invasive tip-fiber interaction upon repeated scanning of the samples of deposited fibers.

For the roughness measurement, standard Tapping mode imaging with a standard (i.e. not metal coated) tip was carried out, not to degrade the spatial resolution of the images. Also, the S_q was calculated over surface areas of 20×20 μm^2, and averaged over five similar images from different regions of the samples.

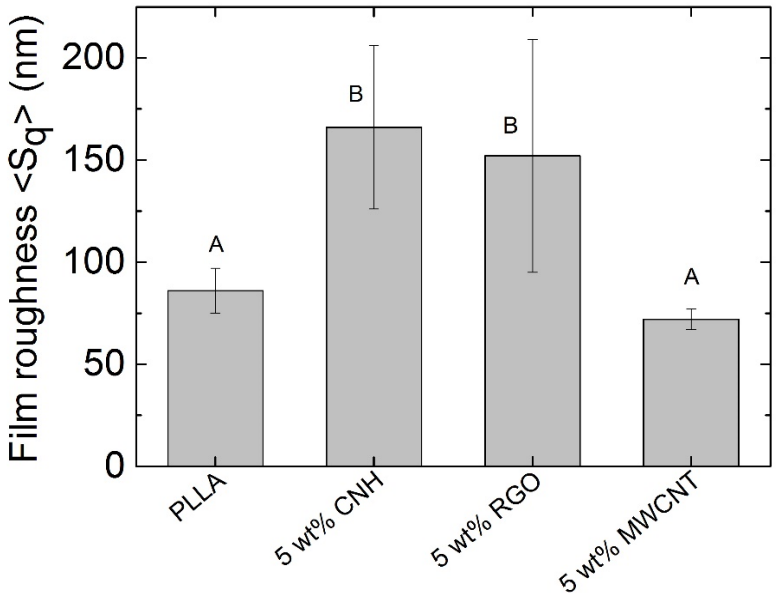

Fig. S14. Root-mean-square of the height images, i.e. 2D roughness parameter Sq, for the films of different material composites (red columns), together with the bare PLLA (black column). The bars heights are the means, and the error bars extend ±1 standard error of the mean (SEM). The groups that present statistically significant differences ($p<0.05$) have been identified by different letter labels.

Cell death and proliferation assessment

Resazurin reduction assay was performed to quantify the metabolically active living cells and thus to monitor how do the scaffolds affect proliferation of the cell populations tested. The assay is based on reduction of the indicator dye, resazurin (not fluorescent), to the highly fluorescent resorufin (Ex. 569 nm, Em. 590 nm) by viable cells. Non-viable cells rapidly lose their metabolic capacity to reduce resazurin and, thus, do not produce fluorescent signals anymore. Briefly, the culture medium was replaced by 500 µL of resazurin solution (Resazurin Sigma 15 µg/mL in complete medium without phenol red) and cells were incubated for 4 h in dark at 37°C and 5% CO_2. Then, 200 µL of resazurin solution were removed twice from each well and transfer to a 96 well plate (technical duplicates). Fluorescence, directly correlated with cell quantity, was read in a plate reader (Ascent Fluoroscan, excitation 540 nm, emission 590 nm). Background values from wells without cells were subtracted and average values for the duplicates calculated. Cell proliferation was calculated from a calibration curve by linear regression using Microsoft Excel. The CytoTox-ONE™ Homogeneous Membrane Integrity Assay (Promega) was used to quantify the lactate dehydrogenase (LDH) release by cells having lost membrane integrity. Briefly, 100 µL of culture medium were transferred to a new 96 well plate. 50 µL of the reaction solution from the kit, containing the detection dye and the catalyst were then added to culture supernatants and fluorescence was measured after 10 minutes in the plate reader as reported above. Cell death was calculated from a calibration curve by linear regression after 100% cell lysis of known cell quantities.

References

[1] T. Gatti, S. Casaluci, M. Prato, M. Salerno, F. Di Stasio, A. Ansaldo, E. Menna, A. Di Carlo, F. Bonaccorso, Boosting Perovskite Solar Cells Performance and Stability through Doping a Poly-3(hexylthiophene) Hole Transporting Material with Organic Functionalized Carbon Nanostructures, Adv. Funct. Mater. 26(41) (2016) 7443-7453.

[2] N. Vicentini, T. Gatti, P. Salice, G. Scapin, C. Marega, F. Filippini, E. Menna, Covalent functionalization enables good dispersion and anisotropic orientation of multi-walled carbon nanotubes in a poly(l-lactic acid) electrospun nanofibrous matrix boosting neuronal differentiation, Carbon 95 (2015) 725-730.

3.1.2 Effect of different CNS@PLLA composites on neuronal differentiation

On-going work is addressing to check eventual effects of the new PhOMe-functionalized-CNS@PLLA composites, and consequentially of their different physical characteristics, on cellular behaviour. We have checked the neuronal differentiation of a human neuroblastoma cell line when they are seeded onto our different nanocomposite scaffolds.

First, we have explored effect of increasing MWCNT concentration in PLLA matrix on SH-SY5Y cells. Previously, PhOMe-functionalized- MWCNT@PLLA have been tested with these cells at 0.25%, proving to be biocompatible and able to enhance the neuritogenic effect of biomimetic peptides (Scapin et al.2015). Also, a neuritogenic effect was observed using MWCNT-PhOMe@PLLA electrospun nanofibrous matrix, showing neurites extension along the direction of nanofibers [46]. These results suggested PhOMe-functionalized-MWCNT@PLLA properties may influence neuronal differentiation in our cell system. However, we didn't observe any significant effect on neuronal differentiation when using films of such nanocomposite. Such results can be attributed to the low dose of CNT; therefore, we have developed film of MWCNT@PLLA composites containing increasing concentration of functionalized MWCNT in PLLA (0, 0.1, 0.25, 0.5, 1 and 5 wt%) [192].

Once these new CNS concentrations were found to be biocompatible, we decided to test the effect on neuronal differentiation of three MWCNT concentrations: i) 0.25% that represent the percolation threshold of MWCNTS ii)1% representing the limit concentration to obtain homogeneity of the dispersion of functionalized MWCNT within the PLLA phase iii)5% that is the maximum MWCNT content in our nanocomposite and shows the higher electrical conductivity. As controls, we used cells seeded on poly-L-lysine coated wells (without any scaffolds) to monitor the physiological cell condition, and cells on films of bare PLLA to distinguish nanocomposite-dependent effects. Cell morphologies were observed using Calcein-AM staining 48 hours after the differentiation induction with RA. Also, not differentiated cells are analysed.

Following the classic neuritogenic parameters, total neurite length and neurite/cell, only 5% CNT has a significant effect on total neurite length compared to PLLA control (**Fig. 1**). Such result is supported by several studies indicating that increasing scaffold electrical conductivity influence neuronal elongation and growth[151,152]. Thus, we decided to focus on neurite elongation observing a striking inductive effect of 5%MWCNT on the number of

neurites longer than 100 micrometer. The effect is further increased if we consider the neurites longer than 150 micrometer.

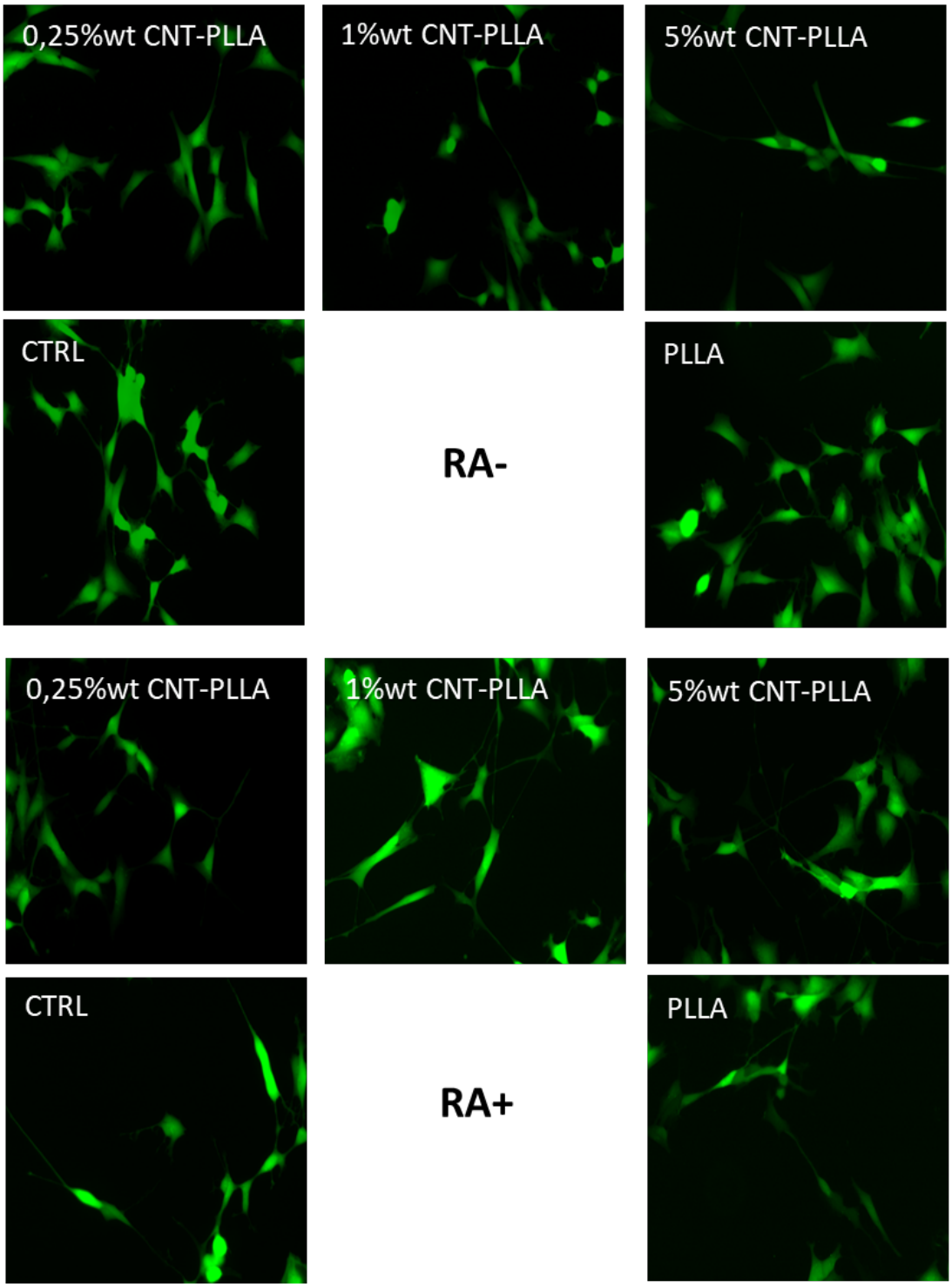

Figure 1. Representative microscopy fields of SH-SY5Y cells from experiments in Figure 2. Cells are stained with Calcein-AM. Image magnification is 32X.

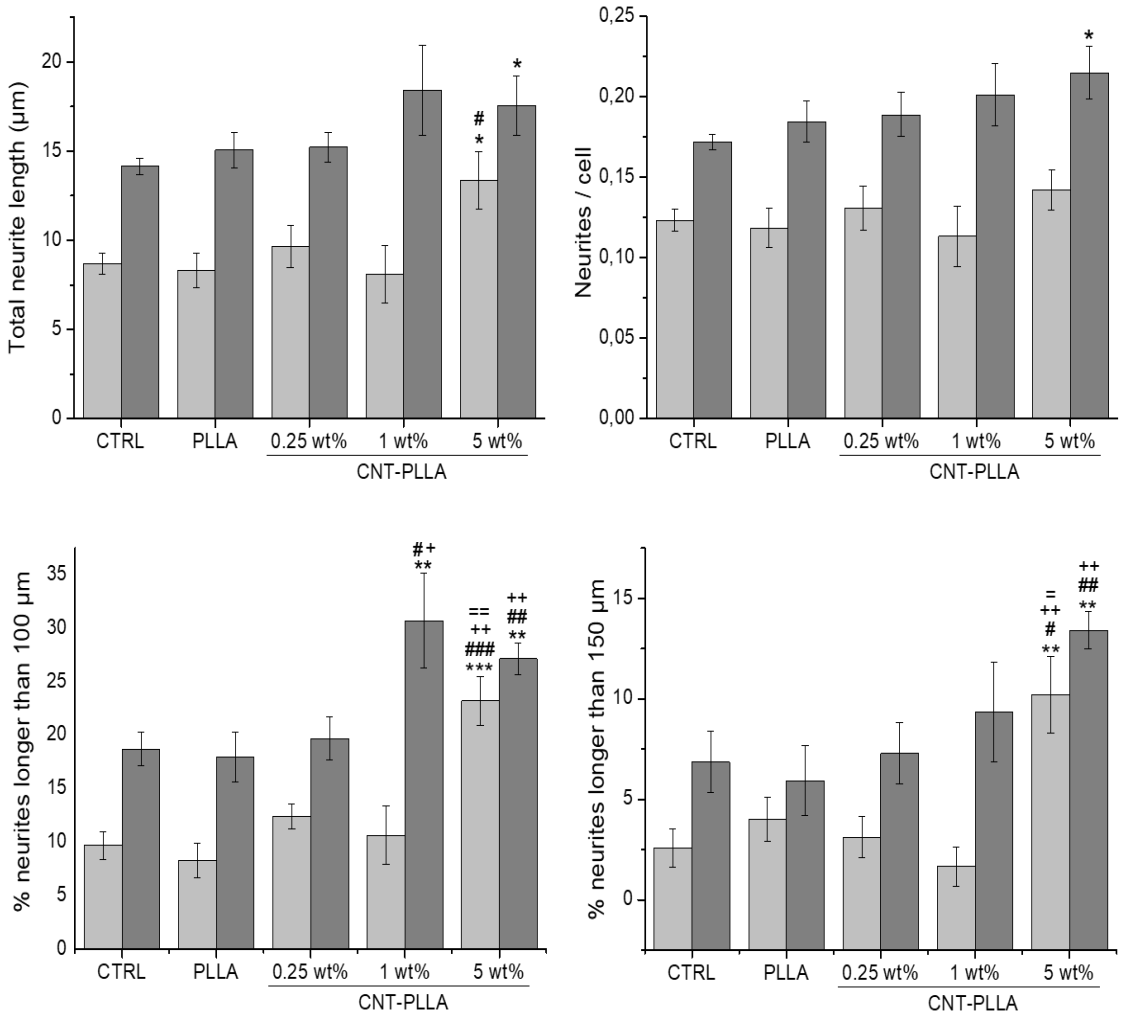

Figure 2: effect of increasing CNT concentrations in our composite films on SH-SY5Y differentiation. Total neurite length **(A)**, neurites per cell **(B)**, neurites longer than 100 µm **(C),** neurites longer than 150 µm **(D)**. Data represent the mean ± SEM of four independent experiments performed in duplicate. *shows significance at $p<0.05$ between cells seeded onto scaffolds and control (poly-L-lysine coated wells). #shows significance at $p<0.05$ between cells seeded onto CNT-PLLA scaffolds and PLLA films. +shows significance at $p<0.05$ between cells seeded onto CNT-PLLA scaffolds and 0.25%wtCNT-PLLA scaffolds. =shows significance at $p<0.05$ between cells seeded onto CNT-PLLA scaffolds and 1%CNT-PLLA scaffolds Dark grey bars refer to the corresponding RA treated samples. Light grey bars refer to the corresponding not-treated samples.

This result demonstrates that enhanced electrical conductivity influence more neuronal elongation than neurite outgrowth. The role of CNTs could be to create a direct electronic current transfer, by which coupling neurons seeded on them. In fact, it is known that electrical signals strongly influence neuronal behaviour. However, the exact mechanism by which conductive substrates and electrical stimulation affect cell growth and differentiation have to be exploited yet.

In the meantime, we have decided to test the eventual effect on neuronal differentiation of our new nanocarbon structures. In these analyses we have used the lowest and highest concentrations (0.25% and 5%) of our CNS dispersed in the PLLA matrix. As shown in **Fig. 20**, 5%wt of RGO have a positive effect on both total neurite length and neurite/cell.
RGO and CNH are less effective than CNT in conferring conductive properties to insulating polymers [192], making not necessary further analysis on neurite elongation.

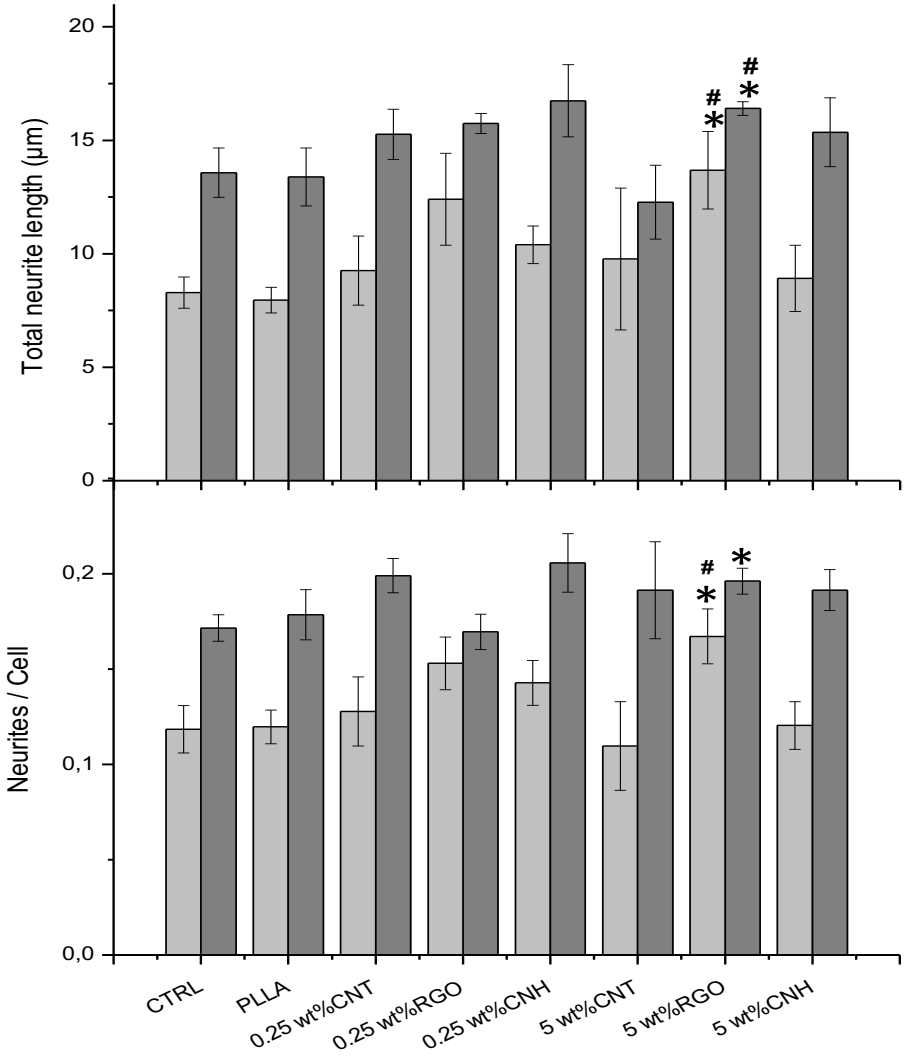

Figure 3: Effect of different carbon nanostructure as nanofillers in our composite films on SH-SY5Y differentiation. Total neurite length **(A)**, neurites per cell **(B)**. Data represent the mean ± SEM of three independent experiments performed in duplicate. *shows significance at p<0.05 between cells seeded onto scaffolds and control (poly-L-lysine coated wells). #shows significance at p<0.05 between cells seeded onto CNS-PLLA scaffolds and PLLA films. Dark grey bars refer to the corresponding RA treated samples. Light grey bars refer to the corresponding not-treated samples.

3.1.3 Effect of patterned scaffolds on cellular behaviour

We already demonstrated that electrospun CNT-PLLA fibers, used to mimic the neuronal processes and the fibrillar collagenous and laminin component of the ECM, allow to obtain neurite elongation that follow the scaffold fiber orientation [46]. Now, we are using 3D-printing with graphene-PLA filament to obtain patterned scaffold eventually able to guide cell growth. The results are reported in the following paper in preparation.

3D printed graphene-PLA scaffolds promote neuronal differentiation and neurite orientation in human circulating multipotent stem cells.

Pietro Bellet[1]*, Matteo Gasparotto[1]*, Yuriko Suemi Hernandez Gomez[1], Rosa Di Liddo[2], Francesco Filippini[1§]

Department of [1] Biology, and [2] Pharmaceutical and Pharmacological Sciences, University of Padua, Italy.

* Equal contributions; § Corresponding author

Keywords: graphene, PLA, scaffod, neuronal differentiation, hCMC, stem cells, 3D printing, regenerative medicine

Abstract

Graphene-based nanocomposites are a most promising material for regenerative medicine applications, especially when mixed to biocompatible polymers such as e.g. polylactides. Starting from our recent discovery that an autologous population of human multipotent cells can be committed to the neuronal lineage by conductive scaffolds, we used 3D printing by additive manufacturing and commercially available graphene-PLLA filaments to develop scaffolds which were able *per se* to induce neuronal differentiation in the absence of exogenously added neurotrophins. Moreover, patterned printing proved able to strongly enhance neuronal differentiation and to drive oriented growth and axon elongation, opening the route to design and production of self-standing scaffolds for designed repopulation of central nervous system injuries as well as for artificial neural circuit design.

Introduction

Nanotopographical and biochemical cues play a pivotal role in stimulating stem cell differentiation and cell orientation; in general, scaffolds mimicking such tissue environment stimuli able to promote stem cell differentiation are crucial in regenerative medicine and in tissue engineering projects (Sampogna et al., 2015). Decellularized tissues from donor animals or human cadavers are promising 'physiological' scaffolds recapitulating the natural composition and tridimensional organization of the extracellular matrix (ECM) (Kobayashi, 2016). Unfortunately, antigens from such scaffolds may elicit adverse immune response leading to transplant failure (Badylak, 2014). Moreover, genetic and epigenetic variation among animal and human donors impairs reliability in protocols and results, and size compatibility can be a further issue (Edgar et al., 2016).

There is not a singular scaffold formulation or biomaterial that is universally optimal; however, recent years have seen a great advancement in the design and development of synthetic biocompatible polymers and nanocomposites for drug delivery, biosensors and tissue engineering applications (Follmann et al., 2017). In general, nanocomposite scaffolds most often overperform single-component matrices in regenerative medicine as they better mimic the multiple stimuli from any tissue environment (Dvir et al., 2011; Edgar et al., 2016). A number of bioplastics and related polymers is currently used in regenerative medicine because of their advantages in terms of lack of immunogenicity, very low batch variation, easy and cost-effective scaffold manufacturing, easy modulation of physical and biochemical features by blending together different matrices and nanofillers as well as by chemical functionalisation for binding of specific molecules. In particular, Poly-L-Lactic Acid (PLLA) is easily manageable in nanocomposites fabrications and it has been approved by FDA for regenerative medicine purposes. PLLA-based scaffolds are self-standing and can be used for cell growth and differentiation, once they are transplanted, the slow hydrolytic degradation into lactic acid, a metabolic by-product, also makes PLLA scaffolds suitable for planned reabsorption (Santoro et al., 2016). Even though PLLA is most often combined to other polymers and nanofillers, PLLA alone proved to be suitable for the fabrication of artificial tissue or scaffolds for bone regeneration (Chiulian et al., 2017).

In neural regenerative projects, a very important feature to be reproduced is the electrical conductivity (Kabiri et al., 2012). To this aim in recent years several conductive carbon-based nanomaterials have been tested such as e.g. carbon nanotubes (CNT) and graphene (John et al., 2015). CNTs have been widely used because of their nanotophographic

features resembling neuronal processes; however, careful purification and chemical functionalisation are needed to prevent cell damage depending on toxic heavy metal residuals from the production processes or intracellular aggregation due to the hydrophobic interactions (Malarkey & Parpura, 2010; Fabbro et al., 2013). Nanocomposite CNT-PLLA scaffolds with very low nanofiller concentration were able to keep positive features of CNTs while dramatically reducing residual impurities and costs and they proved to strongly boost neuronal differentiation and growth (Scapin et al., 2015). When electrospinning such nanocomposite material, neuronal processes were observed to follow nanofibers organisation (Vicentini et al., 2015).

Currently, graphene-based materials are considered among the most promising nanomaterials for cellular applications including regenerative medicine (Huang et al., 2018; Kenry et al., 2018). In particular, when compared to CNTs, they are less expensive, easier to obtain and show less intrinsic toxicity while maintaining the main peculiar feature of carbon-based nanomaterials including conductivity (Gardin et al., 2016). For central nervous system (CNS) regenerative medicine purposes, cell repopulation and differentiation are needed at the injury site. To this aim, self-standing scaffolds are expected to stimulate *in situ* commitment of stem cells towards the neuronal lineage and then to support neuronal differentiation and growth. Most protocols for stem cells commitment and differentiation strongly depend on the exogenous addition of a complex mixture of neurotrophins and supporting factors. Recently however, CNT-PLLA scaffolds proved able to induce *per se* (i.e. in the absence of exogenously added factors) neuronal lineage commitment and differentiation of a population of autologous multipotent stem cells (Scapin et al., 2016). Such promising features were also confirmed by the electrospun version of these scaffolds; however, regular orientation of neuronal processes could not be obtained because of the random deposition of nanofibers.

Indeed, graphene-PLLA composites hold great promise in tissue engineering and in other biomedical fields (Bayer, 2017). At the same time, additive manufacturing (AM) via 3D printing of PLLA has become in recent years more and more feasible, cheap and reliable. Therefore, we decided to develop 3D printed scaffolds based on either PLLA or graphene-PLLA for commitment of hCMCs to either osteoblastic or neuronal lineage. After demonstrating that these scaffolds are not cytotoxic and thus suitable for regenerative medicine purposes, we designed patterned graphene-PLLA scaffold that proved able to

further support neuronal differentiation and, in addition, to mediate oriented neurite elongation.

Materials and Methods

Informatics and 3D-printing

Fusion 360 (Autodesk) and Simplify3D softwares were used to create the STL files of the scaffolds and then for slicing, respectively. A dual-nozzle 3D printer (NG model, Sharebot, Italy) was used for printing. Adhesion of the first layer was improved by coating of the stage with a saturated solution of sucrose in MIlli-Q water. Both pure PLA and graphene-PLA (GRAFYLON®) ø 1.75 mm filaments were purchased from FILOALFA. GRAFYLON® consists of pure PLLA matrix embedded with roughly 1% Graphene Plus (Directa Plus). Printing was performed with nozzle temperature at 195ºC, using the same GCODE file for both pure PLLA and GRAFYLON® scaffolds.

Cell culture and scaffold preparation

SH-SY5Y cells were grown or differentiated via retinoic acid induction 24 hours after seeding (Day 1) as reported in our previous work (Scapin et al., 2015); hCMCs were cultured according to Scapin et al., 2016.

After printing, scaffolds were washed to remove sucrose residuals and air-dried. Sterilization was obtained under UV-light, 30 minutes on all sides. Pure PLLA and GRAFYLON® 3D-printed scaffolds were pre-incubated in DMEM/F-12 10% FBS (growth medium) and then washed thoroughly with Milli-Q water in sterile conditions before sowing. Experiments were performed in 24-well plates filled with 500 µL culture medium, by seeding 15000 cells per well onto either the scaffolds or control wells coated with gelatin/poly-*L*-lysine.

Cell proliferation assay.

Cell proliferation was measured using the Resazurin reduction assay. The culture medium was replaced by 500 µL of resazurin solution (Resazurin, 15 µg/mL in growth medium; Sigma) and cells were incubated for 4 h in the dark at 37°C, 5% CO_2. 200 µL of the resazurin solution was then removed, twice from each well (technical replicate), and transferred to a 96-well plate. Fluorescence was detected every 5 minutes at 590 nm using a Fluoroscan fluorometer (Ascent).

Cell proliferation was calculated from a calibration curve by linear regression using Microsoft Excel. Cell proliferation was determined as the 72 h/24 h cell quantity ratio.

Cell viability assay.

A commercial kit (CytoTox-ONE™ Homogeneous Membrane Integrity Assay, Promega) based on LDH assay was used to measure the number of non-viable cells in the multi-well plates.

Assay plates were equilibrated to room temperature (~25ºC) and 100 µL of culture medium were transferred to a new 96 well plate. 50 µL of the reaction solution from the kit, containing the detection dye and the catalyst were then added to culture supernatants and fluorescence was measured after 10 minutes in a plate reader (Ascent Fluoroscan, excitation 540 nm, emission 590 nm). Background values from wells without cells were subtracted and average values for the duplicates calculated. Cell death was calculated from a calibration curve by linear regression after 100% cell lysis of known cell quantities. Cell viability was then calculated according to the following equation: Cell viability (%) = (number of live cells) / (number of dead cells + number of living cells) x100.

Results and discussion

Cell viability and proliferation.

Even though carbon based nanofillers, including graphene have been reported to be biocompatible at concentrations up to 3-5% in either PLLA (Vicentini et al., 2018) or other matrices (Cheng et al., 2018) and although graphene concentration in GRAFYLON® is as low as roughly 1%, we tested viability and proliferation of cells cultured onto both GRAFYLON® and corresponding pure PLLA filaments to exclude any negative effect from eventual impurities could impair biocompatibility. **Figure 1A** shows that viability of SH-SY5Y cells at 24 h and 72 h after seeding onto GRAFYLON® and corresponding pure PLLA scaffolds is not significantly different from control. In particular, viability ranges 90%-100% in both proliferative and differentiation conditions. Slightly lower values at day 0 are known to depend on post-detachment stress (Vicentini et al 2018). Once cytotoxicity is excluded, we aimed at checking eventual effects on cell proliferation, because exogenous materials eventually stimulating cell division are potentially tumorigenic. **Figure 1B** shows that proliferation of cells grown on the scaffolds is never faster than control and conversely, they even show lower proliferation rates, in agreement with the overall ability of carbon based, nanocomposite scaffolds to favour differentiation (see introduction for references).

Neuronal commitment of multipotent stem cells.

Recently we could address human circulating multipotent cells (hCMCs) towards neuronal lineage in the absence of any exogenously added neurotrophin or other inducing factor by just seeding these cells onto CNT-PLLA scaffolds (Scapin et al., 2016). In scaffolds used in that work, CNTs were dispersed in PLLA at 0.25% concentration, i.e. lower than 1% graphene in GRAFILON®. On the other hand, graphene is less conductive than CNTs (Vicentini et al., 2018) and show a different nanotopography (planar vs tubular). Therefore, in order to check whether hCMC commitment towards neuronal lineage could be induced by graphene-PLLA as well, hCMCs seeded onto 3D-printed pure PLLA or GRAFILON® scaffolds were compared to control samples. **Figure 2A** shows that, at least morphologically, GRAFILON® seems to be able to induce commitment to neuronal lineage as well. Moreover, cells grown onto pure PLLA were found to resemble the morphology of osteoblasts (figure 2B). Indeed, this latter finding is in agreement with evidence that osteoblasts are one out of the four cell lineages that can be derived from hCMCs (Scapin et al., 2016).

In order to confirm cell lineage commitment by molecular evidence, qPCR experiments were performed using a number of marker genes specific to the neuronal lineage. In particular, we used Nestin, which is expressed in both neural progenitor cells (Dahlstrand et al., 1995) and endothelial precursors (Mokrý et al., 2004); Tubulin β3 (TUBB3), specific to immature and post-mitotic neurons (Tischfield et al., 2010); and Microtubule Associated Protein 2 (MAP2), a late marker involved in the coordinated reorganization of cytoskeleton networks of microtubules and filamentous actin (Dehmelt & Halpain, 2005).

(ongoing experiments..... results to be added once available)

Scaffold patterning and neurites orientation

In order to achieve oriented neuronal differentiation and neurite elongation, a new series of scaffolds was printed alternating pure PLLA and GRAFILON® tracks with roughly 100 μM track width. When seeding and growing hCMC onto these scaffolds, the effect was dramatically evident. Figure 3 shows representative fields for hCMCs seeded in non differentiative conditions onto the scaffolds and observed after three days: when compared to control sample (panel A) cells seeded onto the scaffolds rapidly differentiated into neuronal lineage both on non-patterned GRAFILON® (panels B-C) or on patterned PLLA-GRAFILON® (panels D-E). In particular, even if some cell orientation - likely depending on pattern-like deposition typical for additive printing - is observed also in panels B-C, hCMCs

grown onto the patterned scaffolds showed faster differentiation and very long neurites (hundreds of μM) that are clearly oriented along the pattern tracks (panels D-E).

Concluding remarks

The recent discovery that an autologous population of multipotent stem cells (hCMCs) can be induced towards neuronal lineage and differentiation by self-standing CNT-PLLA scaffolds *per se*, i.e. in the absence of any exogenously added neurotrophin (Scapin et al., 2016), opened the route to encouraging CNS regenerative medicine perspectives. However, electrospun scaffolds did not allow for oriented differentiation and neurite elongation and CNT-PLLA scaffold had to be handmade, with associated batch variation. Graphene-based nanocomposites are emerging as a most promising material for regenerative medicine (see introduction for references) and PLLA has become the most commonly used bio-plastic for 3D-printing by additive manufacturing. We tested GRAFILON®, an already available (as filaments for 3D printers) and cheap graphene-PLLA material and demonstrated that scaffolds printed with this nanocomposite are able as well to induce, without neurotrophin addition, neuronal differentiation of hCMCs. Furthermore, additive manufacturing allowed for patterned printing, which was reliably able to strongly enhance neuronal differentiation (at never-observed-rates) and to provide orientation of neuronal cells and their axons along the designed tracks, opening the perspective for neural circuit design. Last but not least, preliminary evidence needing for further analyses suggested that 3D-printed scaffolds consisting of patterned or non-patterned pure PLLA might be of help in bone regenerative medicine.

Individual contributions

PB and MG performed most of the experiments and wrote the manuscript; YSHG coordinated the cell viability and proliferation assays; RDL supervised work with hCMCs, FF conceived and supervised the project and wrote the manuscript.

Acknowledgements

This work was supported by funding from the Padua University (Project PRAT2015 CPDA151948 to FF; PhD fellowship to YSHG and 'Mille e una lode' fellowship to PB). We thank Marco Fontana for help in some of the experiments, Antonio Berera for useful discussions and Denis Bison for technical support at the microscopy facility.

References

- Badylak SF. Decellularized allogeneic and xenogeneic tissue as a bioscaffold for regenerative medicine: factors that influence the host response. Ann Biomed Eng. 2014 Jul;42(7):1517-27.

- Bayer IS. Thermomechanical Properties of Polylactic Acid-Graphene Composites: A State-of-the-Art Review for Biomedical Applications. Materials (Basel). 2017 Jul 4;10(7).

- Cheng X, Wan Q, Pei X. Graphene Family Materials in Bone Tissue Regeneration: Perspectives and Challenges. Nanoscale Res Lett. 2018 Sep 18;13(1):289.

- Chiulan I, Frone AN, Brandabur C, Panaitescu DM. Recent Advances in 3D Printing of Aliphatic Polyesters. Bioengineering (Basel). 2017 Dec 24;5(1). pii: E2.

- Dahlstrand J, Lardelli M, Lendahl U. Nestin mRNA expression correlates with the central nervous system progenitor cell state in many, but not all, regions of developing central nervous system. Brain Res Dev Brain Res. 1995 Jan 14;84(1):109-29.

- Dehmelt L, Halpain S. The MAP2/Tau family of microtubule-associated proteins. Genome Biol. 2005;6(1):204.

- Dvir T, Timko BP, Kohane DS, Langer R. Nanotechnological strategies for engineering complex tissues. Nat Nanotechnol. 2011 Jan;6(1):13-22

- Edgar L, McNamara K, Wong T, Tamburrini R, Katari R, Orlando G. Heterogeneity of Scaffold Biomaterials in Tissue Engineering. Materials (Basel). 2016 May 3;9(5).

- Fabbro A, Prato M, Ballerini L. Carbon nanotubes in neuroregeneration and repair. Adv Drug Deliv Rev. 2013 Dec;65(15):2034-44.

- Follmann HDM, Naves AF, Araujo RA, Dubovoy V, Huang X, Asefa T, Silva R, Oliveira ON. Hybrid Materials and Nanocomposites as Multifunctional Biomaterials. Curr Pharm Des. 2017;23(26):3794-3813.

- Gardin C, Piattelli A, Zavan B. Graphene in Regenerative Medicine: Focus on Stem Cells and Neuronal Differentiation. Trends Biotechnol. 2016 Jun;34(6):435-437.

- John AA, Subramanian AP, Vellayappan MV, Balaji A, Mohandas H, Jaganathan SK. Carbon nanotubes and graphene as emerging candidates in neuroregeneration and neurodrug delivery. Int J Nanomedicine. 2015 Jul 2;10:4267-77.

- Huang W, Sunami Y, Kimura H, Zhang S. Applications of Nanosheets in Frontier Cellular Research. Nanomaterials (Basel). 2018 Jul 12;8(7). pii: E519.

- Kabiri M, Soleimani M, Shabani I, Futrega K, Ghaemi N, Ahvaz HH, Elahi E, Doran MR. Neural differentiation of mouse embryonic stem cells on conductive nanofiber scaffolds. Biotechnol Lett. 2012 Jul;34(7):1357-65.
- Kenry, Lee WC, Loh KP, Lim CT. When stem cells meet graphene: Opportunities and challenges in regenerative medicine. Biomaterials. 2018 Feb;155:236-250.
- Kobayashi E. Challenges for Production of Human Transplantable Organ Grafts. Cell Med. 2016 Oct 21;9(1-2):9-14.
- Malarkey EB, Parpura V. Carbon nanotubes in neuroscience. Acta Neurochir Suppl. 2010;106:337-41.
- Mokrý J, Cízková D, Filip S, Ehrmann J, Osterreicher J, Kolár Z, English D. Nestin expression by newly formed human blood vessels. Stem Cells Dev. 2004 Dec;13(6):658-64.
- Sampogna G, Guraya SY, Forgione A. Regenerative medicine: Historical roots and potential strategies in modern medicine. J Microsc Ultrastruct. 2015 Jul-Sep;3(3):101-107.
- Santoro M, Shah SR, Walker JL, Mikos AG. Poly(lactic acid) nanofibrous scaffolds for tissue engineering. Adv Drug Deliv Rev. 2016 Dec 15;107:206-212.
- Scapin G, Salice P, Tescari S, Menna E, De Filippis V, Filippini F. Enhanced neuronal cell differentiation combining biomimetic peptides and a carbon nanotube-polymer scaffold. Nanomedicine. 2015 Apr;11(3):621-32.
- Scapin G, Bertalot T, Vicentini N, Gatti T, Tescari S, De Filippis V, Marega C, Menna E, Gasparella M, Parnigotto PP, Di Liddo R, Filippini F. Neuronal commitment of human circulating multipotent cells by carbon nanotube-polymer scaffolds and biomimetic peptides. Nanomedicine (Lond). 2016 Aug;11(15):1929-46.
- Tischfield MA, Baris HN, Wu C, Rudolph G, Van Maldergem L, He W, Chan WM, Andrews C, Demer JL, Robertson RL, Mackey DA, Ruddle JB, Bird TD, Gottlob I, Pieh C, Traboulsi EI, Pomeroy SL, Hunter DG, Soul JS, Newlin A, Sabol LJ, Doherty EJ, de de Uzcátegui CE, de de Uzcátegui N, Collins ML, Sener EC, Wabbels B, Hellebrand H, Meitinger T, de Berardinis T, Magli A, Schiavi C, Pastore-Trossello M, Koc F, Wong AM, Levin AV, Geraghty MT, Descartes M, Flaherty M, Jamieson RV, Møller HU, Meuthen I, Callen DF, Kerwin J, Lindsay S, Meindl A, Gupta ML Jr, Pellman D, Engle EC. Human TUBB3 mutations perturb microtubule dynamics, kinesin interactions, and axon guidance. Cell. 2010 Jan 8;140(1):74-87.

- Vicentini N, Gatti T, Salice P, Scapin G, Marga C, Filippini F, Menna E. Covalent functionalization enables good dispersion and anisotropic orientation of multi-walled carbon nanotubes in a poly(L-lactic acid) electrospun nanofibrous matrix boosting neuronal differentiation. Carbon 2015 Sep; 95:725-30.

Figure with captions

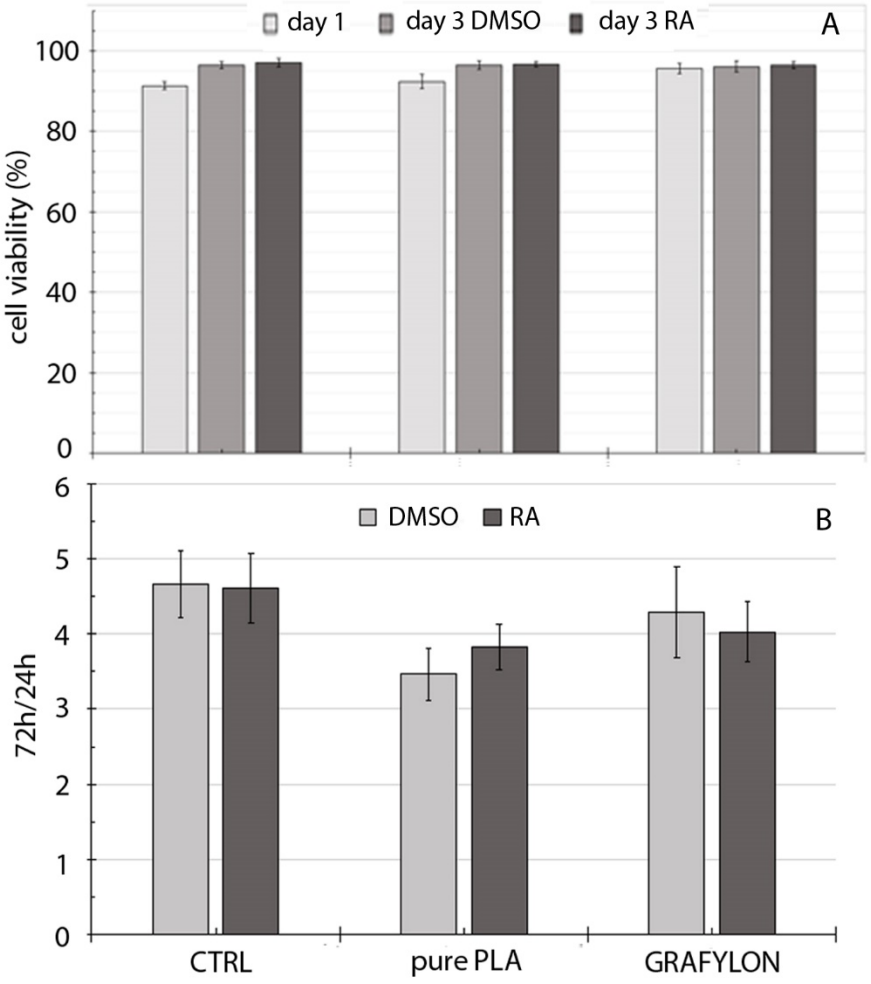

Figure 1. Viability (panel A) and proliferation (panel B) of SH-SY5Y cells grown (proliferative medium with DMSO) or differentiating (RA induced) on the indicated scaffolds or coated control wells. Error bars are reported, and data represent the mean ± SEM of four (A) and two (B) independent experiments performed in duplicate.

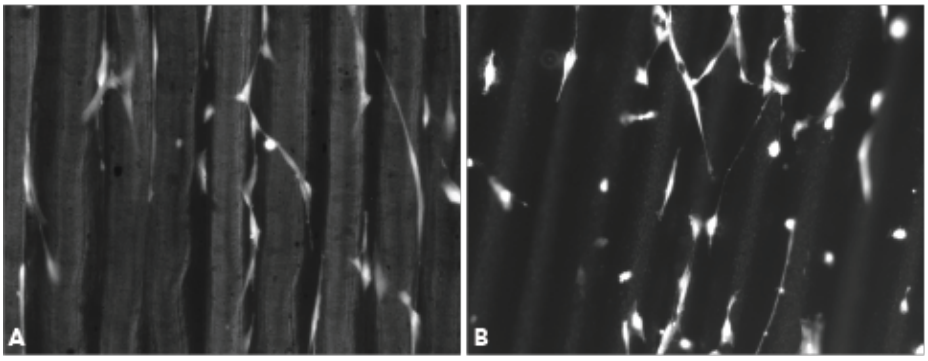

Figure 2. Representative microscopy fields of hCMCs seeded onto 3D-printed GRAFILON® (panel A) and corresponding pure PLA (panel B) scaffolds. Cells were stained with Calcein-AM and images were captured using an Olympus CKX53 inverted fluorescence microscope.

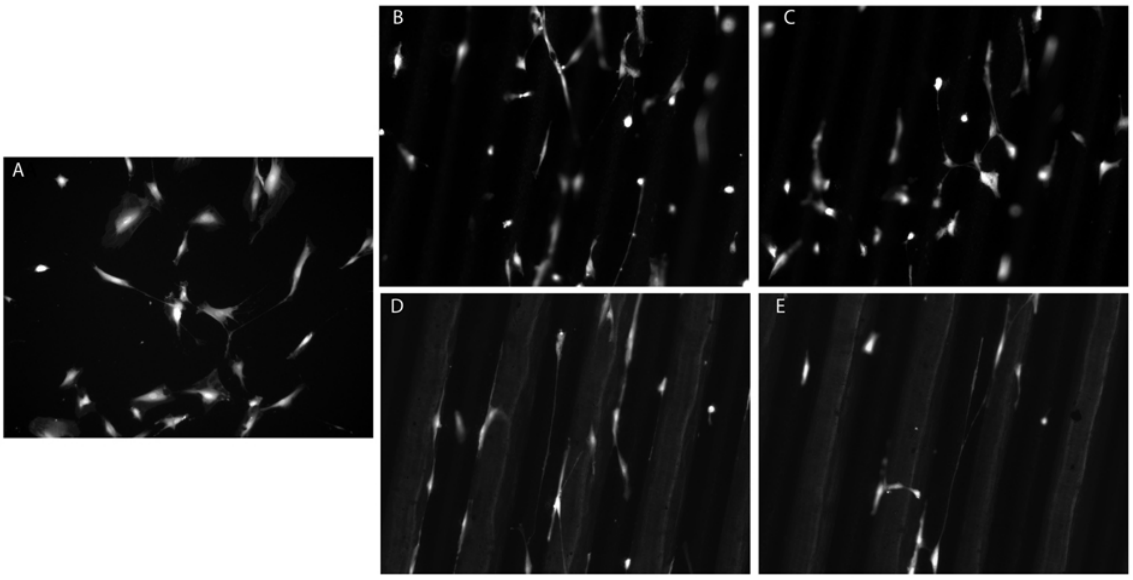

Figure 3. Representative microscopy fields of hCMCs seeded onto control wells (panel A) or 3D-printed scaffolds consisting of non-patterned GRAFILON® (panels B-C) or patterned PLA- GRAFILON® (panels D-E). Cells were stained with Calcein-AM and images were captured using an Olympus CKX53 inverted fluorescence microscope.

3.2 THE BIOMIMETIC PEPTIDES

In the first prototype of our biomimetic nanosystems, two biomimetic peptides were designed using structural bioinformatic analysis and literature and database search, and then they were synthetized using F-moc chemistry. These peptides reproduce motifs from Ig domain of the extracellular domains of the two proteins, both involved in attractive or repulsive signalling that drive neurite guidance and fasciculation and in the modulation of neurite outgrowth, elongation and regeneration. Both peptides proved to be endowed with biomimetic capacity to improve neuronal differentiation of human neuroblastoma SH-SY5Y cells and showed synergistic effect in combination with both the CNT-PLLA scaffold (Scapin et al., 2015) and electrospun CNT-PLLA fibers (Vicentini et al., 2015). Moreover, they were used to induce neuronal differentiation of human CMCs (Scapin and Bertalot et al., 2017). Using the same design-strategy, we have developed a number of new peptides from proteins playing important role in neuronal differentiation and elongation. Such peptides have been derived from the Ig-like domain of specific neural CAM and ECM proteins: CHL1, Neurofascin, NrCAM, DCC, ROBO2 and 3, Contactin 1, 2 and 5. Interestingly, all of them have Ig-like extracellular repeats in their extracellular domains by which mediate their homo and/or heterophilic binding suggesting a conservation in their sequences.

Since we wanted to shed light on the mechanism by which our peptides act, we studied L1-A peptide in comparison to L1CAM protein it is derived from. We used the recombinant L1CAM ectodomain as a positive control reproducing the natural homo/heterophilic binding by which L1CAM regulates neuronal differentiation. As a negative control, we used a scrambled version of the L1-A peptide to distinguish between composition or sequence-dependent effect. In addition, we created two mutants of the L1-A peptide to check the essential role played by arginine 184 in the peptide sequence. The first mutant, R184Q, reproduces a natural point mutation of L1CAM protein leading to the CRASH syndrome. The second mutant, R184A, is an artificial mutation already characterized by Zhao as causing loss of L1-A binding properties.

The results are reported in the following paper in preparation.

A conserved Neurite Outgrowth and Guidance motif with biomimetic potential shared by neuronal Cell Adhesion Molecules.

Yuriko Suemi Hernandez Gomez[1]*, Giorgia Scapin[1]*, Laura Acquasaliente[2], Daniele Peterle[2], Simone Tescari[2], Elena Porcellato[2], Irene Righetto[1], Alberto Piovesan[1,2], Matteo Gasparotto[1], Valeria Rossi[1], Giulia Pontarollo[2], Tommaso De Re[1], Vincenzo De Filippis[2§], Francesco Filippini[1§]

Department of [1] Biology, and [2] Pharmaceutical and Pharmacological Sciences, University of Padua, Italy.

* Equal contributions; § Corresponding authors

Abstract

In addition to intrinsic programming, a complex network of tissue environmental stimuli mediated by cell-cell and cell-extracellular matrix interactions via homo- and heterophilic binding of extracellular protein domains regulates neuronal differentiation, neurite growth, elongation, and connections. Such guidance cues also play crucial roles in neural damage repair and their dysfunction may result in severe neural disorders. We report here the identification and characterization of a conserved binding motif shared among the extracellular domains of a number of neuronal CAMs, Cell Adhesion Molecule family proteins involved in the regulation of Neurite Outgrowth and Guidance, and regeneration. Synthetic peptides derived from the NOG motif of such CAMs proved biomimetic potential in boosting neuritogenesis and neuronal differentiation. In silico simulations suggested a molecular rationale for their action, then confirmed by in vitro characterization and comparison of natural NOG sequences vs mutant and scrambled peptides, as well as by experiments in combination with a whole ectodomain and transfected SH-SY5Y cells. This work opens the route to further investigation on the role played by the conserved NOG motif in neural functions and to design and use of a novel class of biomimetics in regenerative medicine and therapeutical strategies.

Keywords: neurite growth, axon guidance, nerve injury, axon regeneration, conserved protein motif, homophilic binding, immunoglobulin fold, biomimetic peptides; regenerative medicine; neuronal differentiation.

Introduction

Human and mammalian organisms consist of a very complex and highly coordinated network of tissues and organs having developed starting by a single zygote. Such an extraordinary programme is not challenged only by 'intrinsic instructions' provided by genetic and epigenetic information. Indeed, differentiation towards each specific cell lineage is strongly influenced by ‘extrinsic instructions’ such as tissue environmental signals - sensed by cells and their processes - that are capable to modulate cell differentiation, shaping, migration, and the overall developmental programme. Signals from the tissue environment depend on both nanotopographical features (e.g. local shape, roughness, stiffness, conductivity etc.) and molecular cues, of which some are mediated by gradients of ions, hormones etc. while others are biomolecular signals, such as active binding motifs from the protein or sugar moieties exposed at the cell surfaces or present as soluble factors in the extracellular matrix (ECM) (Dalby et al., 2014; Atmanli & Domian, 2017).

The formation of neural circuits in the central (CNS) and peripheral (PNS) nervous system requires that a correct connectivity is established between neurons during development. To this aim, neural precursors need to migrate and appropriately position their cell bodies for projecting their axons to synaptic targets, and failure to achieve correct connectivity results in a dysfunctional nervous system. Every neural circuit is represented by the structure of axons and dendrites, with individual axons stimulating multiple targets, and single dendrites assimilating inputs from various sources. During nervous system development, neurons extend axons to find their final destination in a complex and changing environment and establish a functional synaptic network. Each axon is tipped with the growth cone; such a specialized structure shows highly dynamic behaviour and responsiveness to multiple sources of spatial information and it is hence able to guide the axon itself toward right targets with an impressive level of accuracy (McFarlane, 2000). The growth cone travels on a road made up of guidance cues (Tamariz and Varela-Echavarrìa, 2015), which either are protruding from the extracellular domain (ED) of transmembrane proteins from the cell adhesion molecule (CAM) families, presented on a neighbouring cell surface, or are assembled into a dense ECM including multiple ECM proteins such as e.g. laminin and fibronectin (Halper et al, 2014; Seiradake et al, 2016). These molecules provide defined 'roadway' surfaces to which growth cone receptors can adhere, but they also activate intracellular signalling pathways utilized by the growth cone guidance machinery (Lemons et al., 2013). Additionally, anti-adhesive surface-bound motifs from other protein EDs can

prohibit growth cone advance thus providing 'guardrails' that determine roadway boundaries. Finally, diffusible chemotropic cues represent the 'road signs' that present further steering instructions to the travelling growth cone (Baker et al, 2006). Secretion of extracellular signalling motifs can result from the production of alternative splice variants consisting of ED alone (e.g. Treutlein et al., 2014) and/or from proteolytic cleavage of the ED close to the membrane by ECM proteases (Montes de Oca-B, 2010). It is now clear that the response of attraction versus repulsion is not due to the intrinsic property of the cue, but rather to the specific receptors engaged and the internal signalling milieu of the growth cone (Lowery & Van Vactor, 2009).

CAMs from the immunoglobulin family play a fundamental role in cell-cell and cell-ECM interactions in both mature and developing nervous system, as well as in axonal regeneration and neural repair (Zhang et al., 2008). These proteins are prototyped by L1 CAM family proteins, which show a large ED consisting of even more than 1000 amino acids and are endowed at the N-terminus with six repeats having immunoglobulin fold (shortly named Ig domains), followed by a variable number of fibronectin type III regions (shortly, FnIII repeats). The homo/heterophilic ED-ED binding is prototyped for L1 CAM family proteins (and in general, for CAMs with Ig repeats based ED) by the homodimer structure of Neurofascin, in which Ig1 to Ig4 domains of each monomer form a horseshoe structure and the two Ig2 domains bind each other (Liu et al., 2011). A motif involved in homophilic binding of L1CAM was identified using synthetic peptides in competition experiments; in particular, peptide L1-A was able to inhibit binding and thus was suggested to correspond (or to be part of) the binding region (Zhao et al., 1998). L1-A sequence is part of L1CAM Ig2, and its involvement in the binding region was then confirmed by structural evidence from the Neurofascin homodimer (Liu et al., 2011). Given that in 1998 such structure was not available yet, Zhao and coworkers designed L1-A sequence around the arginine residue (R184) of L1 CAM Ig2, which when mutated to glutamine (R184Q) is causative for a severe neurodevelopmental spectrum disorder named the CRASH syndrome (Yamasaki et al., 1997). Based on the established role of L1 CAM as a positive regulator of neuronal differentiation, neuritogenesis and axon regeneration (Maness et al, 2007), we recently used L1-A as a possible tool, in combination with nanocomposite scaffolds, for neural regenerative medicine, and it reliably proved to act as biomimetic signals boosting neuronal differentiation of SH-SY5Y cells (Scapin et al., 2015). The combination scaffold-biomimetic peptides also showed ability to favour the differentiation of

human circulating multipotent cells (hCMCs) towards the neuronal lineage and in particular to influence the expression of neuronal markers such as Nestin, TUBβ3, MAP2 and Synaptophysin (a synaptic vesicle marker related to neuron maturation) (Scapin et al., 2016).

Evidence that the L1-A peptide region is part of a conserved Ig fold shared among several CAMs prompted us to perform work presented in this paper. Taking advantage from sequence and structural bioinformatic analyses, we could identify the NOG motif and based on it we developed novel peptides, both 'natural' (i.e. derived in sequence from corresponding EDs) and 'recombinant' (sequence chimeras), which all confirmed the suggested biomimetic potential of the conserved motif. Indeed, we also provided a model for the biomimetic mechanism of action of peptides reproducing the NOG motif by comparison of a model, recombinant whole ectodomain (L1CAM ED), the synthetic peptide reproducing its natural NOG motif and related scramble and mutant peptides. This work opens the route to both further basic research on NOG and other conserved binding motifs in neural and tissue differentiation, and to biotechnological and biomedical development of novel biomimetic tools for tissue analysis, engineering and regeneration.

Materials and methods

Bioinformatics

Sequence-based analyses. Homology searches were carried out using blastp application (Altschul et al., 1997) with default settings and L1CAM Ig2 or L1CAM family proteins Ig sequence queries for defining an initial dataset for multiple alignments. Then, regular expressions for positions centred around the peptide regions were inferred and merged to derive a single pattern, written in PROSITE syntax (Sigrist et al., 2010). Pattern refinement was performed by iterative scanning with ScanProsite (de Castro et al., 2006) of Chordata and Mammalia proteome sections of the UniProtKB database (Boutet et al., 2016), excluding splice isoforms and protein fragments. Pairwise sequence comparison by global William Pearson's alignment for sequences corresponding to the different Ig regions that were superimposed (see section below) was performed at the Lalign server (https://embnet.vital-it.ch/software/LALIGN_form.html) with default settings, except for matrix set to BLOSUM62. The Lalign program implements the algorithm of Huang and Miller (1991).

Structural bioinformatics. The following structures from the Protein Data Bank (PDB) were used as templates for modeling: 3P3Y (Neurofascin), 2OM5 (CNTN2), 2V9T (ROBO1). Structural superpositions and Root Mean Square Deviation (RMSD) evaluation were performed and viewed using UCSF Chimera (Pettersen et al., 2004; Huang et al., 2014) v. 1.8.1 (free download from http://www.cgl.ucsf.edu/chimera/). Models of L1CAM, CHL1, NrCAM, CNTN1, CNTN3, CNTN4, CNTN5, CNTN6 and DCC/NetrinR were obtained via SWISSMODEL (Biasini *et al.*, 2014). Then, modeled structures were refined using SCWRL (Canutescu *et al*., 2003; Wang et al., 2008). Model quality was checked via QMEAN server (Benkert *et al*., 2011). Docking of synthetic peptides to their targets was simulated using PepDock at GalaxyWeb server (Lee *et al*., 2015). Docking results were then refined using GalaxyRefineComplex (Heo *et al*., 2016) at GalaxyWeb server. Prior to performing docking runs, targets were submitted to UCSF Chimera Dockprep routine. Interactions between biomimetic peptides and their targets were evaluated using UCSF Chimera. Isopotential contours were calculated using UCSF Chimera through Opal web server connected to the Adaptive Poisson-Boltzmann Solver (APBS) server (http://www.poissonboltzmann.org). Isopotential contours were then plotted at $\pm 1 k_B T/e$. PDB2PQR (Dolinsky et al., 2007) was used to assign partial charges and van der Waals radii according to the PARSE force field (Sitkoff *et al*., 1994). Interior $\varepsilon_p = 2$ and $\varepsilon_s = 78.5$ were chosen for respectively the protein and the solvent, T = 298.15K. Probe radius for dielectric surface and ion accessibility surface were set to be r = 1.4 Å and r = 2.0 Å, respectively. The electrostatic distance was calculated using the Hodgkin and Carbo indexes (Good, 1992) at the WebPIPSA (Richter et al., 2008) server (http://pipsa.eml.org/pipsa).

Biochemistry and biophysics

Peptide synthesis. Peptides were synthesized by the solid-phase method using the flurenylmethyloxycabonyl(Fmoc)-chemistry (Atherton et al., 1989) on a model PS3 automated synthesizer from Protein Technologies International (Tucson, AZ, USA). The peptides were assembled stepwise on a Wang Resin (Novabiochem, Switzerland) derivatized with the desired corresponding C-terminal amino acid. Tert-butyl side-chain protecting group was used for Tyr, Asp, Glu, Ser, and Thr; tert-butyloxycarbonyl for Lys; trityl for His, Gln and Asn; and 2,2,4,6,7-pentamethyldihydrobenzofuran-5-sulfonyl group was used for Arg. Removal of N^a-Fmoc-protecting groups was achieved by treatment for 20 minutes at room temperature with deprotection solution (20% piperidine in N-

methylpirrolidone - NMP). Standard coupling reactions were performed with an equal molar ratio of 2-(1H-benzotriazol-1-yl)-1,1,3,3-tetramethyluronium hexafluorophosphate (HBTU) and 1H-hydroxy-benzotriazole (HOBt) as activating agents, with a fourfold molar excess of N^{α}-Fmoc-protected amino acids in activation solution (0.35 M diisopropylethylamine in dymethylformamide - DMF). Both deprotection and activation solution were freshly prepared to overcome collateral reaction caused by ammine degradation. The anhydrous solvent is strictly required in order to improve production yields. For double couplings at peptide bonds, the stronger activator 2-(7-aza-1H-benzotriazol-1-yl)-1,1,3,3-tetramethyluronium hexafluorophosphate was used (HATU). Once peptide assembly was completed, the side chain-protected peptidyl resin was treated for 90 min at room temperature with the following mixture: 92.5% TFA, 2.5% H_2O, 2.5% ethandithiol, 2.5% triisopropylsilane. The resin was removed by filtration, and the acidic solution, containing the unprotected peptide, was precipitated with ice-cold tertbutyl-methylether and then lyophilized.

Peptide purification and quantitation. The crude peptides were purified to homogeneity (>98%) by semi-preparative RP-HPLC (Jasco HPLC Pu-1575 equipped with 1575 UV-Vis detector) on a Grace-Vydac (Hesperia, CA, USA) C18 column (4.6 x 150 mm, 5mm particle size, 300 Å) equilibrated with 0.1% (v/v) aqueous TFA and eluted with a linear 0.078% (w/w) TFA-acetonitrile gradient at a flow rate of 0.8 ml/min. Absorbance was monitored at 226 nm. Sequences and details about peptides and proteins they are derived from are reported in Table P.

Purified peptides were analyzed by mass spectrometry on a Mariner ESI-TOF instrument from PerSeptive Biosystems (Stafford, TX, USA), which yielded mass values in agreement with the theoretical mass within 20 ppm accuracy. Concentration of peptides with aromatic residues (CHL1-A and CNTN peptides, all containing at least one Phe or Tyr residue) was determined spectrophotometrically on a Jasco (Tokyo, Japan) V-630 spectrophotometer supplied with a Peltier system PAC-743 (Jasco Corporation, Tokyo, Japan) by measuring the absorbance at 257 nm, using a molar absorptivity of 200 $M^{-1}\cdot cm^{-1}$, as calculated from the presence of a Phe-residue. In the absence of any suitable chromophore, the concentration was determined by analytic scaling (E/50 Gibertini, Novate Milanese, Italy). Peptides were dissolved in a PBS solution (5mg/ml) and stored at -80°C before using.

Peptide characterization. Peptide secondary structures were analyzed by circular dichroism (CD). CD spectra in the far-UV region were recorded on a Jasco J-810 spectropolarimeter,

equipped with a thermostatted cell holder and a Peltier PTC-423S temperature control system. The spectra were recorded at 25°C at a peptide concentration of 0.1mg/ml in 10mM phosphate buffer, pH 7.4, NaCl 0.15M (PBS) using a 0.1-cm pathlength cuvette. Each spectrum resulted from the average of four accumulations after baseline subtraction. CD signal was expressed as the mean residue ellipticity:

$[\theta] = q \cdot MRW/10 \cdot l \cdot c$ ($deg \cdot cm^2 \cdot dmol^{-1}$)

where q is the observed ellipticity in deg, MRW is the mean residue weight, l is the path length in cm and c is the peptide concentration in g/ml.

Peptide stability assays. For peptide stability assays, each peptide was added at 20 M final concentration in 600 µl of differentiation medium (see in Molecular and Cellular biology section for composition). At each time point, 500 µl of medium was withdrawn and high MW molecules from FBS or secreted by cells were eliminated by ultrafiltration at 10000xg on Vivaspin 10 kDa cutoff filters (Sartorius). 350 µl of the ultrafiltrated medium was immediately frozen at -20°C for the RP-HPLC analysis. RP-HPLC runs were performed by loading 300 µl of the sample acidified to 0.1% H2O/TFA onto a Zorbax 300SB-C18 column (Agilent) using a linear acetonitrile/0.078% TFA gradient from 5 to 34% in 30 min at of 0.8 ml/min flow rate. Peptide concentration at each time point was inferred from its peak area, normalized vs a reference peak showing constant area during the whole experiment. Then, residual concentration was calculated as time *n*: time 0 ratio.

Surface Plasmon Resonance (SPR) experiments. Binding affinity was carried out using a multi-cycle injection strategy on a dual flow cell Biacore-X100 instrument (GE-Healthcare, Piscataway, NJ, USA). Purified L1CAM ED (Thermofisher Scientific) (5 µg/ml) was immobilized (3300 RU) at pH 4.0 on a carboxymethylated-dextran chip (CM5) using the amine coupling chemistry and increasing concentrations of L1CAM ED solutions were injected in the mobile phase. Titration was performed at 25°C in 10 mM Hepes, pH 7.5, 150 mM NaCl, 3 mM EDTA, 0.05% polyoxyethylene sorbitan (HBS-EP^+), at a flow rate of 10 ml/min. Each binding curve was subtracted for the corresponding baseline, accounting for nonspecific binding (<2% of RU_{max}). The dissociation constant (K_d) of homophilic interaction was obtained as a fitting parameter by plotting the value of the response units at the steady state (RU_{max}) for each concentration of the analyte (i.e., L1CAM ED). Data analysis was

performed by BIAevalution software and OriginPro 2015, using the following equation, describing the one-site binding model:

$$RU_{eq} = RU_{max} \cdot \frac{[analyte]_F}{[analyte]_F + K_d}$$

where RU_{max} is the RU value at saturating analyte concentrations and $[analyte]_F$ is the concentration of the free analyte in equilibrium with the analyte-ligand complex present on the sensor chip surface. Solution competition assay was carried out by incubating constant concentration of L1CAM ED (300 nM) with increasing concentrations of peptides up to 10 μM for 30 min, and then injection over the sensor chip. All measurements were done at the flow rate of 10 ml/min, at 25°C using HBS-EP$^+$ as running buffer. The SPR signal was taken at the end of the association phase and plotted against the logarithm of each peptide concentration. EC50 values (half-maximal effective concentration) were calculated from sigmoidal dose-response curves with OriginPro2015 software.

SH-SY5Y culture and differentiation. Exponential growing human neuroblastoma cell line SH-SY5Y (Ross et al., 1983), were cultured with Dulbecco's Modified Eagle Medium/Nutrient Mixture F-12 (DMEM/F-12) GlutaMAX™ supplement (Invitrogen) supplemented with 10% heat-inactivated foetal bovine serum (FBS, Euroclone) and 25μg/ml of gentamicin (Sigma) (growth medium), in a humidified atmosphere of 5% of CO_2 in air at 37 °C. Cells were maintained in cultures by subculturing 900000 into 25 cm² flasks (Sarstedt) every 2 days (once they reached 90% confluence). Cell differentiation was induced by treating cells with all-*trans*-retinoic acid (RA, Sigma) at 10 mM concentration and lowering the FBS in the culture medium to 2% (differentiation medium) 24h after seeding. In undifferentiated control samples, Dimethyl sulfoxide (DMSO) was added as the equivalent amount (in which RA is dissolved). In experiments with peptides added to culture medium, cells were seeded in a 24-well plate (15000 cells/well) coated with a gelatine (Sigma)/poly-L-lysine (Invitrogen) solution. Poly-L-lysine is widely used as a good substrate for neural cell adhesion and growth. 24h after cell seeding (day 0), the growth medium was replaced by the differentiation medium; then, 24h after RA induction (day 1) peptides were added to the culture medium, except for control samples. Cell viability and proliferation were assessed at reported time points, while neurite numbers and lengths were measured 24h after the peptides addition.

Transfection of SH-SY5Y cells. SH-SY5Y cells in growth and differentiating conditions were transfected using Lipofectamine 2000 (Invitrogen) following manufacturer protocol. In particular, 3.5 x 10^4 cells were transfected with 0.5 µg DNA and 0.75 µl Lipofectamine. The wild type coding sequence of human, neuronal L1CAM (from cDNA received as a kind gift from Prof. Jacopo Meldolesi), fused to a C-terminal EGFP tag by cloning in a slightly modified version of plasmid pEGFP-N1 (Clontech) was used for transfections. The same plasmid expressing EGFP alone was used as control for transfection effect.

Cell proliferation test. Resazurin reduction assay was performed to quantify metabolically active living cells and thus to monitor the effects of peptides and scaffolds on cell proliferation. The assay is based on the reduction of the indicator dye, resazurin (not fluorescent) to the highly fluorescent resorufin (Ex. 569 nm, Em. 590 nm) by viable cells. Non-viable cells rapidly lose their capacity to reduce resazurin and, thus, to emit fluorescent signals anymore. Briefly, the culture medium was replaced by 500 µL of resazurin solution (Resazurin Sigma 15 µg/mL in growth medium without phenol red) and cells were incubated for 4 h in the dark at 37°C, 5% CO2. Then, 200 µL of resazurin solution was removed twice from each well and transfer to a 96 well plate (technical duplicates). Fluorescence, directly correlated with cell quantity, was detected using a plate reader (Ascent Fluoroscan, excitation 540 nm, emission 590 nm). Background values from blank samples were subtracted and average values for the duplicates calculated. Cell proliferation was calculated from a calibration curve by linear regression using Microsoft Excel.

Statistical analysis

Statistical analysis was performed using paired Student's t-test, and results were considered significant when $p < 0.05$.

Results and discussion

Identification of a Neurite Outgrowth and Guidance (NOG) motif

The entire sequences of L1 CAM Ig2 and of the Ig2 repeats from the other three L1 CAM family proteins CHL1, NrCAM and Neurofascin were used as blastp queries to retrieve a dataset of homologous sequences from animals. In addition to L1 CAM family proteins, further homologous sequences from other CAM proteins were retrieved. Then, a multiple alignment including such sequences was transformed into a regular expression (pattern)

written in PROSITE syntax (http:www.prosite.org). The first pattern - originally centered around the 14 aa peptide region - was then extended N-terminally to include two conserved positions for improving the scanning specificity (i.e., pattern precision) and C-terminally to include 5 aa for completing the 19 aa β-hairpin region of the Ig domain. The first cycles of proteome scannings via ScanProsite (see methods) of the UniProtKB animal proteomes with preliminary patterns, intriguingly retrieved - in addition to CAMs from L1 family - a large number of neuronal CAMs involved as well in neuritogenesis and axon guidance, such as e.g. Contactins and Roundabout receptors. Only a few false positives from invertebrates were found. After iteration of a few further tuning and scanning cycles to improve pattern precision (i.e. to cut off false positives) and recall, a regular expression (written as a pattern in PROSITE synthax) could be defined: [FILVY]-x-W-x(6,8)-[FHIKLPRST]-{CHMNWY}(2)-{CFHVWY}-[DEGINRSTV]-[DEGAKLS]-R-{CDENPQW}-[EFINSTVY]-[AIKLMQTV]-[ADFGKLMRS]-{CEFIMWY}-[DEGNKST]-[GKNST]-[DFGILNTYA]-[LIMN]-[YEFMTILQ]-[FVIGSY]-[HAINST]. This pattern retrieved from the Vertebrata section of UniProtKB release 2018_05 (SwissProt+TrEMBL, excluding sequence fragments and splice variants) > 2000 proteins involved in Neurite Outgrowth and Guidance, hence suggesting to name the newly identified conserved pattern as 'NOG motif'. The NOG motif is shared at the Ig2 domain of a high number of neuronal CAMs, including orthologues for the four members of the L1 family (L1 CAM, Close Homolog of L1 or CHL1, Ng-related CAM or NrCAM/Bravo, and Neurofascin or NFASC), all six Contactins (CNTN1 to CNTN6), Roundabout receptors (ROBO1, 2 and 3) and Deleted in Colon Cancer (DCC)/Netrin receptor (see figure FF-TDR 1, in which the ED architecture of human NOG-positive proteins is shown).

Structural and sequence comparison among Ig domains from NOG positive CAM proteins

Given the special role played in homo- and heterophilic binding by neuronal CAMs Ig2 (Liu et al., 2011), we further analyzed NOG-positive CAM Ig2 domains in terms of structural conservation. Figure FF-TDR 1 shows that solved structures are available in Protein Data Bank for at least one representative member from each family of NOG proteins: all depicted proteins but one is from *Homo sapiens*. For DCC/Netrin receptor, the rat protein structure was included as the closest available homologue rather than including a structural model of the human protein, as this would impair the RMSD comparison. The presence of four to six Ig repeats in each CAM ED allows for comparing intra-molecular conservation (i.e., among Ig repeats from the same ED) and inter-molecular conservation (Ig domains from different

proteins). Therefore, pdb structures of each NOG positive CAM Ig were superposed to compare Root Mean Square Deviation (RMSD, considering C-alpha atoms), which is increased by structural distance (closest structures show the lowest RMSDs). Furthermore, corresponding sequences were compared in terms of % identity by global alignment method (common standard, instead of local alignment, when performing structural studies) using the Lalign software (see methods).

Table IR-FF 1 shows that in general, each Ig from any CAM is closer to the same Ig type from other proteins, than to other Igs from the same protein. For instance, when Neurofascin Ig2 is superposed to any Ig2 domain from another CAM, RMSD value fall in the 1.5 Å to 3.9 Å range (average: 2.93 Å). Instead, when such Ig2 is superposed to the other Neurofascin Igs (Ig1 or Ig3 or Ig4), higher values (even > 8 Å) are found. This kind of structural conservation is observed with all four Ig types, as shown by average values in table IR-FF 1. Indeed, Ig4 shows the highest structural conservation (average RMSD for Ig4-Ig4 superposition: 1.90 Å), followed by Ig3 (Ig3-Ig3 value: 2.58 Å) and Ig2 (Ig2-Ig2 value: 2.93 Å). The Ig1 structure is seemingly less conserved (Ig1-Ig1 value: 4.15 Å). Anyway, all these values are better than those observed when considering the average RMSD for intra-protein comparison. Structural conservation of each Ig is higher than corresponding sequence conservation, i.e. when sequences associated to the pdb structures are compared via pairwise global alignment, the difference in % identity values is not so evident. In practice, even though the overall Ig fold is conserved, each Ig (1 to 4) from NOG proteins shows a peculiar structural conservation likely to mediate specific intra- and inter-molecular interactions. Of course, peculiar individual Ig structures are needed to mediate specific binding of Ig1 to Ig4 and Ig2 to Ig3 for horseshoe formation; however, evidence that the average conservation of each Ig is different from that of the partner Ig suggests that a role is played also by Ig-specific intermolecular interactions, of which one is mediated by the NOG motif.

Synthesis and biochemical characterization of a set of novel NOG and related peptides

In order to confirm bioinformatic suggestions by functional evidence, we reproduced as synthetic peptides a number of binding motifs from Ig2 domains of NOG proteins shown in figure FF-TDR. Synthesis, purification and characterization of L1-A and related peptides were previously reported (Scapin et al., 2015). Solid-phase Fmoc-chemistry synthesis and purification of nine, newly designed peptides were carried out as reported in the specific

Methods sub-section. Conformation of the synthetic peptides in solution is essentially disordered, as documented by far-UV CD spectra (in supplementary Figure EL1). In particular, positive band at 210 nm (typical of a n -> π transition) and negative one at 198 nm (due to π-> π* transition) are typical for an unfolded polypeptide chain, in accordance with natural topology (all peptides being part of flexible loops in Ig domains they are derived from).

We tested peptides resistance to degradation by eventual proteolytic cleavage in the media used in our experimental conditions. In preliminary experiments, L1-A was added at 20 μM concentration to the differentiation medium including 2% FBS; then, high MW molecules were eliminated by ultrafiltration (see methods) and RP-HPLC runs confirmed the peptide peak can be reliably identified (not shown). One peptide representative of each family (wherein sequence variation is low) was then used in degradation tests with cells: L1-A (L1 family), CNTN5-A (contactin family), ROBO2-A (Roundabout receptors) and DCC. In addition, L1-A_scr was tested as the negative control missing NOG potential (Scapin et al., 2015). In our experiments, differentiation medium is refreshed (and peptides are added at 1 μM optimal concentration) every two days. Therefore, ultrafiltrated media were analyzed at the 0, 8, 24 and 48 hours time points. At the refresh time, 0.5-0.7 μM of residual peptide was found (Figure AP 1), which is almost as effective as the optimal one (Scapin et al., 2015).

Biomimetic potential of synthetic NOG peptides

The capacity to boost neuronal differentiation was reported for synthetic peptide L1-A and related scrambled control peptide (Scapin et al, 2015 & 2016) and thus we included these two peptides in experiments with the newly synthesized ones, as positive (and negative) control peptides and for comparison. Moreover, experiments were performed according to our previous investigations, i.e. by evaluating the effect on human neuroblastoma derived SH-SY5Y cells, in terms of: (i) total neurite length / number of cells; (ii) neurites / cells and (iii) neurites longer than 100 m. Incremental values with respect to the untreated control (RA-, peptide- = 100%) are reported in Figure GS 1-n. It can be noticed that all nine new NOG peptides confirm their predicted capacity to boost neuronal differentiation, as their incremental effects are comparable to those mediated by the already confirmed, biomimetic L1-A peptide. Figure GS 2 shows representative microscopy fields of SH-SY5Y cells treated with the twelve peptides and stained with Calcein-AM, in proliferative (RA-, upper panel)

and differentiative (RA+, lower panel) conditions. As reported for L1-A (Scapin et al., 2015), also the new NOG peptides do not affect cell proliferation (supplementary Figure GS S1-n). It can be noticed that, in the absence of RA, peptides derived from the ROBO family proteins show the highest values.

Positions 7 and 2 of peptides seem to play a crucial role in binding and NOG potential

The original characterization of synthetic peptide L1-A as the homophilic binding site in the Ig2 domain of L1CAM could explain its capacity to boost neuritogenesis (Zhao et al., 1998). Once novel NOG peptides have confirmed their biomimetic potential, we tried to address some questions, i.e. (i) how do NOG peptides interact with the proteins they are derived from, which are the roles played by (ii) the 100% conserved, central Arg residue in the NOG pattern and (iii) other parts of the sequence. In order to get functional predictions for next wet lab experiments, we performed docking simulations, using a solved structure as protein target (to obtain reliable predictions) and a number of biomimetic, mutant and scrambled peptide binders. Docking simulations and post-simulation refinement were performed using PepDock (Lee *et al*., 2015) and GalaxyRefineComplex (Heo *et al*., 2016) at the GalaxyWeb server (see methods). For L1 family proteins, the Ig1-Ig4 horseshoe of human Neurofascin (PDB accession 3P3Y) was used as the target structure, because the structures for L1-CAM, NrCAM and CHL1 are not available yet. However, homology modelling and superposition analyses (not shown) confirmed a strong structural conservation within this family, according to observed heterophilic interactions of its members (Conacci-Sorrell et al., 2005; Schmid & Maness, 2008; McEwen et al., 2009). Four biomimetic peptides derived from L1 family CAMs (L1-A, NFASC-A, NrCAM-A and CHL1-A) were used as horseshoe binders, together with L1-A related peptides L1-A_scr, L1-A_R184A and L1-A_R184Q (see Table P for sequences and details). As expected, all four biomimetic peptides were predicted to bind Ig2 in the docking simulations (Figure IR 1). Docking results were evaluated in deeper details for peptide-target interactions via UCSF Chimera and the analysis of peptide-horseshoe interactions suggested a special role for the conserved, central Arg residue (position 7 of the NOG motif) and the hydrophobic residue at position 2. In particular, all four Arg residues from the L1 family peptides are predicted to bind His and Phe residues in Ig2 and hydrophobic residues at position 2 also bind to Ig2 (Figure IR 1). Instead, when performing docking simulations with L1-A_R184A mutant peptide (missing functional binding capacity: Zhao et al., 1998), binding contacts to Ig2 are lost and this

peptide shifts towards Ig1; a similar shift is observed with peptide L1-A_scr (Figure IR 1). Peptide L1-A_R184Q (reproducing a mutation observed in the CRASH syndrome) keeps docking to Ig2; however, its Gln residues mediates an altered binding pattern (Figure IR 1). Therefore, based on docking simulations, both Arg to Ala/Gln mutant peptides are predicted to have reduced or null neuritogenic potential in functional assays. It is noteworthy that even though L1-A_scr peptide lacks any neuritogenic potential (Scapin et al., 2015 and 2016), its sequence (designed prior to this work) has kept the central Arg along a randomised sequence. This demonstrates that the conserved central Arg is not sufficient alone for the neuritogenic potential, and other NOG pattern positions are also important.

In order to experimentally validate the inferred relevance of the conserved Arg residue, we compared the neuritogenic capacity of the newly synthesized Arg to Ala/Gln mutant peptides to that of L1-A and L1-A_scr, representing positive and negative control, respectively (Scapin et al., 2015). Both L1-A_R184A and L1-A_R184Q loose the neuritogenic potential of wild-type L1-A, showing values comparable to those of L1-A_scr and control without peptides, even if the effect of the Arg to Gln mutation is less severe than Arg to Ala (Figures GS 3 and GS 4).

Comparison of L1CAM ectodomain and L1-A peptide neuritogenic potential

L1-A was originally suggested to mediate neuritogenesis by mimicking the homophilic binding of the L1CAM extracellular domain (L1CAM_ED) (Zhao et al., 1998). In order to confirm such relationship in our system, we compared the effect of purified L1CAM_ED (see methods) to that of L1-A in experiments with SH-SY5Y cells (RA-induced to maximize the neuritogenic effect). Considering that often whole proteins or their domains are more efficient (at very low concentrations) than mimetic motifs or drugs, the dose-response curve with L1CAM_ED started by femtomolar concentrations. Indeed, meaningful neuritogenic effect by L1CAM_ED was observed since the picomolar range, reaching a plateau at 1nM concentration (Figure YSHG 1-n). Intriguingly, such a plateau with L1CAM_ED corresponds to the peak effect mediated by L1-A at 1□M (Scapin et al., 2015). Concentrations of L1CAM_ED > 1nM and of L1-A > 1□M have no incremental effect, suggesting the cell system is somehow 'saturated' and the two molecules might act via the same path. If so, their combination is expected not to overpass such top (saturation) values; this hypothesis was confirmed by treating cells with 1nM L1CAM_ED and/or 1□M L1-A and, as expected, the ectodomain plus peptide combination was found to have the same neuritogenic potential

as either the ectodomain or peptide alone (Figure YSHG 2-n). It is noteworthy that values from L1CAM (or L1-A) treated cells, grown in the absence of RA, are comparable to those from untreated cells induced by RA. Therefore, both L1CAM and biomimetic peptides are as powerful in boosting neuronal differentiation as the well established inducer RA.

Surface Plasmon Resonance and in vitro analyses of agonist/antagonist binding

Homophilic binding between L1CAM_ED molecules was demonstrated by Surface Plasmon Resonance (SPR) analysis (Gouveia et al., 2008). Therefore, we performed SPR experiments with a Biacore sensor chip coated with the recombinant L1CAM_ED used in our experiments with cells (see methods). Our results confirmed such homophilic binding, with a dissociation constant (102±11nM) very similar to that found by Gouveia & coworkers (Figure LA 1). Then, the L1-A peptide was used in displacement experiments to assess its ability to interfere with the L1CAM_ED homophilic binding. In particular, L1CAM_ED was incubated with increasing concentrations (1nM to 10□M range) of L1-A and then injected over the L1CAM_ED coated sensor chip. The sensograms relative to SPR experiments show that L1-A effectively inhibits the homophilic binding, with IC_{50}=6.7±3.6nM (Figure LA 2). Then, we iterated such displacement experiments with L1-A_scr, L1-A_R184A (Zhao mutation) and L1-A_R184Q (CRASH mutation) and found all these peptides to be able to inhibit homophilic binding as well (Figure LA 3). In particular, binding was inhibited by 80% by addition of 1□M concentration of any of the four peptides (w.t., scrambled and the two mutants) and down to roughly 15% residual binding by 10□M peptide (Figure LA 3).

According to docking simulations, in which L1-A and its scrambled and mutant versions are predicted to bind - even if differently - to the NOG site, experiments confirmed that all four peptides do interfere with homophilic binding; at the same time, finding that only the w.t., L1-A peptide has biomimetic capacity is in agreement with its predicted, specific orientation at the NOG site. Therefore, when considering that binding positions of the scrambled and mutant versions partially overlap with position of L1-A (Figure IR 1), these peptides are expected to compete with L1-A and thus to counteract in dose-dependent manner its capacity to boost neuronal differentiation. In order to validate this hypothesis, RA-induced SH-SY5Y cells were treated with 1□M L1-A (invariant, optimal concentration) in the presence of increasing concentrations (up to tenfold) of the scrambled peptide. Figure YSHG 3 shows that a 10:1 scr:wt peptide ratio is able to revert the biomimetic effect of L1-A, confirming the hypothesized agonist/antagonist mechanism of action at the same binding

site. In further control experiments without L1-A, the scrambled peptide alone showed no neuritogenic effect even at the highest concentrations (not shown), confirming previous findings (Scapin et al., 2015).

Effect of L1CAM ED and biomimetic peptides on SH-SY5Y cells expressing L1CAM-EGFP

We fused the wild type coding sequence of human neuronal L1CAM (kind gift from Prof. Jacopo Meldolesi) to a synthetic C-terminal EGFP tag for transfecting SH-SY5Y cells. As a control for effects mediated by transfection, we also used the same plasmid expressing the EGFP tag alone. In transfected cells, L1CAM-EGFP was found to be expressed at both 24 (higher levels) and 48 (lower levels) hours from transfection. In agreement with literature on the neuritogenic effect of L1CAM, expression of L1CAM-EGFP was found to boost neurite elongation in SH-SY5Y cells growing in proliferative conditions (Figure MG 1A and zoom in panel C) as confirmed by comparison to cells transfected with EGFP alone (Figure MG 1B). Since neurite elongation was not further improved by RA induction in L1CAM transfected cells (not shown), next experiments combining transfections and peptide treatments were performed in proliferative conditions.

Peptides in combination do not have aggregate effect over system saturation

When used at optimal concentration, the neuritogenic effect of combined 1□M L1-A + 1□M Lingo1-A peptides was found to be equal or even lower than that mediated by each peptide alone (Scapin et al., 2015). According to this finding, similar evidence of some 'saturation' of the cellular system is observed in this work with e.g. combined 1nM L1CAM + 1 □M L1-A and it is confirmed by aggregate effect of aforementioned protein and peptide when used at sub-optimal concentrations. In order to further check this phenomenon, a number of two-/three-peptides combinations of the newly characterized biomimetic peptides was tested. In all instances, no cumulative neuritogenic effect was observed when using combined peptides at the optimal (peak effect) concentrations while, once again, aggregate effect was only obtained with combinations of peptides used at sub-optimal concentration (data not shown).

Concluding Remarks

To be written once data from planned work to get the manuscript complete are available.

Individual contributions

Contribution from each author working at the dry or wet lab analyses can be inferred by tagging of the figure numbering with authors initials (e.g. figures tagged by YSHG and GS are results from the co-first authors. VDF and FF conceived, coordinated and supervised the overall project.

Acknowledgements

This work was supported by funding from the Padua University (Project PRAT2015 CPDA151948 to FF).

References

- Altschul SF, Madden TL, Schäffer AA, Zhang J, Zhang Z, Miller W, Lipman DJ. Gapped BLAST and PSI-BLAST: a new generation of protein database search programs. Nucleic Acids Res. 1997 Sep 1;25(17):3389-402.

- Atherton E, Sheppard RC. Solid Phase Peptide Synthesis: a practical approach. IRL Press at Oxford University Press 1989.

- Atmanli A, Domian IJ. Recreating the Cardiac Microenvironment in Pluripotent Stem Cell Models of Human Physiology and Disease. Trends Cell Biol. 2017 May;27(5):352-364.

- Baker KA, Moore SW, Jarjour AA, Kennedy TE. When a diffusible axon guidance cue stops diffusing: roles for netrins in adhesion and morphogenesis. Curr Opin Neurobiol. 2006 Oct;16(5):529-34.

- Benkert P, Biasini M, Schwede T. Toward the estimation of the absolute quality of individual protein structure models. Bioinformatics. 2011 Feb 1;27(3):343-50.

- Biasini M, Bienert S, Waterhouse A, Arnold K, Studer G, Schmidt T, Kiefer F, Gallo Cassarino T, Bertoni M, Bordoli L, Schwede T. SWISS-MODEL: modelling protein tertiary

and quaternary structure using evolutionary information. Nucleic Acids Res. 2014 Jul;42(Web Server issue):W252-8.

- Boutet E, Lieberherr D, Tognolli M, Schneider M, Bansal P, Bridge AJ, Poux S, Bougueleret L, Xenarios I. UniProtKB/Swiss-Prot, the Manually Annotated Section of the UniProt KnowledgeBase: How to Use the Entry View. Methods Mol Biol. 2016;1374:23-54.

- Canutescu AA, Shelenkov AA, Dunbrack RL Jr. A graph-theory algorithm for rapid protein side-chain prediction. Protein Sci. 2003 Sep;12(9):2001-14.

- Conacci-Sorrell M, Kaplan A, Raveh S, Gavert N, Sakurai T, Ben-Ze'ev A. The shed ectodomain of Nr-CAM stimulates cell proliferation and motility, and confers cell transformation. Cancer Res. 2005 Dec 15;65(24):11605-12.

- Dahlstrand J, Lardelli M, Lendahl U. Nestin mRNA expression correlates with the central nervous system progenitor cell state in many, but not all, regions of developing central nervous system. Brain Res Dev Brain Res. 1995 Jan 14;84(1):109-29.

- Dalby MJ, Gadegaard N, Oreffo RO. Harnessing nanotopography and integrin-matrix interactions to influence stem cell fate. Nat Mater. 2014 Jun;13(6):558-69.

- de Castro E, Sigrist CJ, Gattiker A, Bulliard V, Langendijk-Genevaux PS, Gasteiger E, Bairoch A, Hulo N. ScanProsite: detection of PROSITE signature matches and ProRule-associated functional and structural residues in proteins. Nucleic Acids Res. 2006 Jul 1;34(Web Server issue):W362-5.

- Dehmelt L, Halpain S. The MAP2/Tau family of microtubule-associated proteins. Genome Biol. 2005;6(1):204. Epub 2004 Dec 23.

- Dolinsky TJ, Czodrowski P, Li H, Nielsen JE, Jensen JH, Klebe G, Baker NA. PDB2PQR: expanding and upgrading automated preparation of biomolecular structures for molecular simulations. Nucleic Acids Res. 2007 Jul;35(Web Server issue):W522-5.

- Good AC. The calculation of molecular similarity: alternative formulas, data manipulation and graphical display. J Mol Graph. 1992 Sep;10(3):144-51, 162.

- Gouveia RM, Gomes CM, Sousa M, Alves PM, Costa J. Kinetic analysis of L1 homophilic interaction: role of the first four immunoglobulin domains and implications on binding mechanism. J Biol Chem. 2008 Oct 17;283(42):28038-47.

- Halper J, Kjaer M. Basic components of connective tissues and extracellular matrix: elastin, fibrillin, fibulins, fibrinogen, fibronectin, laminin, tenascins and thrombospondins. Adv Exp Med Biol. 2014;802:31-47.

- Heo L, Lee H, Seok C. GalaxyRefineComplex: Refinement of protein-protein complex model structures driven by interface repacking. Sci Rep. 2016 Aug 18;6:32153.

- Huang X, Miller W. A time-efficient, linear-space local similarity algorithm. Adv Appl Math. 1991 12:337-357.

- Huang CC, Meng EC, Morris JH, Pettersen EF, Ferrin TE. Enhancing UCSF Chimera through web services. Nucleic Acids Res. 2014 Jul;42(Web Server issue):W478-84.

- Lee H, Heo L, Lee MS, Seok C. GalaxyPepDock: a protein-peptide docking tool based on interaction similarity and energy optimization. Nucleic Acids Res. 2015 Jul1;43(W1):W431-5.

- Lemons ML, Abanto ML, Dambrouskas N, Clements CC, Deloughery Z, Garozzo J, Condic ML. Integrins and cAMP mediate netrin-induced growth cone collapse. Brain Res. 2013 Nov 6;1537:46-58.

- Liu H, Focia PJ, He X. Homophilic adhesion mechanism of neurofascin, a member of the L1 family of neural cell adhesion molecules. J Biol Chem. 2011 Jan 7;286(1):797-805.

- Lowery LA, Van Vactor D. The trip of the tip: understanding the growth cone machinery. Nat Rev Mol Cell Biol. 2009 May;10(5):332-43.

- Maness PF, Schachner M. Neural recognition molecules of the immunoglobulin superfamily: signaling transducers of axon guidance and neuronal migration. Nat Neurosci. 2007 Jan;10(1):19-26.

- McEwen DP, Chen C, Meadows LS, Lopez-Santiago L, Isom LL. The voltage-gated Na+ channel beta3 subunit does not mediate trans homophilic cell adhesion or associate with the cell adhesion molecule contactin. Neurosci Lett. 2009 Oct 25;462(3):272-5.

- McFarlane S. Attraction vs. repulsion: the growth cone decides. Biochem Cell Biol. 2000;78(5):563-8.

- Montes de Oca-B P. Ectdomain shedding and regulated intracellular proteolysis in the central nervous system. Cent Nerv Syst Agents Med Chem. 2010 Dec 1;10(4):337-59.

- Pettersen EF, Goddard TD, Huang CC, Couch GS, Greenblatt DM, Meng EC, Ferrin TE. UCSF Chimera--a visualization system for exploratory research and analysis. J Comput Chem. 2004 Oct;25(13):1605-12.

- Richter S, Wenzel A, Stein M, Gabdoulline RR, Wade RC. webPIPSA: a web server for the comparison of protein interaction properties. Nucleic Acids Res. 2008 Jul 1;36(Web Server issue):W276-80.

- Ross RA, Spengler BA, Biedler JL. Coordinate morphological and biochemical interconversion of human neuroblastoma cells. J Natl Cancer Inst 1983;71:741-7.

- Scapin G, Salice P, Tescari S, Menna E, De Filippis V, Filippini F. Enhanced neuronal cell differentiation combining biomimetic peptides and a carbon nanotube-polymer scaffold. Nanomedicine. 2015 Apr;11(3):621-32.

- Scapin G, Bertalot T, Vicentini N, Gatti T, Tescari S, De Filippis V, Marega C, Menna E, Gasparella M, Parnigotto PP, Di Liddo R, Filippini F. Neuronal commitment of human circulating multipotent cells by carbon nanotube-polymer scaffolds and biomimetic peptides. Nanomedicine (Lond). 2016 Aug;11(15):1929-46.

- Seiradake E, Jones EY, Klein R. Structural Perspectives on Axon Guidance. Annu Rev Cell Dev Biol. 2016 Oct 6;32:577-608.

- Sigrist CJ, Cerutti L, de Castro E, Langendijk-Genevaux PS, Bulliard V, Bairoch A, Hulo N. PROSITE, a protein domain database for functional characterization and annotation. Nucleic Acids Res. 2010 Jan;38(Database issue):D161-6.

- Sitkoff D, Sharp KA, Honig B. Correlating solvation free energies and surface tensions of hydrocarbon solutes. Biophys Chem. 1994 Aug;51(2-3):397-403; discussion 404-9.

- Schmid RS, Maness PF. L1 and NCAM adhesion molecules as signaling coreceptors in neuronal migration and process outgrowth. Curr Opin Neurobiol. 2008 Jun;18(3):245-50.

- Tamariz E, Varela-Echavarrìa A. The discovery of the growth cone and its influence on the study of axon guidance. Front Neuroanat. 2015 May 15;9:51.

- Tischfield MA, Baris HN, Wu C, Rudolph G, Van Maldergem L, He W, Chan WM, Andrews C, Demer JL, Robertson RL, Mackey DA, Ruddle JB, Bird TD, Gottlob I, Pieh C, Traboulsi EI, Pomeroy SL, Hunter DG, Soul JS, Newlin A, Sabol LJ, Doherty EJ, de Uzcàtegui CE, de Uzcàtegui N, Collins ML, Sener EC, Wabbels B, Hellebrand H, Meitinger T, de Berardinis T, Magli A, Schiavi C, Pastore-Trossello M, Koc F, Wong AM, Levin AV, Geraghty MT, Descartes M, Flaherty M, Jamieson RV, M√∏ller HU, Meuthen I, Callen DF, Kerwin J, Lindsay S, Meindl A, Gupta ML Jr, Pellman D, Engle EC. Human TUBB3 mutations perturb microtubule dynamics, kinesin interactions, and axon guidance. Cell. 2010 Jan 8;140(1):74-87. doi:10.1016/j.cell.2009.12.011.

- Treutlein B, Gokce O, Quake SR, S√ºdhof TC. Cartography of neurexin alternative splicing mapped by single-molecule long-read mRNA sequencing. Proc Natl Acad Sci U S A. 2014 Apr 1;111(13):E1291-9.

- Wang Q, Canutescu AA, Dunbrack RL Jr. SCWRL and MolIDE: computer programs for side-chain conformation prediction and homology modeling. Nat Protoc. 2008;3(12):1832-47.

- Yamasaki M, Thompson P, Lemmon V. CRASH syndrome: mutations in L1CAM correlate with severity of the disease. Neuropediatrics. 1997 Jun;28(3):175-8.

- Zhang Y, Yeh J, Richardson PM, Bo X. Cell adhesion molecules of the immunoglobulin superfamily in axonal regeneration and neural repair. Restor Neurol Neurosci. 2008;26(2-3):81-96.

Figures and tables with captions

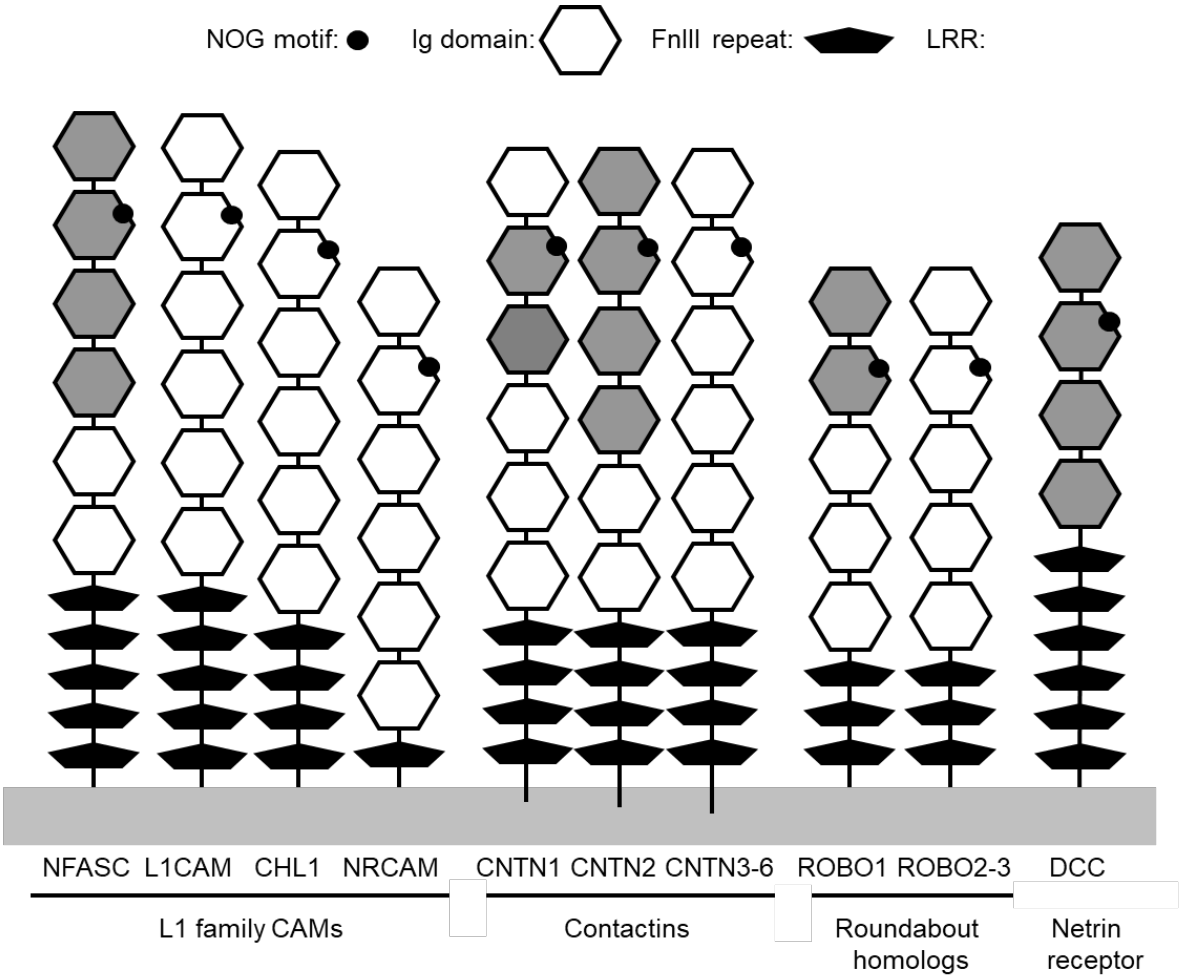

Figure FF-TDR. Extracellular domain (ED) architecture of neuronal CAM proteins positive for the NOG motif. The EDs of human NOG proteins protruding from the plasma membrane (grey horizontal bar) shows a variable number of Immunoglobulin-like (Ig, hexagon, with the grey background when corresponding X-ray structure is available) and Fibronectin III-like (FnIII, black pentagon) domains. NOG motifs are depicted by full black circles. Hereafter the UniprotKB accession numbers for all depicted proteins are reported, followed (when available) between parentheses by the Protein Data Bank (PDB) accessions: NFASC, O94856 (3P3Y, 3P40); L1CAM, P32004; CHL1, O00533; NrCAM, Q92823; CNTN1, Q12860 (3S97); CNTN2, Q02246 (2OM5); CNTN3, Q9P232; CNTN4, Q8IWV2; CNTN5, O94779; CNTN6, Q9UQ52; ROBO1, Q9Y6N7 (2V9R); ROBO2, Q9HCK4; ROBO3, Q96MS0; DCC/Netrin R, P43146 (3LAF*). **rat protein, as the structure of human DCC is not available*.

	Structure comparison		L1 family				Contactin family						Roundabout homologs		Netrin receptor			
Sequence comparison	(rmsd)		Neurofascin				CNTN1		CNTN2				ROBO1		DCC			
	(identity)		Ig1	Ig2	Ig3	Ig4	Ig2	Ig3	Ig1	Ig2	Ig3	Ig4	Ig1	Ig2	Ig1	Ig2	Ig3	Ig4
L1 family	Neurofascin	Ig1		8.19	6.69	4.81	10.13	4.15	7.04	8.51	3.35	8.17	4.64	6.98	3.76	4.02	2.69	4.35
		Ig2	25.9		5.33	4.03	2.17	4.67	6.32	2.65	5.04	3.38	4.43	3.15	7.92	3.92	4.65	5.14
		Ig3	29.0	23.7		4.33	5.25	3.64	7.73	5.12	2.05	3.09	3.92	4.36	5.00	4.17	3.45	4.43
		Ig4	30.5	19.8	41.4		4.76	2.74	4.38	6.23	1.73	1.97	4.46	3.28	3.24	5.84	3.57	2.31
Contactin family	CNTN1	Ig2	19.4	33.0	26.6	16.3		4.51	7.52	1.54	5.33	3.55	4.65	3.08	4.83	3.77	7.18	4.25
		Ig3	25.8	24.2	33.7	23.6	18.7		3.79	4.70	1.77	2.91	2.84	4.07	2.92	4.06	2.52	2.13
	CNTN2	Ig1	23.7	19.3	25.8	28.1	28.1	21.1		4.82	5.83	4.67	3.02	2.32	3.98	6.83	2.30	2.59
		Ig2	17.3	28.0	21.7	18.3	60.0	19.8	25.8		5.44	5.30	4.92	3.39	4.66	3.76	5.52	4.15
		Ig3	21.6	20.9	31.5	21.3	17.2	48.8	24.2	20.4		3.17	4.99	2.07	5.78	6.44	2.03	1.62
		Ig4	27.8	26.7	30.3	36.4	17.6	32.6	29.2	23.1	26.7		4.53	4.21	3.93	4.80	4.92	1.42
Roudabout homologs	ROBO1	Ig1	30.0	24.2	29.0	26.8	14.4	29.6	30.9	19.2	26.5	28.9		3.02	2.47	2.81	2.41	1.98
		Ig2	23.5	23.3	26.4	23.3	14.4	29.6	28.9	22.8	24.7	28.4	39.8		4.15	1.87	3.88	2.17
Netrin receptor	DCC	Ig1	19.4	21.1	30.6	17.9	22.7	26.8	29.2	21.9	24.0	23.2	30.6	24.7		3.52	2.36	2.19
		Ig2	28.6	25.8	31.2	23.1	20.4	31.9	29.7	26.9	26.4	30.8	29.6	26.1	34.6		2.00	2.40
		Ig3	19.2	20.4	26.7	20.9	25.5	22.2	16.3	25.0	21.1	33.3	29.0	31.5	29.5	28.8		1.22
		Ig4	24.7	20.0	31.1	30.7	31.1	29.9	30.0	23.1	29.9	34.9	30.9	30.7	28.2	32.9	40.0	

	Ig1	Ig2	Ig3	Ig4
Ig1	4.15 (27.3%)			
Ig2		2.93 (28.1%)		
Ig3			2.58 (30.7%)	
Ig4				1.90 (34.0%)
other Igs from the same protein	4.61 (29.7%)	4.41 (26.7%)	4.09 (28.2%)	3.57 (30.2%)

Table IR-FF. Structural and sequence comparison among the Ig domains of NOG positive CAM and ECM proteins. In the upper right part of the larger table, RMSD values in Å are shown, while % identity values of corresponding sequences are reported in the lower left part. The smaller table below resumes the average RMSD and identity values for homogeneous Ig type comparison or for comparison with the other Igs from the same protein.

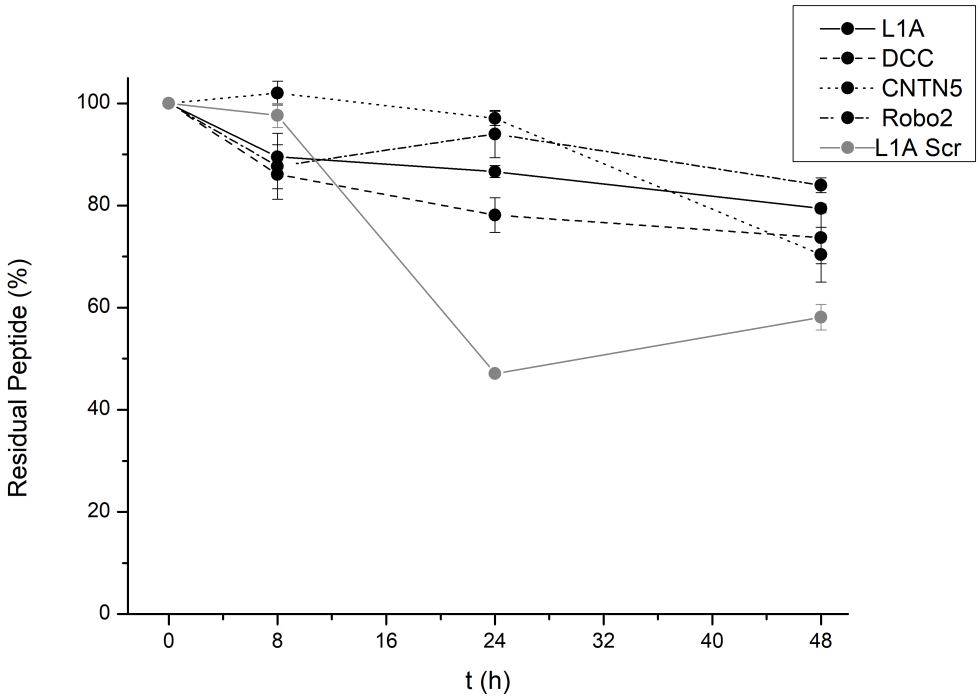

Figure AP 1. Residual concentrations of NOG peptides in media from differentiating SH-SY5Y cells. Medium was collected and ultrafiltrated at the indicated time points covering the 2-days time slot for medium (and peptide) refresh. Data represent the mean ± SEM of at least three independent experiments.

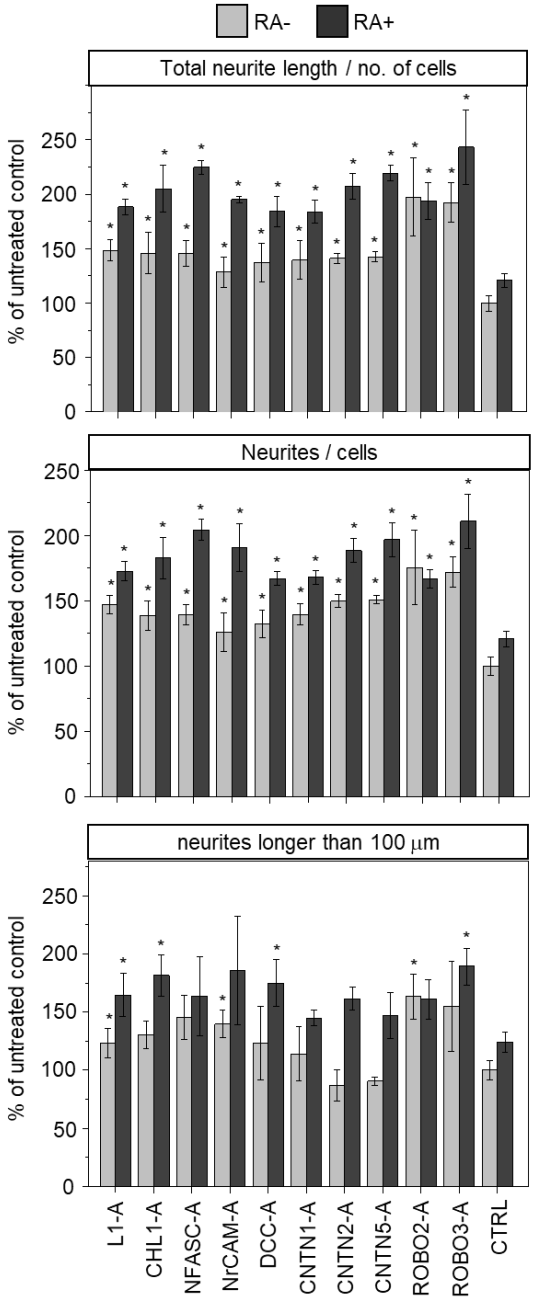

Figure GS 1-n. Effect of NOG and control peptides on neuritogenesis of SH-SY5Y cells. Treatments were performed both in the absence (RA-) and presence (RA+) of the RA inducer; CTRL, untreated control. Measured features are reported at the top of each graph; incremental values are presented as % of RA- CTRL. Data represent the mean ± SEM of at least three independent experiments performed in duplicate. * shows significance at $p<0.05$ between samples treated with peptides and the control without peptides.

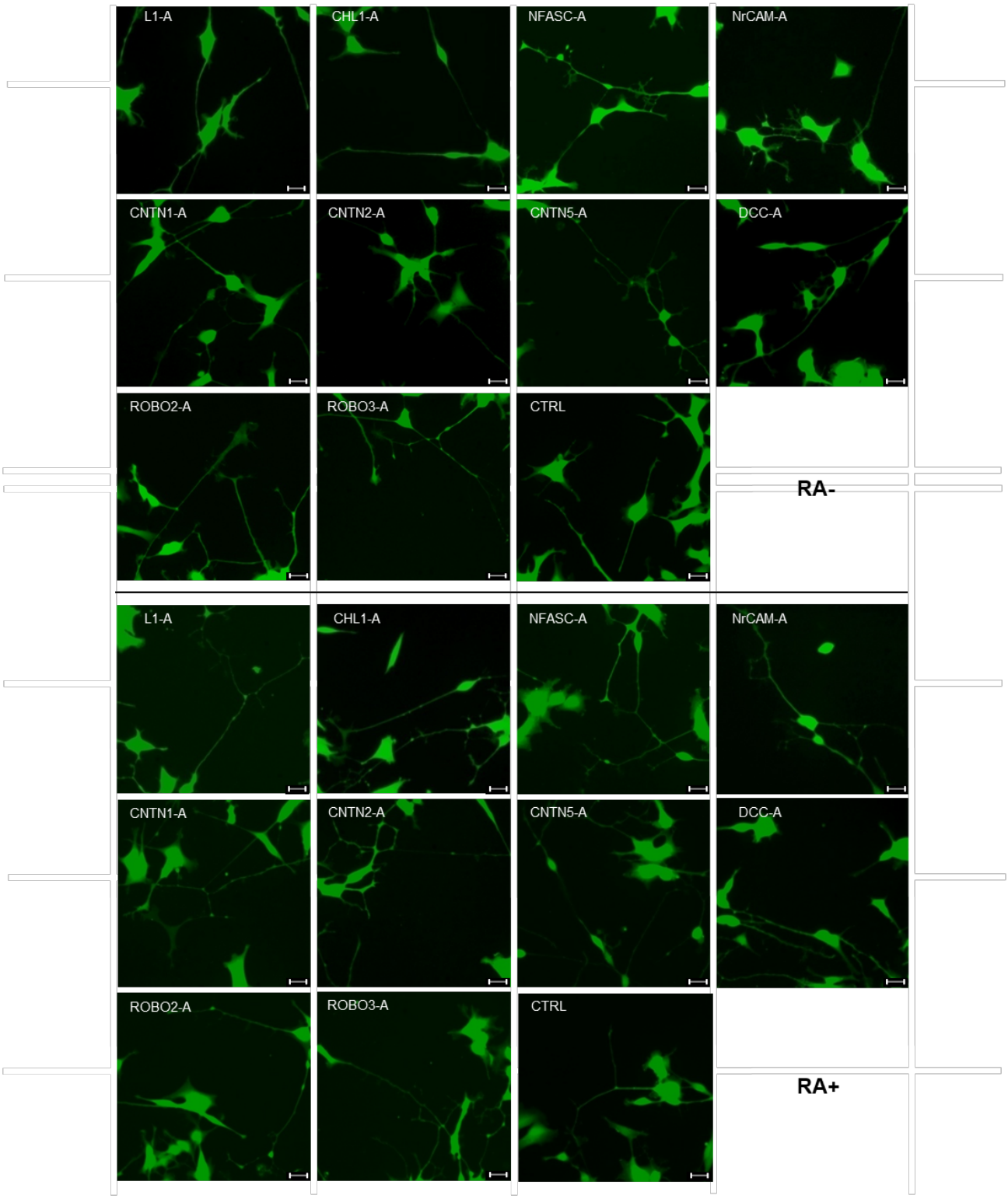

Figure GS 2. Representative microscopy fields of SH-SY5Y cells from experiments in Figure GS 1. Cells are stained with Calcein-AM. Image magnification is 32X. Scale bar is 25 μm.

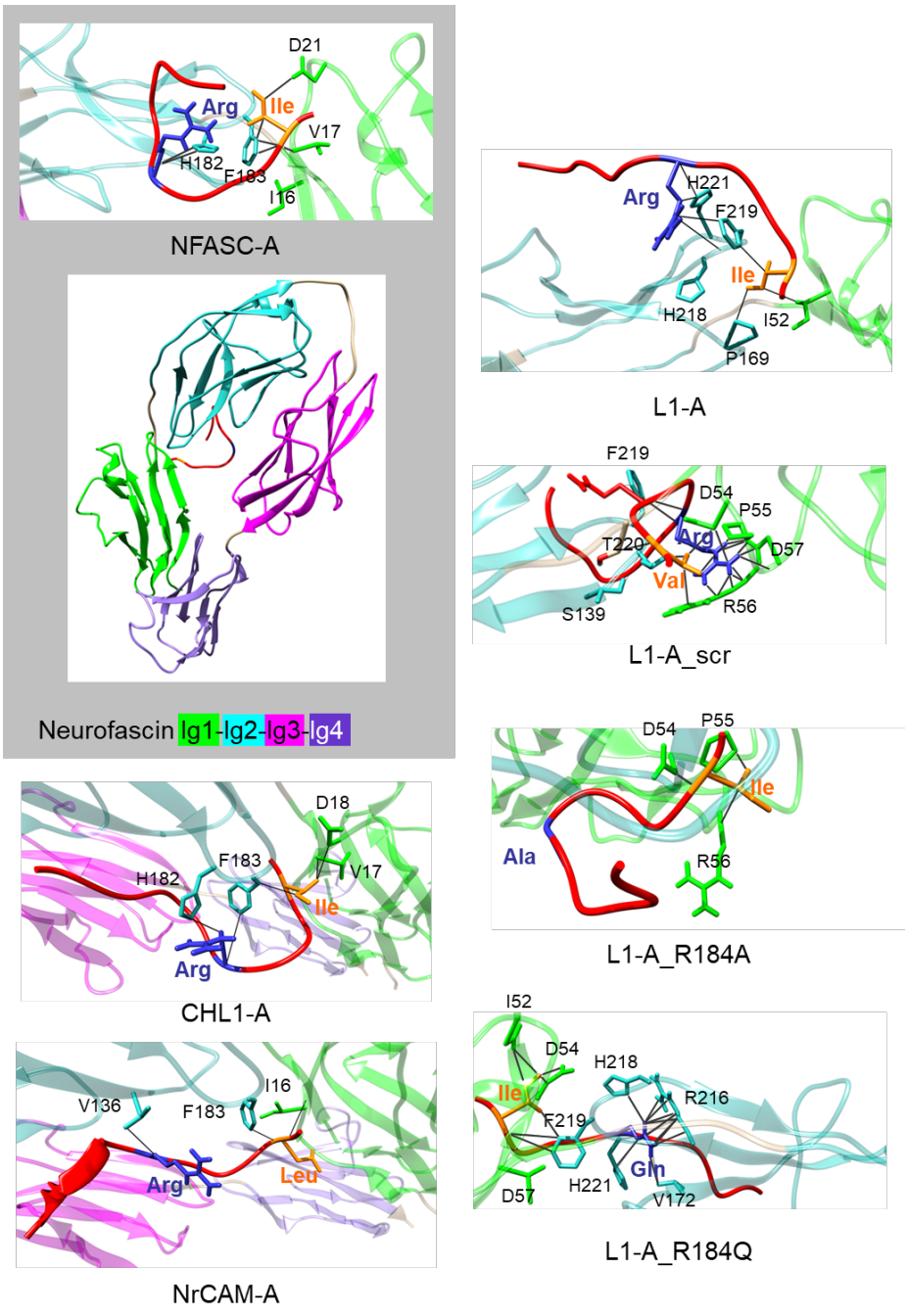

Figure IR 1. Biomimetic, scrambled and mutant peptides docking to Neurofascin horseshoe. Simulation for NFASC-A docking to the Neurofascin horseshoe is shown in the grey box, both in full to tag Ig1 to Ig4 by colour coding and as a close up view of peptide-target bonds; close up views for other peptides are depicted around. Peptides are red, with three-letter coding for their second position (orange) and central position (blue, conserved Arg or mutant residue). Neurofascin Ig2 and Ig1 residues involved in peptide binding are indicated insted by one-letter coding with number.

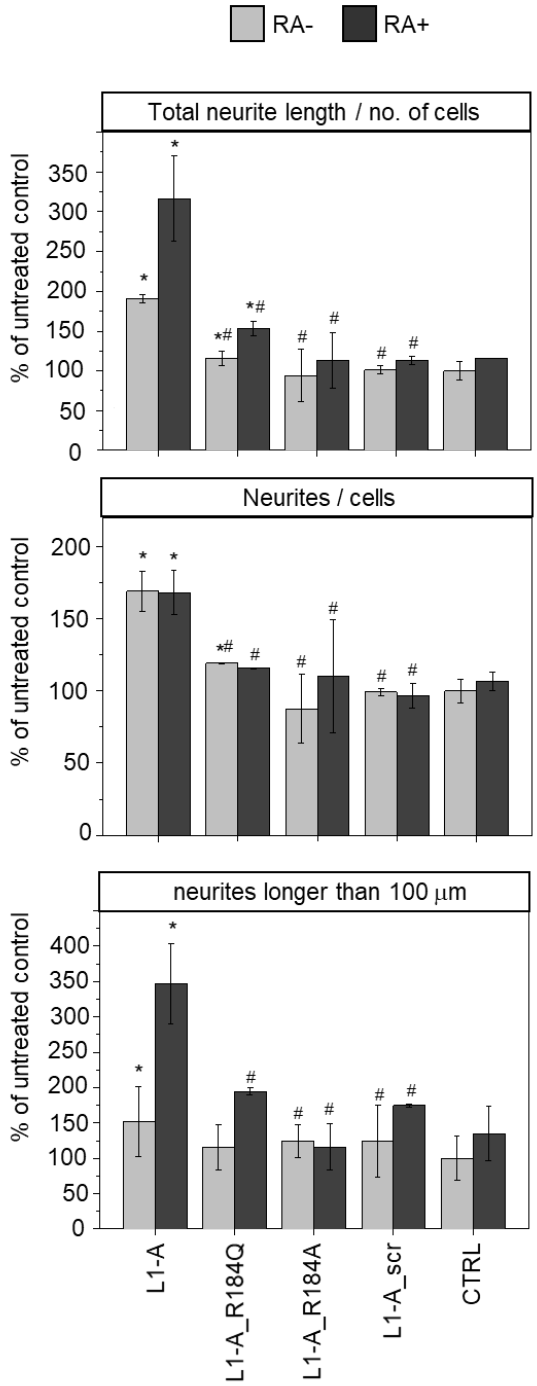

Figure GS 3. Neuritogenic potential in SH-SY5Y cells of wild-type L1-A compared to related scrambled and mutant peptides. Baselines for untreated (dashed grey line) and RA-treated (continuous black line) control cells are shown to highlight incremental values. Data represent the mean ± SEM of three independent experiments performed in duplicate. * shows significance at $p<0.05$ between samples treated with peptides and the control without peptides. # shows significance at $p<0.05$ between wild type and mutants/scrambled.

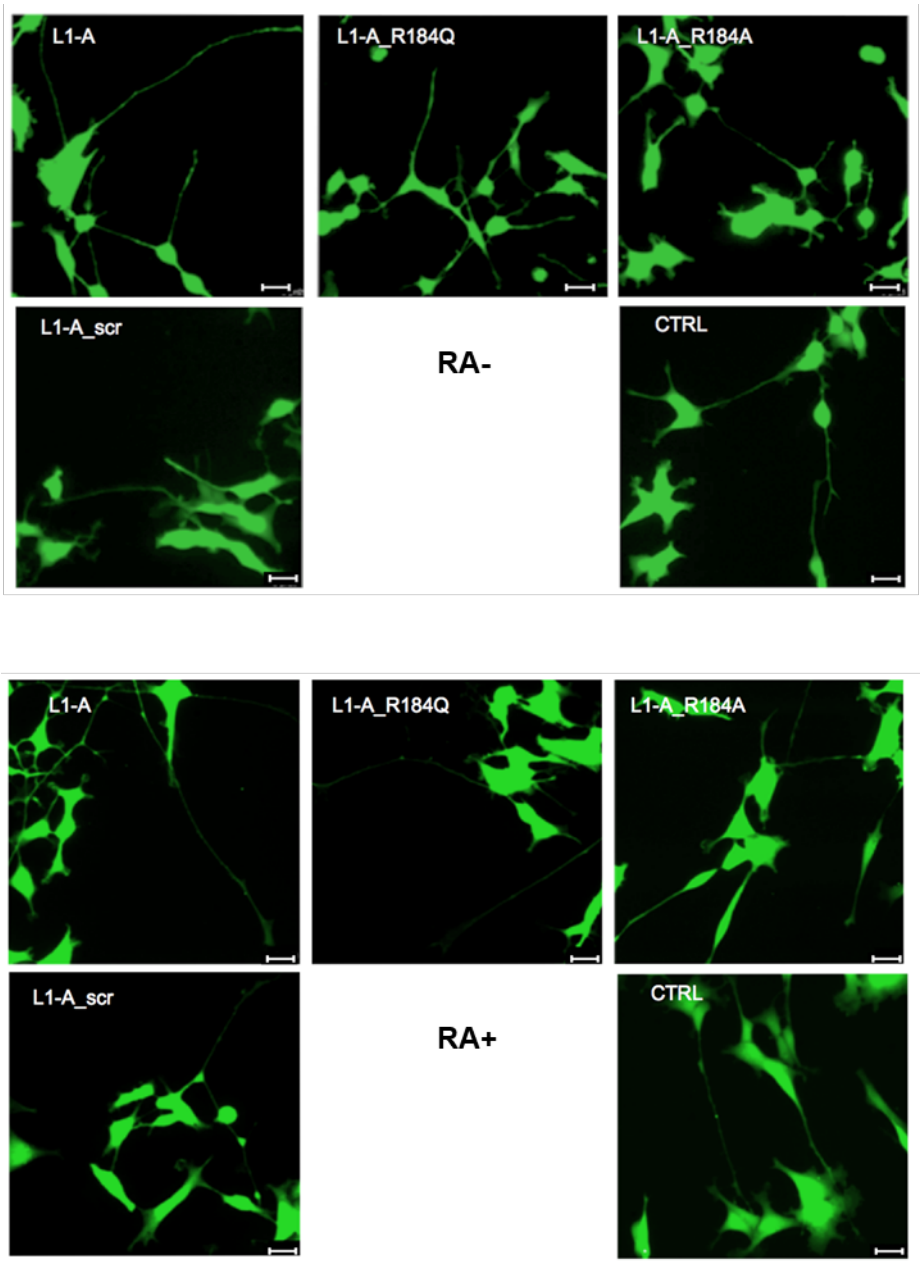

Figure GS 4. Representative microscopy fields of SH-SY5Y cells from experiments in Figure GS 3. Cells are stained with Calcein-AM. Image magnification is 32X. Scale bar is 25 μm.

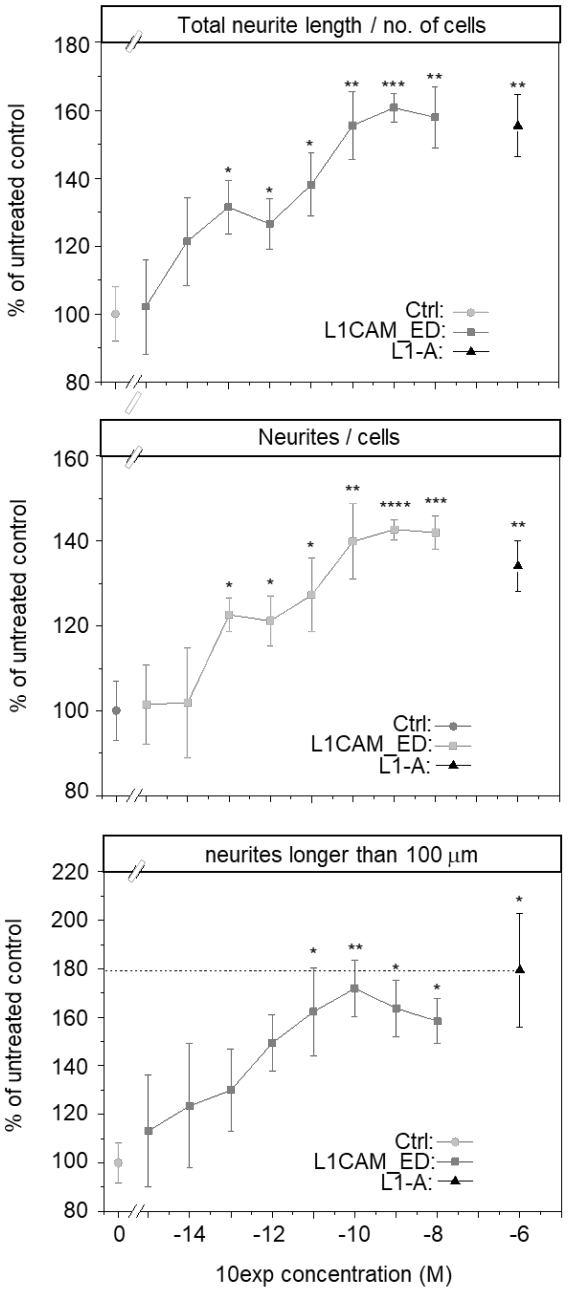

Figure YSHG 1. Comparison of neuritogenic effects mediated by increasing L1CAM_ED concentrations or by L1-A peptide. RA-induced SH-SY5Y cells were treated with tenfold increasing L1CAM_ED concentrations or 1□M L1-A The dashed and the continuous grey lines correspond to values with L1-A and untrated control, respectively. Data represent the mean ± SEM of three independent experiments performed in duplicate. Significance at $p<0.05$ (*), $p<0.005$ (**), $p<0.0005$ (***) and $p<0.00005$ (****) between treated samples and untreated control is reported.

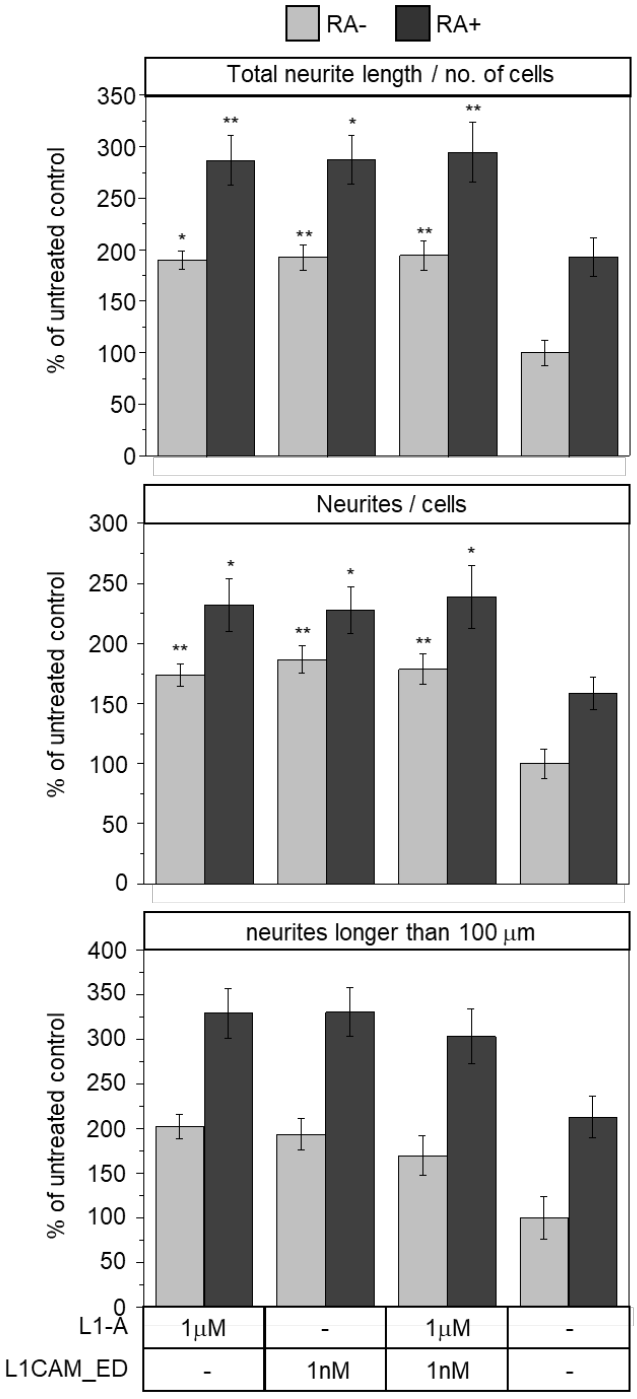

Figure YSHG 2. Comparison of neuritogenic effects mediated by L1CAM_ED, L1-A peptide and their combination. SH-SY5Y cells were treated in the absence or presence of RA with 1nM L1CAM_ED, 1□M L1-A and their combination. Last samples, untreated control cells. Data represent the mean ± SEM of three independent experiments performed in duplicate. Significance at $p<0.05$ (*) and $p<0.005$ (**) between treated samples and untreated control is reported.

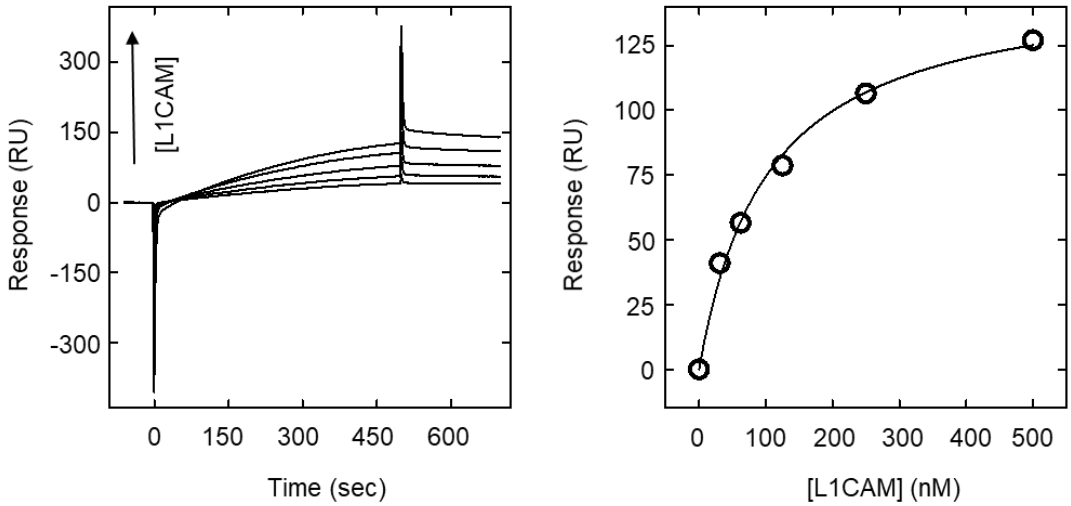

Figure LA 1. Surface Plasmon Resonance analysis of the L1CAM homophilic binding. Left sensogram: increasing concentrations (0 to 0.5mM) of L1CAM are sequentially injected at 25°C over the sensor chip, with flow rate of 10 ml/min, using HBEP (10mM HEPES pH 7.4, 150mM NaCl, 3mM EDTA, 0.005% P20) as running buffer. Each SPR trace is subtracted for unspecific binding (<2% of Rmax) of L1CAM. Response Units (RU) at the steady state are plotted (right graph) as a function of [L1CAM] and fitted to the Langmuir equation to yield the dissociation constant, Kd, for the homophilic interaction.

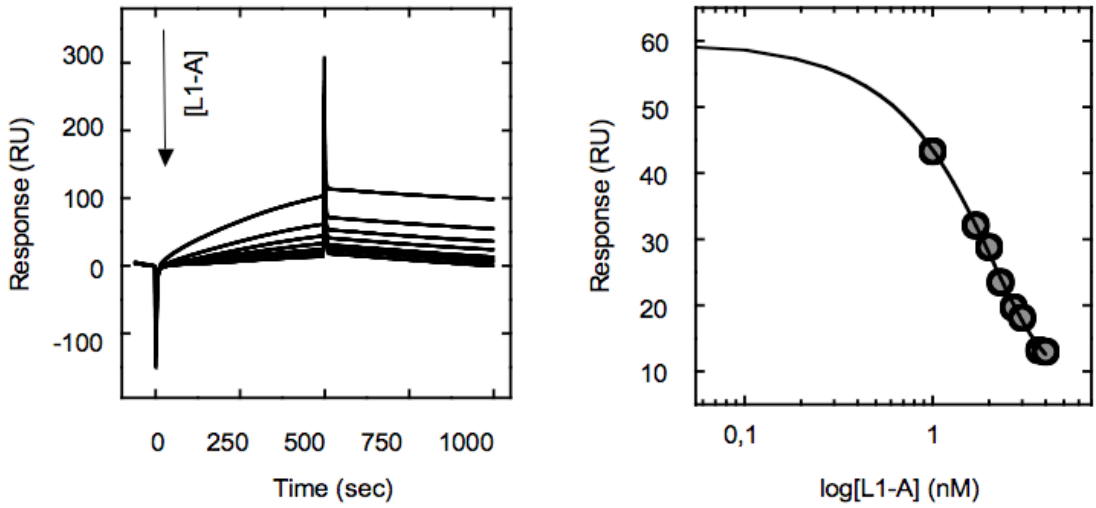

Figure LA 2. SPR analysis of the effect of L1-A peptide on L1CAM homophilic binding. Left sensogram: 300nM L1CAM is first incubated at 25°C with increasing concentrations (1nM to 10□M) of L1A peptide, and then injected over the L1CAM-coated sensor chip. All measurements are carried out at flow rate of 10 ml/min, in HBS-EP^{+}, pH 7.5. Plotted RU_{max} *versus* L1A concentration is shown in the right graph, wherein IC_{50} corresponds to the midpoint of the semilog plot.

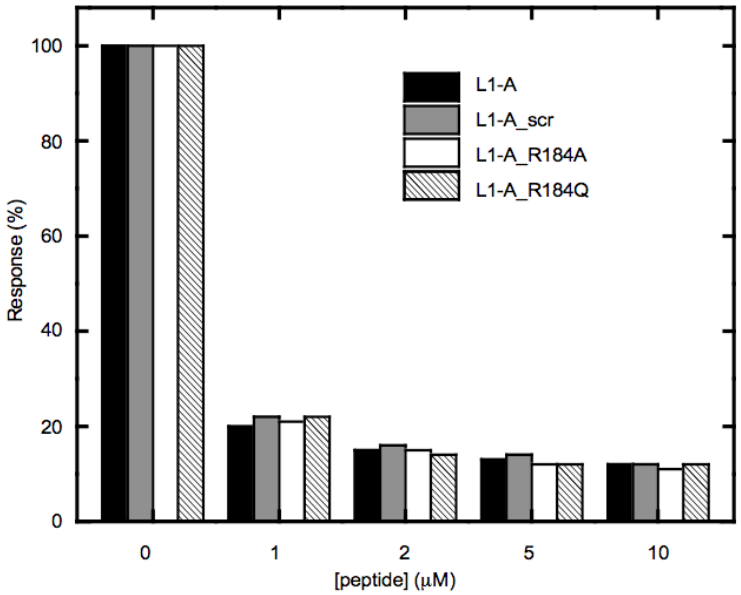

Figure LA 3. SPR analysis of competition by L1-A scrambled and mutant peptides. Percentage reponse units (RU) measured for the binding of L1CAM to sensor chip-immobilized L1CAM in the absence or presence of increasing concentrations (1 to 10□M) of L1-A or its scrambled and mutant peptides.

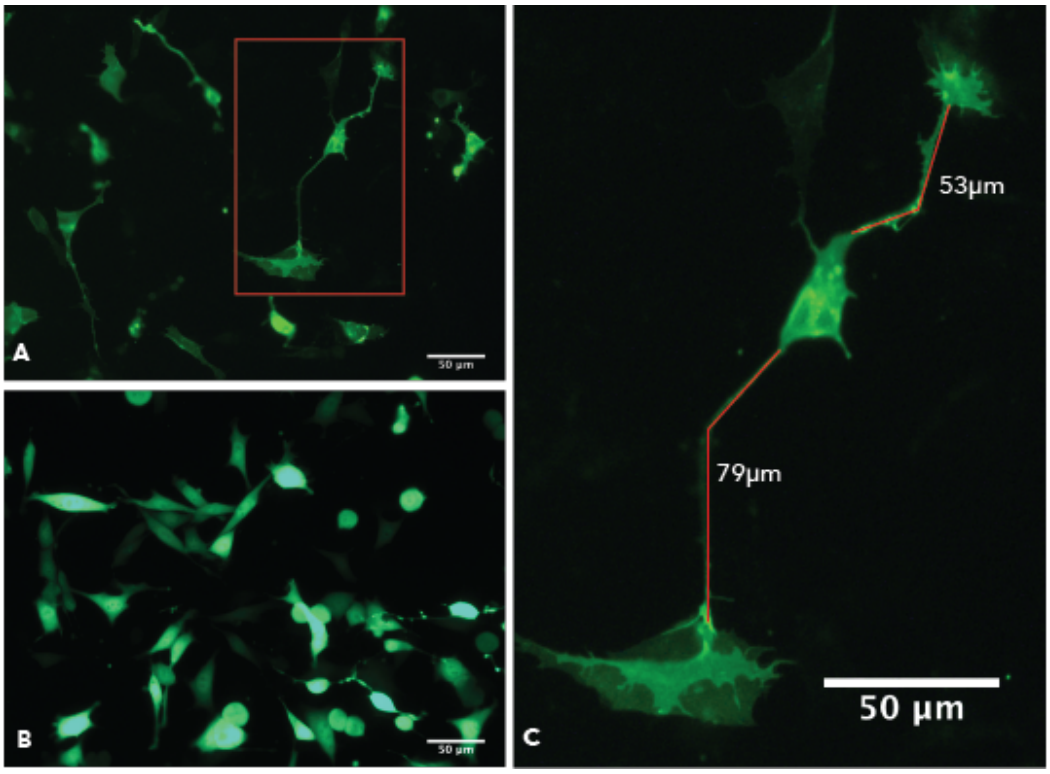

Figure MG 1. Treatment with peptides of SH-SY5Y cells transfected with L1CAM-EGFP. Representative microscopy fields from SH-SY5Y cells transfected with either L1CAM-EGFP (panel A) or EGFP alone (panel B). Red box from panel A is magnificated (C) to better show cell processes and their length.

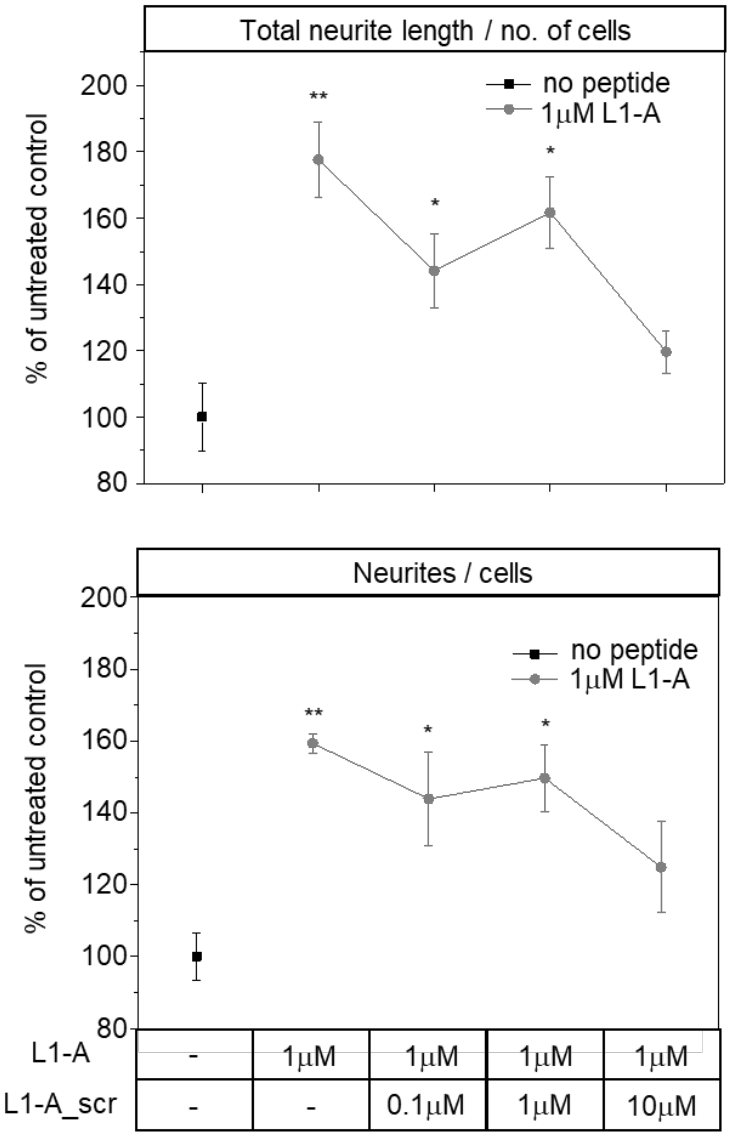

Figure YSHG 3. Competition by increasing [L1-A_scr] of the neuritogenic effect mediated by L1-A peptide. RA-differentiated SH-SY5Y cells were treated in the absence (ctrl) or presence of 1□M L1-A and tenfold-step, increasing concentrations of L1-A_scr. Data represent the mean ± SEM of three independent experiments performed in duplicate. Significance at $p<0.05$ (*) and $p<0.005$ (**) between treated samples and untreated control is reported.

Supplementary informations

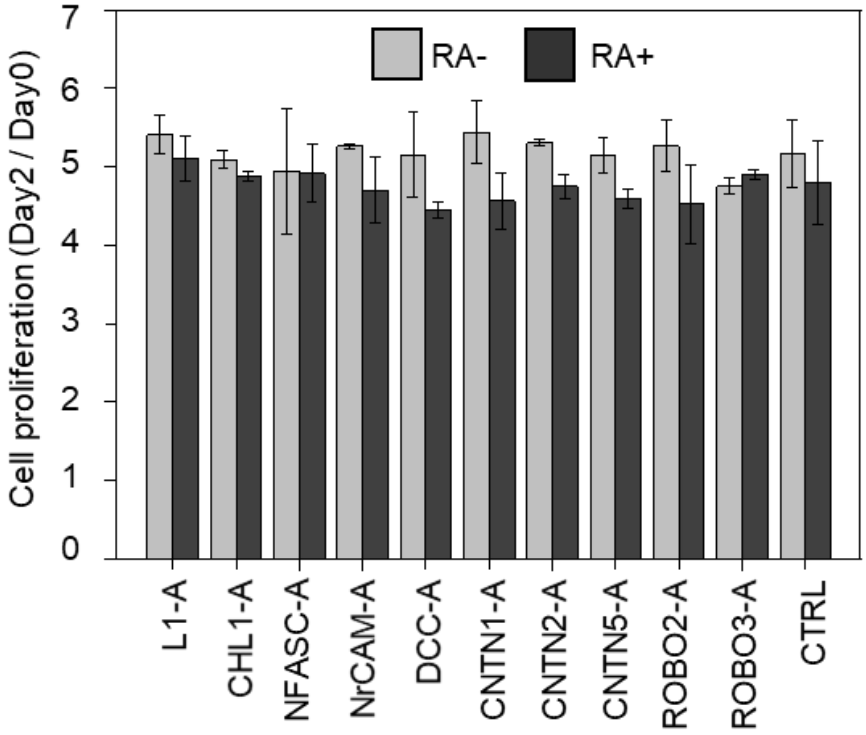

Figure GS S1-n. Effect of NOG peptides on SH-SY5Y cell proliferation. Treatments were performed both in the absence (RA-) and presence (RA+) of the RA inducer; CTRL, untreated control. Data represent the mean ± SEM of at least three independent experiments performed in duplicate. * shows significance at $p<0.05$ between samples treated with peptides and the control without peptides.

CHL1-A

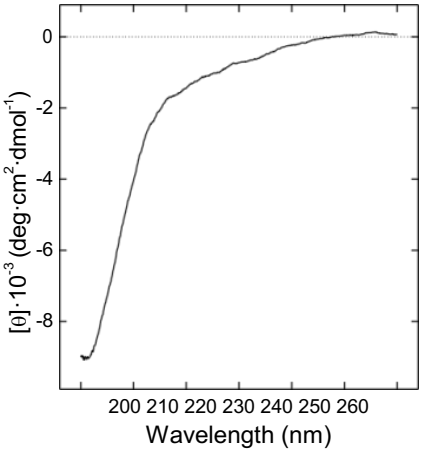

NFASC-A

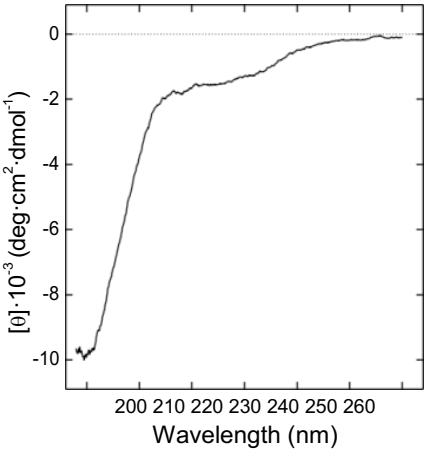

NrCAM-A

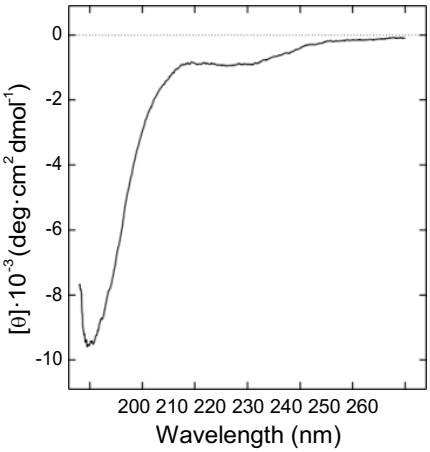

DCC-A

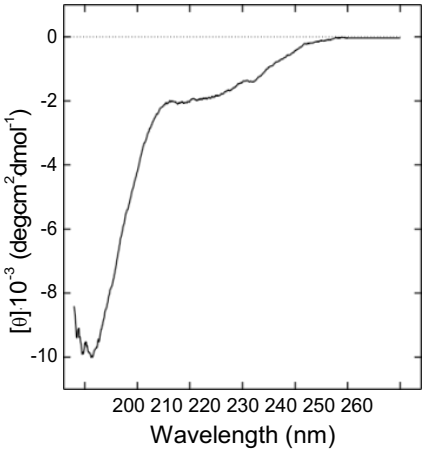

ROBO2-A

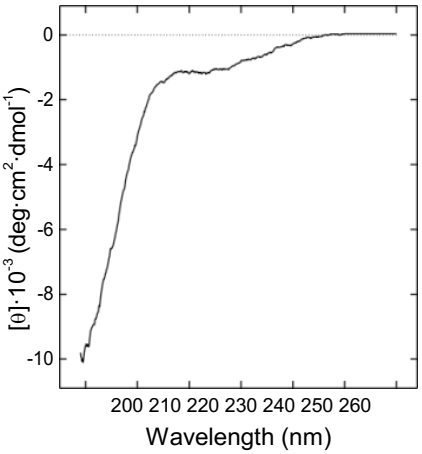

ROBO3-A

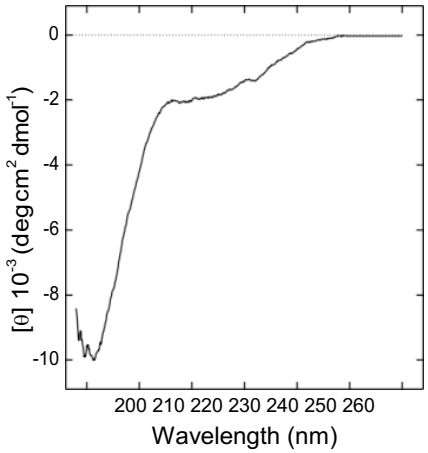

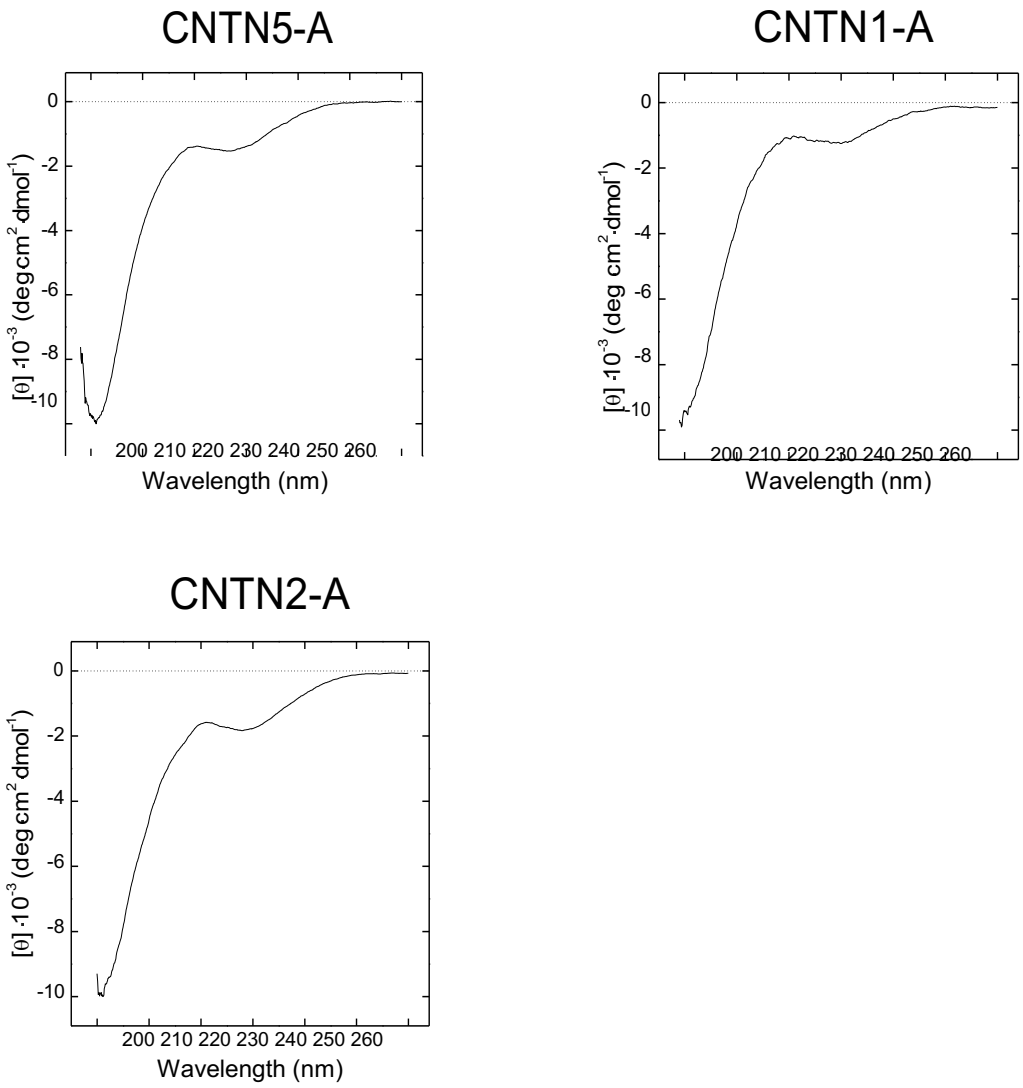

Figure EL1. Far-UV CD spectra of new NOG peptides.

4. CONCLUDING REMARKS

In my PhD project I developed biomimetic nanosystems to be used in neuronal regenerative medicine.

I tested new nanocomposite scaffolds by varying types and concentrations of nanofillers dispersed in PLLA matrix. As nanofillers, we used from 0.25 to 5% of three CNS: MWCNTs, RGO and CNHs. Even if we observed these nanocomposites have different calorimetric response, electrical and mechanical properties, all of them proved to be biocompatible and to support as scaffolds the proliferation of human neuronal precursor cell line SH-SY5Y. Instead, only 5% RGO-PLLA and 5% MWCNT-PLLA showed to boost neurite outgrowth and elongation. In addition, 3D printing with graphene-PLLA filaments has be used to obtain patterned printing scaffolds, which proved to enhance neuronal differentiation of hCMCs and to drive oriented growth and axon elongation. Actually, we started novel experiments after changing the 3D printing nozzle with narrower diameter ones (0.4-0.3 mm diameter). This is expected to provide us with possibility to print with better micrometric precision and to produce patterns with dimensions closer to cells and their processes.

In the meantime, we focused on the characterization of novel biomimetic peptides sharing a conserved motif to better reproduce neuronal biochemical cues and they proved to promote neuritogenesis and neuronal differentiation of SH-SY5Y cells. In silico simulations and in vitro evidence by comparing natural NOG sequences vs mutant and scrambled peptides, suggest an agonist-antagonist mechanism for their action.

Once the best conditions in terms of physical and biochemical stimuli are defined, we could combine them, linking peptides to the scaffolds. Given that peptides are very short, spacer region might be needed and, if so extended peptides should be validated for the biomimetic potential.

In conclusion, our new nanocomposite scaffold and biomimetic peptides are potential tools for neuronal regenerative medicine and this work opens the route to further investigation on the role played by scaffold properties and by biomimetic peptides on neuronal differentiation and regeneration.

5. REFERENCES

1. Kim ES, Ahn EH, Dvir T, Kim DH. Emerging nanotechnology approaches in tissue engineering and regenerative medicine. *Int J Nanomedicine*. 2014;9(SUPPL.1):1-5. doi:10.2147/IJN.S61212

2. Sampogna G, Guraya SY, Forgione A. Regenerative medicine: Historical roots and potential strategies in modern medicine. *J Microsc Ultrastruct*. 2015;3(3):101-107. doi:10.1016/j.jmau.2015.05.002

3. Keung AJ, Kumar S, Schaffer D V. Presentation Counts: Microenvironmental Regulation of Stem Cells by Biophysical and Material Cues. *Annu Rev Cell Dev Biol*. 2010;26(1):533-556. doi:10.1146/annurev-cellbio-100109-104042

4. Furth ME, Atala A, Van Dyke ME. Smart biomaterials design for tissue engineering and regenerative medicine. *Biomaterials*. 2007;28(34):5068-5073. doi:10.1016/j.biomaterials.2007.07.042

5. Perán M, García MA, López-Ruiz E, et al. Functionalized nanostructures with application in regenerative medicine. *Int J Mol Sci*. 2012;13(3):3847-3886. doi:10.3390/ijms13033847

6. Tian L, Prabhakaran MP, Ramakrishna S. Strategies for regeneration of components of nervous system: Scaffolds, cells and biomolecules. *Regen Biomater*. 2015;2(1):31-45. doi:10.1093/rb/rbu017

7. Lee LC, Zhihong Z, Hinson A, Guccione JM. Reduction in Left Ventricular Wall Stress and Improvement in Function in Failing Hearts using Algisyl-LVR. *J Vis Exp*. 2013;(74):1-6. doi:10.3791/50096

8. Cirillo V, Guarino V, Alvarez-Perez MA, Marrese M, Ambrosio L. Optimization of fully aligned bioactive electrospun fibers for “in vitro” nerve guidance. *J Mater Sci Mater Med*. 2014;25(10):2323-2332. doi:10.1007/s10856-014-5214-4

9. Gregor A, Filová E, Novák M, et al. Designing of PLA scaffolds for bone tissue replacement fabricated by ordinary commercial 3D printer. 2017:1-21. doi:10.1186/s13036-017-0074-3

10. Mao AS, Mooney DJ. Regenerative medicine: Current therapies and future directions. *Proc Natl Acad Sci*. 2015;112(47):14452-14459. doi:10.1073/pnas.1508520112

11. Williams DF. The role of short synthetic adhesion peptides in regenerative

medicine; The debate. *Biomaterials*. 2011;32(18):4195-4197. doi:10.1016/j.biomaterials.2011.02.025

12. Collier JH, Segura T. Evolving the use of peptides as components of biomaterials. *Biomaterials*. 2011;32(18):4198-4204. doi:10.1016/j.biomaterials.2011.02.030

13. Gelain F, Horii A, Zhang S. Designer self-assembling peptide scaffolds for 3-D tissue cell cultures and regenerative medicine. *Macromol Biosci*. 2007;7(5):544-551. doi:10.1002/mabi.200700033

14. Takahashi K, Yamanaka S. Induction of Pluripotent Stem Cells from Mouse Embryonic and Adult Fibroblast Cultures by Defined Factors. *Cell*. 2006;126(4):663-676. doi:10.1016/j.cell.2006.07.024

15. Villa-Diaz LG, Ross AM, Lahann J, Krebsbach PH. Concise Review: The Evolution of human pluripotent stem cell culture: From feeder cells to synthetic coatings. *Stem Cells*. 2013;31(1):1-7. doi:10.1002/stem.1260

16. Ding S, Kingshott P, Thissen H, Pera M, Wang PY. Modulation of human mesenchymal and pluripotent stem cell behavior using biophysical and biochemical cues: A review. *Biotechnol Bioeng*. 2017;114(2):260-280. doi:10.1002/bit.26075

17. Lei M, Wang X. Biodegradable polymers and stem cells for bioprinting. *Molecules*. 2016;21(5):1-14. doi:10.3390/molecules21050539

18. Mai JK, Paxinos G. *The Human Nervous System*. Elsevier Academic Press; 2012.

19. Brodal P. *The Central Nervous System : Structure and Function*. Oxford University Press; 2004.

20. Govek E, Newey SE, Aelst L Van. The role of the Rho GTPases in neuronal development The role of the Rho GTPases in neuronal development. 2005:1-49. doi:10.1101/gad.1256405

21. Lalli G. Crucial polarity regulators in axon specification. 2012. doi:10.1042/BSE0530055

22. Stoeckli ET. Understanding axon guidance: are we nearly there yet? *Development*. 2018;145(10):dev151415. doi:10.1242/dev.151415

23. Lowery LA, Vactor D Van. The trip of the tip : understanding the growth cone machinery. 2009;10(5):332-343. doi:10.1038/nrm2679.The

24. Namba T, Funahashi Y, Nakamuta S, Xu C, Takano T, Kaibuchi K. Extracellular and intracellular signaling for neuronal polarity. 2018:995-1024. doi:10.1152/physrev.00025.2014

25. Cattin AL, Lloyd AC. The multicellular complexity of peripheral nerve regeneration. *Curr Opin Neurobiol*. 2016;39:38-46. doi:10.1016/j.conb.2016.04.005

26. Scheib J, Höke A. Advances in peripheral nerve regeneration. *Nat Rev Neurol*. 2013;9(12):668-676. doi:10.1038/nrneurol.2013.227

27. Horner PJ, Gage FH. Regenerating the damaged central nervous system. *Nature*. 2000;407(6807):963-970. doi:10.1038/35039559

28. Pinho AC, Fonseca AC, Serra AC, Santos JD, Coelho JFJ. Peripheral Nerve Regeneration: Current Status and New Strategies Using Polymeric Materials. *Adv Healthc Mater*. 2016;5(21):2732-2744. doi:10.1002/adhm.201600236

29. López Cebral R, Silva-Correia J, Reis RL, Silva TH, Oliveira JM. Peripheral nerve injury: Current challenges, conventional treatment approaches and new trends on biomaterials-based regenerative strategies. *ACS Biomater Sci Eng*. 2017:acsbiomaterials.7b00655. doi:10.1021/acsbiomaterials.7b00655

30. Silver J, Fitch M. CNS Injury, Glial Scars, and Inflammation: Inhibitory extracellular matrices and regeneration failure. 2009;129(1):77-83. doi:10.1021/ja064902

31. Tam RY, Fuehrmann T, Mitrousis N, Shoichet MS. Regenerative therapies for central nervous system diseases: A biomaterials approach. *Neuropsychopharmacology*. 2014;39(1):169-188. doi:10.1038/npp.2013.237

32. Stoll EA. Advances toward regenerative medicine in the central nervous system: challenges in making stem cell therapy a viable clinical strategy. *Mol Cell Ther*. 2014;2:12. doi:10.1186/2052-8426-2-12

33. Su Liu, Yun Qu, Todd J. Stewart, Michael J. Howard, Shushovan Chakrabortty, Terrence F. Holekamp and JWM. Embryonic stem cells differentiate into oligodendrocytes and myelinate in culture and after spinal cord transplantation. *Pnas*. 2000;49(3):385-396. doi:10.1073/pnas.97.11.6126

34. Lee J, Kuroda S, Shichinohe H, et al. Migration and differentiation of nuclear fluorescence-labeled bone marrow stromal cells after transplantation into cerebral infarct and spinal cord injury in mice. *Neuropathology*. 2003;23(3):169-180. doi:10.1046/j.1440-1789.2003.00496

35. Kolb B, Morshead C, Gonzalez C, et al. Growth factor-stimulated generation of new cortical tissue and functional recovery after stroke damage to the motor cortex of rats. *J Cereb Blood Flow Metab*. 2007;27(5):983-997. doi:10.1038/sj.jcbfm.9600402

36. McTigue DM, Horner PJ, Stokes BT, Gage FH. Neurotrophin-3 and brain-derived neurotrophic factor induce oligodendrocyte proliferation and myelination of

regenerating axons in the contused adult rat spinal cord. *J Neurosci*. 1998;18(14):5354-5365. doi:10.1523/JNEUROSCI.18-14-05354.1998

37. Pan H-C, Cheng F-C, Chen C-J, et al. Post-injury regeneration in rat sciatic nerve facilitated by neurotrophic factors secreted by amniotic fluid mesenchymal stem cells. *J Clin Neurosci*. 2007;14(11):1089-1098. doi:10.1016/j.jocn.2006.08.008

38. Dubois-Dalcq M, Ffrench-Constant C, Franklin RJM. Enhancing central nervous system remyelination in multiple sclerosis. *Neuron*. 2005;48(1):9-12. doi:10.1016/j.neuron.2005.09.004

39. Xu X-Y, Li X-T, Peng S-W, et al. The behaviour of neural stem cells on polyhydroxyalkanoate nanofiber scaffolds. *Biomaterials*. 2010;31(14):3967-3975. doi:10.1016/J.BIOMATERIALS.2010.01.132

40. Tonge DA, De Burgh HT, Docherty R, Humphries MJ, Craig SE, Pizzey J. Fibronectin supports neurite outgrowth and axonal regeneration of adult brain neurons in vitro. *Brain Res*. 2012;1453:8-16. doi:10.1016/j.brainres.2012.03.024

41. Hong JY, Lee SH, Lee SC, et al. Therapeutic Potential of Induced Neural Stem Cells for Spinal Cord Injury. *J Biol Chem*. 2014;289(47):32512-32525. doi:10.1074/jbc.M114.588871

42. Maldonado-Soto AR, Oakley DH, Wichterle H, Stein J, Doetsch FK, Henderson CE. Stem cells in the nervous system. *Am J Phys Med Rehabil*. 2014;93(11):S132-S144. doi:10.1097/PHM.0000000000000111

43. Teixeira FG, Carvalho MM, Sousa N, Salgado AJ. Mesenchymal stem cells secretome: A new paradigm for central nervous system regeneration? *Cell Mol Life Sci*. 2013;70(20):3871-3882. doi:10.1007/s00018-013-1290-8

44. Di Liddo R, Bertalot T, Barbon S, Rajendran S, Gasparella M, Parnigotto PP CM. *Differentiative Potential of Fibroblast-like Cells from Human Peripheral Blood*. National congress S.I.A.I. - Società Italiana di Anatomia e Istologia, Pistoia 2012a, Congress book.; 2012.

45. Scapin G, Bertalot T, Vicentini N, et al. Neuronal commitment of human circulating multipotent cells by carbon nanotube-polymer scaffolds and biomimetic peptides. *Nanomedicine*. 2016;11(15):1929-1946. doi:10.2217/nnm-2016-0150

46. Vicentini N, Gatti T, Salice P, et al. Covalent functionalization enables good dispersion and anisotropic orientation of multi-walled carbon nanotubes in a poly(l-lactic acid) electrospun nanofibrous matrix boosting neuronal differentiation. *Carbon N Y*. 2015;95:725-730. doi:10.1016/j.carbon.2015.08.094

47. López-Carballo G, Moreno L, Masiá S, Pérez P, Barettino D. Activation of the phosphatidylinositol 3-kinase/Akt signaling pathway by retinoic acid is required for neural differentiation of SH-SY5Y human neuroblastoma cells. *J Biol Chem*. 2002;277(28):25297-25304. doi:10.1074/jbc.M201869200

48. Shipley MM, Mangold CA, Szpara ML. Differentiation of the SH-SY5Y human neuroblastoma cell line. *J Vis Exp*. 2017;108(108):53193. doi:10.3791/53193

49. Kovalevich J, Langford D. Neuronal Cell Culture. 2013;1078:9-21. doi:10.1007/978-1-62703-640-5

50. Yasushi Shimoda and Kazutada Watanabe. Contactins: Emerging key roles in the development and function of the nervous system. 2009;3(1):64-70.

51. Freigang J, Proba K, Leder L, Diederichs K, Sonderegger P, Welte W. The crystal structure of the ligand binding module of axonin-1/TAG-1 suggests a zipper mechanism for neural cell adhesion. *Cell*. 2000;101(4):425-433. doi:10.1016/S0092-8674(00)80852-1

52. Bouyain S, Watkins DJ. The protein tyrosine phosphatases PTPRZ and PTPRG bind to distinct members of the contactin family of neural recognition molecules. *Proc Natl Acad Sci*. 2010;107(6):2443-2448. doi:10.1073/pnas.0911235107

53. Stoeckli ET. Neural circuit formation in the cerebellum is controlled by cell adhesion molecules of the Contactin family. *Cell Adhes Migr*. 2010;4(4):523-526. doi:10.4161/cam.4.4.12733

54. Mercati O, Danckaert A, Andre-Leroux G, et al. Contactin 4, -5 and -6 differentially regulate neuritogenesis while they display identical PTPRG binding sites. *Biol Open*. 2013;2(3):324-334. doi:10.1242/bio.20133343

55. Colakoglu G, Bergstrom-Tyrberg U, Berglund EO, Ranscht B. Contactin-1 regulates myelination and nodal/paranodal domain organization in the central nervous system. *Proc Natl Acad Sci*. 2014;111(3):E394-E403. doi:10.1073/pnas.1313769110

56. Compton AG, Albrecht DE, Seto JT, et al. Mutations in Contactin-1, a Neural Adhesion and Neuromuscular Junction Protein, Cause a Familial Form of Lethal Congenital Myopathy. *Am J Hum Genet*. 2008;83(6):714-724. doi:10.1016/j.ajhg.2008.10.022

57. Yan J, Ojo D, Kapoor A, et al. Neural cell adhesion protein CNTN1 promotes the metastatic progression of prostate cancer. *Cancer Res*. 2016;76(6):1603-1614. doi:10.1158/0008-5472

58. Masuda T. Contactin-2/TAG-1, active on the front line for three decades. *Cell Adhes Migr*. 2017;11(5-6):524-531. doi:10.1080/19336918.2016.1269998

59. Traka M, Dupree JL, Popko B, Karagogeos D. The neuronal adhesion protein TAG-1 is expressed by Schwann cells and oligodendrocytes and is localized to the juxtaparanodal region of myelinated fibers. *J Neurosci*. 2002;22(8):3016-3024. doi:20026306

60. Stogmann E, Reinthaler E, Eltawil S, et al. Autosomal recessive cortical myoclonic tremor and epilepsy: Association with a mutation in the potassium channel associated gene CNTN2. *Brain*. 2013;136(4):1155-1160. doi:doi:10.1093/brain/awt068

61. Fernandez T, Morgan T, Davis N, et al. Disruption of Contactin 4 (CNTN4) results in developmental delay and other features of 3p deletion syndrome. *Am J Hum Genet*. 2008;82(6):1385. doi:10.1016/j.ajhg.2008.04.021

62. Zuko A, Kleijer KTE, Oguro-Ando A, et al. Contactins in the neurobiology of autism. *Eur J Pharmacol*. 2013;719(1-3):63-74. doi:10.1016/j.ejphar.2013.07.016

63. Shimoda Y, Koseki F, Itoh M, Toyoshima M, Watanabe K. A cis-complex of NB-2/contactin-5 with amyloid precursor-like protein 1 is localized on the presynaptic membrane. *Neurosci Lett*. 2012;510(2):148-153. doi:10.1016/j.neulet.2012.01.026

64. Toyoshima M, Sakurai K, Shimazaki K, Takeda Y, Shimoda Y, Watanabe K. Deficiency of neural recognition molecule NB-2 affects the development of glutamatergic auditory pathways from the ventral cochlear nucleus to the superior olivary complex in mouse. *Dev Biol*. 2009;336(2):192-200. doi:10.1016/j.ydbio.2009.09.043

65. Blockus H, Che A. Slit-Robo signaling. 2016:3037-3044. doi:10.1242/dev.132829

66. Ba-charvet KTN, Brose K, Ma L, et al. Diversity and Specificity of Actions of Slit2 Proteolytic Fragments in Axon Guidance. 2001;21(12):4281-4289.

67. Gara RK, Kumari S, Ganju A, Yallapu MM, Jaggi M, Chauhan SC. Slit/Robo pathway: A promising therapeutic target for cancer. *Drug Discov Today*. 2015;20(1):156-164. doi:10.1016/j.drudis.2014.09.008

68. Andrews WD, Barber M, Parnavelas JG. Slit – Robo interactions during cortical development. 2007:188-198. doi:10.1111/j.1469-7580.2007.00750.x

69. Howitt JA, Clout NJ, Hohenester E. Binding site for Robo receptors revealed by dissection of the leucine-rich repeat region of Slit. 2004;23(22):4406-4412. doi:10.1038/sj.emboj.7600446

70. Hivert B, Liu Z, Chuang C, Doherty P. Robo1 and Robo2 Are Homophilic Binding Molecules That Promote Axonal Growth. 2002;545:534-545. doi:10.1006/mcne.2002.1193

71. Evans TA, Bashaw GJ. Report Functional Diversity of Robo Receptor Immunoglobulin Domains Promotes Distinct Axon Guidance Decisions. *Curr Biol*. 2010;20(6):567-572. doi:10.1016/j.cub.2010.02.021

72. Morlot C, Thielens NM, Ravelli RBG, et al. Structural insights into the Slit-Robo complex. *Proc Natl Acad Sci*. 2007;104(38):14923-14928. doi:10.1073/pnas.0705310104

73. Meglio T Di, Nguyen-ba-charvet KT, Tessier-lavigne M, Sotelo C. Molecular Mechanisms Controlling Midline Crossing by Precerebellar Neurons. 2008;28(25):6285-6294. doi:10.1523/JNEUROSCI.0078-08.2008

74. Guan C, Xu H, Jin M, Yuan X, Poo M. Long-Range Ca 2 + Signaling from Growth Cone to Soma Mediates Reversal of Neuronal Migration Induced by Slit-2. 2007:385-395. doi:10.1016/j.cell.2007.01.051

75. Luis R Hernandez-Miranda JGP and FC. Molecules and mechanisms involved in the generation and migration of cortical interneurons. 2010;2(2):75-86. doi:10.1042/AN20090053

76. Dimitrova S, Reissaus A, Tavosanis G. Slit and Robo regulate dendrite branching and elongation of space- fi lling neurons in Drosophila. *Dev Biol*. 2008;324(1):18-30. doi:10.1016/j.ydbio.2008.08.028

77. Ypsilanti AR, Zagar Y, Chédotal A. Moving away from the midline : new developments for Slit and Robo. 2010;1952:1939-1952. doi:10.1242/dev.044511

78. Fernandis AZ, Ganju RK, Israel B. Slit : A Roadblock for Chemotaxis. 2001;(July):1-4.

79. Barak R, Lahmi R, Gevorkyan-Airapetov L, Levy E, Tzur A, Opatowsky Y. Crystal structure of the extracellular juxtamembrane region of Robo1. *J Struct Biol*. 2014;186(2):283-291. doi:10.1016/j.jsb.2014.02.019

80. Anitha A, Nakamura K, Yamada K, et al. Genetic Analyses of Roundabout (ROBO) Axon Guidance Receptors in Autism. 2008;1027(August 2007):1019-1027. doi:10.1002/ajmg.b.30697

81. Gulsuner S, Walsh T, Watts AC, et al. Spatial and Temporal Mapping of De Novo Mutations in Schizophrenia to a Fetal Prefrontal Cortical Network. 2012. doi:10.1016/j.cell.2013.06.049

82. W-M Chan, E I Traboulsi, B Arthur, N Friedman, C Andrews ECE. Horizontal gaze palsy with progressive scoliosis can result from compound heterozygous mutations in ROBO3. 2006:3-6. doi:10.1136/jmg.2005.035436

83. Chen Z, Gore BB, Long H, Ma L, Tessier-lavigne M. Report Alternative Splicing of the Robo3 Axon Guidance Receptor Governs the Midline Switch from Attraction to Repulsion. 2008:325-332. doi:10.1016/j.neuron.2008.02.016

84. Beamish I V, Kennedy TE. Previews Robo3 : The Road Taken. *Dev Cell*. 2015;32(1):3-4. doi:10.1016/j.devcel.2014.12.021

85. Dickinson RE, Duncan WC. The SLIT / ROBO pathway : a regulator of cell function with implications for the reproductive system. *Reproduction*. 2010;139(4):697-704. doi:10.1530/REP-10-0017.The

86. Hedrick L, Cho KR, Fearon ER, Kinzler KW. The DCC gene product in cellular differentiation and colorectal tumorigenesis. 1994:1174-1183.

87. Stein E, Tessier-lavigne M. Hierarchical Organization of Guidance Receptors : Silencing of Netrin Robo / DCC Receptor Complex Growth cone. *Science (80-)*. 2004;291(March):1928-1939.

88. Finci LI, Kru N, Sun X, et al. The Crystal Structure of Netrin-1 in Complex with DCC Reveals the Bifunctionality of Netrin-1 As a Guidance Cue. 2014:839-849. doi:10.1016/j.neuron.2014.07.010

89. Finci L, Zhang Y, Meijers R, Wang JH. Signaling mechanism of the netrin-1 receptor DCC in axon guidance. *Prog Biophys Mol Biol*. 2015;118(3):153-160. doi:10.1016/j.pbiomolbio.2015.04.001

90. Barallobre MJ, Pascual M, Del Río JA, Soriano E. The Netrin family of guidance factors: Emphasis on Netrin-1 signalling. *Brain Res Rev*. 2005;49(1):22-47. doi:10.1016/j.brainresrev.2004.11.003

91. Boyer NP, Gupton SL, Suter DM, Moore S. Revisiting Netrin-1 : One Who Guides (Axons). 2018;12(July):1-18. doi:10.3389/fncel.2018.00221

92. Dickson BJ, Zou Y. Navigating Intermediate Targets : The Nervous System Midline. 2010:1-16.

93. Maness PF, Schachner M. Neural recognition molecules of the immunoglobulin superfamily: Signaling transducers of axon guidance and neuronal migration. *Nat Neurosci*. 2007;10(1):19-26. doi:10.1038/nn1827

94. Hortsch M. Structural and functional evolution of the L1 family: Are four adhesion

molecules better than one? *Mol Cell Neurosci*. 2000;15(1):1-10. doi:10.1006/mcne.1999.0809

95. Siesser PF, Maness PF, Siesser PF, Maness PF. L1 cell adhesion molecules as regulators of tumor cell invasiveness. 2009;6918:10-13. doi:10.4161/cam.3.3.8689

96. Herron LR, Hill M, Davey F, Gunn-Moore FJ. The intracellular interactions of the L1 family of cell adhesion molecules. *Biochem J*. 2009;419:519-531. doi:10.1042/BJ20082284

97. Hlavin ML, Lemmon V. Molecular structure and functional testing of human L1CAM: An interspecies comparison. *Genomics*. 1991;11(2):416-423. doi:10.1016/0888-7543(91)90150-D

98. Mikulak J, Negrini S, Klajn A, D'Alessandro R, Mavilio D, Meldolesi J. Dual REST-dependence of L1CAM: From gene expression to alternative splicing governed by Nova2 in neural cells. *J Neurochem*. 2012;120(5):699-709. doi:10.1111/j.1471-4159.2011.07626.x

99. Kamiguchi H, Lemmon V. Neural cell adhesion molecule L1: signaling pathways and growth cone motility. *J Neurosci Res*. 1997;49(1):1-8.

100. Schäfer MKE, Frotscher M. Role of L1CAM for axon sprouting and branching. *Cell Tissue Res*. 2012;349(1):39-48. doi:10.1007/s00441-012-1345-4

101. De Angelis E, Watkins A, Schäfer M, Brümmendorf T, Kenwrick S. Disease-associated mutations in L1 CAM interfere with ligand interactions and cell-surface expression. *Hum Mol Genet*. 2002;11(1):1-12. doi:10.1093/hmg/11.1.1

102. Tagliavacca L, Colombo F, Racchetti G, Meldolesi J. L1CAM and its cell-surface mutants: New mechanisms and effects relevant to the physiology and pathology of neural cells. *J Neurochem*. 2013;124(3):397-409. doi:10.1111/jnc.12015

103. Kiefel H, Bondong S, Hazin J, et al. L1CAM: A major driver for tumor cell invasion and motility. *Cell Adhes Migr*. 2012;6(4):374-384. doi:10.4161/cam.20832

104. Maretzky T, Schulte M, Ludwig A, et al. L1 is sequentially processed by two differently activated metalloproteases and presenilin/γ-secretase and regulates neural cell adhesion, cell migration, and neurite outgrowth. *Mol Cell Biol*. 2005;25(20):9040-9053. doi:10.1128/MCB.25.20.9040

105. Zhao X, Siu CH. Colocalization of the homophilic binding site and the neuritogenic activity of the cell adhesion molecule L1 to its second Ig-like domain. *J Biol Chem*. 1995;270(49):29413-29421. doi:10.1074/jbc.270.49.29413

106. Zhao XN, Yip PM, Siu CH. Identification of a homophilic binding site in immunoglobulin-like domain 2 of the cell adhesion molecule L1. *J Neurochem*. 1998;71(3):960-971.

107. De Angelis E, Macfarlane J, Du J-S, et al. Pathological missense mutations of neural cell adhesion molecule L1 affect homophilic and heterphilic binding activities. *Embo J*. 1999;18(17):4744-4753.

108. Gouveia RM, Morais VA, Peixoto C, et al. Production and purification of functional truncated soluble forms of human recombinant L1 cell adhesion glycoprotein from Spodoptera frugiperda Sf9 cells. *Protein Expr Purif*. 2007;52(1):182-193. doi:10.1016/j.pep.2006.10.008

109. Gouveia RM, Gomes CM, Sousa M, Alves PM, Costa J. Kinetic analysis of L1 homophilic interaction: Role of the first four immunoglobulin domains and implications on binding mechanism. *J Biol Chem*. 2008;283(42):28038-28047. doi:10.1074/jbc.M804991200

110. Liu H, Focia PJ, He X. Homophilic adhesion mechanism of neurofascin, a member of the L1 family of neural cell adhesion molecules. *J Biol Chem*. 2011;286(1):797-805. doi:10.1074/jbc.M110.180281

111. Schürmann G, Haspel J, Grumet M, Erickson HP. Cell adhesion molecule L1 in folded (horseshoe) and extended conformations. *Mol Biol Cell*. 2001;12(6):1765-1773. doi:10.1091/mbc.12.6.1765

112. Rathjen FG, Wolff JM, Chang S, Bonhoeffer F, Raper JA. Neurofascin: A novel chick cell-surface glycoprotein involved in neurite-neurite interactions. *Cell*. 1987;51(5):841-849. doi:https://doi.org/10.1016/0092-8674(87)90107-3

113. Zonta B, Tait S, Melrose S, et al. Glial and neuronal isoforms of Neurofascin have distinct roles in the assembly of nodes of Ranvier in the central nervous system. 2007:1169-1177. doi:10.1083/jcb.200712154

114. Suzuki S, Ayukawa N, Okada C, Tanaka M, Takekoshi S. Spatio-temporal and dynamic regulation of neurofascin alternative splicing in mouse cerebellar neurons. *Sci Rep*. 2017;(April):1-13. doi:10.1038/s41598-017-11319-5

115. Kriebel M, Wuchter J, Trinks S, Volkmer H. Neurofascin : A switch between neuronal plasticity and stability. *Int J Biochem Cell Biol*. 2012;44(5):694-697. doi:10.1016/j.biocel.2012.01.012

116. Koticha D, Babiarz J, Kane-goldsmith N, Jacob J, Raju K, Grumet M. Cell adhesion and neurite outgrowth are promoted by neurofascin NF155 and inhibited by NF186.

2005;30:137-148. doi:10.1016/j.mcn.2005.06.007

117. Zelina P, Avci HX, Thelen K, Pollerberg GE. The cell adhesion molecule NrCAM is crucial for growth cone behaviour and pathfinding of retinal ganglion cell axons. 2005:3609-3618. doi:10.1242/dev.01934

118. Sakurai T. The role of NrCAM in neural development and disorders-Beyond a simple glue in the brain. *Mol Cell Neurosci*. 2012;49(3):351-363. doi:10.1016/j.mcn.2011.12.002

119. Atz ME, Rollins B, Vawter MP. NCAM1 association study of bipolar disorder and schizophrenia: Polymorphisms and alternatively spliced isoforms lead to similarities and differences. *Psychiatr Genet*. 2007;17(2):55-67. doi:10.1097/YPG.0b013e328012d850

120. Matzel LD, Babiarz J, Townsend DA. Neuronal cell adhesion molecule deletion induces a cognitive and behavioral phenotype reflective of impulsivity. 2008:470-480. doi:10.1111/j.1601-183X.2007.00382.x

121. Demyanenko GP, Riday TT, Tran TS, et al. NrCAM Deletion Causes Topographic Mistargeting of Thalamocortical Axons to the Visual Cortex and Disrupts Visual Acuity. 2011;31(4):1545-1558. doi:10.1523/JNEUROSCI.4467-10.2011

122. Sakurai T, Ramoz N, Reichert JG, et al. Association analysis of the NrCAM gene in autism and in subsets of families with severe obsessive-compulsive or self-stimulatory behaviors. *Psychiatr Genet*. 2006;16(6):251-257. doi:10.1097/01.ypg.0000242196.81891.c9

123. Custer AW, Kazarinova-noyes K, Sakurai T, et al. The Role of the Ankyrin-Binding Protein NrCAM in Node of Ranvier Formation. 2003;23(31):10032-10039.

124. Feinberg K, Eshed-eisenbach Y, Frechter S, et al. Article A Glial Signal Consisting of Gliomedin and NrCAM Clusters Axonal Na + Channels during the Formation of Nodes of Ranvier. *Neuron*. 2010;65(4):490-502. doi:10.1016/j.neuron.2010.02.004

125. Volkmer H, Leuschner R, Zacharias U, Rathjen FG. Neurofascin induces neurites by heterophilic interactions with axonal NrCAM while NrCAM requires F11 on the axonal surface to extend neurites. *J Cell Biol*. 1996;135(4):1059-1069. doi:10.1083/jcb.135.4.1059

126. Volkmer H, Zacharias U, Nörenberg U, Rathjen FG. Dissection of complex molecular interactions of neurofascin with axonin- 1, F11, and tenascin-R, which promote attachment and neurite formation of tectal cells. *J Cell Biol*. 1998;142(4):1083-1093. doi:10.1083/jcb.142.4.1083

127. Wei MH, Karavanova I, Ivanov S V, et al. In silico-initiated cloning and molecular characterization of a novel human member of the L1 gene family of neural cell adhesion molecules. *Hum Genet*. 1998;103(3):355-364.

128. Hillenbrand R, Molthagen M, Montag D, Schachner M. The close homologue of the neural adhesion molecule L1 (CHL1): Patterns of expression and promotion of neurite outgrowth by heterophilic interactions. *Eur J Neurosci*. 1999;11(3):813-826. doi:10.1046/j.1460-9568.1999.00496.x

129. Demyanenko GP, Schachner M, Anton E, et al. Close homolog of L1 modulates area-specific neuronal positioning and dendrite orientation in the cerebral cortex. *Neuron*. 2004;44(3):423-437. doi:10.1016/j.neuron.2004.10.016

130. Angeloni D, Lindor NM, Pack S, Latif F, Wei M-H, Lerman MI. CALL gene is haploinsufficient in a 3p? syndrome patient. *Am J Med Genet*. 1999;86(5):482-485. doi:10.1002

131. Sakurai K, Migita O, Toru M, Arinami T. An association between a missense polymorphism in the close homologue of L1 (CHL1 , CALL) gene and. 2002:412-415. doi:10.1038/sj/mp/4000973

132. Guseva D, Jakovcevski I, Irintchev A, et al. Cell Adhesion Molecule Close Homolog of L1 (CHL1) Guides the Regrowth of Regenerating Motor Axons and Regulates Synaptic Coverage of Motor Neurons. 2018;11(May):1-14. doi:10.3389/fnmol.2018.00174

133. Katic J, Loers G, Kleene R, et al. Interaction of the Cell Adhesion Molecule CHL1 with Vitronectin , Integrins , and the Plasminogen Activator Inhibitor-2 Promotes CHL1-Induced Neurite Outgrowth and Neuronal Migration. 2014;34(44):14606-14623. doi:10.1523/JNEUROSCI.3280-13.2014

134. Wei CH, Ryu SE. Homophilic interaction of the L1 family of cell adhesion molecules. *Exp Mol Med*. 2012;44(7):413-423. doi:10.3858/emm.2012.44.7.050

135. Barão S, Gärtner A, Leyva-Díaz E, et al. Antagonistic Effects of BACE1 and APH1B-γ-Secretase Control Axonal Guidance by Regulating Growth Cone Collapse. *Cell Rep*. 2015;12(9):1367-1376. doi:10.1016/j.celrep.2015.07.059

136. Wu J, Wrathall JR, Schachner M. Phosphatidylinositol 3-Kinase / Protein Kinase C d Activation Induces Close Homolog of Adhesion Molecule L1 (CHL1) Expression in Cultured Astrocytes. 2010;328:315-328. doi:10.1002/glia.20925

137. Huang Z, Gao Y, Sun Y, et al. NB-3 signaling mediates the cross-talk between post-traumatic spinal axons and scar-forming cells. 2016;35(16):1745-1765. doi:doi:

10.15252/embj.201593460

138. Gatti T, Vicentini N, Mba M, Menna E. Organic Functionalized Carbon Nanostructures for Functional Polymer-Based Nanocomposites. 2016:1071-1090. doi:10.1002/ejoc.201501411

139. Ilie I, Ilie R, Mocan T, Bartos D, Mocan L. Influence of nanomaterials on stem cell differentiation: Designing an appropriate nanobiointerface. *Int J Nanomedicine*. 2012;7:2211-2225. doi:10.2147/IJN.S29975

140. Iglesias D, Bosi S, Melchionna M, Da Ros T, Marchesan S. The Glitter of Carbon Nanostructures in Hybrid/Composite Hydrogels for Medicinal Use. *Curr Top Med Chem*. 2016;16(18):1976-1989. doi:10.2174/1568026616666160215154807

141. Sucapane A, Cellot G, Prato M, Giugliano M, Ballerini L. Interactions Between Cultured Neurons and Carbon Nanotubes: A Nanoneuroscience Vignette. 2009;1(1):10-16.

142. Iijima S. Helical microtubules of graphitic carbon. *Nature*. 1991;354:56. http://dx.doi.org/10.1038/354056a0.

143. Saito N, Haniu H, Usui Y, et al. Safe clinical use of carbon nanotubes as innovative biomaterials. *Chem Rev*. 2014;114(11):6040-6079. doi:10.1021/cr400341h

144. Ribeiro B, Cocchieri Botelho E, Costa M, Fourquet Bandeira C. *Carbon Nanotube Buckypaper Reinforced Polymer Composites: A Review*. Vol 27.; 2017. doi:10.1590/0104-1428.03916

145. Fabbro A, Prato M, Ballerini L. Carbon nanotubes in neuroregeneration and repair. *Adv Drug Deliv Rev*. 2013;65(15):2034-2044. doi:10.1016/j.addr.2013.07.002

146. Sorkin R, Greenbaum A, David-pur M, Anava S. Process entanglement as a neuronal anchorage mechanism to rough surfaces. 2009. doi:10.1088/0957-4484/20/1/015101

147. Park SY, Choi DS, Jin HJ, et al. Polarization-Controlled Differentiation of Human Neural Stem Cells Using Synergistic Cues from the Patterns of Carbon Nanotube Monolayer Coating. *ACS Nano*. 2011;5(6):4704-4711. doi:10.1021/nn2006128

148. Jin G-Z, Kim M, Shin US, Kim H-W. Neurite outgrowth of dorsal root ganglia neurons is enhanced on aligned nanofibrous biopolymer scaffold with carbon nanotube coating. *Neurosci Lett*. 2011;501(1):10-14. doi:10.1016/j.neulet.2011.06.023

149. Mazzatenta A, Giugliano M, Campidelli S, et al. Interfacing neurons with carbon

nanotubes: electrical signal transfer and synaptic stimulation in cultured brain circuits. *J Neurosci*. 2007;27(26):6931-6936. doi:10.1523/JNEUROSCI.1051-07.2007

150. Cellot G, Toma FM, Kasap Varley Z, et al. Carbon nanotube scaffolds tune synaptic strength in cultured neural circuits: novel frontiers in nanomaterial-tissue interactions. *J Neurosci*. 2011;31(36):12945-12953. doi:10.1523/JNEUROSCI.1332-11.2011

151. Malarkey EB, Fisher KA, Bekyarova E, Liu W, Haddon RC, Parpura V. Conductive single-walled carbon nanotube substrates modulate neuronal growth. *Nano Lett*. 2009;9(1):264-268. doi:10.1021/nl802855c

152. Cho Y, Borgens R Ben. The effect of an electrically conductive carbon nanotube/collagen composite on neurite outgrowth of PC12 cells. *J Biomed Mater Res Part A*. 2010;95A(2):510-517. doi:10.1002/jbm.a.32841

153. Huang YJ, Wu HC, Tai NH, Wang TW. Carbon nanotube rope with electrical stimulation promotes the differentiation and maturity of neural stem cells. *Small*. 2012;8(18):2869-2877. doi:10.1002/smll.201200715

154. Landers J, Turner JT, Heden G, et al. Carbon Nanotube Composites as Multifunctional Substrates for In Situ Actuation of Differentiation of Human Neural Stem Cells. *Adv Healthc Mater*. 2014;3(11):1745-1752. doi:10.1002/adhm.201400042

155. David-Pur M, Bareket-Keren L, Beit-Yaakov G, Raz-Prag D, Hanein Y. All-carbon-nanotube flexible multi-electrode array for neuronal recording and stimulation. *Biomed Microdevices*. 2014;16(1):43-53. doi:10.1007/s10544-013-9804-6

156. Hu H, Ni Y, Montana V, Haddon RC, Parpura V. Chemically Functionalized Carbon Nanotubes as Substrates for Neuronal Growth. *Nano Lett*. 2004;4(3):507-511. doi:10.1021/nl035193d

157. Mattson MP, Haddon RC, Rao AM. Molecular Functionalization of Carbon Nanotubes and Use as Substrates for Neuronal Growth. *J Mol Neurosci*. 2000;14(3):175-182. doi:10.1385/JMN:14:3:175

158. Matsumoto K, Sato C, Naka Y, Kitazawa A, Whitby RLD, Shimizu N. Neurite outgrowths of neurons with neurotrophin-coated carbon nanotubes. *J Biosci Bioeng*. 2007;103(3):216-220. doi:10.1263/jbb.103.216

159. Kharaziha M, Shin SR, Nikkhah M, et al. Tough and flexible CNT–polymeric hybrid scaffolds for engineering cardiac constructs. *Biomaterials*. 2014;35(26):7346-7354.

doi:10.1016/j.biomaterials.2014.05.014

160. Lizundia E, Sarasua JR, D'Angelo F, et al. Biocompatible Poly(L-lactide)/MWCNT Nanocomposites: Morphological Characterization, Electrical Properties, and Stem Cell Interaction. *Macromol Biosci*. 2012;12(7):870-881. doi:10.1002/mabi.201200008

161. Yu W, Jiang X, Cai M, et al. A novel electrospun nerve conduit enhanced by carbon nanotubes for peripheral nerve regeneration. *Nanotechnology*. 2014;25(16). doi:10.1088/0957-4484/25/16/165102

162. Ahn H-S, Hwang J-Y, Kim MS, et al. Carbon-nanotube-interfaced glass fiber scaffold for regeneration of transected sciatic nerve. *Acta Biomater*. 2015;13:324-334. doi:10.1016/j.actbio.2014.11.026

163. Porter AE, Gass M, Muller K, Skepper JN, Midgley PA, Welland M. Direct imaging of single-walled carbon nanotubes in cells. *Nat Nanotechnol*. 2007;2(11):713-717. doi:10.1038/nnano.2007.347

164. Kolosnjaj-Tabi J, Hartman KB, Boudjemaa S, et al. In Vivo Behavior of Large Doses of Ultrashort and Full-Length Single-Walled Carbon Nanotubes after Oral and Intraperitoneal Administration to Swiss Mice. *ACS Nano*. 2010;4(3):1481-1492. doi:10.1021/nn901573w

165. Cui HF, Vashist SK, Al-Rubeaan K, Luong JHT, Sheu FS. Interfacing carbon nanotubes with living mammalian cells and cytotoxicity issues. *Chem Res Toxicol*. 2010;23(7):1131-1147. doi:10.1021/tx100050h

166. Lacerda L, Herrero MA, Venner K, Bianco A, Prato M, Kostarelos K. Carbon-Nanotube Shape and Individualization Critical for Renal Excretion. *Small*. 2008;4(8):1130-1132. doi:10.1002/smll.200800323

167. Kumar S, Chatterjee K. Comprehensive Review on the Use of Graphene-Based Substrates for Regenerative Medicine and Biomedical Devices. *ACS Appl Mater Interfaces*. 2016;8(40):26431-26457. doi:10.1021/acsami.6b09801

168. Gardin C, Piattelli A, Zavan B. Graphene in Regenerative Medicine: Focus on Stem Cells and Neuronal Differentiation. *Trends Biotechnol*. 2016;34(6):435-437. doi:10.1016/j.tibtech.2016.01.006

169. Jimenez-Cervantes E, López-Barroso J, Martínez-Hernández AL, Velasco-Santos C. Graphene-Based Materials Functionalization with Natural Polymeric Biomolecules. In: *Recent Advances in Graphene Research*. InTech; 2016. doi:10.5772/64001

170. Zhang Y, Nayak TR, Hong H, Cai W. Graphene: A versatile nanoplatform for biomedical applications. *Nanoscale*. 2012;4(13):3833-3842. doi:10.1039/c2nr31040f

171. Kostarelos K, Vincent M, Hebert C, Garrido JA. Graphene in the Design and Engineering of Next-Generation Neural Interfaces. *Adv Mater*. 2017;29(42):1-7. doi:10.1002/adma.201700909

172. Park SY, Park J, Sim SH, et al. Enhanced differentiation of human neural stem cells into neurons on graphene. *Adv Mater*. 2011;23(36):263-267. doi:10.1002/adma.201101503

173. Yang D, Li T, Xu M, et al. Graphene oxide promotes the differentiation of mouse embryonic stem cells to dopamine neurons. *Nanomedicine*. 2014;9(16):2445-2455. doi:10.2217/nnm.13.197

174. Duan S, Yang X, Mei F, et al. Enhanced osteogenic differentiation of mesenchymal stem cells on poly(L-lactide) nanofibrous scaffolds containing carbon nanomaterials. *J Biomed Mater Res - Part A*. 2015;103(4):1424-1435. doi:10.1002/jbm.a.35283

175. Chen G-Y, Pang DW-P, Hwang S-M, Tuan H-Y, Hu Y-C. A graphene-based platform for induced pluripotent stem cells culture and differentiation. *Biomaterials*. 2012;33(2):418-427. doi:10.1016/J.BIOMATERIALS.2011.09.071

176. Li N, Zhang X, Song Q, et al. The promotion of neurite sprouting and outgrowth of mouse hippocampal cells in culture by graphene substrates. *Biomaterials*. 2011;32(35):9374-9382. doi:10.1016/j.biomaterials.2011.08.065

177. Guo W, Qiu J, Liu J, Liu H. Graphene microfiber as a scaffold for regulation of neural stem cells differentiation. *Sci Rep*. 2017;7(1):1-8. doi:10.1038/s41598-017-06051-z

178. Weaver CL, Cui XT. Directed Neural Stem Cell Differentiation with a Functionalized Graphene Oxide Nanocomposite. *Adv Healthc Mater*. 2015;4(9):1408-1416. doi:10.1002/adhm.201500056

179. Shah S, Yin PT, Uehara TM, Chueng S-TD, Yang L, Lee K-B. Guiding Stem Cell Differentiation into Oligodendrocytes Using Graphene-Nanofiber Hybrid Scaffolds. *Adv Mater*. 2014;26(22):3673-3680. doi:10.1002/adma.201400523

180. Pampaloni NP, Lottner M, Giugliano M, et al. Single-layer graphene modulates neuronal communication and augments membrane ion currents. *Nat Nanotechnol*. 2018;13(8):755-764. doi:10.1038/s41565-018-0163-6

181. Akhavan O, Ghaderi E, Shirazian SA, Rahighi R. Rolled graphene oxide foams as three-dimensional scaffolds for growth of neural fibers using electrical stimulation of stem cells. *Carbon N Y*. 2016;97:71-77. doi:10.1016/j.carbon.2015.06.079

182. Yan L, Zhao B, Liu X, et al. Aligned Nanofibers from Polypyrrole/Graphene as Electrodes for Regeneration of Optic Nerve via Electrical Stimulation. 2016. doi:10.1021/acsami.5b12843

183. Iijima S, Yudasaka M, Yamada R, et al. Nano-aggregates of single-walled graphitic carbon nano-horns. *Chem Phys Lett*. 1999;309(3-4):165-170. doi:10.1016/S0009-2614(99)00642-9

184. Karousis N, Suarez-Martinez I, Ewels CP, Tagmatarchis N. Structure, Properties, Functionalization, and Applications of Carbon Nanohorns. *Chem Rev*. 2016;116(8):4850-4883. doi:10.1021/acs.chemrev.5b00611

185. Miyawaki J, Yudasaka M, Azami T, Kubo Y, Iijima S. Toxicity of Single-Walled Carbon Nanohorns. *ACS Nano*. 2008;2(2):213-226. doi:10.1021/nn700185t

186. Zhang M, Yamaguchi T, Iijima S, Yudasaka M. Size-dependent biodistribution of carbon nanohorns in vivo. *Nanomedicine Nanotechnology, Biol Med*. 2013;9(5):657-664. doi:10.1016/j.nano.2012.11.011

187. Yang M, Zhang M, Tahara Y, et al. Lysosomal membrane permeabilization: Carbon nanohorn-induced reactive oxygen species generation and toxicity by this neglected mechanism. *Toxicol Appl Pharmacol*. 2014;280(1):117-126. doi:10.1016/j.taap.2014.07.022

188. Lahiani MH, Chen J, Irin F, Puretzky AA, Green MJ, Khodakovskaya M V. Interaction of carbon nanohorns with plants: Uptake and biological effects. *Carbon N Y*. 2015;81(1):607-619. doi:10.1016/j.carbon.2014.09.095

189. Zhu S, Xu G. Single-walled carbon nanohorns and their applications. *Nanoscale*. 2010;2(12):2538-2549. doi:10.1039/c0nr00387e

190. Ajima K, Yudasaka M, Murakami T, Maigné A, Shiba K, Iijima S. Carbon nanohorns as anticancer drug carriers. *Mol Pharm*. 2005;2(6):475-480. doi:10.1021/mp0500566

191. Wu Y, Shi X, Li Y, et al. Carbon Nanohorns Promote Maturation of Neonatal Rat Ventricular Myocytes and Inhibit Proliferation of Cardiac Fibroblasts: a Promising Scaffold for Cardiac Tissue Engineering. *Nanoscale Res Lett*. 2016;11(1). doi:10.1186/s11671-016-1464-z

192. Vicentini N, Gatti T, Salerno M, et al. Effect of different functionalized carbon

nanostructures as fillers on the physical properties of biocompatible poly(L-lactic acid) composites. *Mater Chem Phys*. 2018;214:265-276. doi:10.1016/j.matchemphys.2018.04.042